Dipl.-Ing. Florian Pichler, BSc.

Multibody dynamics of jointed flexible structures

DISSERTATION

zur Erlangung des akademischen Grades
Doktor der technischen Wissenschaften

eingereicht an der
Technischen Universität Graz

Betreuer
Univ.-Prof. Dipl.-Ing. Dr.techn. Peter Fischer
Institut für Fahrzeugtechnik

Mitwirkung
Dipl.-Ing. Dr.techn. Wolfgang Witteveen

Graz, Juli 2018

Eidesstattliche Erklärung

Ich erkläre an Eides statt, dass ich die vorliegende Arbeit selbstständig verfasst, andere als die angegebenen Quellen/Hilfsmittel nicht benutzt, und die den benutzten Quellen wörtlich und inhaltlich entnommenen Stellen als solche kenntlich gemacht habe. Das in TUGRAZonline hochgeladene Textdokument ist mit der vorliegenden Dissertation identisch.

Graz, am _____ _____

Datum Unterschrift

Statutory Declaration

I declare that I have authored this thesis independently, that I have not used other than the declared sources/resources, and that I have explicitly marked all material which has been quoted either literally or by content from the used sources. The text document uploaded in TUGRAZonline is identical to the present dissertation.

Graz, _____ _____

Date Signature

Danksagung

Die vorliegende Dissertation entstand im Rahmen des Doktoratsstudiums an der Technischen Universität Graz am Institute für Fahrzeugtechnik. Mein Dank gilt Herrn Univ.-Prof. Dipl.-Ing. Dr.techn. Peter Fischer für seinen Einsatz, welcher es mir ermöglicht hat diese Arbeit an der Technischen Universität Graz anzufertigen. Die fachlichen Diskussionen und die konstruktive Betreuung haben wesentlich zum Gelingen dieser Arbeit beigetragen.

Ich möchte mich auch bei Herrn Univ.-Prof. Dr.-Ing. habil. Alexander Lion von der Universität der Bundeswehr München für die Begutachtung dieser Arbeit bedanken.

Ein ganz herzliches und freundschaftliches Dankeschön gebührt Herrn FH-Prof. Dipl.-Ing. Dr.techn. Wolfgang Witteveen. Ohne dessen Inspiration, Anleitung und unermüdlichen Einsatz wäre die Umsetzung und Fertigstellung dieser Arbeit nicht möglich gewesen.

Auch bedanken möchte ich mich bei all meinen Kollegen aus der Forschungsgruppe für Mehrkörperdynamik der Fachhochschule Wels. Besonders meinen Bürokollegen für ihre Unterstützung, Hilfsbereitschaft und die freundschaftliche Arbeitsatmosphäre.

Bedanken möchte ich mich auch bei unserem Industriepartner, der mir die Anwendung der erarbeiteten Theorie an praxisrelevanten Beispielen ermöglicht hat.

Am allerherzlichsten möchte ich mich bei meiner ganzen Familie und besonders bei meiner großen Liebe Susanne bedanken. Sie haben mich zu jeder Zeit zur Durchführung und Fertigstellung dieser Arbeit ermutigt und mir geholfen den Fokus für die wirklich wichtigen Dinge im Leben nicht zu verlieren.

Die Anstellung als wissenschaftlicher Mitarbeiter an der FH OÖ Forschungs und Entwicklungs GmbH wurde zum Teil aus dem Forschungsprojekt "MKS 2020", welches über das Förderprogramm "Regionale Wettbewerbsfähigkeit OÖ 2010-2013" finanziert wurde, möglich. Zusätzlich wurde mir ein Teil der Anstellung durch das Amt der Oö Landesregierung über ein Förderprogramm für wissenschaftlichen Nachwuchs finanziert.

Kurzfassung

Komplexe mechanische Strukturen bestehen häufig aus mehreren Substrukturen, welche durch Schraubverbindungen, Pressverbindungen oder andere Verbindungen zusammengebaut sind. Die nichtlinearen Kontakt- und Reibkräfte welche an den Fügestellen solcher Verbindungen auftreten, können das globale und lokale dynamische Verhalten maßgeblich beeinflussen. In die Mehrkörperdynamik werden lineare flexible Körper häufig via Modellreduktion (z.B. component mode synthesis) eingebunden. Solche Reduktionsmethoden erlauben im Allgemeinen keine genaue Berechnung der lokalen Deformationen innerhalb der Fügestelle. Infolgedessen führen unrealistische Kontakt- und Reibkräfte zu fragwürdigen Ergebnissen hinsichtlich der Verformungen und Spannungen.

In der vorliegenden Dissertation wird eine vollständige Strategie für eine effiziente und genaue Berücksichtigung der nichtlinearen Fügestellenkräfte innerhalb eines flexiblen Mehrkörpersystems präsentiert. Dazu werden die Bewegungsgleichungen um den Vektor der generalisierten Fügestellenkräfte erweitert. Eine numerisch günstige Formulierung dieser generalisierten Fügestellenkräfte und den dazugehörenden Termen in der Jakobimatrix wird vorgestellt.
Um Fügestellendeformationen mit der notwendigen Genauigkeit abbilden zu können wird eine problemorientierte Erweiterung klassischer Reduktionsbasen (wie z.B. Craig/Bampton) mit sogenannten Kontaktmoden (joint modes) präsentiert. Drei unterschiedliche Berechnungsansätze für diese Kontaktmoden werden vorgestellt und numerisch untersucht. Alle drei Methoden basieren auf sogenannten modalen Ableitungen. Für alle Berechnungsmethoden wurde eine Ergebnisgenauigkeit vergleichbar zu Ergebnissen der Finiten Elemente Methode erzielt. Dabei ist die Anzahl an Kontaktmoden um bis zu 95% geringer als die Fügestelle Knotenfreiheitsgrade hat. Für die praktische Anwendung werden schließlich jene Kontaktmoden vorgeschlagen die basierend auf einer gewichteten „proper orthogonal decomposition“ der modalen Ableitungen berechnet werden. Zusätzlich wird eine optimierte Berechnung dieser Kontaktmoden für vorgespannte Strukturen vorgestellt.
Für eine realistische Abbildung von Trockenreibung innerhalb der Fügestelle werden unterschiedliche Kontakt- und Reibmodelle untersucht. Diese Modelle wurden hinsichtlich numerischer Effizienz und anderer Kriterien bewertet. Basierend auf numerischen Untersuchungen wird ein adaptiertes exponentielles Kontaktmodell und ein drei Parameter Coulomb Reibmodell empfohlen.

Die vorgestellte Strategie erlaubt eine effiziente Mehrkörpersimulation von gefügten flexiblen Strukturen wobei die Ergebnisqualität hinsichtlich Verformungen und Spannungen mit der finiten Elemente Methode vergleichbar ist. Zwei exemplarische Anwendungen aus dem Gebiet der Fahrzeugtechnik (Zweimassenschwungrad und Lagerstuhl einer Verbrennungskraftmaschine) bestätigen die praktische Relevanz.

Abstract

Complex mechanical structures are often an assembly of substructures which are connected by some type of joints, like screwed joints, crimp connections and others. The nonlinear contact and friction forces, which act on the involved surfaces of such joints, may influence the global and local dynamic behavior significantly. In multibody dynamic simulations, linear flexible bodies are often considered via model order reduction techniques like component mode synthesis. Such reduction methods do not allow an accurate computation of the local deformations inside the latter mentioned joints. Consequently, unrealistic contact and friction forces lead to questionable results in terms of deformations and stresses.

In this thesis, a complete strategy for the efficient and accurate consideration of nonlinear joint forces within flexible multibody dynamics is presented. For this purpose, the jointed structure is considered as one flexible body in a multibody system. Furthermore, the equations of motion of a flexible multibody system are extended by the vector of generalized joint forces. A computational efficient formulation of these generalized joint forces and the associated terms in the system's Jacobian is derived.
A problem-oriented extension of common reduction basis with so-called joint modes is introduced in order to enable an accurate approximation of the joint deformations. Three different approaches for the computation of these joint modes are presented. All three methods are based on the use of trial vector derivatives and were investigated with respect to the number of required joint modes for accurate results. An accuracy comparable to the finite element method was achieved by a number of joint modes which is up to 95% lower than the number of nodal degrees of freedom inside the joint. Joint modes computed by a stiffness weighted proper orthogonal decomposition of all trial vector derivatives are recommended for practical application. Furthermore, an optimized computation of these joint modes for preloaded structures has been developed.
For the realistic representation of dry friction joint properties different contact and friction models are reviewed. These models have been rated in terms of numerical efficiency and other criteria. Based on different numerical studies, a joint adapted exponential contact penalty model and a three-parameter Coulomb-type friction model are recommended.

In conclusion, the presented strategy permits efficient multibody simulation of jointed flexible structures with a result quality in terms of displacements and stresses comparable to the finite element method. Two exemplary applications from the field of automotive engineering confirm the practical relevance of the presented strategy.

Contents

List of Figures

List of Figures

List of Tables

Abbreviations

APHR	A priori hyper-reduction
CMS	Component mode synthesis
CPU	Central processing unit
DEIM	Discrete empirical interpolation method
ECSW	Energy-conserving (mesh) sampling and weighting
EMA	Experimental modal analysis
FE	Finite element
FEM	Finite element method
FFRF	Floating frame of reference formulation
HFM	High frequency mode
HHT	Hilbert-Hughes-Taylor
LFM	Low frequency mode
MBS	Multibody simulation
MD(s)	Modal derivative(s)
PLM(s)	Preload mode(s)
POD	Proper orthogonal decomposition
POMs	Proper orthogonal mode(s)
POVs	Proper orthogonal value(s)
TVDs	Trial vector derivative(s)
UDEIM	Unassembled discrete empirical interpolation method
wPOD	Weighted proper orthogonal decomposition

Nomenclature

$()^i$	Quantities described for body i
$\lvert(\,)\rvert$	Absolute value of $(\,)$
${}^{C_i}(\,)$	Quantitiy $(\,)$ described in the local coordinate system C_i of the contact pair
$\Delta(\,)$	Difference of quantity $(\,)$
${}^{B}(\,)$	Quantitiy $(\,)$ described in the body coordinate system B
$(\,)^{-1}$	Inverse of matrix $(\,)$
$\operatorname{sgn}(\,)$	Signum function of $(\,)$
$\tilde{(\,)}$	Skew-symmetric matrix representation of the corresponding vector $\vec{(\,)}$
$\lVert(\,)\rVert_2$	Euclidian norm of quantitiy $(\,)$
$\dot{(\,)}$	Time derivative $\frac{d()}{dt}$ of $(\,)$
$\ddot{(\,)}$	Second time derivative $\frac{d^2()}{dt^2}$ of $(\,)$
$(\,)^{\mathsf{T}}$	Transpose of matrix or vector $(\,)$
$\delta(\,)$	Virtual variation of quantity $(\,)$

Scalars

A_{gap}	Gaping part of joint area
A	Joint area
A,B,γ, n	Parameters of the Bouc–Wen friction model
A_{slip}	Sliping part of joint area
A_{stick}	Sticking part of joint area
$\alpha;\beta;\gamma$	Parameters for HHT and Newmark formulas
$c_1;c_2$	Stiffness parameters of reference friction model
E_0,E_t,κ, λ	Parameters of the Valanis friction model
ε_N	Contact stiffness
ε_{T}	Tangential stiffness of friction model
$\varepsilon_{\mathrm{T,sl}}$	Sliding stiffness of friction model
$\varepsilon_{\mathrm{T,st}}$	Sticking stiffness of friction model
g	Number of joint modes
g_N,$g_{N,i}$	Normal gap (of contact pair i)
$g_{N,i}$	Normal gap of contact pair i
$\Gamma_c^M;\,\Gamma_c^S$	Contacting surfaces on the master and slave side
h	Time step size
k	Number of trial vector derivatives

k_{PL}	Number of preload mode related TVDs
μ	Friction coefficient
n_{CP}	Number of contact pairs
n_b	Number of bodies in the multibody system
n_c	Number of constraint equations
n_{FE}	Number of FE coordinates
n_B	Number of boundary DOFs
$N_i(\xi;\eta)$	Finite element shape function
n_I	Number of inner DOFs
ω_i	Eigenfrequency of vibration mode i
p_N,$p_{N,i}$	Contact pressure (of contact pair i)
p	Number of preload modes
$P^M; P^S$	Contacting particles $P^M; P^S$ at master and slave side
$p_{N,i}$	Contact pressure of contact pair i
R_G	Sticking stress limit
r	Number of reduced coordinates
m	Number of CMS trial vectors
ρ^i	Mass density
s	Number of deformation shapes
$s_{1,i,t^*}; s_{2,i,t^*}$	Tangential displacements before contact closure
$s_i; (s)$	Relative tangential displacement of contact pair i
$s_{1,i}; s_{2,i}$	Relative tangential displacements in principal directions of contact pair i
$R_{G,i}$	Sticking stress limit
$a_k; b_k; c_k$	Scaling factors
$f_k; g_k; h_k$	Shape functions
σ_0,α	Parameters of the Dahl friction model
t	Time
T^i	Kinetic energy
t^*	Contact closure time
τ_F,$\tau_{F,i}$	Frictional stress (of contact pair i)
τ_{BW}	Frictional stress computed with the Bouc–Wen friction model
τ_D	Frictional stress computed with the Dahl friction model
$\tau_{F,BW}$	Frictional stress computed with the extended Bouc–Wen friction model
$\tau_{F,D}$	Frictional stress computed with the extended Dahl friction model
$\tau_{F,V}$	Frictional stress computed with the Valanis friction model
$\tau_{F,i}$	Frictional stress of contact pair i
v	Number of vibration modes
V^i	Volume of body
w	Ratio for estimating the number of joint modes
δW^i	Virtual work of all acting forces
δW^i_f	Virtual work of elastic forces
δW^i_e	Virtual work of external forces
δW_{nl}	Virtual work of joint forces
$\xi; \eta$	Isoparametric coordinates of 2D finite element shape functions

ζ_i	Reduced coordinate (also called scaling factor)
$\hat{\zeta}_i$	Reduced coordinate (also called scaling factor) at reference configuration

Vectors and matrices

$\vec{f}_i^{\,M}$	Nodal force on master node
$\vec{f}_i^{\,S}$	Nodal force on slave node
$\vec{n}_i$	Surface normal vector of contact pair i
$\vec{n}^M\left(\overline{\xi};\overline{\eta}\right)$	Normal vector of the master surface
$\vec{p}_{N,i}$	Contact pressure vector of contact pair i
$\delta\vec{r}^M;\delta\vec{r}^S$	Virtual displacement of the contacting particles $P^M;P^S$
$\vec{r}^i$	Absolute position vector of point P^i
$\vec{R}^i$	Location of the origin of the body reference frame
$\vec{t}_i$	Tangential vector of contact pair i (in direction of tangential displacement)
$\vec{t}_i^{\,1};\vec{t}_i^{\,2}$	Tangential vectors in principal directions of contact pair i
$\vec{t}_{nl}$	Contact interface stress vector
$\vec{t}_{nl}^{\,M};\vec{t}_{nl}^{\,S}$	Contact interface stress vector at the master and slave side
$\vec{\tau}_{F,i}$	Tangential surface stress vector or friction stress vector of contact pair i
$\vec{u}_f^{\,i}$	Elastic displacement vector
$\vec{u}^M;\vec{u}^S$	Position of contacting particles $P^M;P^S$ (defined in body coordinate system)
$\vec{u}^i$	Position vector of point P^i (defined in body coordinate system)
$\vec{u}_0^{\,i}$	Position vector of point P^i in undeformed state
$\vec{X}$	Arbitraty point of FE model
$\vec{x}_i^{\,M};\vec{x}_i^{\,S}$	Displacement vectors of translational DOFs of contact pair i at the master and slave surfaces
$\vec{X}^M\left(\overline{\xi},\overline{\eta}\right)$	Intersection point on the master surface of contact pair
$\vec{X}^S$	Slave node of contact pair
$\vec{y}_i^{\,MS}$	Relative displacement between slave node and intersection point

$\mathbf{A}_i$	Surface integrals of finite elements connected to slave node of contact pair i
$\mathbf{B}^i$	Rotation matrix
$\mathbf{C}$	Compliance matrix of the FE structure
$\mathbf{C}_{\mathbf{q}^i}^{\mathsf{T}}$	Constraint Jacobian matrix
$\mathbf{C}$	Vector of constraint equations
$C_i\{\vec{n};\vec{t}_i^{\,1};\vec{t}_i^{\,2}\}$	Coordinate system for contact pair i
$\mathbf{D}$	Damping matrix of the FE structure
$B\{\tilde{\mathbf{e}}_1^i;\tilde{\mathbf{e}}_2^i;\tilde{\mathbf{e}}_3^i\}$	Floating frame of reference or body coordinate system
$\{\mathbf{e}_1;\mathbf{e}_2;\mathbf{e}_3\}$	Inertial frame or inertial global frame of reference
$\mathbf{F}$	Matrix containing fictive forces of all TVDs
$\mathbf{f}$	Vector of external applied forces

$\mathbf{f}_B$	Vector of external applied forces on boundary DOFs
$\mathbf{f}_F$	Vector of nodal friction forces
$\mathbf{f}_F^m$	Vector of modal reduced friction forces
$\mathbf{f}_{i,j}$	Vector of fictive force corresponding to $\frac{\partial \boldsymbol{\phi}_i}{\partial \zeta_j}$
$\overline{\mathbf{f}}_{i,j}$	Vector of normalized fictive force
$\mathbf{f}_i^{m,M}$	Vector of modal master forces for cantact pair i
$\mathbf{f}_i^m$	Vector of modal forces for cantact pair i
$\mathbf{f}_i^{m,S}$	Vector of modal slave forces for cantact pair i
$\mathbf{f}_N$	Vector of nodal contact forces
$\mathbf{f}_N^m$	Vector of modal reduced contact forces
$\mathbf{f}_{nl}$	Vector of nodal nonlinear forces
$\mathbf{f}_{nl}^m$	Vector of modal nonlinear forces
$\mathbf{f}_{\mathrm{PL},i}$	Prelaod froces
$\overline{\mathbf{F}}$	Matrix containing all normalized fictive forces
$\mathbf{g}(\zeta)$	Reduced order representation
$\mathbf{G}^i$	G-Matrix
$\mathbf{g}_N$	Vector containing normal gaps of all contact pairs
$\mathbf{I}$	Identity matrix
$\mathbf{J}$	System's Jacobian matrix
$\mathbf{K}$	Stiffness matrix of the FE structure
$\mathbf{K_c}$	Stiffnes matrix at the reverence state
$\boldsymbol{\mathcal{K}}$	Stiffness matrix of the entire multibody system
$\mathbf{K}_{nl}$	Nonlinear stiffness matrix of the FE structure
$\boldsymbol{\mathcal{K}}^i$	Stiffness matrix
$\widetilde{\mathbf{K}}$	Reduced stiffness matrix
$\widetilde{\mathbf{f}}$	Reduced force vector
$\boldsymbol{\mathcal{M}}^i$	Mass matrix
$\mathbf{M}$	Mass matrix of the FE structure
$\boldsymbol{\mathcal{M}}$	Mass matrix of the entire multibody system
$\widetilde{\mathbf{M}}$	Reduced mass matrix
$\overline{\mathbf{N}}_i^e$	FE shape function matrix of intersection points
$\mathbf{p}$	Vector of combined linear and nonlinear state dependent forces
$\mathbf{P}$	Mapping matrix
$\mathbf{p}_N$	Contact pressure vector
$\mathbf{q}$	Vector of all generalized coordinates of the multibody system
$\mathbf{Q}_e^i$	Vector of generalized external forces
$\mathbf{q}^i$	Vector of generalized coordinates
$\mathbf{Q}^i$	Vector of generalized forces
$\mathbf{Q}_{nl}$	Vector of generalized nonlinear joint forces
$\mathbf{q}_r^i$	Vector of reference coordinates
$\mathbf{Q}_v^i$	Quadratic velocity vector
$\ddot{\mathbf{q}}$	Vector of all generalized accelerations of the multibody system
$\dot{\mathbf{q}}$	Vector of all generalized velocities of the multibody system

$\mathbf{R}^i$	Vector of translational coordinates
res	Residual vector
$\mathbf{S}^i$	Shape function matrix
$\mathbf{S}^M$; $\vec{S}^S$	Shape function matrix of particles P^M; P^S
$\mathbf{W}$	Projection space
$\mathbf{x}$	Vector of nodal DOFs of the FE structure
$\mathbf{x}_B$	Vector of boundary DOFs of the FE structure
$\mathbf{x}_I$	Vector of inner DOFs of the FE structure
$\mathbf{x}_{\mathrm{PL}}$	Preload deformations (preload state)
$\mathbf{Q}_i$	Transformation matrix between body coordinate system B and contact pair coordinate system C_i

$\boldsymbol{\epsilon}^i$	Strain vector
$\boldsymbol{\lambda}$	Vector of Lagrange multipliers
$\vec{\omega}^i$	Angular velocity vector
$\boldsymbol{\Phi}$	General reduction basis
$\boldsymbol{\phi}_i^{\mathrm{CM}}$	Constraint mode
$\boldsymbol{\Phi}_{\mathrm{CMS}}$	Reduction basis for CMS methods
$\boldsymbol{\phi}_i^{\mathrm{CNM}}$	Fixed boundary normal mode
$\frac{\partial \boldsymbol{\phi}_i}{\partial \zeta_j}$; $\boldsymbol{\phi}_{\mathrm{T},i}$	First order trial vector derivative
$\boldsymbol{\Phi}_i^e$	Mode shape matrix of finite element of the intersection point
$\boldsymbol{\Phi}_{free}$	Reduction basis containing free-free modes
$\boldsymbol{\phi}_i$	Trial vector (also called mode shape) number i
$\boldsymbol{\Phi}_i^M$; $\boldsymbol{\Phi}_i^S$	Matrices containing the translational DOFs of contact pair i for all trial vectors
$\boldsymbol{\Phi}_{\mathrm{PL}}$	Matrix containing all p preload modes
$\boldsymbol{\phi}_{\mathrm{PL},i}$	Prelaod mode i
$\boldsymbol{\Phi}_{\mathrm{S}}$	Reduction basis containing static deformation shape
$\boldsymbol{\Phi}_i^S$	Mode shape matrix of slave node
$\boldsymbol{\Phi}_{\mathrm{T}}$	Matrix containing all TVDs
$\overline{\boldsymbol{\Phi}}_{\mathrm{T}}$	Matrix containing all normalized TVDs
$\overline{\boldsymbol{\phi}}_{\mathrm{T},i}$	Normalized TVD
$\Phi_{\mathrm{TVD,PL}}$	Matrix containing all preload mode related TVDs
$\boldsymbol{\Phi}_{\mathrm{V}}$	Reduction basis containing vibration modes
$\boldsymbol{\Phi}_{\mathrm{J}}$	Matrix of joint modes
$\boldsymbol{\phi}_{\mathrm{J},i}$	Joint mode number i
$\boldsymbol{\sigma}^i$	Stress vector
$\boldsymbol{\tau}_F$	Friction stress vector
$\boldsymbol{\theta}^i$	Vecotr of rotational coordinates
$\boldsymbol{\zeta}$	Vector of reduced coordinates or scaling factors
$\hat{\boldsymbol{\zeta}}$	Vector of reduced coordinates or scaling factors at the reference configuration
$\hat{\boldsymbol{\zeta}}_{\mathrm{PL}}$	Vector of reduced coordinates or scaling factors at the preload state
$\boldsymbol{\zeta}^i$	Vector of generalized flexible coordinates

1 Introduction

Multibody system dynamics has become an important discipline in modern engineering mechanics. A multibody system consists of rigid or flexible bodies which may undergo large translational and rotational motions. These bodies are interconnected with different types of mechanical connectors or force elements. In modern computer-aided engineering, such multibody systems are analyzed by computer programs which are called *multibody simulation* (MBS) programs. MBS programs are used in automotive and aerospace engineering, in robotics, biomechanics and other technological fields to model and analyze complex mechanical systems.
Different methods for modeling flexible bodies within multibody dynamics have been presented over the last decades. A very common approach for linear flexible bodies is the combination of a *floating frame of reference formulation* (FFRF) [115] with model order reduction techniques like the *component mode synthesis* (CMS) [21]. To describe the large rigid body motion, the FFRF uses a body coordinates system (reference frame) which rotates and translates with the flexible body. The small flexible deformations are superimposed to the rigid body motion and described with respect to the reference frame. The CMS allows to approximate the deformations of the flexible body by a linear combination of global deformation shapes weighted with time-varying scaling factors. The deformation shapes are often denoted as trial vectors (in German "Ansatzvektor") or modes and the scaling factors are also called modal coordinates. The trial vectors of the CMS reduction basis are a combination of vibration modes and static displacement shapes computed from specific loads at interface nodes.

Nevertheless, the modeling of flexible bodies is an exciting field of research since the complexity of the flexible structures and the therein considered nonlinear effects is still growing. For complex mechanical structures, which are commonly an assembly of several substructures, joint forces are one major nonlinear effect. The term "joint" is from now on used to denote the region where the substructures interact with each other via nonlinear contact and friction forces. These forces may have global and local influences on the dynamic behavior of the jointed structure. Global effects are observable by changes in amplitude, frequency, and damping of the motion. Local effects are noticeable in the deformation and stress distribution inside the joint area which is crucial for subsequent fatigue analysis. For these reasons, the nonlinear contact and friction forces cannot be ignored if the dynamics of the structure is investigated or the structure is included in an MBS. In this dissertation only permanent joints without lubrication are of interest. This includes that the relative displacements of the involved surfaces with respect to each other remain small (small sliding contact). Such joints like bolted joints, clamped connections, spot welded seams and interference fits can be found in many mechanical structures and are of high technical

relevance. For these type of joints it is advantageous to consider the jointed structure as one flexible body and to treat the contact and friction forces as internal nonlinear forces of this flexible body.

Due to the strong nonlinear characteristics of contact and friction forces, these effects are a very challenging problem for numerical simulation. For this reason, jointed structures are analyzed in engineering practice frequently with the finite element method (FEM). The strength of the FEM is the static analysis of large structures. For this type of computations the FEM achieves highly accurate results. Based on a finite element (FE) discretization such structures can have up to 10^7 degrees of freedom (DOFs) for industrial applications. Due to this high number of DOFs, dynamic analyses are in general not reasonably possible because of the high computational effort for time integration.

On the other hand, model order reduction techniques can be used in combination with a simplified contact assumption for the computation of the jointed structure. Common assumptions for a simplified contact are a linear contact model (tied contact) or complete negligence of the contact. This leads to greatly reduced computational effort, but the influence of the nonlinear joint forces is not considered. An academic example of a simple friction bar is used to demonstrate the disadvantages of these two approaches. In fig. 1.1 a schematic sketch of a friction bar is denoted. The two metal sheets of the friction bar are connected at the two middle spots. One side of the friction bar is fixed while on the other side an external force is applied. This model is used throughout the dissertation to demonstrate the advantages of the novel approaches and it is described in chapter 4 in detail.

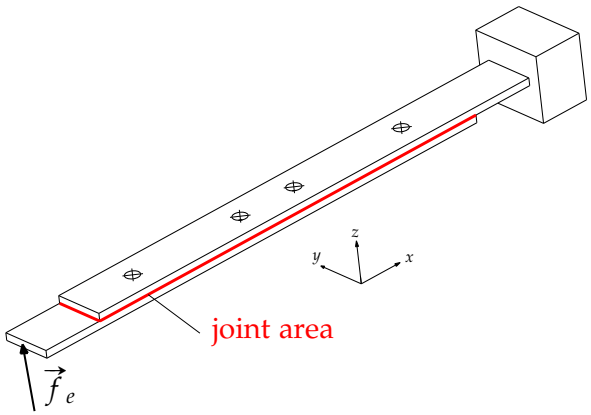

Figure 1.1: Schematic draft of the friction bar

For an applied external step load the response of the tip of the structure is shown in fig. 1.2.

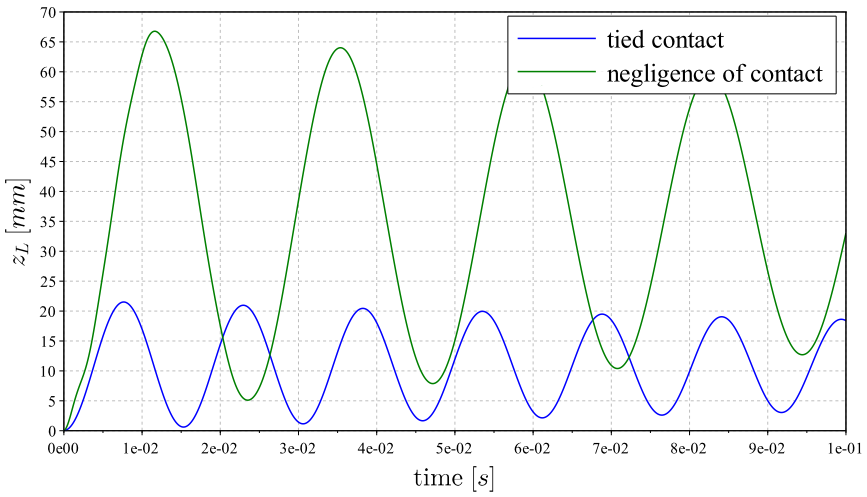

Figure 1.2: Global deformation with tied contact and negligence of contact

Obviously, the two simple approaches (tied contact or negligence of the contact) lead to completely different results. Moreover, the local deformations (as shown in fig. 1.3) and consequently the stresses inside the structure are different for these approaches. The negligence of the contact leads to a nonphysical behavior since the connected substructures can penetrate each other. On the other hand, for the tied contact the substructures cannot separate. Hence, such simplified approaches for jointed structures lead to questionable quality of the results and a realistic consideration of jointed structures is not possible.

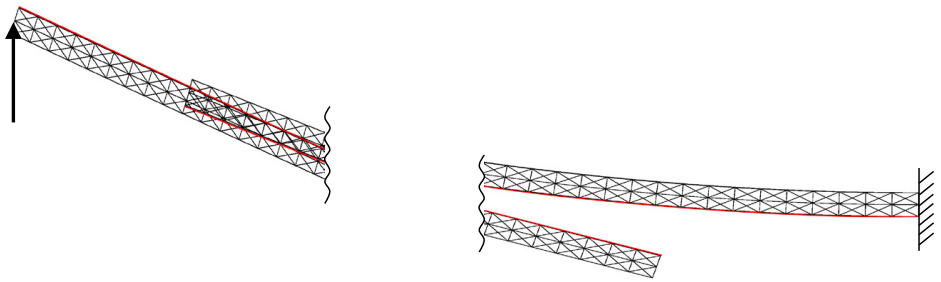

(a) Negligence of contact

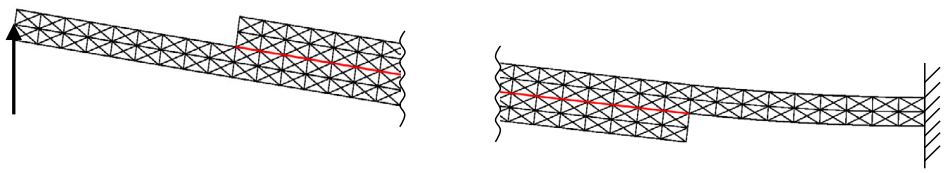

(b) Tied contact

Figure 1.3: Local deformation of the joint with tied contact and negligence of contact

1.1 Aim of this dissertation

The aim of this dissertation is to present a novel, efficient and accurate strategy for the consideration of jointed structures inside flexible multibody simulations. This strategy is divided into three main parts, namely

a) inclusion of joint forces into the equations of motion of a flexible multibody system,
b) extension of common reduction basis with special joint modes,
c) evaluation of contact and friction models based on efficiency criteria.

Moreover, the presented theory is investigated on academic and industrial applications in order to underline the practical relevance.

1.2 Outline of the dissertation

Chapter 2 - State of the art
The equations of motion of a flexible multibody system and some approaches for the numerical time integration are outlined in this chapter. Furthermore, the concept of projective model order reduction is outlined and a review on reduction strategies for jointed structures is given. A literature review on contact and friction models for dry friction joints is presented at the end of this chapter.

Chapter 3 - A new approach for joint contact in flexible multibody systems
In this chapter the novel approach for efficient consideration of jointed structures in a flexible MBS is presented.
At the beginning of this chapter, the consideration of nonlinear contact and friction forces in the vector of generalized forces together with their contribution to the system's Jacobian is derived on an analytical basis. This allows an efficient implementation into existing flexible multibody software.
Furthermore, an extension of common reduction basis with special joint modes is presented. These joint modes are based on the approximation of a nonlinear system with trial vector derivatives (TVDs). Three different computation strategies for joint modes based on TVDs and an a-priori estimator of the required number of joint modes are presented. Additionally, an optimized computation of joint modes for preloaded structures (called preloaded joint modes) is derived.
Finally, the implementation of the presented theory in an MBS software is outlined and some features of the developed pre- and postprocessing tool are presented.

Chapter 4 - Examples and evaluation
The presented approaches for joint modes are evaluated on two numerical examples and the application of the a-priori estimator for the required number of joint modes is discussed. Moreover, different contact and friction models are compared and rated in the context of flexible MBS with a special focus on numerical efficiency. Furthermore, two industrial applications are presented.

Chapter 5 - Outlook
An outlook on possible future research topics is given in this chapter. These topics deal mainly with the reduction of the computational effort for numerical time integration.

Chapter 6 - Summary and conclusions
In this final chapter the essential insights are summarized and the conclusions of this dissertation are presented.

General notice

Parts of this dissertation have already been published by the author in peer-reviewed journals [89, 91, 141] or have been presented at international conferences [88, 90, 142, 143]. Hence, some text blocks of this thesis might be found in the latter cited literature.

2 State of the art

2.1 Flexible multibody dynamics

Flexible multibody dynamics is an important subject in modern computer-aided engineering. It deals with the analysis of rigid and/or flexible bodies that undergo large displacements, including rigid body motions, large rotations, and elastic deformations. The bodies of a flexible multibody system are connected by mechanical connectors and/or force elements among each other or to ground. Mechanical connectors might be spherical joints, revolute joints, cylindrical joints and others. Dampers, springs, bushings and actuators are examples for force elements in a multibody system. A schematic sketch of a simple multibody system is depicted in fig. 2.1. Due to the connection of the bodies, their displacements are not independent.

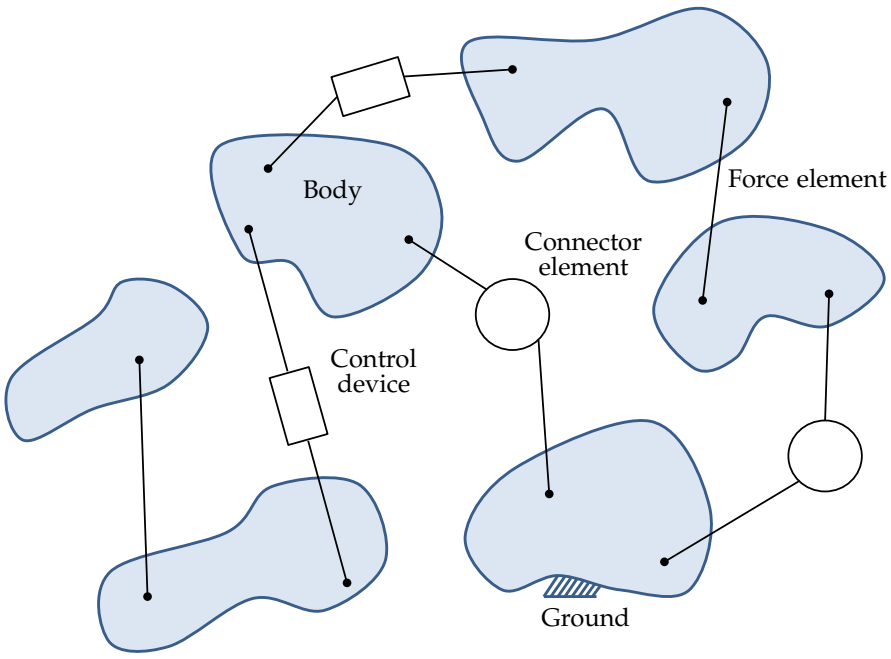

Figure 2.1: Flexible multibody system (see similar figure in [114])

Traditionally, multibody systems were analyzed using the assumptions of rigid body dynamics. The physics and mathematical description of a rigid multibody system is well-known and documented in many textbooks and research papers (see [1, 95, 104, 108, 114] among others). Different flexible multibody formulations (like absolute nodal coordinate formulation [46,

113] or floating frame of reference formulation [115, 134]) have been developed in the last decades. A good overview and comparison of the different formulations can be found in [8, 115].

In the following section 2.1.1 the floating frame of reference formulation (FFRF) is outlined and the equations of motion of a flexible multibody system are reviewed. In section 2.1.2 strategies for the numerical solution of the resulting differential algebraic equations are briefly outlined.

In order to keep this chapter short and easy readable, some mathematical transformations in the context of multibody dynamics are shifted to appendix B.

2.1.1 Floating frame of reference formulation (FFRF)

The FFRF uses two sets of coordinates to describe the configuration of the flexible body. So-called reference coordinates are used to describe the position and orientation of the floating reference frame of the body. The origin of this floating reference frame can be chosen arbitrarily, but it is required that there is no rigid body motion between the coordinate system and the body itself. On the other hand, elastic coordinates are used to describe the deformations with respect to this frame.

In the following sections the global position and velocity vector of an arbitrary point of a flexible body are described by the FFRF. Furthermore, the kinetic energy and the forces acting on the body are written in terms of reference and elastic coordinates. On this basis the equations of motion are derived.

The description of the FFRF presented in this section closely follows the textbook of Shabana on "Dynamics of Multibody Systems" [114].

Kinematic description

To describe the configuration of a deformable body i in the FFRF two different coordinate systems are used. A schematic draft of one flexible body and the corresponding coordinate systems is depicted in fig. 2.2. The coordinate system $\{\mathbf{e}_1; \mathbf{e}_2; \mathbf{e}_3\}$ which is fixed in time and space is denoted as *inertial frame* or *inertial global frame of reference*. The second coordinate system, which is called *floating frame of reference* or *body coordinate system*, is attached to the flexible body and translates and rotates with the body. The location and orientation of this body coordinate system $\{\bar{\mathbf{e}}_1^i; \bar{\mathbf{e}}_2^i; \bar{\mathbf{e}}_3^i\}$ is defined with respect to the inertial frame by a set of coordinates $\mathbf{q}_r^i$ called reference coordinates.

The location of the origin of the body reference frame is described with respect to the inertial frame by the position vector $\vec{R}^i = \begin{bmatrix} R_1^i & R_2^i & R_3^i \end{bmatrix}^\mathsf{T}$. The components of this vector can be directly interpreted as translational coordinates of the body $\mathbf{R}^i = \vec{R}^i$. The orientation of the body reference frame can be described by three independent coordinates, as *Euler angles*, *Rodriguez parameters* or four dependent *Euler parameters* which are collected in the vector of

rotational coordinates $\boldsymbol{\theta}^i$. More details on different types of rotational coordinates can be found in [8, 114]. The vector of reference coordinates can be written as

$$\mathbf{q}_r^i = \begin{bmatrix} \mathbf{R}^{i\mathsf{T}} & \boldsymbol{\theta}^{i\mathsf{T}} \end{bmatrix}^{\mathsf{T}}. \tag{2.1}$$

These reference coordinates are sufficient to describe the location and kinematics of an arbitrary point P^i on a rigid body since the distance between the point P^i and the body coordinate system remains constant. This is in general not the case for a flexible body.

For a flexible body the absolute position vector of an arbitrary point P^i can be written as [66, 114, 115]

$$\vec{r}^{\,i} = \mathbf{R}^i + \mathbf{B}^i \vec{u}^{\,i}, \tag{2.2}$$

where $\mathbf{B}^i$ is the orthogonal rotation matrix and $\vec{u}^{\,i}$ is the position vector of the point P^i defined in the body coordinate system. For a deformable body the distance $\vec{u}^{\,i}$ is in general not constant, and hence this vector can be split up in two parts

$$\vec{u}^{\,i} = \vec{u}_0^{\,i} + \vec{u}_f^{\,i}. \tag{2.3}$$

In the latter equation, $\vec{u}_0^{\,i}$ is the position vector in the undeformed configuration and $\vec{u}_f^{\,i}$ represents the elastic displacement. A schematic draft of these vectors is depicted in fig. 2.2.

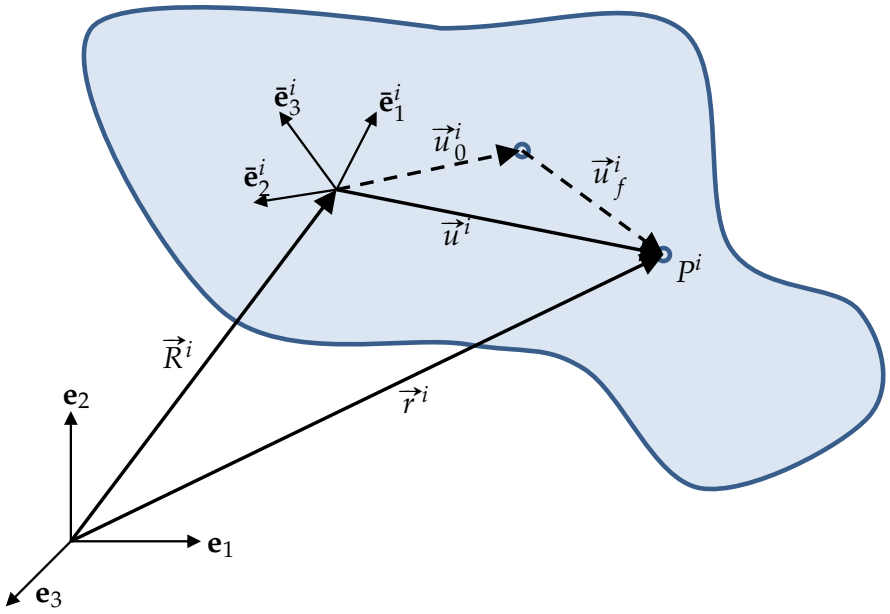

Figure 2.2: Coordinates of the deformable body i in the FFRF (see similar figure in [114])

The time and space-dependent displacement vector $\vec{u}_f^{\,i} = \begin{bmatrix} u_{f1}^i & u_{f2}^i & u_{f3}^i \end{bmatrix}^{\mathsf{T}}$ can be approximated by the *Ritz method* in the form

$$\vec{u}_f^{\,i} = \begin{bmatrix} u_{f1}^i \\ u_{f2}^i \\ u_{f3}^i \end{bmatrix} \approx \begin{bmatrix} \sum_{k=1}^{l} a_k(t)\, f_k\left(x_1^i, x_2^i, x_3^i\right) \\ \sum_{k=1}^{m} b_k(t)\, g_k\left(x_1^i, x_2^i, x_3^i\right) \\ \sum_{k=1}^{n} c_k(t)\, h_k\left(x_1^i, x_2^i, x_3^i\right) \end{bmatrix}, \tag{2.4}$$

where f_k, g_k, h_k are predefined space-dependent shape functions and a_k, b_k, c_k are time-dependent scaling factors. The preceding eq. (2.4) can be written in matrix form as

$$\vec{u}_f^i = \mathbf{S}^i \boldsymbol{\zeta}^i, \tag{2.5}$$

where

$$\mathbf{S}^i = \mathbf{S}^i\left(x_1^i, x_2^i, x_3^i\right) = \begin{bmatrix} f_1 & \cdots & f_l & 0 & \cdots & 0 & 0 & \cdots & 0 \\ 0 & \cdots & 0 & g_1 & \cdots & g_m & 0 & \cdots & 0 \\ 0 & \cdots & 0 & 0 & \cdots & 0 & h_1 & \cdots & h_n \end{bmatrix} \tag{2.6}$$

is the space-dependent shape function matrix whose elements are the shape functions f_k, g_k, h_k. The vector of generalized elastic coordinates

$$\boldsymbol{\zeta}^i = \boldsymbol{\zeta}^i(t) = \begin{bmatrix} a_1 & \cdots & a_l & b_1 & \cdots & b_m & c_1 & \cdots & c_n \end{bmatrix}^\mathsf{T} \tag{2.7}$$

contains the time-dependent scaling factors a_k, b_k, c_k. A comment on an advantageous selection of shape functions is given in section 2.1.1. In section 2.2.3 common computation methods for the shape function matrix using a finite element discretization are reviewed.

Inserting eq. (2.5) into eq. (2.3) leads to

$$\vec{u}^i = \vec{u}_0^i + \vec{u}_f^i = \vec{u}_0^i + \mathbf{S}^i \boldsymbol{\zeta}^i. \tag{2.8}$$

By substituting $\vec{u}^i$ in eq. (2.2) with the definition of eq. (2.8), the global position vector can be written as

$$\vec{r}^i = \mathbf{R}^i + \mathbf{B}^i\left(\vec{u}_0^i + \mathbf{S}^i \boldsymbol{\zeta}^i\right). \tag{2.9}$$

This description of the position vector is used to determine the absolute velocity vector $\dot{\vec{r}}^i$ and the kinetic energy T^i of the deformable body.

With the translational coordinate vector $\mathbf{R}^i$, the vector of rotational coordinates $\boldsymbol{\theta}^i$, and the vector of elastic coordinates $\boldsymbol{\zeta}^i$ the total vector of generalized coordinates can be written as

$$\mathbf{q}^i = \begin{bmatrix} q_1^i & q_2^i & \cdots & q_n^i \end{bmatrix}^\mathsf{T} = \begin{bmatrix} \mathbf{R}^i \\ \boldsymbol{\theta}^i \\ \boldsymbol{\zeta}^i \end{bmatrix}. \tag{2.10}$$

Velocity equation

Differentiating eq. (2.2) with respect to time leads to the absolute velocity vector $\dot{\vec{r}}^i = \frac{d\vec{r}^i}{dt}$ which can be written as

$$\dot{\vec{r}}^i = \dot{\mathbf{R}}^i + \dot{\mathbf{B}}^i \vec{u}^i + \mathbf{B}^i \dot{\vec{u}}^i, \tag{2.11}$$

where $\dot{(\,)}$ denotes the time derivative. Using the definition of eq. (2.3), the time derivative of the position vector can be written as

$$\dot{\vec{u}}^i = \dot{\vec{u}}_0^i + \dot{\vec{u}}_f^i = \mathbf{S}^i \dot{\boldsymbol{\zeta}}^i, \tag{2.12}$$

where $\vec{\dot{u}}_0^i = \vec{0}$ is used and $\dot{\zeta}^i$ is the vector of generalized elastic velocities.

Using the time derivative of the rotation matrix as defined in appendix B.1 by eq. (B.7), the middle term on the right side of eq. (2.11) can be written as

$$\dot{\mathbf{B}}^i \vec{u}^i = \mathbf{B}^i \tilde{\omega}^i \vec{u}^i, \tag{2.13}$$

where the symbol $\tilde{(\,)}$ describes a skew-symmetric matrix representation of the corresponding vector. The latter equation is equal to

$$\dot{\mathbf{B}}^i \vec{u}^i = \mathbf{B}^i \tilde{\omega}^i \vec{u}^i = \mathbf{B}^i \left(\vec{\omega}^i \times \vec{u}^i \right) = -\mathbf{B}^i \left(\vec{u}^i \times \vec{\omega}^i \right) = -\mathbf{B}^i \tilde{\mathbf{u}}^i \vec{\omega}^i, \tag{2.14}$$

where $\vec{\omega}^i$ is the angular velocity vector defined in the body coordinate system. In eq. (2.14) the relationship

$$\tilde{\mathbf{x}} \vec{y} = \vec{x} \times \vec{y} = -\vec{y} \times \vec{x} = -\tilde{\mathbf{y}} \vec{x} \tag{2.15}$$

between the cross product of two three dimensional vectors $\vec{x}$, $\vec{y}$ and their according skew-symmetric matrices $\tilde{\mathbf{x}}, \tilde{\mathbf{y}}$ is used.

Irrespective of the rotational coordinates used in the rotational coordinate vector $\boldsymbol{\theta}^i$, the angular velocity vector $\vec{\omega}^i$ can be expressed as

$$\vec{\omega}^i = \mathbf{G}^i \dot{\boldsymbol{\theta}}^i, \tag{2.16}$$

where $\dot{\boldsymbol{\theta}}^i$ is the time derivative of the rotational coordinate vector, and $\mathbf{G}^i = \mathbf{G}^i(\boldsymbol{\theta}^i)$ is a matrix which is depending on the rotational coordinates. A detailed derivation of the matrix $\mathbf{G}^i$ is given in appendix B.1 or can be found in [114, 126]. Inserting eq. (2.16) in eq. (2.14) yields

$$\dot{\mathbf{B}}^i \vec{u}^i = -\mathbf{B}^i \tilde{\mathbf{u}}^i \mathbf{G}^i \dot{\boldsymbol{\theta}}^i. \tag{2.17}$$

Combining eqs. (2.11), (2.12) and (2.17), the absolute velocity vector of an arbitrary point can be written as

$$\vec{\dot{r}}^i = \dot{\mathbf{R}}^i - \mathbf{B}^i \tilde{\mathbf{u}}^i \mathbf{G}^i \dot{\boldsymbol{\theta}}^i + \mathbf{B}^i \mathbf{S}^i \dot{\boldsymbol{\zeta}}^i, \tag{2.18}$$

or in abbreviated form

$$\vec{\dot{r}}^i = \mathbf{L}^i \dot{\mathbf{q}}^i \tag{2.19}$$

with

$$\mathbf{L}^i = \begin{bmatrix} \mathbf{I} & -\mathbf{B}^i \tilde{\mathbf{u}}^i \mathbf{G}^i & \mathbf{B}^i \mathbf{S}^i \end{bmatrix} \tag{2.20}$$

and the total vector of generalized velocities

$$\dot{\mathbf{q}}^i = \begin{bmatrix} \dot{q}_1^i & \dot{q}_2^i & \cdots & \dot{q}_n^i \end{bmatrix}^\mathrm{T} = \begin{bmatrix} \dot{\mathbf{R}}^i \\ \dot{\boldsymbol{\theta}}^i \\ \dot{\boldsymbol{\zeta}}^i \end{bmatrix}. \tag{2.21}$$

Equations of motion

The *Lagrange formalism* (see for instance [82, 85, 114, 148]) is applied to derive the equations of motion for one deformable body i in the multibody system. Other formalisms can be found in literature (see[1, 86]), but are not reviewed in this dissertation.

Lagrange's equation takes for one constrained body i in the multibody system the form

$$\frac{d}{dt}\left(\frac{\partial T^i}{\partial \dot{\mathbf{q}}^i}\right)^{\mathsf{T}} - \left(\frac{\partial T^i}{\partial \mathbf{q}^i}\right)^{\mathsf{T}} + \mathbf{C}_{\mathbf{q}^i}^{\mathsf{T}}\boldsymbol{\lambda} = \mathbf{Q}^i, \tag{2.22}$$

where T^i is the kinetic energy of the body, $\mathbf{C}_{\mathbf{q}^i}$ is the constraint Jacobian, $\boldsymbol{\lambda}$ is the vector of Lagrange multipliers, and $\mathbf{Q}^i$ is the vector of generalized forces. The Lagrange multipliers together with the constraint Jacobian can be used to determine the generalized reaction forces given by $\mathbf{C}_{\mathbf{q}^i}^{\mathsf{T}}\boldsymbol{\lambda}$.

In the latter equation the following definitions are used:

$$\frac{\partial T^i}{\partial \dot{\mathbf{q}}^i} = \begin{bmatrix} \frac{\partial T^i}{\partial \dot{q}_1^i} & \frac{\partial T^i}{\partial \dot{q}_2^i} & \cdots & \frac{\partial T^i}{\partial \dot{q}_n^i} \end{bmatrix} \tag{2.23a}$$

$$\frac{\partial T^i}{\partial \mathbf{q}^i} = \begin{bmatrix} \frac{\partial T^i}{\partial q_1^i} & \frac{\partial T^i}{\partial q_2^i} & \cdots & \frac{\partial T^i}{\partial q_n^i} \end{bmatrix} \tag{2.23b}$$

$$\mathbf{Q}^i = \begin{bmatrix} Q_1^i & Q_2^i & \cdots & Q_n^i \end{bmatrix}^{\mathsf{T}} \tag{2.23c}$$

$$\mathbf{C}_{\mathbf{q}^i} = \begin{bmatrix} \frac{\partial C_1}{\partial q_1^i} & \cdots & \frac{\partial C_1}{\partial q_n^i} \\ \vdots & & \vdots \\ \frac{\partial C_{n_c}}{\partial q_1^i} & \cdots & \frac{\partial C_{n_c}}{\partial q_n^i} \end{bmatrix} \tag{2.23d}$$

The kinetic energy T^i and the vector of generalized forces $\mathbf{Q}^i$ are derived for one deformable body i in the following.

Kinetic energy The kinetic energy T^i of a deformable body is defined as

$$T^i = \frac{1}{2}\int_{V^i} \dot{\vec{r}}^{i\mathsf{T}} \dot{\vec{r}}^i \rho^i \, dV^i, \tag{2.24}$$

where ρ^i is the mass density, V^i is the volume of the body, and $\dot{\vec{r}}^i$ is the global velocity vector of an arbitrary point on the body. Using the definition of the velocity vector given by eq. (2.19) the kinetic energy can be written as

$$T^i = \frac{1}{2}\int_{V^i} \dot{\mathbf{q}}^{i\mathsf{T}} \mathbf{L}^{i\mathsf{T}} \mathbf{L}^i \dot{\mathbf{q}}^i \rho^i \, dV^i. \tag{2.25}$$

Assuming that the vector of generalized velocities $\dot{\mathbf{q}}^i$ is not space-dependent, eq. (2.25) can be written in the compact form

$$T^i = \frac{1}{2}\dot{\mathbf{q}}^{i\mathsf{T}} \left(\int_{V^i} \mathbf{L}^{i\mathsf{T}} \mathbf{L}^i \rho^i \, dV^i \right) \dot{\mathbf{q}}^i = \frac{1}{2}\dot{\mathbf{q}}^{i\mathsf{T}} \boldsymbol{\mathcal{M}}^i \dot{\mathbf{q}}^i, \tag{2.26}$$

where $\boldsymbol{\mathcal{M}}^i$ is the symmetric mass matrix of the deformable body. This matrix is given by

$$\boldsymbol{\mathcal{M}}^i = \int_{V^i} \mathbf{L}^{i\mathsf{T}} \mathbf{L}^i \rho^i \, dV^i = \begin{bmatrix} \boldsymbol{\mathcal{M}}^i_{RR} & \boldsymbol{\mathcal{M}}^i_{R\theta} & \boldsymbol{\mathcal{M}}^i_{Rf} \\ & \boldsymbol{\mathcal{M}}^i_{\theta\theta} & \boldsymbol{\mathcal{M}}^i_{\theta f} \\ \text{sym.} & & \boldsymbol{\mathcal{M}}^i_{ff} \end{bmatrix} \tag{2.27}$$

with the submatrices defined as

$$\begin{aligned} \boldsymbol{\mathcal{M}}^i_{RR} &= \mathbf{I} \int_{V^i} \rho^i \, dV^i; & \boldsymbol{\mathcal{M}}^i_{R\theta} &= -\mathbf{B}^i \left[\int_{V^i} \tilde{\mathbf{u}}^i \rho^i \, dV^i \right] \mathbf{G}^i; \\ \boldsymbol{\mathcal{M}}^i_{\theta\theta} &= \mathbf{G}^{i\mathsf{T}} \left[\int_{V^i} \tilde{\mathbf{u}}^{i\mathsf{T}} \tilde{\mathbf{u}}^i \rho^i \, dV^i \right] \mathbf{G}^i; & \boldsymbol{\mathcal{M}}^i_{\theta f} &= \mathbf{G}^{i\mathsf{T}} \int_{V^i} \tilde{\mathbf{u}}^i \mathbf{S}^i \rho^i \, dV^i; \\ \boldsymbol{\mathcal{M}}^i_{Rf} &= \mathbf{B}^i \int_{V^i} \mathbf{S}^i \rho^i \, dV^i; & \boldsymbol{\mathcal{M}}^i_{ff} &= \int_{V^i} \mathbf{S}^{i\mathsf{T}} \mathbf{S}^i \rho^i \, dV^i; \end{aligned} \tag{2.28}$$

A derivation and detailed insight into the separate submatrices of $\boldsymbol{\mathcal{M}}^i$ can be found in [30, 114, 118]. Furthermore, in [114] it is mentioned that the submatrices $\boldsymbol{\mathcal{M}}^i_{RR}$ and $\boldsymbol{\mathcal{M}}^i_{ff}$ are constant. All other submatrices are depending on the generalized coordinates and are hence implicitly a function of time. Finally, the kinetic energy of the deformable body can be written with the submatrices defined in eq. (2.28) as

$$\begin{aligned} T^i &= \frac{1}{2}\dot{\mathbf{q}}^{i\mathsf{T}} \boldsymbol{\mathcal{M}}^i \dot{\mathbf{q}}^i \\ &= \frac{1}{2} \left(\dot{\mathbf{R}}^{i\mathsf{T}} \boldsymbol{\mathcal{M}}^i_{RR} \dot{\mathbf{R}}^i + 2\dot{\mathbf{R}}^{i\mathsf{T}} \boldsymbol{\mathcal{M}}^i_{R\theta} \dot{\boldsymbol{\theta}}^i + 2\dot{\mathbf{R}}^{i\mathsf{T}} \boldsymbol{\mathcal{M}}^i_{Rf} \dot{\boldsymbol{\zeta}}^i + \dot{\boldsymbol{\theta}}^{i\mathsf{T}} \boldsymbol{\mathcal{M}}^i_{\theta\theta} \dot{\boldsymbol{\theta}}^i + 2\dot{\boldsymbol{\theta}}^{i\mathsf{T}} \boldsymbol{\mathcal{M}}^i_{\theta f} \dot{\boldsymbol{\zeta}}^i + \dot{\boldsymbol{\zeta}}^{i\mathsf{T}} \boldsymbol{\mathcal{M}}^i_{ff} \dot{\boldsymbol{\zeta}}^i \right). \end{aligned} \tag{2.29}$$

Generalized forces The virtual work δW^i of all forces acting on the body i can be written as

$$\delta W^i = \delta W^i_f + \delta W^i_e, \tag{2.30}$$

where δW^i_f is the virtual work of elastic forces and δW^i_e is the virtual work due to external forces.

The virtual work resulting from the deformation of the body can be written with the stress vector $\boldsymbol{\sigma}^i$ and the strain vector $\boldsymbol{\epsilon}^i$ as

$$\delta W^i_f = -\int_{V^i} \boldsymbol{\sigma}^{i\mathsf{T}} \delta\boldsymbol{\epsilon}^i \, dV^i. \tag{2.31}$$

Considering the constitutive equations of a linear isotropic material yields

$$\delta W^i_f = -\boldsymbol{\zeta}^{i\mathsf{T}} \boldsymbol{\mathcal{K}}^i_{ff} \delta\boldsymbol{\zeta}^i. \tag{2.32}$$

In the latter equation eq. (2.32) $\mathcal{K}^i_{ff}$ denotes the positive definite stiffness matrix associated with the elastic coordinates of the body. Equation (2.32) can be written in partitioned form for the generalized coordinates $\mathbf{q}^i$ as

$$\delta W^i_f = -\begin{bmatrix}\mathbf{R}^{i\mathsf{T}} & \boldsymbol{\theta}^{i\mathsf{T}} & \boldsymbol{\zeta}^{i\mathsf{T}}\end{bmatrix}\begin{bmatrix}\mathbf{0} & \mathbf{0} & \mathbf{0}\\ \mathbf{0} & \mathbf{0} & \mathbf{0}\\ \mathbf{0} & \mathbf{0} & \mathcal{K}^i_{ff}\end{bmatrix}\begin{bmatrix}\delta\mathbf{R}^i\\ \delta\boldsymbol{\theta}^i\\ \delta\boldsymbol{\zeta}^i\end{bmatrix} = -\mathbf{q}^{i\mathsf{T}}\mathcal{K}^i\delta\mathbf{q}^i, \tag{2.33}$$

where $\mathcal{K}^i$ is the stiffness matrix of the body. A detailed derivation of the stiffness matrix is given in [114].

The virtual work of all external applied forces (including gravity effects, spring and damping forces, and control forces) can be written with the vector of external generalized forces $\mathbf{Q}^i_e$ as

$$\delta W^i_e = \mathbf{Q}^{i\mathsf{T}}_e\delta\mathbf{q}^i. \tag{2.34}$$

The external generalized forces may depend on the generalized coordinates, velocities and on time $\mathbf{Q}^i_e = \mathbf{Q}^i_e(\mathbf{q}^i, \dot{\mathbf{q}}^i, t)$. Partitioning $\mathbf{Q}^i_e$ with respect to the translational, rotational and elastic coordinates the external virtual work can be written in matrix notation as

$$\delta W^i_e = \begin{bmatrix}(\mathbf{Q}^i_e)_R\\ (\mathbf{Q}^i_e)_\theta\\ (\mathbf{Q}^i_e)_f\end{bmatrix}^{\mathsf{T}}\begin{bmatrix}\delta\mathbf{R}^i\\ \delta\boldsymbol{\theta}^i\\ \delta\boldsymbol{\zeta}^i\end{bmatrix}. \tag{2.35}$$

The virtual work of all forces (see eq. (2.30)) can be written by using eqs. (2.33) and (2.34) as

$$\delta W^i = -\mathbf{q}^{i\mathsf{T}}\mathcal{K}^i\delta\mathbf{q}^i + \mathbf{Q}^i_e\delta\mathbf{q}^i. \tag{2.36}$$

This equation can be written in a more compact form as

$$\delta W^i = \mathbf{Q}^i\delta\mathbf{q}^i, \tag{2.37}$$

where $\mathbf{Q}^i$ is the vector of generalized forces defined by

$$\mathbf{Q}^i = -\mathcal{K}^i\mathbf{q}^i + \mathbf{Q}^i_e. \tag{2.38}$$

Equations of motion Using the definition of the kinetic energy of eq. (2.26) the first two terms of the Lagrange's equation (see eq. (2.22)) can be written as

$$\frac{d}{dt}\left(\frac{\partial T^i}{\partial\dot{\mathbf{q}}^i}\right)^{\mathsf{T}} - \left(\frac{\partial T^i}{\partial\mathbf{q}^i}\right)^{\mathsf{T}} = \mathcal{M}^i\ddot{\mathbf{q}}^i + \dot{\mathcal{M}}^i\dot{\mathbf{q}}^i - \left[\frac{\partial}{\partial\mathbf{q}^i}\left(\frac{1}{2}\dot{\mathbf{q}}^{i\mathsf{T}}\mathcal{M}^i\dot{\mathbf{q}}^i\right)\right]^{\mathsf{T}}. \tag{2.39}$$

The last two terms of the latter equation are defined as the quadratic velocity vector

$$\mathbf{Q}^i_v = -\dot{\mathcal{M}}^i\dot{\mathbf{q}}^i + \left[\frac{\partial}{\partial\mathbf{q}^i}\left(\frac{1}{2}\dot{\mathbf{q}}^{i\mathsf{T}}\mathcal{M}^i\dot{\mathbf{q}}^i\right)\right]^{\mathsf{T}}, \tag{2.40}$$

which contains gyroscopic, centrifugal and Coriolis force components. With this definition of the quadratic velocity vector and the vector of generalized forces $\mathbf{Q}^i$ defined by eq. (2.38) the equations of motion of the entire multibody system can be written as

$$\boldsymbol{\mathcal{M}}^i \ddot{\mathbf{q}}^i + \boldsymbol{\mathcal{K}}^i \mathbf{q}^i + \mathbf{C}_{\mathbf{q}^i}^{\mathsf{T}} \boldsymbol{\lambda} = \mathbf{Q}_e^i + \mathbf{Q}_v^i, \qquad i = 1, 2, \ldots, n_b, \tag{2.41}$$

where n_b is the number of bodies in the multibody system. The system of second-order differential equations defined by eq. (2.41) can be written in partitioned matrix form as

$$\begin{aligned} &\begin{bmatrix} \boldsymbol{\mathcal{M}}_{RR}^i & \boldsymbol{\mathcal{M}}_{R\theta}^i & \boldsymbol{\mathcal{M}}_{Rf}^i \\ & \boldsymbol{\mathcal{M}}_{\theta\theta}^i & \boldsymbol{\mathcal{M}}_{\theta f}^i \\ \text{sym.} & & \boldsymbol{\mathcal{M}}_{ff}^i \end{bmatrix} \begin{bmatrix} \ddot{\mathbf{R}}^i \\ \ddot{\boldsymbol{\theta}}^i \\ \ddot{\boldsymbol{\zeta}}^i \end{bmatrix} + \begin{bmatrix} \mathbf{0} & \mathbf{0} & \mathbf{0} \\ \mathbf{0} & \mathbf{0} & \mathbf{0} \\ \mathbf{0} & \mathbf{0} & \boldsymbol{\mathcal{K}}_{ff}^i \end{bmatrix} \begin{bmatrix} \mathbf{R}^i \\ \boldsymbol{\theta}^i \\ \boldsymbol{\zeta}^i \end{bmatrix} + \begin{bmatrix} \mathbf{C}_{\mathbf{R}^i}^{\mathsf{T}} \\ \mathbf{C}_{\boldsymbol{\theta}^i}^{\mathsf{T}} \\ \mathbf{C}_{\boldsymbol{\zeta}^i}^{\mathsf{T}} \end{bmatrix} \boldsymbol{\lambda} \\ &\qquad = \begin{bmatrix} \left(\mathbf{Q}_e^i\right)_R \\ \left(\mathbf{Q}_e^i\right)_\theta \\ \left(\mathbf{Q}_e^i\right)_f \end{bmatrix} + \begin{bmatrix} \left(\mathbf{Q}_v^i\right)_R \\ \left(\mathbf{Q}_v^i\right)_\theta \\ \left(\mathbf{Q}_v^i\right)_f \end{bmatrix}, \qquad i = 1, 2, \ldots, n_b. \end{aligned} \tag{2.42}$$

The solution of the equations of motion has to satisfy n_c algebraic constraint equations

$$\mathbf{C}(\mathbf{q}, t) = \mathbf{0}, \tag{2.43}$$

which describe the mechanical connectors and the specified trajectories in the multibody system. Equation (2.41)and eq. (2.43) form a set of differential-algebraic equations that have to be solved simultaneously. Numerical techniques for solving this differential-algebraic equations are shortly discussed in section 2.1.2.

In eq. (2.41) no damping effects are considered explicitly. In MBS, inner damping of a flexible body, like material damping, is very often considered via a modal damping approach. On the other hand, friction between two bodies of the multibody system can be considered in the vector $\mathbf{Q}_e^i$. Furthermore, contact between two bodies can be included via a unilateral constraint in the equations of motion.

Shape functions

So far, the selection of appropriate shape functions for the shape matrix $\mathbf{S}^i$ has not been discussed. Common approaches are a finite element discretization or the use of trial vectors (also called mode shapes) obtained from a finite element model. A more detailed review on the computation of trial vectors is given in section 2.2.3.

A simplification of the mass matrix $\boldsymbol{\mathcal{M}}^i$ and consequently of the quadratic velocity vector $\mathbf{Q}_v^i$ can be achieved by choosing the shape functions respectively the trial vectors to be so-called *free-free modes* (see [30, 117]) and by setting the body coordinate system to the center of mass in the undeformed state. Free-free modes are vibration modes with zero-stress boundary conditions applied to the body. Thereby, the terms $\boldsymbol{\mathcal{M}}_{R\theta}^i = \mathbf{0}, \boldsymbol{\mathcal{M}}_{Rf}^i = \mathbf{0}$ and $\left(\mathbf{Q}_v^i\right)_R = \mathbf{0}$ in eq. (2.42) vanish.

In general, arbitrary trial vectors do not fulfill the criteria of free-free modes. If an FFRF is used to describe the flexible body, it is furthermore required that the chosen trial vectors do not contain any rigid body content. In the literature two different strategies can be found to transform an arbitrary set of shape functions into free-free modes. A short discussion on these methods is given in section 2.2.3. Moreover, Sherif [118] mentioned that the use of free-free modes allows a simplified and more efficient computation of the components of the quadratic velocity vector.

2.1.2 Numerical simulation of flexible multibody systems

For a constrained multibody system consisting of rigid and flexible bodies the number of differential-algebraic equations can become quite large. By solving the set of differential-algebraic equations, the generalized accelerations, velocities and coordinates as well as the Lagrange multipliers are obtained.

Although the augmented formulation using Lagrange multipliers is widely used in multibody simulation, this is not mandatory. An alternative strategy is to identify a set of independent coordinates and express the dependent variables in terms of the independent ones. This strategy is not further discussed, but detailed information can be found in [1, 114].

The differential equations of motion for all n_b bodies in the multibody system (see eq. (2.42)) can be written in matrix form as

$$\mathcal{M}\ddot{\mathbf{q}} + \mathbf{C}_\mathbf{q}^\mathsf{T}\boldsymbol{\lambda} = \mathbf{Q}_e + \mathbf{Q}_v - \mathcal{K}\mathbf{q}, \tag{2.44}$$

where $\mathbf{q}$ is the vector of all generalized coordinates and $\ddot{\mathbf{q}}$ the vector of all generalized accelerations defined as

$$\mathbf{q} = \begin{bmatrix} \mathbf{q}^{1\mathsf{T}} & \mathbf{q}^{2\mathsf{T}} & \dots & \mathbf{q}^{n_b\mathsf{T}} \end{bmatrix}^\mathsf{T}, \tag{2.45a}$$

$$\ddot{\mathbf{q}} = \begin{bmatrix} \ddot{\mathbf{q}}^{1\mathsf{T}} & \ddot{\mathbf{q}}^{2\mathsf{T}} & \dots & \ddot{\mathbf{q}}^{n_b\mathsf{T}} \end{bmatrix}^\mathsf{T}. \tag{2.45b}$$

The block diagonal mass matrix and stiffness matrix of the multibody system are given by

$$\mathcal{M} = \begin{bmatrix} \mathcal{M}^1 & \mathbf{0} & & \\ \mathbf{0} & \mathcal{M}^2 & \mathbf{0} & \\ & \mathbf{0} & \ddots & \mathbf{0} \\ & & \mathbf{0} & \mathcal{M}^{n_b} \end{bmatrix}, \qquad \mathcal{K} = \begin{bmatrix} \mathcal{K}^1 & \mathbf{0} & & \\ \mathbf{0} & \mathcal{K}^2 & \mathbf{0} & \\ & \mathbf{0} & \ddots & \mathbf{0} \\ & & \mathbf{0} & \mathcal{K}^{n_b} \end{bmatrix}. \tag{2.46}$$

The transposed constraint Jacobian, the external generalized forces and the quadratic velocity vector of the entire multibody system are given as

$$\mathbf{C}_\mathbf{q}^\mathsf{T} = \begin{bmatrix} \mathbf{C}_{\mathbf{q}^1}^\mathsf{T} \\ \mathbf{C}_{\mathbf{q}^2}^\mathsf{T} \\ \vdots \\ \mathbf{C}_{\mathbf{q}^{n_b}}^\mathsf{T} \end{bmatrix}, \qquad \mathbf{Q}_e = \begin{bmatrix} \mathbf{Q}_e^1 \\ \mathbf{Q}_e^2 \\ \vdots \\ \mathbf{Q}_e^{n_b} \end{bmatrix}, \qquad \mathbf{Q}_v = \begin{bmatrix} \mathbf{Q}_v^1 \\ \mathbf{Q}_v^2 \\ \vdots \\ \mathbf{Q}_v^{n_b} \end{bmatrix}. \tag{2.47}$$

If the vector $\mathbf{C} = \begin{bmatrix} C_1 & C_2 & \dots & C_{n_c} \end{bmatrix}^\mathsf{T}$ containing all n_c linear independent kinematic constraint equations can be written as

$$\mathbf{C}(\mathbf{q}, t) = \mathbf{0}, \tag{2.48}$$

the system is called holonomic. In this case the constraint vector is a function of the total vector of generalized coordinates $\mathbf{q}$ and time t. Furthermore, if all constraint equations do not depend explicitly on time t, the system is called scleronomic; otherwise it is called rheonomic.

A variation of the generalized coordinates yields for eq. (2.48)

$$\mathbf{C}_\mathbf{q} \delta \mathbf{q} = \mathbf{0}, \tag{2.49}$$

where $\mathbf{C}_\mathbf{q}$ is called the Jacobian of the constraints. In general, for a multibody system the constraint Jacobian matrix $\mathbf{C}_\mathbf{q}$ is a nonlinear function of the generalized coordinates.

Differentiating the constraint equation eq. (2.48) with respect to time leads to

$$\mathbf{C}_\mathbf{q} \dot{\mathbf{q}} = -\mathbf{C}_t, \tag{2.50}$$

where $\mathbf{C}_t = \frac{\partial \mathbf{C}}{\partial t}$ contains the partial derivatives of the constraint functions with respect to time. This vector vanishes if the constraint equations do not depend explicitly on time. By differentiating eq. (2.50) with respect to time the kinematic equations can be described at acceleration level as

$$\mathbf{C}_\mathbf{q} \ddot{\mathbf{q}} = -\left[\frac{\partial \mathbf{C}_t}{\partial t} + \frac{\partial \left(\mathbf{C}_\mathbf{q} \dot{\mathbf{q}} \right)}{\partial \mathbf{q}} \dot{\mathbf{q}} + 2 \frac{\partial \mathbf{C}_\mathbf{q}}{\partial t} \dot{\mathbf{q}} \right]. \tag{2.51}$$

A detailed insight into the terms of eq. (2.51) can be found in [114]. Note that eq. (2.51) is mathematically equivalent to the constraint equations given by eq. (2.48). By defining the vector

$$\mathbf{Q}_c = -\frac{\partial \mathbf{C}_t}{\partial t} - \frac{\partial \left(\mathbf{C}_\mathbf{q} \dot{\mathbf{q}} \right)}{\partial \mathbf{q}} \dot{\mathbf{q}} - 2 \frac{\partial \mathbf{C}_\mathbf{q}}{\partial t} \dot{\mathbf{q}} \tag{2.52}$$

the second-order differential equation eq. (2.44) and eq. (2.51) can be written as so-called *index 1 equation* as

$$\mathcal{M} \ddot{\mathbf{q}} + \mathbf{C}_\mathbf{q}^\mathsf{T} \boldsymbol{\lambda} = \mathbf{Q}_e + \mathbf{Q}_v - \mathcal{K} \mathbf{q} \tag{2.53a}$$

$$\mathbf{C}_\mathbf{q} \ddot{\mathbf{q}} = \mathbf{Q}_c \tag{2.53b}$$

or in matrix form as

$$\begin{bmatrix} \mathcal{M} & \mathbf{C}_\mathbf{q}^\mathsf{T} \\ \mathbf{C}_\mathbf{q} & \mathbf{0} \end{bmatrix} \begin{bmatrix} \ddot{\mathbf{q}} \\ \boldsymbol{\lambda} \end{bmatrix} = \begin{bmatrix} \mathbf{Q}_e + \mathbf{Q}_v - \mathcal{K} \mathbf{q} \\ \mathbf{Q}_c \end{bmatrix}. \tag{2.54}$$

Although the constraint equations are included at acceleration level in eq. (2.54), it has to be ensured for stability that the constraint equations are also satisfied at position level. Due to numerical discretization for time integration, the system may drift from the constraint equations at position and velocity level. Different numerical strategies for solving the described differential-algebraic equations can be found for instance in [1, 3, 8, 9, 28, 108, 114] and the references therein.

HHT algorithm

In compact form the equations describing the dynamics of a constrained multibody system can be written for as

$$\boldsymbol{\mathcal{M}}\ddot{\mathbf{q}} + \mathbf{C}_{\mathbf{q}}^{\mathsf{T}}\boldsymbol{\lambda} = \mathbf{Q}\left(\dot{\mathbf{q}}, \mathbf{q}, t\right) \tag{2.55a}$$

$$\mathbf{C}\left(\mathbf{q}, t\right) = \mathbf{0}, \tag{2.55b}$$

where $\mathbf{Q}\left(\dot{\mathbf{q}}, \mathbf{q}, t\right)$ holds the complete right side of eq. (2.44). Equations (2.55a) and (2.55b) form an *index 3* differential-algebraic equation which is also called *descriptor system*.

Due to the project in which this dissertation is embedded, the used *Hilbert-Hughes-Taylor* (HHT) algorithm [52] for the developed software *FreeDyn* [132] is shortly reviewed. The HHT algorithm which is also known as alpha-method is a direct *index 3* approach. A detailed investigation on the numerical implementation to the multibody dynamics problem can be found in [75, 76]. The algorithm described therein uses the implicit Newmark formulas to discretize the equations of motion and also requires that the constraint equations are satisfied at position level at the end of each time step.

The Newmark formulas (see [78])

$$\mathbf{q}_{n+1} = \mathbf{q}_n + h\dot{\mathbf{q}}_n + \frac{1}{2}\left[\left(1-2\beta\right)\ddot{\mathbf{q}}_n + 2\beta\ddot{\mathbf{q}}_{n+1}\right] \tag{2.56a}$$

$$\dot{\mathbf{q}}_{n+1} = \dot{\mathbf{q}}_n + h\left[\left(1-\gamma\right)\ddot{\mathbf{q}}_n + \gamma\ddot{\mathbf{q}}_{n+1}\right] \tag{2.56b}$$

define $\mathbf{q}_{n+1}, \dot{\mathbf{q}}_{n+1}$ at the time t_{n+1} as a function of $\ddot{\mathbf{q}}_{n+1}$ with the according time step size h. According to the proposed idea in [52] the discretized equations of motion of the multibody system (eq. (2.55a)) can be written as

$$\frac{1}{1+\alpha}\left(\boldsymbol{\mathcal{M}}\ddot{\mathbf{q}}\right)_{n+1} + \left(\mathbf{C}_{\mathbf{q}}^{\mathsf{T}}\boldsymbol{\lambda} - \mathbf{Q}\right)_{n+1} - \frac{\alpha}{1+\alpha}\left(\mathbf{C}_{\mathbf{q}}^{\mathsf{T}}\boldsymbol{\lambda} - \mathbf{Q}\right)_{n} = \mathbf{0}. \tag{2.57}$$

In the latter equation, the dependency of some quantities on $\mathbf{q}, \dot{\mathbf{q}}, t$ is omitted. Morover, a scaling of the equation by $\frac{1}{1+\alpha}$ is performed. The value α controls the numerical damping of the HHT method whereby $\alpha = 0$ leads to no numerical damping at all. The parameters for the Newmark formulas can be expressed as

$$\gamma = \frac{1-2\alpha}{2} \qquad \beta = \frac{\left(1-\alpha\right)^2}{4}, \tag{2.58}$$

and stability of the HHT method is provided for $\alpha \in \left[-\frac{1}{3}, 0\right]$ (see [53]).

The algebraic constraint equation eq. (2.55b) can be written in discretized form as

$$\mathbf{C}\left(\mathbf{q}_{n+1}, t_{n+1}\right) = \mathbf{0}. \tag{2.59}$$

To solve the resulting system of nonlinear equations for the unknowns $\ddot{\mathbf{q}}$ and $\boldsymbol{\lambda}$ a Newton-like algorithm (see [4, 127]) is used. Therefore, the linear system

$$\underbrace{\begin{bmatrix} \hat{\boldsymbol{\mathcal{M}}} & \mathbf{C}_\mathbf{q}^\mathsf{T} \\ \mathbf{C}_\mathbf{q} & \mathbf{0} \end{bmatrix}}_{\mathbf{J}} \begin{bmatrix} \Delta\ddot{\mathbf{q}} \\ \Delta\boldsymbol{\lambda} \end{bmatrix}^{(k)} = \begin{bmatrix} -\mathbf{e}_1 \\ -\mathbf{e}_2 \end{bmatrix}^{(k)} \tag{2.60}$$

has to be solved at each iteration (k). In this equation, $\mathbf{J}$ is the system's Jacobian and $\hat{\boldsymbol{\mathcal{M}}}$ is defined as

$$\hat{\boldsymbol{\mathcal{M}}} = \frac{1}{1+\alpha}\boldsymbol{\mathcal{M}} + \left(\frac{1}{1+\alpha} \left(\boldsymbol{\mathcal{M}}\ddot{\mathbf{q}}\right)_\mathbf{q} + \left(\mathbf{C}_\mathbf{q}^\mathsf{T}\boldsymbol{\lambda}\right)_\mathbf{q} - \mathbf{Q}_\mathbf{q} \right) \beta h^2 - \mathbf{Q}_{\dot{\mathbf{q}}} h\gamma. \tag{2.61}$$

In eq. (2.61) the subscripts $(\,)_\mathbf{q}$ and $(\,)_{\dot{\mathbf{q}}}$ denote the derivatives with respect to the vector of generalized coordinates and the vector of generalized velocities. The vectors $\mathbf{e}_1, \mathbf{e}_2$ are the residual vectors for the equation of motion and the constraint equations, respectively.

In [75] different scaling strategies are mentioned to improve the condition number of the Jacobian $\mathbf{J}$. Furthermore, strategies for error estimation, step-size control and stopping criteria are presented in the latter mentioned work.

The inclusion of linear flexible bodies is with the reviewed FFRF a standard procedure in many MBS programs. Nevertheless, the consideration of jointed flexible structures is not immediately possible with this approach. Hence, in section 3.1 the extension of the equations of motion concerning nonlinear contact and friction forces is presented.

2.2 Model order reduction

In this section a short introduction and overview on projective model order reduction techniques for linear and nonlinear systems is given. Detailed information can be found among others in the textbooks of Craig [23] and Qu [93].

In the finite element method (FEM) [7, 53, 149] a continuum is discretized in space and approximated by a finite number n_{FE} of degrees of freedom (DOFs). In general the equation of motion for a linear or nonlinear system can be written in the finite element (FE) context as

$$\mathbf{M}\ddot{\mathbf{x}}(t) + \mathbf{D}\dot{\mathbf{x}}(t) + \mathbf{K}\mathbf{x}(t) = \mathbf{f}(t) - \mathbf{f}_{nl}(\mathbf{x}(t), \dot{\mathbf{x}}(t)), \tag{2.62}$$

where $\mathbf{x}(t)$ is the $(n_{\mathrm{FE}} \times 1)$ vector of nodal DOFs, $\mathbf{M}$, $\mathbf{D}$ and $\mathbf{K}$ denote the structure's $(n_{\mathrm{FE}} \times n_{\mathrm{FE}})$ mass matrix, damping matrix and stiffness matrix, respectively. The damping matrix combines dissipative effects which can be considered to be velocity dependent (like material damping). The $(n_{\mathrm{FE}} \times 1)$ vector $\mathbf{f}(t)$ contains the time depended external applied forces, and the $(n_{\mathrm{FE}} \times 1)$ vector $\mathbf{f}_{nl}(\mathbf{x}(t), \dot{\mathbf{x}}(t))$ denotes the vector of nonlinear forces. In the case of jointed structures, the nonlinear forces are contact and friction forces inside the joint. Hence, damping due to friction is considered in the vector $\mathbf{f}_{nl}(\mathbf{x}(t), \dot{\mathbf{x}}(t))$ and not in the damping matrix. For the following investigations the dissipative effects considered in

the damping matrix are neglected ($\mathbf{D} = \mathbf{0}$). This may have influence on the stability of the system, but the interesting damping due to friction forces is still considered in the vector $\mathbf{f}_{nl}$. Equation (2.62) can be written in a more compact form as

$$\mathbf{M}\ddot{\mathbf{x}}(t) + \mathbf{p}(\mathbf{x}(t), \dot{\mathbf{x}}(t)) = \mathbf{f}(t), \tag{2.63}$$

where the linear and nonlinear state dependent forces are combined in the $(n_{\mathrm{FE}} \times 1)$ vector $\mathbf{p}(\mathbf{x}(t), \dot{\mathbf{x}}(t)) = \mathbf{K}\mathbf{x}(t) + \mathbf{f}_{nl}(\mathbf{x}(t), \dot{\mathbf{x}}(t))$. For simplicity and readability reasons the time dependency is omitted from now on.

For industrial applications the dimension of the coupled nonlinear differential equation eq. (2.63) or eq. (2.62) is usually too large for a direct time integration. One possible strategy to reduce the number of unknowns for dynamic analysis is model order reduction via projection.

In general, projective model order reduction can be divided into three steps:

a) **Choose a reduced order representation:**
The first step is to choose an appropriate reduced order representation in the form

$$\mathbf{x} \approx \mathbf{g}(\boldsymbol{\zeta}). \tag{2.64}$$

The dimension of the $(r \times 1)$ vector of reduced coordinates $\boldsymbol{\zeta}$ should thereby be much smaller than the number of FE DOFs ($r << n_{\mathrm{FE}}$). Inserting the reduced order representation of eq. (2.64) into the equation of motion eq. (2.63) yields

$$\mathbf{M}\ddot{\mathbf{g}}(\boldsymbol{\zeta}) + \mathbf{p}(\mathbf{g}(\boldsymbol{\zeta}), \dot{\mathbf{g}}(\boldsymbol{\zeta})) = \mathbf{f} + \mathbf{res}(t). \tag{2.65}$$

It is in general not possible to find r variables in $\boldsymbol{\zeta}$ that satisfy n_{FE} equations of eq. (2.63). Hence, in the latter equation a $(n_{\mathrm{FE}} \times 1)$ residual vector $\mathbf{res}(t)$ remains.

b) **Choose a projection space:**
In the second step a $(n_{\mathrm{FE}} \times r)$ projection space $\mathbf{W}$ is chosen. It is claimed, that the projection of the residual vector onto this projection space should become zero

$$\mathbf{W}^{\mathsf{T}}\mathbf{res} = \mathbf{0}. \tag{2.66}$$

Note that the projection space $\mathbf{W}$ is not specified with the latter equation.

c) **Build the reduced order model:**
By pre-multiplying eq. (2.65) with $\mathbf{W}^{\mathsf{T}}$ the reduced order model can be written as

$$\mathbf{W}^{\mathsf{T}}\left(\mathbf{M}\ddot{\mathbf{g}}(\boldsymbol{\zeta}) + \mathbf{p}\left(\mathbf{g}(\boldsymbol{\zeta}), \dot{\mathbf{g}}(\boldsymbol{\zeta})\right)\right) = \mathbf{W}^{\mathsf{T}}\mathbf{f}, \tag{2.67}$$

which is a set of differential equations for the reduced coordinates $\boldsymbol{\zeta}$.

In the following subsections different strategies for the reduced order modeling of linear and nonlinear systems are presented in more detail.

2.2.1 Reduced order modeling of linear systems

For linear systems the reduced order representation can be chosen in form of a linear reduction basis. Therefore, time invariant $(n_{\mathrm{FE}} \times 1)$ trial vectors $\boldsymbol{\phi}_i$ together with the time varying scaling factors ζ_i are used to approximate the nodal DOFs

$$\mathbf{x} \approx \sum_{i=1}^{r} \boldsymbol{\phi}_i \zeta_i = \boldsymbol{\Phi}\boldsymbol{\zeta}. \tag{2.68}$$

In the latter equation, the r trial vectors are collected as columns in the $(n_{\mathrm{FE}} \times r)$ matrix $\boldsymbol{\Phi}$ and the scaling factors in the $(r \times 1)$ vector $\boldsymbol{\zeta}$ which is also called the vector of reduced flexible coordinates. In the literature [23, 59, 93] different strategies for computing the trial vectors can be found (like Eigenmodes, Krylov space methods, Moment matching, Balanced truncation, Interface loading modes, and others). In the context of MBS the already mentioned CMS has become an established method which is available in many commercial FE packages, and hence is reviewed in section 2.2.3.

For a undamped linear structure the equation of motion given by eq. (2.62) simplifies to

$$\mathbf{M}\ddot{\mathbf{x}} + \mathbf{K}\mathbf{x} = \mathbf{f}. \tag{2.69}$$

Inserting the reduced order representation of eq. (2.68) into this equation of motion yields

$$\mathbf{M}\boldsymbol{\Phi}\ddot{\boldsymbol{\zeta}} + \mathbf{K}\boldsymbol{\Phi}\boldsymbol{\zeta} = \mathbf{f} + \mathbf{res}. \tag{2.70}$$

For the reduced equation of motion it is claimed, that the equilibrium residual vector $\mathbf{res}$ vanishes by a projection on the r-dimensional subspace ($\mathbf{W}^{\mathsf{T}}\mathbf{res} = \mathbf{0}$). A symmetric projection with $\mathbf{W} = \boldsymbol{\Phi}$ is usually chosen for this task. This leads to the reduced equation of motion in the form

$$\widetilde{\mathbf{M}}\ddot{\boldsymbol{\zeta}} + \widetilde{\mathbf{K}}\boldsymbol{\zeta} = \widetilde{\mathbf{f}}, \tag{2.71}$$

with the $(r \times r)$ reduced mass matrix and stiffness matrix $\widetilde{\mathbf{M}} = \boldsymbol{\Phi}^{\mathsf{T}}\mathbf{M}\boldsymbol{\Phi}, \widetilde{\mathbf{K}} = \boldsymbol{\Phi}^{\mathsf{T}}\mathbf{K}\boldsymbol{\Phi}$, and the $(r \times 1)$ reduced force vector $\widetilde{\mathbf{f}} = \boldsymbol{\Phi}^{\mathsf{T}}\mathbf{f}$.

2.2.2 Reduced order modeling of nonlinear systems

The literature offers several strategies for model order reduction of nonlinear systems. These strategies can be divided into two main groups, namely a) applying a linear reduction basis to the nonlinear system or, b) applying a nonlinear manifold reduction.

Linear reduction basis

Inserting the approach of a linear reduction basis defined by eq. (2.68) into the nonlinear equation of motion (eq. (2.63)) yields

$$\mathbf{M}\boldsymbol{\Phi}\ddot{\boldsymbol{\zeta}} + \mathbf{p}(\boldsymbol{\Phi}\boldsymbol{\zeta}, \boldsymbol{\Phi}\dot{\boldsymbol{\zeta}}) = \mathbf{f} + \mathbf{res}. \tag{2.72}$$

As for the model reduction of linear systems a symmetric projection with $\mathbf{W} = \mathbf{\Phi}$ is usually used to obtain the reduced equations of motion in the form

$$\mathbf{\Phi}^{\mathsf{T}} \left(\mathbf{M}\mathbf{\Phi}\ddot{\boldsymbol{\zeta}} + \mathbf{p}(\mathbf{\Phi}\boldsymbol{\zeta}, \mathbf{\Phi}\dot{\boldsymbol{\zeta}}) \right) = \mathbf{\Phi}^{\mathsf{T}}\mathbf{f}. \tag{2.73}$$

This is an intuitive approach and leads to the same structure of the reduced equations of motion as the reduced linear system. An open question within this approach is how proper trial vectors can be computed for nonlinear systems. One possibility is to compute trial vectors as linearized Eigenmodes and/or static responses for different loadings. A different approach is to use the dynamic responses of the full nonlinear system based on excitations similar to the dynamic loading expected in the later simulation. The solutions of the full dynamic nonlinear system at different time steps (called snapshots) are further analyzed via a *proper orthogonal decomposition* (POD) in order to obtain the trial vectors (see [34, 58, 65, 125]). An obvious disadvantage of this approach is that the full nonlinear system needs to be time integrated at least once.

Nonlinear manifold

Beside the use of a linear reduction basis also the use of a nonlinear manifold is possible. This can be in general written as

$$\mathbf{x} \approx \mathbf{g}(\boldsymbol{\zeta}). \tag{2.74}$$

More details on a quadratic modal manifold reduction can be found in [57, 100, 147]. Inserting eq. (2.74) into the nonlinear equation of motion eq. (2.63) yields

$$\mathbf{M}\ddot{\mathbf{g}}(\boldsymbol{\zeta}) + \mathbf{p}(\mathbf{g}(\boldsymbol{\zeta}), \dot{\mathbf{g}}(\boldsymbol{\zeta})) = \mathbf{f} + \mathbf{res}. \tag{2.75}$$

The equilibrium residual should again vanish by a projection of the form $\mathbf{W}^{\mathsf{T}}\mathbf{res} = \mathbf{0}$. One possible projection basis is $\mathbf{W} = \frac{\partial \mathbf{g}}{\partial \boldsymbol{\zeta}}$, which implies a projection onto the current tangent space of the manifold, and hence leads to the reduced equation of motion

$$\left(\frac{\partial \mathbf{g}}{\partial \boldsymbol{\zeta}}\right)^{\mathsf{T}} \left(\mathbf{M}\ddot{\mathbf{g}}(\boldsymbol{\zeta}) + \mathbf{p}(\mathbf{g}(\boldsymbol{\zeta}), \dot{\mathbf{g}}(\boldsymbol{\zeta}))\right) = \left(\frac{\partial \mathbf{g}}{\partial \boldsymbol{\zeta}}\right)^{\mathsf{T}} (\mathbf{f}) \,. \tag{2.76}$$

The nonlinear manifold reduction leads to a change in structure of the reduced equations of motion compared to linear systems. Hence, a straight forward implementation into existing MBS software is difficult.

The computation of the nonlinear forces remains for both reduction strategies (linear reduction basis or nonlinear manifold) a bottleneck. The reduced nonlinear forces need to be computed in the physical DOFs and reprojected at every iteration step. Techniques to reduce the computational effort for the nonlinear forces are still an open research question and are discussed in the context of nonlinear joint forces in section 5.1.

2.2.3 Component mode synthesis (CMS)

For linear structures component mode synthesis (CMS) has become an established tool for model order reduction. The method was originally developed to couple several FE substructures. Nevertheless, CMS has become over the last decades very popular for the representation of flexible structures inside an MBS.

The CMS was first introduced by Hurty [54] and Craig and Bampton [22] in the 1960's. Different extensions, generalizations and evaluations in terms of efficiency and accuracy of the CMS have been published in several papers and textbooks. Reviews on different CMS methods (like Rubin's method [99], MacNeal's method [67], Rixen's dual Craig-Bampton method [96]) can be found among others in [20, 21, 23, 70, 93, 112, 122].

In this section only the most common used fixed boundary CMS [22] is discussed in more detail. Alternative formulations like free boundary and hybrid boundary CMS are equivalent to the fixed boundary CMS (see [20]).

Fixed boundary CMS

For the fixed boundary CMS, an FE model as depicted in fig. 2.3 is considered.

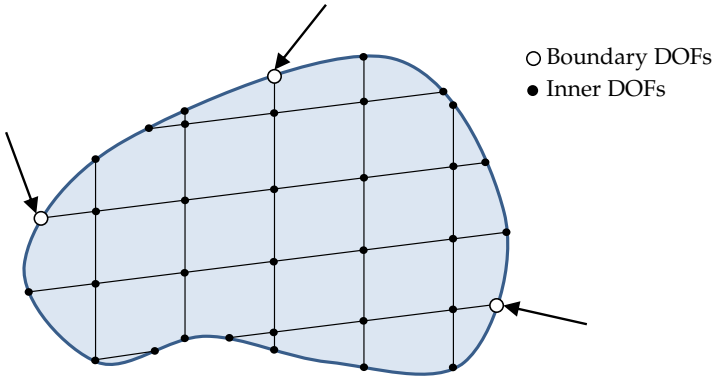

Figure 2.3: FE model with boundary and inner DOFs (see similar figure in [138])

The structure interacts only via the boundary DOFs (also called interface DOFs) with other components. Hence, the $(n_{\mathrm{FE}} \times 1)$ vector $\mathbf{x}$ of nodal DOFs of the FE model can be separated into boundary DOFs represented in the $(n_B \times 1)$ vector $\mathbf{x}_B$ and inner DOFs collected in the $(n_I \times 1)$ vector $\mathbf{x}_I$. According to this subdivision the linear equation of motion (eq. (2.69)) can be written in partitioned form as

$$\begin{bmatrix} \mathbf{M}_{BB} & \mathbf{M}_{BI} \\ \mathbf{M}_{IB} & \mathbf{M}_{II} \end{bmatrix} \begin{bmatrix} \ddot{\mathbf{x}}_B \\ \ddot{\mathbf{x}}_I \end{bmatrix} + \begin{bmatrix} \mathbf{K}_{BB} & \mathbf{K}_{BI} \\ \mathbf{K}_{IB} & \mathbf{K}_{II} \end{bmatrix} \begin{bmatrix} \mathbf{x}_B \\ \mathbf{x}_I \end{bmatrix} = \begin{bmatrix} \mathbf{f}_B \\ \mathbf{0} \end{bmatrix}. \tag{2.77}$$

Due to the fact that all external loads act only on the boundary DOFs, $\mathbf{f}_I = \mathbf{0}$ is used in the previous equation.

For the fixed boundary CMS the reduction basis is a combination of fixed boundary normal modes $\boldsymbol{\phi}_i^{\mathrm{CNM}}$ and constraint modes $\boldsymbol{\phi}_i^{\mathrm{CM}}$. The fixed boundary normal modes $\boldsymbol{\phi}_i^{\mathrm{CNM}}$ are obtained by computing the corresponding eigenvalue problem at $\mathbf{x}_B = \mathbf{0}$. Hence, only the second row of eq. (2.77) is considered, leading to the eigenvalue problem

$$\left(\mathbf{K}_{II} - \omega_i^2 \mathbf{M}_{II}\right) \boldsymbol{\phi}_{II,i}^{\mathrm{CNM}} = \mathbf{0}, \quad i = 1, \ldots, n_I. \tag{2.78}$$

For this eigenvalue problem n_I eigenvectors $\boldsymbol{\phi}_{II,i}^{\mathrm{CNM}}$ with the corresponding eigenvalues ω_i^2 can be computed. In practice the consideration of $v << n_I$ fixed boundary normal modes is sufficient for acceptable accuracy. The actual number v is problem dependent and often chosen based on the highest frequency of interest. The matrix containing all v fixed boundary normal modes can be written as

$$\boldsymbol{\Phi}_{\mathrm{V}}^{\mathrm{CB}} = \begin{bmatrix} \mathbf{0} & \cdots & \mathbf{0} \\ \boldsymbol{\phi}_{II,i}^{\mathrm{CNM}} & \cdots & \boldsymbol{\phi}_{II,v}^{\mathrm{CNM}} \end{bmatrix}, \quad i = 1, \ldots, v. \tag{2.79}$$

The computation of the constraint modes $\boldsymbol{\phi}_i^{\mathrm{CM}}$ is based on a static *Guyan reduction* [49]. Thereby the displacements of the inner DOFs are estimated by the static deformation resulting from a deflection of the boundary DOFs. Hence, the static problem

$$\mathbf{K}\mathbf{x} = \mathbf{f} \tag{2.80}$$

is considered. This equation can be written in partitioned form

$$\begin{bmatrix} \mathbf{K}_{BB} & \mathbf{K}_{BI} \\ \mathbf{K}_{IB} & \mathbf{K}_{II} \end{bmatrix} \begin{bmatrix} \mathbf{x}_B \\ \mathbf{x}_I \end{bmatrix} = \begin{bmatrix} \mathbf{f}_B \\ \mathbf{0} \end{bmatrix}, \tag{2.81}$$

where $\mathbf{f}_I = \mathbf{0}$ is used. From the second row of the latter equation $\mathbf{x}_I$ can be computed directly for a prescribed deflection of the boundary DOFs $\mathbf{x}_B$ by

$$\mathbf{x}_I = -{\mathbf{K}_{II}}^{-1} \mathbf{K}_{IB}\, \mathbf{x}_B. \tag{2.82}$$

This allows to express all FE DOFs $\mathbf{x}$ by the boundary DOFs $\mathbf{x}_B$ as

$$\mathbf{x} = \begin{bmatrix} \mathbf{I}_{BB} \\ -{\mathbf{K}_{II}}^{-1} \mathbf{K}_{IB} \end{bmatrix} \mathbf{x}_B = \boldsymbol{\Phi}_{\mathrm{S}}^{\mathrm{CB}}\, \mathbf{x}_B, \tag{2.83}$$

where $\mathbf{I}_{BB}$ denotes a $(n_B \times n_B)$ identity matrix. In eq. (2.83) the $(n_{\mathrm{FE}} \times n_B)$ matrix $\boldsymbol{\Phi}_{\mathrm{S}}^{\mathrm{CB}}$ can be identified as a matrix containing the constraint modes $\boldsymbol{\phi}_i^{\mathrm{CM}}$ in its columns. The k-th constraint mode can be obtained from a static FE analysis where at the k-th component of $\mathbf{x}_B$ a unit displacement is applied while all other components of $\mathbf{x}_B$ are forced to be zero.

The final reduction basis for the fixed boundary CMS can be written as

$$\mathbf{x} \approx \boldsymbol{\Phi}_{\mathrm{CMS}}^{\mathrm{CB}}\, \boldsymbol{\zeta} = \begin{bmatrix} \boldsymbol{\Phi}_{\mathrm{V}}^{\mathrm{CB}} & \boldsymbol{\Phi}_{\mathrm{S}}^{\mathrm{CB}} \end{bmatrix} \begin{bmatrix} \boldsymbol{\zeta}_I \\ \mathbf{x}_B \end{bmatrix}, \tag{2.84}$$

whereby the boundary DOFs $\mathbf{x}_B$ remain in the vector reduced flexible coordinates together with the modal coordinates for the fixed boundary normal modes $\boldsymbol{\zeta}_I$.

In general, for all CMS methods the $(n_{\mathrm{FE}} \times m)$ reduction basis

$$\boldsymbol{\Phi}_{\mathrm{CMS}} = \begin{bmatrix} \boldsymbol{\Phi}_{\mathrm{V}} & \boldsymbol{\Phi}_{\mathrm{S}} \end{bmatrix}, \tag{2.85}$$

is a combination of s trial vectors which are basically deformation shapes due to static loads $\boldsymbol{\Phi}_{\mathrm{S}}$ and v vibration mode shapes $\boldsymbol{\Phi}_{\mathrm{V}}$.

Free-free mode shapes

The equations of motion of a flexible multibody system using an FFRF can be simplified if the used mode shapes are so-called *free-free modes* (see [30, 117]). In general, the trial vectors computed by CMS methods do not fulfill the criteria of free-free modes. Furthermore, for the FFRF it is required that the trial vectors do not contain any rigid body content. In the literature two different strategies can be found to transform an arbitrary set of trial vectors into trial vectors that have the advantageous properties of free-free modes.

Most commonly the *mode shape orthogonalization* (see [37]) is used. For this strategy a generalized eigenvalue problem of the reduced equation of motion (see eq. (2.71)) with the $(m \times m)$ reduced mass and stiffness matrix $\widetilde{\mathbf{M}} = \boldsymbol{\Phi}_{\mathrm{CMS}}{}^{\mathsf{T}} \mathbf{M} \boldsymbol{\Phi}_{\mathrm{CMS}}$, $\widetilde{\mathbf{K}} = \boldsymbol{\Phi}_{\mathrm{CMS}}{}^{\mathsf{T}} \mathbf{K} \boldsymbol{\Phi}_{\mathrm{CMS}}$ is solved additionally. This eigenvalue problem can be written as

$$\left(\widetilde{\mathbf{K}} - \lambda_i \widetilde{\mathbf{M}} \right) \mathbf{y}_i = \mathbf{0}, \quad i = 1, \ldots, m \tag{2.86}$$

and be solved to obtain a new set of trial vectors

$$\boldsymbol{\Phi}_{free} = \boldsymbol{\Phi}_{\mathrm{CMS}} \mathbf{Y}. \tag{2.87}$$

The $(n_{FE} \times m)$ matrix $\boldsymbol{\Phi}_{free}$ contains trial vectors which are free-free modes and the $(m \times m)$ matrix $\boldsymbol{Y}$ contains m eigenvectors $\mathbf{y}_i$ computed from eq. (2.86). The rigid body content is removed by rejecting the columns of the matrix $\boldsymbol{\Phi}_{free}$ which correspond to zero eigenvalues of eq. (2.86).

In [117] a different method for separating a set of trial vectors into pseudo-free-surface modes and rigid body modes is proposed. This method also leads to a set of new trial vectors which have the advantageous properties of free-free modes.

2.2.4 Trial vector derivatives (TVDs)

The trial vectors for the CMS reduction basis are a function of the structure's mass and stiffness matrix. For linear structures these matrices are not a function of the deformation state, and hence, time-invariant. Therefore, the CMS trial vector of linear systems are time and

state independent ($\boldsymbol{\phi}_i \neq \boldsymbol{\phi}_i(\mathbf{x})$). For nonlinear systems the undamped equation of motion eq. (2.62) can be rewritten with a state dependent stiffness matrix $\mathbf{K}_{nl}(\mathbf{x})$ as

$$\mathbf{M}\ddot{\mathbf{x}} + \mathbf{K}_{nl}(\mathbf{x})\mathbf{x} = \mathbf{f}. \tag{2.88}$$

Due to the state dependency of $\mathbf{K}_{nl}(\mathbf{x})$, the trial vectors are depending on the deformation state for nonlinear systems ($\boldsymbol{\phi}_i = \boldsymbol{\phi}_i(\mathbf{x})$). As a consequence of model order reduction, the deformation dependency can be expressed as a dependency on the trial vector scaling factors ($\boldsymbol{\phi}_i(\mathbf{x}) = \boldsymbol{\phi}_i(\boldsymbol{\Phi}\boldsymbol{\zeta}) = \boldsymbol{\phi}_i(\boldsymbol{\zeta})$). Often, trial vectors are computed based on a linear assumption at some reference state $\hat{\mathbf{x}} = \boldsymbol{\Phi}\hat{\boldsymbol{\zeta}}$ or by neglecting the nonlinear parts. The difference between these linearized trial vectors compared to the trial vectors of the full nonlinear system can be approximated by a Taylor series expansion around the reference state. For the trial vector $\boldsymbol{\phi}_i$ the Taylor serias expansion can be written as

$$\boldsymbol{\phi}_i(\boldsymbol{\zeta}) = \boldsymbol{\phi}_i|_{\hat{\boldsymbol{\zeta}}} + \sum_{j=1}^{m} \left.\frac{\partial \boldsymbol{\phi}_i}{\partial \zeta_j}\right|_{\hat{\boldsymbol{\zeta}}} (\zeta_j - \hat{\zeta}_j) + \textit{terms of higher order}, \tag{2.89}$$

with $\hat{\boldsymbol{\zeta}} = [\hat{\zeta}_1 \cdots \hat{\zeta}_m]^\mathsf{T}$ being the scaling factors at the reference state. This reference state is not further specified at this point. For many structures the undeformed state ($\hat{\mathbf{x}} = \mathbf{0}; \hat{\boldsymbol{\zeta}} = \mathbf{0}$) is a good choice but also a certain preload state ($\hat{\mathbf{x}} = \mathbf{x}_{\mathrm{PL}}; \hat{\boldsymbol{\zeta}} = \boldsymbol{\zeta}_{\mathrm{PL}}$) might be a possible choice for the reference state.

In eq. (2.89), the term $\frac{\partial \boldsymbol{\phi}_i}{\partial \zeta_j}$ denotes the first order *trial vector derivative* (TVD) of the i-th trial vector with respect to the j-th modal coordinate. The TVD is also called *modal derivative* (MD) in the literature. The TVD represents the sensitivity of the trial vector $\boldsymbol{\phi}_i$ corresponding to a deflection in the direction of the trial vector $\boldsymbol{\phi}_j$.

Based on the Taylor series expansion, a non-flat Galerkin projection using a quadratic manifold can be formulated. Such a quadratic manifold projection using TVDs is presented in [57, 123] for geometric nonlinearities. This strategy leads to a change of the structure of the reduced equations of motion. This drawback causes a more complex computation of the equations themselves and the Jacobian matrix. These disadvantages make the use of a quadratic manifold in combination with commercial availably multibody software unattractive. Another approach is to consider the TVDs $\frac{\partial \boldsymbol{\phi}_i}{\partial \zeta_j}$ as independent trial vectors for an extension of the reduction basis. Such an approach is considered in [55, 56, 121, 129]. This is a possible approach to capture nonlinear effects due to the connection between TVDs and the sensitivity of a trial vector. Due to the high number of possible TVDs and their redundant information content, the a-priori selection of TVDs is still an open issue. Different selection criteria for the direct use of TVDs are reviewed in appendix C.1. In a parallel work of Wu [147] TVDs are used in the context of MBS for an efficient reduction of structures showing geometric nonlinearities.

In the following, the general computation of first order TVDs for the CMS reduction basis is reviewd.

TVDs for vibration modes

Vibration modes are computed based on an eigenvalue problem of the form

$$\left(\mathbf{K_c} - \omega_i^2 \mathbf{M}\right) \boldsymbol{\phi}_i = \mathbf{0}, \tag{2.90}$$

where $\mathbf{K_c} = \mathbf{K}_{nl}(\boldsymbol{\Phi}\hat{\boldsymbol{\zeta}})$ denotes the stiffness matrix at the chosen reverence state. One way to determine the TVDs $\frac{\partial \boldsymbol{\phi}_i}{\partial \zeta_j}$ for vibration modes is to compute the derivative of this eigenvalue problem with respect to the modal coordinates. This can be written as

$$\frac{\partial}{\partial \zeta_j}\left[\left(\mathbf{K_c} - \omega_i^2 \mathbf{M}\right) \boldsymbol{\phi}_i = \mathbf{0}\right]. \tag{2.91}$$

Applying the product rule leads to

$$\left(\mathbf{K_c} - \omega_i^2 \mathbf{M}\right) \frac{\partial \boldsymbol{\phi}_i}{\partial \zeta_j} + \left(\frac{\partial \mathbf{K_c}}{\partial \zeta_j} - \frac{\partial \omega_i^2}{\partial \zeta_j}\mathbf{M}\right) \boldsymbol{\phi}_i = \mathbf{0}, \tag{2.92}$$

whereby the derivative $\frac{\partial \mathbf{M}}{\partial \zeta_j}$ has been set to zero, since the mass matrix does not depend on the deformation.

This equation cannot be solved directly for $\frac{\partial \boldsymbol{\phi}_i}{\partial \zeta_j}$ since the coefficient matrix $\left(\mathbf{K_c} - \omega_i^2 \mathbf{M}\right)$ is singular per definition of eq. (2.90). One way to solve this system for $\frac{\partial \boldsymbol{\phi}_i}{\partial \zeta_j}$ is to use the normalization condition of the mode shapes. In [120] a generalized method for different normalization conditions is shown. The common mass normalization $\boldsymbol{\phi}_i{}^{\mathsf{T}} \mathbf{M} \boldsymbol{\phi}_i = 1$ is used herein exemplary. Differentiating this normalization condition with respect to the modal coordinate leads to

$$\boldsymbol{\phi}_i{}^{\mathsf{T}} \mathbf{M} \frac{\partial \boldsymbol{\phi}_i}{\partial \zeta_j} = 0, \tag{2.93}$$

whereby the symmetry of the mass matrix is used for simplification (see [57]). With eqs. (2.92) and (2.93) the following system

$$\begin{bmatrix} \left(\mathbf{K_c} - \omega_i^2 \mathbf{M}\right) & \left(-\mathbf{M}\boldsymbol{\phi}_i\right) \\ -\left(\mathbf{M}\boldsymbol{\phi}_i\right)^{\mathsf{T}} & 0 \end{bmatrix} \begin{bmatrix} \frac{\partial \boldsymbol{\phi}_i}{\partial \zeta_j} \\ \frac{\partial \omega_i^2}{\partial \zeta_j} \end{bmatrix} = \begin{bmatrix} -\frac{\partial \mathbf{K_c}}{\partial \zeta_j}\boldsymbol{\phi}_i \\ 0 \end{bmatrix}, \tag{2.94}$$

can be formed which allows the direct computation of $\frac{\partial \boldsymbol{\phi}_i}{\partial \zeta_j}$. Jain [57] mentioned that other approaches like the use of a pseudo inverse (see [44]) or the Nelson method [77] could be used to compute the TVD $\frac{\partial \boldsymbol{\phi}_i}{\partial \zeta_j}$. The full computation of TVDs for vibration modes along eq. (2.94) requires the factorization of a high dimensional matrix for each ω_i, as mentioned in [57]. This reduces the efficiency and is not easy to compute for large FE structures with commercial FE solvers.

However, in [55, 56] it is proposed to neglect the inertia related terms for a simplified computation of TVDs. The conclusions in [121] confirm that neglecting this terms has only small influence on the result quality. This leads to a simplification for the computation of TVDs in the form

$$\mathbf{K_c} \frac{\partial \boldsymbol{\phi}_i}{\partial \zeta_j} = -\frac{\partial \mathbf{K_c}}{\partial \zeta_j}\boldsymbol{\phi}_i. \tag{2.95}$$

TVDs for static modes

The static modes of the CMS reduction basis are computed based on a static problem in the form

$$\mathbf{K_c}\boldsymbol{\phi}_i = \mathbf{f}_i. \tag{2.96}$$

Differentiating this equation with respect to the modal coordinate ζ_j yields

$$\frac{\partial \mathbf{K_c}}{\partial \zeta_j}\boldsymbol{\phi}_i + \mathbf{K_c}\frac{\partial \boldsymbol{\phi}_i}{\partial \zeta_j} = \mathbf{0}. \tag{2.97}$$

To derive the latter equation the product rule has been applied and it has been considered that $\mathbf{f}_i$ is not state dependent. Rearranging this equation leads to

$$\mathbf{K_c}\frac{\partial \boldsymbol{\phi}_i}{\partial \zeta_j} = -\frac{\partial \mathbf{K_c}}{\partial \zeta_j}\boldsymbol{\phi}_i \tag{2.98}$$

which is formally equivalent to eq. (2.95).

Based on the theoretical formulas for TVDs of the CMS reduction basis, their practical computation and physical interpretation for contact problems is presented in section 3.2.1.

2.2.5 Proper orthogonal decomposition (POD)

Proper orthogonal decomposition (POD) is a powerful method for data analysis with the aim of representing the essential information of a high dimensional space with a low dimensional subspace. POD provides an efficient way of finding the dominant components of a high dimensional matrix with only a few basis vectors [17]. In the last years, POD has been used in various fields of engineering, like fluid dynamics, experimental data analysis, nonlinear dynamics, image processing, multibody dynamics (see [124]), and others. A good overview of different applications can be found in [58, 64]. Furthermore, POD is closely related to principal component analysis (PCA), Karhunen-Loève decomposition (KLD) and singular value decomposition (SVD). The connections between these methods are discussed in [64]. In the cited literature [17, 58, 64], among others, more detailed information can be found. POD can also be used in combination with measured response data to determine mode shapes of the measured structure (see [51]).

The mathematical description of POD briefly outlined in this section is closely related to [133]. Assuming that the $(n \times p)$ matrix $\mathbf{Y} = \left[\mathbf{y}_1, \ldots, \mathbf{y}_p\right]$ contains in its columns the $(n \times 1)$ vectors $\mathbf{y}_i, i = 1, \ldots, p$, POD of rank g delivers a set of $(n \times 1)$ orthonormal vectors $\mathbf{u}_1, \ldots, \mathbf{u}_g$, which approximate the space spanned by $\mathbf{Y}$ optimal in an Euclidean sense. Mathematically, this can be described by an optimization problem maximizing the function

$$J = \sum_{i=1}^{g}\sum_{j=1}^{p}\left(\mathbf{y}_j{}^{\mathsf{T}}\mathbf{u}_i\right)^2 \quad \rightarrow \max. \tag{2.99}$$

The vectors $\mathbf{u}_1, \ldots, \mathbf{u}_g$ are called *proper orthogonal modes* (POMs) and fulfill the condition

$$\left(\mathbf{u}_i{}^\mathsf{T}\mathbf{u}_j\right)^2 = \begin{cases} 1 & i = j, \\ 0 & i \neq j. \end{cases} \tag{2.100}$$

According to [133], the POMs can be computed by taking the first g eigenvectors of the $(p \times p)$ eigenvalue problem

$$\left(\mathbf{Y}^\mathsf{T}\mathbf{Y}\right)\hat{\mathbf{u}}_i = \lambda_{\mathrm{POV},i}\hat{\mathbf{u}}_i \quad \text{for } i = 1, \ldots, g \tag{2.101}$$

followed by a transformation of the form

$$\mathbf{u}_i = \frac{1}{\sqrt{\lambda_{\mathrm{POV},i}}}\mathbf{Y}\hat{\mathbf{u}}_i \quad \text{for } i = 1, \ldots, g, \tag{2.102}$$

where $\lambda_{\mathrm{POV},i} \geq 0$ are the so called *proper orthogonal values* (POVs). For all further investigations it is assumed that the eigenvalue problems are solved with the characteristics $\lambda_{\mathrm{POV},1} > \lambda_{\mathrm{POV},2} >, \ldots, \lambda_{\mathrm{POV},i}$.

A slightly modified form of POD can be computed by a weighted inner product with a symmetric and positive definite $(n \times n)$ matrix $\mathbf{A}$ which means maximizing the function

$$J = \sum_{i=1}^{g}\sum_{j=1}^{p}\left(\mathbf{y}_j{}^\mathsf{T}\mathbf{A}\mathbf{u}_i\right)^2 \quad \rightarrow \max. \tag{2.103}$$

Again the POMs $\mathbf{u}_1, \ldots, \mathbf{u}_g$ of the weighted POD can be computed from the first g eigenvectors of the eigenvalue problem

$$\left(\mathbf{Y}^\mathsf{T}\mathbf{A}\mathbf{Y}\right)\hat{\mathbf{u}}_i = \lambda_{\mathrm{POV},i}\hat{\mathbf{u}}_i \quad \text{for } i = 1, \ldots, g, \tag{2.104}$$

with following transformation along eq. (2.102). The POMs computed by weighted POD and also fulfill the orthonormal condition of eq. (2.100). Obviously the POD with inner weighting can be easily transformed into the POD defined by eqs. (2.99) and (2.101) by substituting $\mathbf{A}$ with an $(n \times n)$ identity matrix $\mathbf{I}$.

For the sake of completeness it is mentioned that instead of an eigenvalue problem also an SVD (see appendix A.2) can be used to compute the POD. Thereby, the POMs are the left singular vectors and the POVs are the squares of the singular values.

2.3 Reduction strategies for jointed flexible bodies

The consideration of contact and friction forces, with common reduction techniques like CMS, leads to unpredictable (probably poor) result quality. Hence, different extension strategies of the CMS reduction basis with special trial vectors have been presented in the last decades.

Some publications suggest to preserve all nodal FE DOFs which are involved in the nonlinearity (see [35, 38, 47, 50, 94, 98]). For jointed structures each FE node inside the joint area would be preserved in the reduced system. Depending on the size of the joint and the used FE mesh this approach leads to several hundreds or even thousands DOFs in the reduced system. Hence, the computational effort would be again very high.

So-called *interface modes* have been introduced in the 1990's and generalize the space spanned by the constraint modes corresponding to the boundary DOFs. Detailed information on interface modes can be found among others in [5, 12, 13, 32, 131]. Interface modes are not specialized for joints and can be applied to any other kind of interface.

A specialized development of interface modes for jointed structures was presented by Witteveen [138, 140] by so-called *joint interface modes*. These joint interface modes are based on a generalized eigenvalue problem of the static reduced mass and stiffness matrices of the structure. According to [138, 140], these joint interface modes show a much faster convergence than the general interface modes. In [111] a generalization of this approach for local nonlinearities (not joint focused) is presented. The joint interface modes of this approach require static responses due to imposed unit displacements. Witteveen mentioned in [139] that this leads to a high computational effort, especially if the number of interface nodes in the joint area is large. Hence, a development of the joint interface modes by subdividing the joint area in certain subareas is provided in [139]. These subareas are loaded with unity pressure loads for the computation of the joint interface modes. Furthermore, in [144] it is proposed to use a POD instead of the generalized eigenvalue problem. A very similar approach was later suggested in [45]. An open question in this procedure is the number of chosen subareas. It should be mentioned, that the joint interface modes presented in [144] are available in the commercial software package *MAMBA* [29].

Breitfuss recommended in [14] the computation of joint interface modes based on contact forces obtained from simulations of the full nonlinear system. For this purpose, different (meaningful) load combinations for the system have to be chosen. The tremendous computational burden which arises for the time integration of the full nonlinear system is a major disadvantage of this approach. This is especially true for complex structures with a high number of FE DOFs.

All of the reviewed strategies have at least one major disadvantage. Hence, a novel computation approach for joint modes based on the theoretical basis of TVDs is presented in section 3.2.

2.4 Contact and friction models for dry friction joints

In this section a short review of the properties of dry friction joints is given. Furthermore, a literature review on contact and friction models is presented.

2.4.1 Characteristics of joints with dry friction

A detailed investigation of dry friction inside joints has been performed by Gaul and his associates [40, 42, 61, 62]. These latter contributions are based on an experiment in which a generic joint was isolated and systematically investigated. The tangential stiffness and damping properties of the joint were studied with respect to normal pressure, excitation frequency, and amplitude. The fundamental characteristics of the experimental results can be analytically or numerically reproduced if the friction model can capture three different states, namely:

- Gaping: The surfaces are not in contact. Consequently, there is no friction stress $\tau_F = 0$.
- Sticking: The surfaces are in contact and the local friction stress τ_F is lower than a certain sticking stress limit R_G. The sticking stress limit normally depends on the contact pressure p_N and a friction coefficient μ. During sticking no energy is dissipated and the relative tangential displacement s of the two surfaces is zero or elastic (reversible).
- Slipping: The surfaces are in contact and the local friction stress is higher than the sticking stress limit. Slipping leads to energy dissipation since the relative tangential displacement of the involved surfaces is irreversible. The frequency dependency of the energy dissipation is small and can be neglected. Note that also in the case of local sliding, the small displacement assumption still holds due to the construction of the joint.

Furthermore, the cited literature mentions that the described behavior can be captured with a three-parameter Coulomb-type friction model, as shown in fig. 2.4, where τ_F denotes the friction stress, s is the relative tangential displacement, $(c_1 + c_2)$ is the slope of the stick motion, c_2 is the slope of slip motion, and R_G is the sticking stress limit. The stick motion slope $(c_1 + c_2)$ and the slip motion slope c_2 are both nonzero for the investigated metallic joints. In [61] it is mentioned that the common approach for the sticking limit $R_G = \mu p_N$ is valid for the friction model defined by eq. (2.113). Furthermore, in [61] the friction coefficient μ has been computed based on the measured data and it is revealed that the computed values are similar to those known from the literature. These experiments also confirmed that the friction coefficient μ does not depend on the contact pressure p_N.

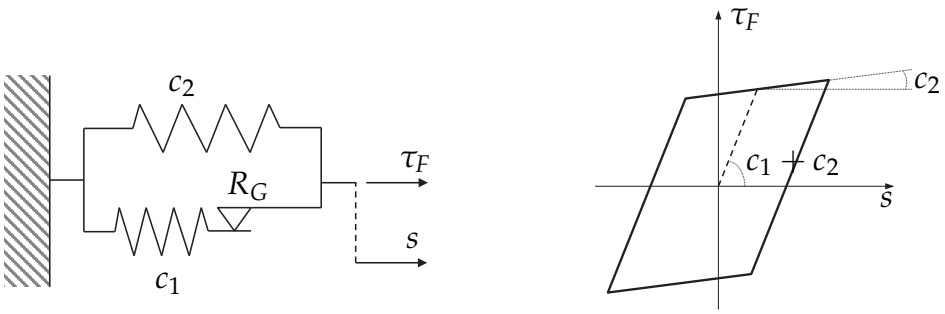

Figure 2.4: Three-parameter Coulomb-type friction model: model and hysteresis

The resulting frictional characteristic of a distributed joint and its effect on the entire structure is given as the sum of all gaping, sticking, and slipping areas inside the joint. Consequently, the local friction model shown in fig. 2.4 has to be applied to the relevant degrees of freedom over the entire joint in case of a discrete approach like the FEM. According to the three occurring states the entire joint area A can be subdivided into three subsections A_{gap}, A_{stick}, and A_{slip}. The area in which gaping takes place is denoted as A_{gap}, A_{stick} is the area where both involved contact surfaces are sticking with respect to each other, and A_{slip} is representing the area where the contact surfaces slip with respect to each other. Each of these three subareas may be arbitrarily distributed throughout the joint and their distribution is time-dependent. However, for the entire joint area

$$A = A_{gap} + A_{stick} + A_{slip} \tag{2.105}$$

must hold at any time.

For the contacting area of the joint $A_c = A_{stick} + A_{slip}$ three different states can occur, namely:

- The sticking condition is satisfied at each location ($A_c = A_{stick},\ A_{slip} = 0$).
- The contacting area is partially slipping and sticking ($A_{stick} \neq 0,\ A_{slip} \neq 0$). This state often denoted as *microslip* in the literature.
- The entire contacting area is slipping, and hence there is no sticking subarea ($A_c = A_{slip},\ A_{stick} = 0$). This state is commonly referred to as *macroslip*. Note that in such a case, the former restriction of small relative displacement of the joint surfaces with respect to each other no longer holds. For many types of joints, the appearance of macroslip indicates joint failure. Hence, the macroslip state lies outside the scope of this dissertation.

2.4.2 Contact models

Contact models have to ensure that the contacting surfaces do not penetrate (or at least not perceptibly penetrate). In the following subsections, different penalty contact models are reviewed. Nonpenalty methods, like the Lagrange method or the augmented Lagrange method (see [60, 146]), are not included in this review.

Linear penalty model

The linear penalty model (see [60, 146]) is a widely used approach for the computation of contact problems. This model describes the pressure-gap relationship by

$$p_N = \begin{cases} 0 & \text{if } g_N \geq 0, \\ \varepsilon_N(-g_N) & \text{if } g_N < 0, \end{cases} \tag{2.106}$$

where $\varepsilon_N > 0$ is the contact penalty parameter. This model requires only one parameter ε_N, which can be physically interpreted as a linear spring stiffness. The pressure-gap relationship for this model is plotted in fig. 2.5.

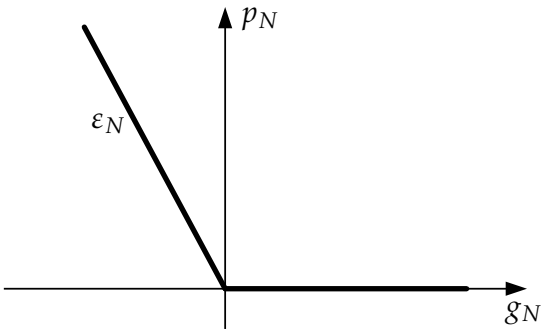

Figure 2.5: Linear penalty model

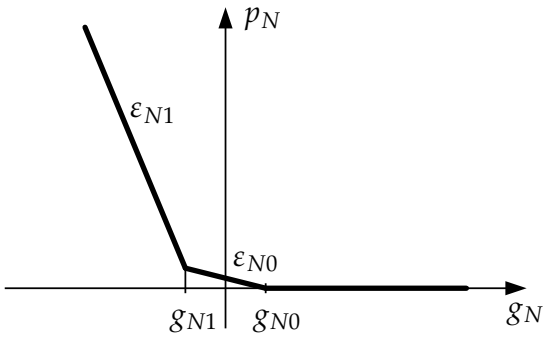

Figure 2.6: Multi-stage linear penalty model

Multi-stage linear penalty model

The multi-stage linear penalty model is an extension of the linear penalty model. The idea is that the pressure-gap relationship is divided into k sections with different penalty parameters ε_{Nk}. The model is often used by Gaul and his associates in their work [10, 11, 41, 69]. In [10, 41] a two-stage version of this model is used, and the contact parameters for a best match between simulation and experiment are given. For the two-stage linear penalty model, the pressure-gap relationship is plotted in fig. 2.6. Mathematically, this relationship can be written for $g_{N0} > g_{N1}$ and $\varepsilon_{N1} > \varepsilon_{N0} > 0$ as

$$p_N = \begin{cases} 0 & \text{if } g_N \geq g_{N0}, \\ \varepsilon_{N0}\left(g_{N0} - g_N\right) & \text{if } g_{N0} > g_N > g_{N1}, \\ \varepsilon_{N0}\left(g_{N0} - g_{N1}\right) + \varepsilon_{N1}\left(g_{N1} - g_N\right) & \text{if } g_N \leq g_{N1}. \end{cases} \tag{2.107}$$

For the two-stage linear penalty model, the parameters $(\varepsilon_{N0}, \varepsilon_{N1}, g_{N0}, g_{N1})$ are required. A physical interpretation of the parameters, similar to the linear penalty model, is possible.

Power-function-based nonlinear penalty model

This pressure-gap relationship uses the power function and can be found in [136, 145]. The pressure-gap relationship is plotted in fig. 2.7 and mathematically described by

$$p_N = \begin{cases} 0 & \text{if } g_N \geq 0, \\ \varepsilon_N \left| g_N \right|^m & \text{if } g_N < 0. \end{cases} \tag{2.108}$$

This relationship was developed based on statistical models. For most metallic materials, the parameter ε_N is proportional to the modulus of elasticity and the parameter m can be approximately set to $m \approx 2$ (see [145]).

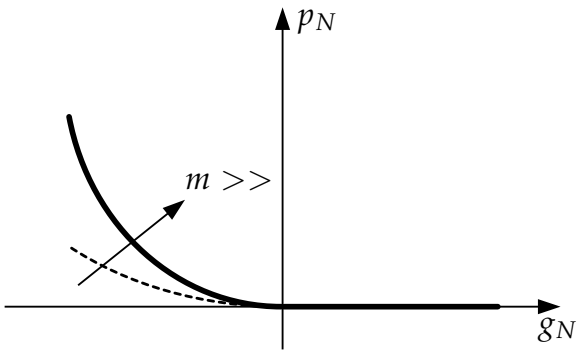

Figure 2.7: Power-function-based penalty model

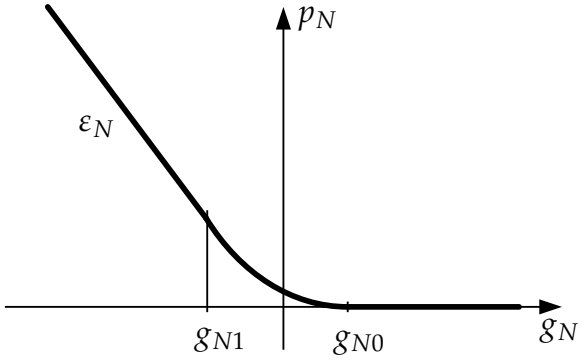

Figure 2.8: Quadratic-linear penalty model

Combined quadratic-linear penalty model

This model is used in [87, 92] and combines quadratic and linear penalty models in order to get a smoothed transition between gaping and penetration. The pressure-gap relationship plotted in fig. 2.8 is mathematically formulated as

$$p_N = \begin{cases} 0 & \text{if } g_N \geq g_0, \\ -\frac{1}{2(g_{N1}-g_{N0})}\varepsilon_N \left(g_N - g_{N0}\right)^2 & \text{if } g_{N0} > g_N > g_{N1}, \\ -\varepsilon_N g_N + \frac{1}{2}\varepsilon_N \left(g_{N1} + g_{N0}\right) & \text{if } g_N \leq g_{N1}. \end{cases} \tag{2.109}$$

This model has a continuous slope of the pressure-gap relationship at the points g_{N0}, g_{N1} and requires three parameters $(\varepsilon_N, g_{N0}, g_{N1})$.

Exponential penalty model

An exponential penalty model can be found in [27] and is implemented in the commercially available FE software *Abaqus* [26]. For this model, the pressure-gap relationship is depicted in fig. 2.9 and mathematically defined as

$$p_N = \begin{cases} 0 & \text{if } g_N \geq g_{N0}, \\ \frac{p_{N0}}{\exp(1)-1}\left[\left(\frac{-g_N}{g_{N0}}+1\right)\left(\exp\left(\frac{-g_N}{g_{N0}}+1\right)-1\right)\right] & \text{if } g_N < g_{N0}. \end{cases} \tag{2.110}$$

In the latter equation p_{N0} is the contact pressure at $g_N = 0$, and $g_{N0} > 0$ is the gap at which $p_N = 0$.

For this penalty model, two parameters (p_{N0}, g_{N0}) are needed.

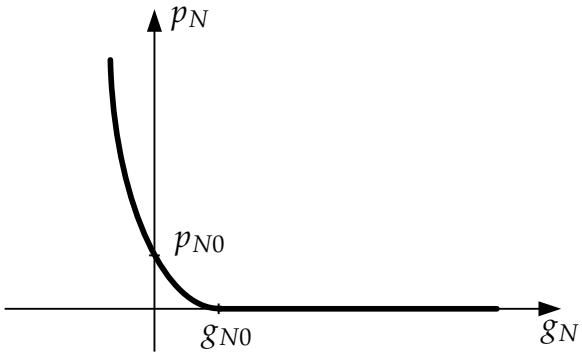

Figure 2.9: Exponential penalty model

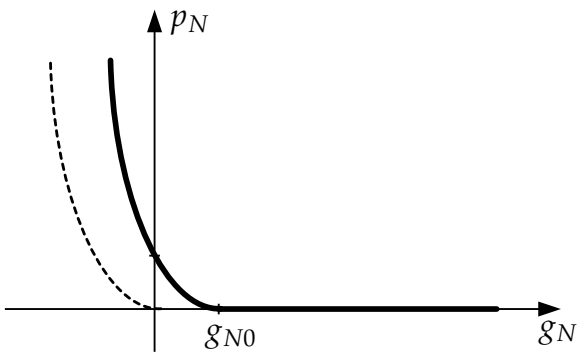

Figure 2.10: Joint adapted exponential penalty model

Joint-adapted exponential penalty model

A joint-adapted exponential penalty model which is based on statistical approaches for describing the height distribution of the asperity summits as used in [43, 137], is presented in this section. Due to the roughness of metallic surfaces, contact only occurs on the summits of the asperities of the surfaces. The Hertzian normal contact of two elastic spheres is applied to model the contact of one single asperity of the surfaces. Furthermore, it is assumed that the height distribution of the asperity summits can be described by an exponential distribution [43, 137]. The statistical approach leads to a penalty model with physically meaningful contact parameters [136]. The mathematical formulation of the pressure-gap relationship is given by

$$p_N = p_{N0} \exp\left(-\lambda_N \left(g_N - g_{N0}\right)\right), \tag{2.111}$$

where λ_N is a statistical parameter, $g_{N0} > 0$ is the initial distance between the highest peak of the rough surface and the reference plane, and $p_{N0} > 0$ is the pressure at $g_N = g_{N0}$. The parameter λ_N is defined as $\lambda_N = 1/\sigma > 0$, where σ is the standard deviation of the height profile of the rough surface. Hence, a relationship between profile roughness parameters of the surfaces and the parameter λ_N can be derived.

For the numerical computation of eq. (2.111) the contact pressure is never exactly zero, and hence needs to be evaluated for all values of g_N which is a major disadvantage of this model. Hence, a modified exponential pressure-gap relationship is defined by

$$p_N = \begin{cases} 0 & \text{if } g_N \geq g_0, \\ \varepsilon_N \left(-g_N + g_{N0}\right) \left(\exp\left(\lambda_N \left(-g_N + g_{N0}\right)\right) - 1\right) & \text{if } g_{N,i} < g_{N0}. \end{cases} \tag{2.112}$$

The pressure-gap relationship defined by this equation is plotted in fig. 2.10.

For this joint-adapted exponential penalty model, three parameters $(g_{N0}, \lambda_N, \varepsilon_N)$ are required. The parameter g_{N0} can in most cases be set to zero. For some investigations, it might be a numerical advantage to have a small negative value for g_{N0}.

In [136] a normal distribution is supposed for the height distribution of the summits of the rough surface. According to [136], this leads to a pressure-gap relationship comparable to

the power-function-based contact model. The idea of using statistical models for describing asperity heights is also used in [48]. Furthermore, in the mentioned paper it is noted that the height distribution of the asperity summits tends to be rather a normal distribution than an exponential distribution. Nevertheless, the latter is sufficient to describe the uppermost 25% of the asperities of most surfaces.

2.4.3 Friction models

Different models for computing the magnitude of the friction stress τ_F found in the literature are reviewed in this section. A good starting point for a literature review on friction models is given by [2, 40, 80, 84]. An investigation of alternatives to the Coulomb friction model can also be found in [81], where especially the continuity of the models is investigated. The difficulties with the discontinuity of the Coulomb model in dynamic simulations are discussed in [83]. The focus of this dissertation is on friction models for dry friction inside joints that can capture the microslip range mentioned in section 2.4.1. Hence, friction models describing sliding friction (like LuGre friction model, signum-friction models, Karnopp model, etc.) are not included in this review. The interested reader is referred to [2, 68, 80, 84].

For the reviewed friction models the hysteresis curves are depicted. For these plots the frictional stress is plotted as a function of the relative displacement and all plotted hysteresis curves are determined for one specific parameter set of the friction model.

Three-parameter Coulomb-type friction model

Based on the characteristics of dry friction joint a three-parameter Coulomb-type model has been introduced in [61, 62]. This model is also depicted and described by fig. 2.4. The frictional stress of this model $\tau_{F,C}$ can be computed along

$$\begin{aligned} \tau_{F,C} &= \tau_{F,C1} + \tau_{F,C2}, \\ \tau_{F,C2} &= c_2 s, \\ \tau_{F,C1} &= \begin{cases} c_1 \left(s - s_G\right) + R_G \operatorname{sgn}\left(\dot{s}_G\right) & \text{if } \left|\tau_{F,C1}\right| < R_G, \\ R_G \operatorname{sgn}\left(\dot{s}_G\right) & \text{if } \quad |\dot{s}| \neq 0, \end{cases} \end{aligned} \tag{2.113}$$

where $\tau_{F,C1}, \tau_{F,C2}$ denote the friction stresses according to the springs, s_G is the displacement at the switching point between sticking and slipping, and $\operatorname{sgn}()$ represents the signum function. The parameters of this model are the sticking stress limit R_G and two stiffness parameters c_1, c_2 representing the slope of the sticking and slipping motion.

This three-parameter Coulomb-type friction model is used as a reference model for the computation of dry friction inside joints.

Adapted Dahl friction model

The Dahl friction model [24, 25] was developed in 1968. The frictional stress computed with the Dahl model τ_D is described by

$$\frac{d\tau_D}{dt} = \frac{d\tau_D}{ds}\frac{ds}{dt}. \tag{2.114}$$

This equation implies that the friction stress is only a function of the tangential displacement. The displacement dependency of the friction stress $\frac{d\tau_D}{ds}$ was described in further studies (see [25]) by

$$\frac{d\tau_D}{ds} = \sigma_0 \left| 1 - \frac{\tau_D}{R_G} \operatorname{sgn}(\dot{s}) \right|^{\alpha} \operatorname{sgn}\left(1 - \frac{\tau_D}{R_G} \operatorname{sgn}(\dot{s}) \right), \tag{2.115}$$

where σ_0 is a stiffness parameter, and α is a model parameter. In this form the Dahl friction model is well documented (see [2, 80] among others). The tangential velocity $\dot{s}$ appears in eq. (2.115) only within the signum function, and hence the Dahl friction model is frequency-independent. To achieve two stiffness regimes for sticking and slipping, it is necessary to extend the Dahl friction model with a parallel linear spring. This leads for the final frictional stress to

$$\tau_{F,D} = c_2 s + \tau_D. \tag{2.116}$$

In the discussed form the Dahl friction model has three parameters (σ_0, c_2, α). The two stiffness parameters can be related to the reference model as $\sigma_0 = c_1; c_2 = c_2$. The parameter α determines the shape of the hysteresis curve (see fig. 2.11a) and is commonly set to $\alpha = 1$. This assumption simplifies eq. (2.115) to

$$\frac{d\tau_D}{ds} = \sigma_0 \left(1 - \frac{\tau_D}{R_G} \operatorname{sgn}(\dot{s}) \right). \tag{2.117}$$

By inserting eq. (2.117) into eq. (2.114) the Dahl friction model can also be written as differential equation in the form of

$$\frac{d\tau_D}{dt} = \sigma_0 \left(1 - \frac{\tau_D}{R_G} \operatorname{sgn}(\dot{s}) \right) \dot{s}. \tag{2.118}$$

It must be mentioned that, for $R_G \to 0$, numerical problems and a division by zero can occur, and hence precautions need to be applied to capture this case.

Valanis friction model

The Valanis model, originally known from plasticity theory, is used as friction model in [40, 42, 61]. In [61] a detailed derivation from the original plasticity model to the Valanis friction

model can be found. The final equation for the friction stress computed with the Valanis model $\tau_{F,V}$ is given by the differential equation

$$\dot{\tau}_{F,V} = \frac{E_0 \dot{s} \left[1 + \frac{\lambda}{E_0} \frac{\Delta \dot{s}}{|\dot{s}|} \left(E_t s - \tau_{F,V}\right)\right]}{1 + \kappa \frac{\lambda}{E_0} \frac{\dot{s}}{|\dot{s}|} \left(E_t s - \tau_{F,V}\right)}. \tag{2.119}$$

Four model parameters $(E_0, E_t, \kappa, \lambda)$ for which a physical interpretation for joints is possible are required for this model. A detailed investigation of the parameters in [61] results in the conclusion that $E_0 = c_1 + c_2$ represents the sticking stiffness, and $E_t = c_2$ the sliding stiffness analogous to the reference model. The parameter κ influences transition between sticking and sliding, and hence the shape of the hysteresis curve. For a physical meaningful hysteresis $(E_0 > E_t)$, this parameter has to be chosen between $0 < \kappa < 1$. The best fit of the hysteresis curve compared to the reference model can be achieved with high values of κ (see fig. 2.11b). By defining an equivalent limit of sticking

$$H_V = \frac{E_0}{\lambda \left(1 - \kappa \frac{E_t}{E_0}\right)}, \tag{2.120}$$

the parameter λ can be computed as

$$\lambda = \frac{E_0 \left(E_0 - E_t\right)}{R_G \left(E_0 - \kappa E_t\right)}. \tag{2.121}$$

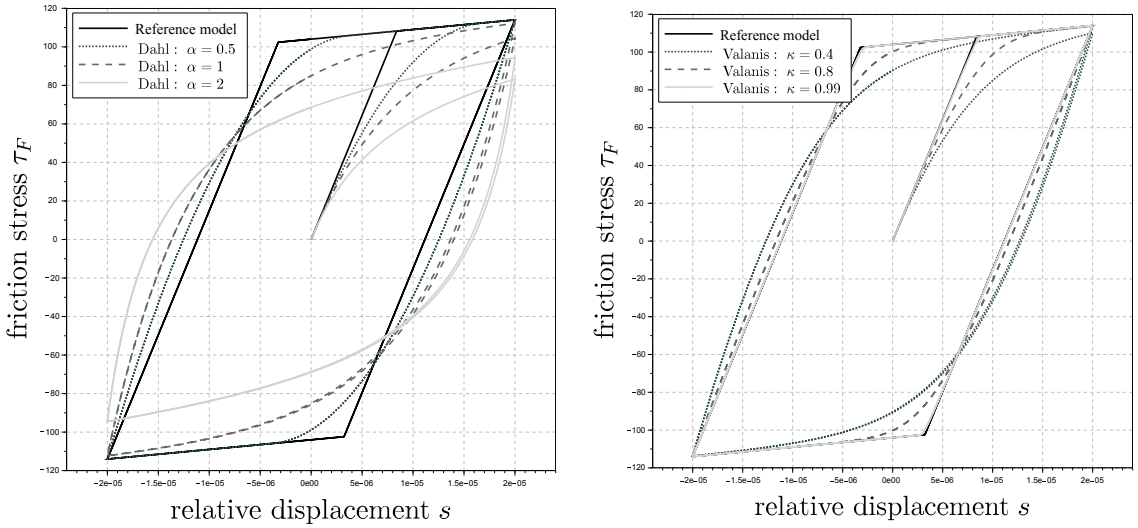

(a) Dahl friction model

(b) Valanis friction model

Figure 2.11: Hysteresis of Dahl and Valanis friction model

Bouc–Wen friction model

A further possibility for describing the hysteresis curve is the Bouc–Wen friction model (see [61]). The friction stress computed with the Bouc–Wen friction model τ_{BW} is mathematically

given by the differential equation

$$\dot{\tau}_{BW} = \dot{s}\left(A - \left(B + \gamma \operatorname{sgn}\left(\dot{s}\tau_{BW}\right)\right)\left|\tau_{BW}\right|^{n}\right), \tag{2.122}$$

where n determines the shape of the hysteresis (see fig. 2.13a). Similarly to the Dahl friction model, it is necessary to extend the Bouc–Wen friction model with a parallel linear spring, and hence the final friction stress is given by

$$\tau_{F,BW} = c_2 s + \tau_{BW}. \tag{2.123}$$

A detailed investigation of the Bouc–Wen model is given in [61], where the model parameters (A, B, γ, n) are identified with respect to the reference model as

$$A = c_1, \quad B = \gamma, \quad 2B = \frac{A}{(R_G)^n}. \tag{2.124}$$

Viscous damping models

A widely used method for the inclusion of local joint damping in a jointed structure is the application of viscous dampers inside the joint as described in [36]. Figure 2.12 shows exemplary three common spring damper elements. Note that several combinations with a different number of serial and/or parallel springs and/or dampers exist. The computed frictional stress is for all viscous damping models velocity dependent.

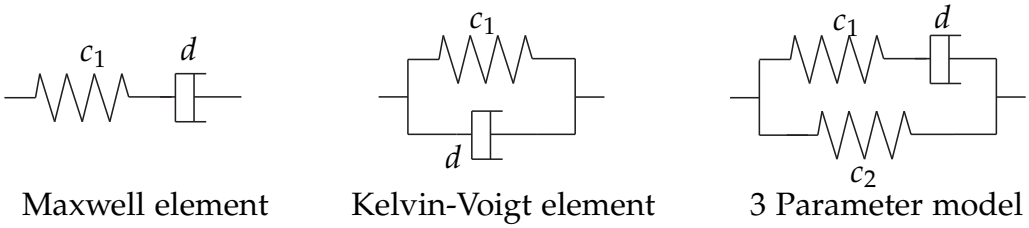

Figure 2.12: Three types of viscous damping models

The hysteresis curves of the different viscous damping models are depicted in fig. 2.13b.

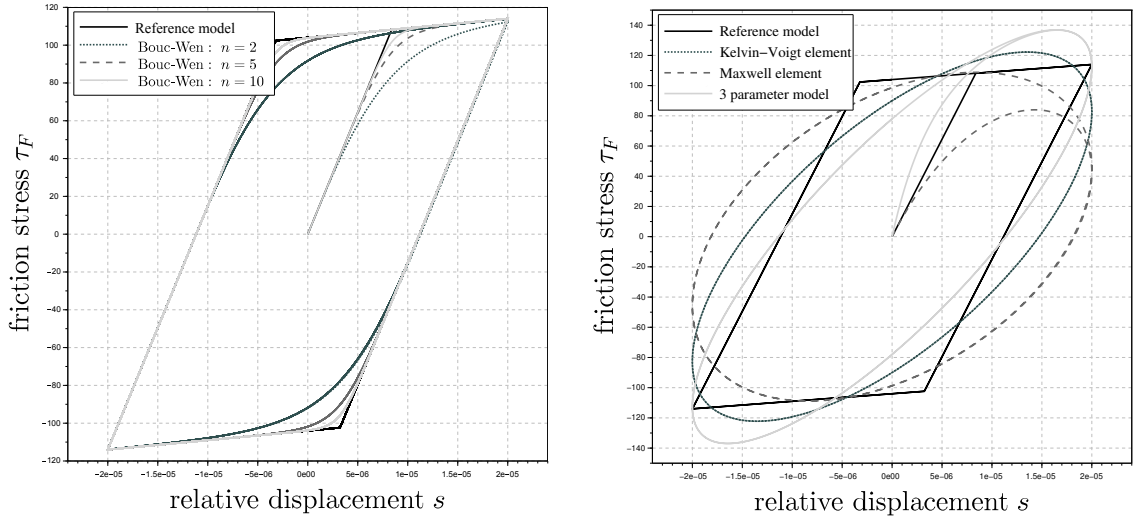

(a) Bouc–Wen friction model

(b) Viscous damping models

Figure 2.13: Hysteresis of Bouc–Wen friction model and viscous damping models

3 A new approach for joint contact in flexible multibody systems

For the consideration of jointed flexible bodies in a multibody simulation, the equations of motion need to be adapted. The nonlinear joint forces are thereby considered to **act inside one flexible body** (see fig. 3.1) and not between two flexible bodies in the multibody system. Based on the virtual work of the nonlinear joint forces an extension of the equations of motion is presented in section 3.1. Furthermore, the efficient computation of contact pressure and friction stress in the context of reduced flexible structures is discussed in sections 3.1.1 and 3.1.2.

For an accurate computation of the nonlinear joint forces the quality of the trial vectors (also called mode shapes) is crucial. Hence, an approach for computing suitable mode shapes, called *joint modes* $\boldsymbol{\phi}_{\mathrm{J},i}$, is presented in section 3.2. These joint modes add local flexibility to the joint area to ensure an accurate computation of gaping or penetrating areas inside the joint. The joint modes are used to build a problem-oriented extension for the common CMS reduction basis in the form

$$\boldsymbol{\Phi} = \begin{bmatrix} \boldsymbol{\Phi}_{\mathrm{CMS}} & \boldsymbol{\phi}_{\mathrm{J},1}, \ldots, \boldsymbol{\phi}_{\mathrm{J},g} \end{bmatrix} = \begin{bmatrix} \boldsymbol{\Phi}_{\mathrm{CMS}} & \boldsymbol{\Phi}_{\mathrm{J}} \end{bmatrix}. \tag{3.1}$$

In the latter equation $\boldsymbol{\Phi}$ is the extended reduction basis, $\boldsymbol{\Phi}_{\mathrm{CMS}}$ denotes the CMS reduction basis and $\boldsymbol{\Phi}_{\mathrm{J}} = \begin{bmatrix} \boldsymbol{\phi}_{\mathrm{J},1}, \ldots, \boldsymbol{\phi}_{\mathrm{J},g} \end{bmatrix}$ is the matrix of joint modes. For the computation of joint modes the theory of trial vector derivatives (TVDs) is properly adapted and a strategy for the practical computation of TVDs for joint nonlinearities is presented.

Many types of joints, for example, bolted joints, clamped connections or interference fits are determined by some kind of preload state. Hence, a specialization of joint modes for preloaded structures is presented in section 3.2.3.

3.1 Consideration of nonlinear joint forces in the context of flexible multibody systems

A schematic draft of a jointed flexible body is depicted in fig. 3.1a. In fig. 3.1b the contact situation of two particles P^M, P^S is shown in more detail. Although the contact is considered within one flexible body, the contacting surfaces are denoted as master and slave surface. Quantities for the master surface are marked with $(\,)^M$ while quantities describing the slave surface are marked with $(\,)^S$.

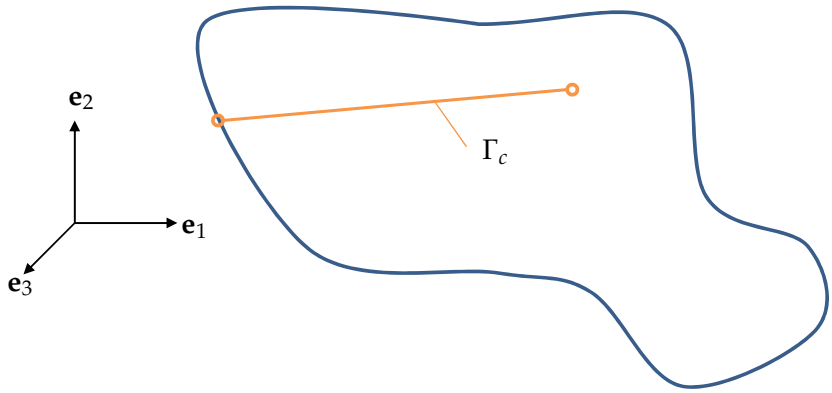

(a) Flexible body with joint area Γ_c

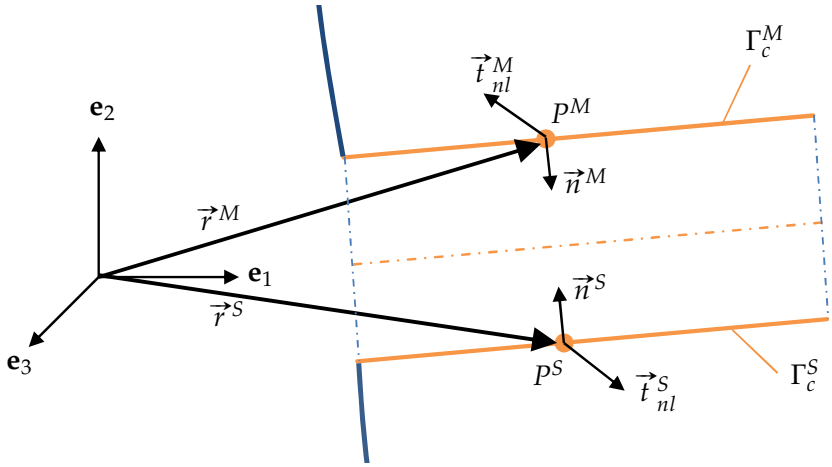

(b) Contact situation of particles P^M, P^S

Figure 3.1: Jointed flexible body

The equation of motion for one flexible body in the multibody system (see eq. (2.41)) can be extended with the vector of generalized nonlinear joint forces $\mathbf{Q}_{nl}$, yielding

$$\boldsymbol{\mathcal{M}}\ddot{\mathbf{q}} + \boldsymbol{\mathcal{K}}\mathbf{q} + \mathbf{C}_\mathbf{q}^\mathsf{T}\boldsymbol{\lambda} = \mathbf{Q}_e + \mathbf{Q}_v + \mathbf{Q}_{nl}. \tag{3.2}$$

Note that the superscript i denoting the index of the body is omitted for better readability.

The vector of generalized nonlinear joint forces $\mathbf{Q}_{nl}$ can be derived from the virtual work of the joint forces given by

$$\delta W_{nl} = -\int_{\Gamma_c^M} \left(\mathbf{B}\,\vec{t}^{\,M}_{nl}\right) \cdot \delta\vec{r}^{\,M}\, d\Gamma_c - \int_{\Gamma_c^S} \left(\mathbf{B}\,\vec{t}^{\,S}_{nl}\right) \cdot \delta\vec{r}^{\,S}\, d\Gamma_c. \tag{3.3}$$

In this equation $\vec{t}^{\,M}_{nl}$, $\vec{t}^{\,S}_{nl}$ denote the contact interface stress vector acting on the surface of the master and slave side of the contact interface. These vectors $\vec{t}^{\,M}_{nl}$, $\vec{t}^{\,S}_{nl}$ are described in the body coordinate system. The corresponding virtual displacement of the contacting particles

P^M, P^S are denoted as $\delta\vec{r}^M, \delta\vec{r}^S$. Using the definition of the position vector of an arbitrary point (eqs. (2.2) and (2.9)), the virtual changes $\delta\vec{r}^M, \delta\vec{r}^S$ can be written as

$$\delta\vec{r}^M = \delta\mathbf{R} + \frac{\partial}{\partial\boldsymbol{\theta}}\left[\mathbf{B}\vec{u}^M\right]\delta\boldsymbol{\theta} + \mathbf{B}\mathbf{S}^M\delta\boldsymbol{\zeta} = \delta\mathbf{R} + \left[-\mathbf{B}\tilde{\mathbf{u}}^M\mathbf{G}\right]\delta\boldsymbol{\theta} + \mathbf{B}\mathbf{S}^M\delta\boldsymbol{\zeta}, \tag{3.4a}$$

$$\delta\vec{r}^S = \delta\mathbf{R} + \frac{\partial}{\partial\boldsymbol{\theta}}\left[\mathbf{B}\vec{u}^S\right]\delta\boldsymbol{\theta} + \mathbf{B}\mathbf{S}^S\delta\boldsymbol{\zeta} = \delta\mathbf{R} + \left[-\mathbf{B}\tilde{\mathbf{u}}^S\mathbf{G}\right]\delta\boldsymbol{\theta} + \mathbf{B}\mathbf{S}^S\delta\boldsymbol{\zeta}. \tag{3.4b}$$

Due to the fact that the contacting particles are inside the same flexible body, the quantities $\mathbf{R}, \boldsymbol{\theta}, \boldsymbol{\zeta}, \mathbf{B}, \mathbf{G}$ in eq. (3.4) are equal for the master P^M and slave P^S particle. In the latter equations, $\vec{u}^M$ and $\vec{u}^S$ denote the local position of the contacting particles with respect to the body coordinate system and $\mathbf{S}^M, \mathbf{S}^S$ are the shape functions of these particles.

Utilizing Newton's Third Law, the principle of actio and reactio, the contact interface stress vector of an arbitrary contact pair P^M, P^S on the contact surface can be written as

$$\vec{t}_{nl} = \vec{t}^M_{nl} = -\vec{t}^S_{nl}. \tag{3.5}$$

Inserting eqs. (3.4) and (3.5) in the virtual work of joint forces (eq. (3.3)) yields

$$\begin{aligned}\delta W_{nl} = &-\int_{\Gamma_c^M}\left(\mathbf{B}\vec{t}_{nl}\right)\cdot\left(\delta\mathbf{R} + \left[-\mathbf{B}\tilde{\mathbf{u}}^M\mathbf{G}\right]\delta\boldsymbol{\theta} + \mathbf{B}\mathbf{S}^M\delta\boldsymbol{\zeta}\right)\,d\Gamma_c \\ &+\int_{\Gamma_c^S}\left(\mathbf{B}\vec{t}_{nl}\right)\cdot\left(\delta\mathbf{R} + \left[-\mathbf{B}\tilde{\mathbf{u}}^S\mathbf{G}\right]\delta\boldsymbol{\theta} + \mathbf{B}\mathbf{S}^S\delta\boldsymbol{\zeta}\right)\,d\Gamma_c.\end{aligned} \tag{3.6}$$

For a closed contact situation $\vec{u}^M = \vec{u}^S$ respectively $\tilde{\mathbf{u}}^M = \tilde{\mathbf{u}}^S$ has to be fulfilled. Otherwise, no contact occurs and the contact interface stress vector is zero $\vec{t}_{nl} = \vec{0}$. The claim that the local position of the particles is equal ($\vec{u}^M = \vec{u}^S$) does not imply that there is no flexible deformation between the master and slave surface. For the considered FFRF a flexible deformation between the master and slave particle is still possible ($\vec{u}^M_f \neq \vec{u}^S_f$) . Furthermore, for closed contact the surfaces on the master and slave side are equal, and the following integrals vanish in eq. (3.6)

$$-\int_{\Gamma_c^M}\left(\mathbf{B}\vec{t}_{nl}\right)\cdot\delta\mathbf{R}\,d\Gamma_c + \int_{\Gamma_c^S}\left(\mathbf{B}\vec{t}_{nl}\right)\cdot\delta\mathbf{R}\,d\Gamma_c = 0 \tag{3.7a}$$

$$-\int_{\Gamma_c^M}\left(\mathbf{B}\vec{t}_{nl}\right)\cdot\left(\left[-\mathbf{B}\tilde{\mathbf{u}}^M\mathbf{G}\right]\delta\boldsymbol{\theta}\right)\,d\Gamma_c + \int_{\Gamma_c^S}\left(\mathbf{B}\vec{t}_{nl}\right)\cdot\left(\left[-\mathbf{B}\tilde{\mathbf{u}}^S\mathbf{G}\right]\delta\boldsymbol{\theta}\right)\,d\Gamma_c = 0 \tag{3.7b}$$

Hence, the virtual work of joint forces simplifies to

$$\delta W_{nl} = -\int_{\Gamma_c^M}\left(\mathbf{B}\vec{t}_{nl}\right)\cdot\left(\mathbf{B}\mathbf{S}^M\delta\boldsymbol{\zeta}\right)\,d\Gamma_c + \int_{\Gamma_c^S}\left(\mathbf{B}\vec{t}_{nl}\right)\cdot\left(\mathbf{B}\mathbf{S}^S\delta\boldsymbol{\zeta}\right)\,d\Gamma_c. \tag{3.8}$$

The dot product in this equation can be written in matrix notation as

$$\delta W_{nl} = -\int_{\Gamma_c^M}\vec{t}^{\,\mathsf{T}}_{nl}\mathbf{B}^{\mathsf{T}}\mathbf{B}\mathbf{S}^M\delta\boldsymbol{\zeta}\,d\Gamma_c + \int_{\Gamma_c^S}\vec{t}^{\,\mathsf{T}}_{nl}\mathbf{B}^{\mathsf{T}}\mathbf{B}\mathbf{S}^S\delta\boldsymbol{\zeta}\,d\Gamma_c. \tag{3.9}$$

By using the orthogonality of the rotation matrix ($\mathbf{B}^{\mathsf{T}}\mathbf{B} = \mathbf{I}$), eq. (3.8) can be simplified to

$$\delta W_{nl} = -\int_{\Gamma_c^M}\vec{t}^{\,\mathsf{T}}_{nl}\mathbf{S}^M\delta\boldsymbol{\zeta}\,d\Gamma_c + \int_{\Gamma_c^S}\vec{t}^{\,\mathsf{T}}_{nl}\mathbf{S}^S\delta\boldsymbol{\zeta}\,d\Gamma_c. \tag{3.10}$$

The vector of flexible coordinates $\boldsymbol{\zeta}$ depends only on time, and hence this equation can be written as

$$\delta W_{nl} = \left[-\int_{\Gamma_c^M} \vec{t}_{nl}^{\,\mathsf{T}} \mathbf{S}^M \, d\Gamma_c + \int_{\Gamma_c^S} \vec{t}_{nl}^{\,\mathsf{T}} \mathbf{S}^S \, d\Gamma_c \right] \delta\boldsymbol{\zeta}. \tag{3.11}$$

Expanding this equation to all generalized coordinates $\mathbf{q}$, the virtual work of the joint forces can be written as

$$\delta W_{nl} = \mathbf{Q}_{nl}^{\mathsf{T}} \delta\mathbf{q} = \begin{bmatrix} (\mathbf{Q}_{nl})_R^{\mathsf{T}} & (\mathbf{Q}_{nl})_\theta^{\mathsf{T}} & (\mathbf{Q}_{nl})_f^{\mathsf{T}} \end{bmatrix} \begin{bmatrix} \delta\mathbf{R} \\ \delta\boldsymbol{\theta} \\ \delta\boldsymbol{\zeta} \end{bmatrix}, \tag{3.12}$$

where the vector generalized nonlinear joint forces $\mathbf{Q}_{nl}$ is defined as

$$\mathbf{Q}_{nl} = \begin{bmatrix} (\mathbf{Q}_{nl})_R \\ (\mathbf{Q}_{nl})_\theta \\ (\mathbf{Q}_{nl})_f \end{bmatrix} = \begin{bmatrix} \mathbf{0}_R \\ \mathbf{0}_\theta \\ \left[-\int_{\Gamma_c^M} \left(\mathbf{S}^M\right)^{\mathsf{T}} \vec{t}_{nl} \, d\Gamma_c + \int_{\Gamma_c^S} \left(\mathbf{S}^S\right)^{\mathsf{T}} \vec{t}_{nl} \, d\Gamma_c \right] \end{bmatrix}. \tag{3.13}$$

Note that $\mathbf{Q}_{nl}$ is a self-equilibrated force which has no contribution to the rigid body components since the terms $(\mathbf{Q}_{nl})_R = \mathbf{0}_R$ and $(\mathbf{Q}_{nl})_\theta = \mathbf{0}_\theta$ vanish.

An alternative formulation of the virtual work of joint forces yielding to the same result for the vector of generalized nonlinear joint forces $\mathbf{Q}_{nl}$ can be found in appendix B.2.

Assuming a finite element (FE) discretization of the flexible body with n_{FE} nodal DOFs, the surface integrals of eq. (3.13) have to be computed using the finite element shape functions. The integration over element shape functions is a well-documented task in finite element analysis (see the textbooks [7, 53, 149]) and is not further discussed in this dissertation.

For an FE discretized flexible structure the generalized nonlinear joint forces can be written as

$$\mathbf{Q}_{nl} = \begin{bmatrix} (\mathbf{Q}_{nl})_R \\ (\mathbf{Q}_{nl})_\theta \\ (\mathbf{Q}_{nl})_f \end{bmatrix} = \begin{bmatrix} \mathbf{0}_R \\ \mathbf{0}_\theta \\ (\mathbf{Q}_{nl})_f \end{bmatrix} \approx \begin{bmatrix} \mathbf{0}_R \\ \mathbf{0}_\theta \\ \left(\boldsymbol{\Phi}^{\mathsf{T}} \mathbf{f}_{nl}\right)_f \end{bmatrix}, \tag{3.14}$$

where $\mathbf{f}_{nl}$ denotes the $(n_{\mathrm{FE}} \times 1)$ vector of nodal nonlinear joint forces, and the $(n_{\mathrm{FE}} \times r)$ matrix $\boldsymbol{\Phi}$ contains the free-free modes of the flexible body.

The accuracy of the computed generalized nonlinear joint forces $\mathbf{Q}_{nl}$ depends on the reduction basis $\boldsymbol{\Phi}$. In section 3.2 a problem oriented extension of common reduction basis with so-called joint modes is presented. These joint modes allow an accurate computation of $\mathbf{Q}_{nl}$.

Inserting eq. (3.14) into the equations of motion (eq. (3.2)) and applying the simplifications achieved by using free-free modes (see section 2.1.1) the equations of motion can be written

in partitioned matrix form as

$$\begin{aligned}\begin{bmatrix} \boldsymbol{\mathcal{M}}_{RR} & \mathbf{0}_{R\theta} & \mathbf{0}_{Rf} \\ & \boldsymbol{\mathcal{M}}_{\theta\theta} & \boldsymbol{\mathcal{M}}_{\theta f} \\ \text{sym.} & & \boldsymbol{\mathcal{M}}_{ff} \end{bmatrix} \begin{bmatrix} \ddot{\mathbf{R}} \\ \ddot{\boldsymbol{\theta}} \\ \ddot{\boldsymbol{\zeta}} \end{bmatrix} + \begin{bmatrix} \mathbf{0} & \mathbf{0} & \mathbf{0} \\ \mathbf{0} & \mathbf{0} & \mathbf{0} \\ \mathbf{0} & \mathbf{0} & \mathcal{K}_{ff} \end{bmatrix} \begin{bmatrix} \mathbf{R} \\ \boldsymbol{\theta} \\ \boldsymbol{\zeta} \end{bmatrix} + \begin{bmatrix} \mathbf{C}_{\mathbf{R}}^{\mathsf{T}} \\ \mathbf{C}_{\boldsymbol{\theta}}^{\mathsf{T}} \\ \mathbf{C}_{\boldsymbol{\zeta}}^{\mathsf{T}} \end{bmatrix} \boldsymbol{\lambda} \\ = \begin{bmatrix} (\mathbf{Q}_e)_R \\ (\mathbf{Q}_e)_\theta \\ (\mathbf{Q}_e)_f \end{bmatrix} + \begin{bmatrix} \mathbf{0} \\ (\mathbf{Q}_v)_\theta \\ (\mathbf{Q}_v)_f \end{bmatrix} + \begin{bmatrix} \mathbf{0}_R \\ \mathbf{0}_\theta \\ \left(\boldsymbol{\Phi}^{\mathsf{T}} \mathbf{f}_{nl}\right)_f \end{bmatrix}. \end{aligned} \tag{3.15}$$

The vector $\mathbf{f}_{nl}$ can be partitioned into the $(n_{FE} \times 1)$ vectors of contact $\mathbf{f}_N$ and friction forces $\mathbf{f}_F$, yielding

$$\mathbf{f}_{nl} = \mathbf{f}_N + \mathbf{f}_F. \tag{3.16}$$

The contact forces $\mathbf{f}_N$ act normal to the joint surface and the friction forces $\mathbf{f}_F$ act in tangential direction. Since the vector of nonlinear forces contributes to the generalized forces, the derivatives $\frac{\partial\left(\boldsymbol{\Phi}^{\mathsf{T}} \mathbf{f}_{nl}\right)}{\partial \mathbf{q}}, \frac{\partial\left(\boldsymbol{\Phi}^{\mathsf{T}} \mathbf{f}_{nl}\right)}{\partial \dot{\mathbf{q}}}$ need to be computed for the system's Jacobian $\mathbf{J}$.

As a consequence of the considered penalty formulation for contact forces and the claimed velocity independence of the friction model for dry friction joints the derivative with respect to the generalized velocities can be set to zero $\frac{\partial\left(\boldsymbol{\Phi}^{\mathsf{T}} \mathbf{f}_{nl}\right)}{\partial \dot{\mathbf{q}}} = \mathbf{0}$. The claimed velocity independence is only valid for the considered microslip regime. In this case it is sufficient to describe the friction force as a function of the relative displacement (see section 2.4.1 and [40, 42, 61, 62]). Furthermore, the nonlinear forces are only a function of the flexible coordinates $\boldsymbol{\zeta}$ and not of the other components of the generalized coordinates. Hence, only the derivative $\frac{\partial\left(\boldsymbol{\Phi}^{\mathsf{T}} \mathbf{f}_{nl}\right)}{\partial \boldsymbol{\zeta}}$ has to be computed.

By introducing the $(r \times 1)$ vector of reduced nonlinear forces $\mathbf{f}_{nl}^m = \boldsymbol{\Phi}^{\mathsf{T}} \mathbf{f}_{nl}$ and the $(r \times 1)$ vectors of reduced contact and friction forces $(\mathbf{f}_N^m = \boldsymbol{\Phi}^{\mathsf{T}} \mathbf{f}_N, \mathbf{f}_F^m = \boldsymbol{\Phi}^{\mathsf{T}} \mathbf{f}_F)$ the required derivative can be written as

$$\frac{\partial \mathbf{f}_{nl}^m}{\partial \boldsymbol{\zeta}} = \frac{\partial \mathbf{f}_N^m}{\partial \boldsymbol{\zeta}} + \frac{\partial \mathbf{f}_F^m}{\partial \boldsymbol{\zeta}}. \tag{3.17}$$

The contact and friction force vectors $\mathbf{f}_N$ and $\mathbf{f}_F$ can be directly computed from the $(3n_{\mathrm{CP}} \times 1)$ contact pressure vector $\mathbf{p}_N$ and the $(3n_{\mathrm{CP}} \times 1)$ friction stress vector $\boldsymbol{\tau}_F$

$$\begin{aligned} \mathbf{f}_N &= \mathbf{P}\mathbf{p}_N, \\ \mathbf{f}_F &= \mathbf{P}\boldsymbol{\tau}_F. \end{aligned} \tag{3.18}$$

In these equations the $(n_{\mathrm{FE}} \times 3n_{\mathrm{CP}})$ matrix $\mathbf{P}$ denotes a time and state independent mapping matrix which is defined by the FE shape functions and the FE mesh. The vectors $\mathbf{p}_N, \boldsymbol{\tau}_F$

contain the contact pressure vectors $\vec{p}_{N,i}$ and the tangential surface stress vectors $\vec{\tau}_{F,i}$ for all n_{CP} contact pairs. Hence, the $(3n_{\mathrm{CP}} \times 1)$ vectors $\mathbf{p}_N$ and $\boldsymbol{\tau}_F$ can be written as

$$\begin{aligned} \mathbf{p}_N &= \begin{bmatrix} \vec{p}_{N,1}^{\,\mathsf{T}} & \cdots & \vec{p}_{N,i}^{\,\mathsf{T}} & \cdots & \vec{p}_{N,n_{\mathrm{CP}}}^{\,\mathsf{T}} \end{bmatrix}^{\mathsf{T}}, \\ \boldsymbol{\tau}_F &= \begin{bmatrix} \vec{\tau}_{F,1}^{\,\mathsf{T}} & \cdots & \vec{\tau}_{F,i}^{\,\mathsf{T}} & \cdots & \vec{\tau}_{F,n_{\mathrm{CP}}}^{\,\mathsf{T}} \end{bmatrix}^{\mathsf{T}}. \end{aligned} \tag{3.19}$$

The matrices $\boldsymbol{\Phi}$ and $\mathbf{P}$ are both constant, and hence the derivatives $\frac{\partial \mathbf{p}_N}{\partial \zeta}$, $\frac{\partial \boldsymbol{\tau}_F}{\partial \zeta}$ can be computed instead of the derivatives required in eq. (3.17). The computation of these derivatives is discussed in the following subsections.

For readability reasons only a node-to-node contact is considered and the derivatives are only computed for one single contact pair. A general extension to the vector containing all contact pairs is quite straightforward.

3.1.1 Computation of the contact pressure vector

For a penalty formulation the contact pressure vector $\vec{p}_{N,i}$ for the i-th contact pair is given by

$$\vec{p}_{N,i} = \vec{n}_i \, p_{N,i}\left(g_{N,i}\right), \tag{3.20}$$

with the surface normal vector $\vec{n}_i$ of the contact pair and the scalar contact pressure $p_{N,i}$. The normal vector is therein normalized to length $\|\vec{n}_i\|_2 = 1$. For all penalty formulations the scalar contact pressure $p_{N,i}$ is a function of the normal gap $g_{N,i}$ defined as

$$g_{N,i} = \left(\vec{x}_i^{\,M} - \vec{x}_i^{\,S}\right) \cdot \vec{n}_i = \vec{n}_i^{\,\mathsf{T}} \left(\vec{x}_i^{\,M} - \vec{x}_i^{\,S}\right). \tag{3.21}$$

In this equation $\vec{x}_i^{\,M}$, $\vec{x}_i^{\,S}$ represent the displacement vectors of translational DOFs from the corresponding FE nodes of the master and slave surfaces. These quantities $\vec{x}_i^{\,M}$, $\vec{x}_i^{\,S}$ are equal to the flexible deformation of the contacting particles $\vec{u}_f^{\,M}$, $\vec{u}_f^{\,S}$. In terms of trial vector based model order reduction the normal gap becomes a function of the flexible coordinates leading to

$$g_{N,i}\left(\boldsymbol{\zeta}\right) = \vec{n}_i^{\,\mathsf{T}} \left[\left(\boldsymbol{\Phi}_i^M - \boldsymbol{\Phi}_i^S\right) \boldsymbol{\zeta}\right]. \tag{3.22}$$

In the latter equation, $\boldsymbol{\Phi}_i^M, \boldsymbol{\Phi}_i^S$ are $(3 \times r)$ matrices containing the translational DOFs of the i-th master-slave contact pair for all trial vectors.

In general the normal vector $\vec{n}_i$ is a function of the deformation state and consequently a function of the flexible coordinates ($\vec{n}_i = \vec{n}_i(\boldsymbol{\zeta})$). For the derivation of eq. (3.20) with respect to the flexible coordinates $\boldsymbol{\zeta}$, this dependency leads to the $(3 \times r)$ matrix

$$\frac{\partial \vec{p}_{N,i}}{\partial \boldsymbol{\zeta}} = p_{N,i} \frac{\partial \vec{n}_i}{\partial \boldsymbol{\zeta}} + \vec{n}_i \frac{\partial p_{N,i}}{\partial g_{N,i}} \frac{\partial g_{N,i}}{\partial \boldsymbol{\zeta}}. \tag{3.23}$$

In this equation the derivative $\frac{\partial g_{N,i}}{\partial \zeta}$ is required. Performing a derivation of eq. (3.22) with respect to the flexible coordinates leads to the $(1 \times r)$ row vector

$$\frac{\partial g_{N,i}}{\partial \zeta} = \left[\left(\boldsymbol{\Phi}_i^M - \boldsymbol{\Phi}_i^S\right)\boldsymbol{\zeta}\right]^\mathsf{T} \frac{\partial \vec{n}_i}{\partial \boldsymbol{\zeta}} + \vec{n}_i^{\,\mathsf{T}} \left(\boldsymbol{\Phi}_i^M - \boldsymbol{\Phi}_i^S\right). \tag{3.24}$$

For the application of jointed structures, with small sliding and the use of an FFRF, it can be assumed that the normal vector does not change significantly with respect to the initial reference configuration. Hence, the derivative $\frac{\partial \vec{n}_i}{\partial \boldsymbol{\zeta}}$ vanishes and eq. (3.24) simplifies to

$$\frac{\partial g_{N,i}}{\partial \boldsymbol{\zeta}} = \vec{n}_i^{\,\mathsf{T}} \left(\boldsymbol{\Phi}_i^M - \boldsymbol{\Phi}_i^S\right). \tag{3.25}$$

Consequently eq. (3.23) simplifies to

$$\frac{\partial \vec{p}_{N,i}}{\partial \boldsymbol{\zeta}} = \mathbf{0} + \vec{n}_i \frac{\partial p_{N,i}}{\partial g_{N,i}} \vec{n}_i^{\,\mathsf{T}} \left(\boldsymbol{\Phi}_i^M - \boldsymbol{\Phi}_i^S\right). \tag{3.26}$$

Since the contact pressure of the contact pair i is only depending on the corresponding normal gap $g_{N,i}$ the derivative $\frac{\partial \mathbf{p}_N}{\partial \boldsymbol{\zeta}}$ can be written as $(3n_{\mathrm{CP}} \times r)$ matrix

$$\frac{\partial \mathbf{p}_N}{\partial \boldsymbol{\zeta}} = \begin{bmatrix} \frac{\partial p_{N,1}}{\partial g_{N,1}} \vec{n}_1 \vec{n}_1^{\,\mathsf{T}} \left(\boldsymbol{\Phi}_1^M - \boldsymbol{\Phi}_1^S\right) \\ \vdots \\ \frac{\partial p_{N,i}}{\partial g_{N,i}} \vec{n}_i \vec{n}_i^{\,\mathsf{T}} \left(\boldsymbol{\Phi}_i^M - \boldsymbol{\Phi}_i^S\right) \\ \vdots \\ \frac{\partial p_{N,n_{\mathrm{CP}}}}{\partial g_{N,n_{\mathrm{CP}}}} \vec{n}_{n_{\mathrm{CP}}} \vec{n}_{n_{\mathrm{CP}}}^{\,\mathsf{T}} \left(\boldsymbol{\Phi}_{n_{\mathrm{CP}}}^M - \boldsymbol{\Phi}_{n_{\mathrm{CP}}}^S\right) \end{bmatrix}. \tag{3.27}$$

The derivatives $\frac{\partial p_{N,i}}{\partial g_{N,i}}$ are depending on the used penalty formulation. For some penalty models the derivative $\frac{\partial p_{N,i}}{\partial g_{N,i}}$ is computed in appendix E.2.

3.1.2 Computation of the friction stress vector

Depending on the friction model, the relative tangential displacement s_i and the sticking stress limit $R_{G,i}$ of the contact pair are used to describe the magnitude of the friction stress $\tau_{F,i}$. The friction stress vector $\vec{\tau}_{F,i}$ can be written as

$$\vec{\tau}_{F,i} = \vec{t}_i \tau_{F,i}\left(s_i, R_{G,i}\right), \tag{3.28}$$

where the normalized tangential vector $\vec{t}_i$ is used. The quantities $\vec{t}_i = \vec{t}_i(\boldsymbol{\zeta})$, $s_i = s_i(\boldsymbol{\zeta})$, $R_{G,i} = R_{G,i}(\boldsymbol{\zeta})$ are thereby depending on the flexible coordinates.

Similar to the normal gap $g_{N,i}$ (see eq. (3.22)) the tangential displacement s_i can be computed based on the trial vectors of the i-th contact pair along

$$s_i = \vec{t}_i^{\,\mathsf{T}} \left[\left(\boldsymbol{\Phi}_i^M - \boldsymbol{\Phi}_i^S \right) \boldsymbol{\zeta} \right]. \tag{3.29}$$

For each contact pair, there exist two constant and normalized tangential vectors $\vec{t}_i^{\,1}$, $\vec{t}_i^{\,2}$ which describe the principal directions of the contact pair's coordinate system (see section 3.3.1). With the two tangential displacements in these principal directions

$$s_{1,i} = \vec{t}_i^{\,1\mathsf{T}} \left(\boldsymbol{\Phi}_i^M - \boldsymbol{\Phi}_i^S \right) \boldsymbol{\zeta}, \tag{3.30a}$$

$$s_{2,i} = \vec{t}_i^{\,2\mathsf{T}} \left(\boldsymbol{\Phi}_i^M - \boldsymbol{\Phi}_i^S \right) \boldsymbol{\zeta}, \tag{3.30b}$$

the total tangential displacement can also be computed along

$$s_i = \sqrt{{s_{1,i}}^2 + {s_{2,i}}^2}. \tag{3.31}$$

Based on eq. (3.30), the normalized tangential vector can be written as

$$\vec{t}_i = \frac{s_{1,i}\,\vec{t}_i^{\,1} + s_{2,i}\,\vec{t}_i^{\,2}}{\sqrt{{s_{1,i}}^2 + {s_{2,i}}^2}}. \tag{3.32}$$

For the computation of the system's Jacobian matrix the derivative $\frac{\partial \vec{\tau}_{F,i}}{\partial \boldsymbol{\zeta}}$ is required. Considering the mentioned dependencies on the flexible coordinates this derivative can be written as a $(3 \times r)$ matrix, yielding

$$\frac{\partial \vec{\tau}_{F,i}}{\partial \boldsymbol{\zeta}} = \frac{\partial \vec{t}_i}{\partial \boldsymbol{\zeta}} \tau_{F,i} + \vec{t}_i \left[\frac{\partial \tau_{F,i}}{\partial s_i} \frac{\partial s_i}{\partial \boldsymbol{\zeta}} + \frac{\partial \tau_{F,i}}{\partial R_{G,i}} \frac{\partial R_{G,i}}{\partial \boldsymbol{\zeta}} \right]. \tag{3.33}$$

The derivatives $\frac{\partial \tau_{F,i}}{\partial s_i}$, $\frac{\partial \tau_{F,i}}{\partial R_{G,i}}$ in eq. (3.33) depend on the friction model. All other terms in eq. (3.33) can be evaluated in general and do not depend on the friction model itself.

The derivative of the tangential vector $\vec{t}_i$ (as defined in eq. (3.32)) with respect to the flexible coordinates can be written as a $(3 \times r)$ matrix

$$\frac{\partial \vec{t}_i}{\partial \boldsymbol{\zeta}} = \frac{\left(s_{1,i}\,\vec{t}_i^{\,2} - s_{2,i}\,\vec{t}_i^{\,1} \right) \left(-s_{2,i} \frac{\partial s_{1,i}}{\partial \boldsymbol{\zeta}} + s_{1,i} \frac{\partial s_{2,i}}{\partial \boldsymbol{\zeta}} \right)}{\left({s_{1,i}}^2 + {s_{2,i}}^2 \right)^{3/2}}. \tag{3.34}$$

In this equation the derivatives of the principal tangential displacements with respect to the flexible coordinates $\frac{\partial s_{1,i}}{\partial \boldsymbol{\zeta}}$, $\frac{\partial s_{2,i}}{\partial \boldsymbol{\zeta}}$ are required. These derivatives can be computed by differentiating eq. (3.30), yielding the $(1 \times r)$ matrices

$$\frac{\partial s_{1,i}}{\partial \boldsymbol{\zeta}} = \vec{t}_i^{\,1\mathsf{T}} \left(\boldsymbol{\Phi}_i^M - \boldsymbol{\Phi}_i^S \right), \tag{3.35a}$$

$$\frac{\partial s_{2,i}}{\partial \boldsymbol{\zeta}} = \vec{t}_i^{\,2\mathsf{T}} \left(\boldsymbol{\Phi}_i^M - \boldsymbol{\Phi}_i^S \right). \tag{3.35b}$$

Furthermore, in eq. (3.33) the derivative $\frac{\partial s_i}{\partial \zeta}$ is required. This term can be computed by using the definition eq. (3.31) and yields the $(1 \times r)$ matrix

$$\frac{\partial s_i}{\partial \zeta} = \frac{s_{1,i} \frac{\partial s_{1,i}}{\partial \zeta} + s_{2,i} \frac{\partial s_{2,i}}{\partial \zeta}}{s_i}. \tag{3.36}$$

The therein required derivatives $\frac{\partial s_{1,i}}{\partial \zeta}$, $\frac{\partial s_{2,i}}{\partial \zeta}$ are already defined by eq. (3.35).

Moreover, the derivative of the sticking stress limit with respect to the flexible coordinates $\frac{\partial R_{G,i}}{\partial \zeta}$ is needed. The sticking stress limit is usually defined as a function of the contact pressures magnitude $R_G = R_G(p_{N,i})$, and hence this derivative can be written in a $(1 \times r)$ matrix

$$\frac{\partial R_{G,i}}{\partial \zeta} = \frac{\partial R_{G,i}}{\partial p_{N,i}} \frac{\partial p_{N,i}}{\partial \zeta}. \tag{3.37}$$

The derivative $\frac{\partial p_{N,i}}{\partial \zeta} = \frac{\partial p_{N,i}}{\partial g_{N,i}} \vec{n}_i^{\mathsf{T}} \left(\mathbf{\Phi}_i^M - \mathbf{\Phi}_i^S \right)$ has been already computed in the previous section 3.1.1. For many engineering applications it is sufficient to describe the sticking stress limit by $R_G = \mu p_{N,i}$ where μ denotes the friction coefficient. This leads for eq. (3.37) to

$$\frac{\partial R_{G,i}}{\partial \zeta} = \mu \frac{\partial p_{N,i}}{\partial g_{N,i}} \vec{n}_i^{\mathsf{T}} \left(\mathbf{\Phi}_i^M - \mathbf{\Phi}_i^S \right). \tag{3.38}$$

The sticking stress limit $R_{G,i}$ defines the switching between sticking and sliding friction. For dynamic analysis the transition between sticking and sliding friction is important to get a realistic representation of the friction behavior. For some engineering applications static or quasi-static analysis are sufficient to determine the status (sliding/sticking) of the contact.

3.2 Joint modes based on trial vector derivatives

3.2.1 Trial vector derivatives (TVDs) for joint nonlinearities

In this section the computation of TVDs for joint nonlinearities is presented. Note that only initially closed contact situations are considered for this description. Furthermore, it is assumed, that the reduction basis $\mathbf{\Phi}_{\mathrm{CMS}}$ is computed based on the undeformed reference configuration $\hat{\zeta} = \mathbf{0}$. A comment on how to deal with reduction basis built around a deformed state, like a preload deformation state, is given in section 3.2.3.

TVDs $\frac{\partial \boldsymbol{\phi}_i}{\partial \zeta_j}$ can be computed for all m trial vectors in the CMS reduction basis (static modes and vibration modes) along

$$\mathbf{K_c} \frac{\partial \boldsymbol{\phi}_i}{\partial \zeta_j} = -\frac{\partial \mathbf{K_c}}{\partial \zeta_j} \boldsymbol{\phi}_i \qquad \text{for } i, j = 1 \dots m, \tag{3.39}$$

as long as inertia related terms are neglected. The matrix $\frac{\partial \mathbf{K_c}}{\partial \zeta_j}$ represents qualitatively the change in stiffness of the structure due to a deflection of mode shape $\boldsymbol{\phi}_j$. To determine this

matrix, the structure is deformed according to mode shape $\boldsymbol{\phi}_j$. Based on this deformation, contact stiffness ε_N and tangential stiffness ε_T is applied on the corresponding DOFs of contacting and penetrating contact pairs. On the other hand no stiffness is applied on gaping contact pairs.

Considering eq. (3.39), the computation of TVDs can be interpreted as static response due to a fictive force $\mathbf{f}_{i,j}$

$$\mathbf{K_c} \frac{\partial \boldsymbol{\phi}_i}{\partial \zeta_j} = \mathbf{f}_{i,j}, \tag{3.40}$$

which can be identified as

$$\mathbf{f}_{i,j} = -\frac{\partial \mathbf{K_c}}{\partial \zeta_j} \boldsymbol{\phi}_i. \tag{3.41}$$

For the case $i = j$ the fictive force $\mathbf{f}_{i,j}$ represents the nonlinear contact and friction forces caused by a deformation with $\boldsymbol{\phi}_i$.

Considering all m trial vectors of the CMS reduction basis and the thereof resulting TVDs, eq. (3.40) can be written as

$$\mathbf{K_c} \boldsymbol{\Phi}_\mathrm{T} = \mathbf{F}, \tag{3.42}$$

where $\boldsymbol{\Phi}_\mathrm{T}$ and $\mathbf{F}$ hold in the columns the particular TVDs and fictive forces

$$\boldsymbol{\Phi}_\mathrm{T} = \left[\frac{\partial \boldsymbol{\phi}_1}{\partial \zeta_1}, \ldots, \frac{\partial \boldsymbol{\phi}_m}{\partial \zeta_1}, \ldots, \frac{\partial \boldsymbol{\phi}_1}{\partial \zeta_j}, \ldots, \frac{\partial \boldsymbol{\phi}_m}{\partial \zeta_j}, \ldots, \frac{\partial \boldsymbol{\phi}_1}{\partial \zeta_m}, \ldots, \frac{\partial \boldsymbol{\phi}_m}{\partial \zeta_m} \right], \tag{3.43}$$

$$\mathbf{F} = \left[\mathbf{f}_{1,1}, \ldots, \mathbf{f}_{m,1}, \ldots, \mathbf{f}_{1,j}, \ldots, \mathbf{f}_{m,j}, \ldots, \mathbf{f}_{1,m}, \ldots, \mathbf{f}_{m,m} \right]. \tag{3.44}$$

Equation (3.42) leads to an efficient computation algorithm for TVDs which uses a onetime factorization of the stiffness matrix for multiple load cases. This is the strength of commercial FE software. Investigations in a preceding diploma thesis [87] showed that the consideration of the tangential stiffness ε_T inside the matrix $\frac{\partial \mathbf{K_c}}{\partial \zeta_j}$ does not lead to essentially better quality of the computed TVDs. Hence for the TVDs used in the following sections only the contact stiffness ε_N is considered. An algorithm summarizing this computation procedure for TVDs is given in section 3.3 (algorithm 3.1).

Comment on characteristics of TVDs for joint nonlinearities

In [57, 135] it is stated that TVDs computed by neglecting the terms related to inertia are symmetric ($\frac{\partial \boldsymbol{\phi}_i}{\partial \zeta_j} = \frac{\partial \boldsymbol{\phi}_j}{\partial \zeta_i}$). This assertion is based on the use of Schwarz's theorem and is not true in the considered case of contact and friction forces. The change in stiffness for joint nonlinearities is described by a function with a non continuous second order partial derivative (see contact and friction models reviewed in sections 2.4.2 and 2.4.3). Hence, the theorem of Schwarz cannot be applied in this case and for TVDs computed for joint nonlinearities the symmetry condition is not fulfilled

$$\frac{\partial \boldsymbol{\phi}_i}{\partial \zeta_j} \neq \frac{\partial \boldsymbol{\phi}_j}{\partial \zeta_i}. \tag{3.45}$$

Furthermore, for joint nonlinearities the change in stiffness of the structure is completely different if a positive or negative scaling of $\boldsymbol{\phi}_j$ is considered. The asymmetry of the nonlinearity leads to a direction-dependent matrix

$$\frac{\partial \mathbf{K_c}}{\partial \zeta_j} \neq -\frac{\partial \mathbf{K_c}}{\partial(-\zeta_j)}. \tag{3.46}$$

From a mechanical point of view this relation is quite obvious. Considering one particular contact pair, a positive scaling of $\boldsymbol{\phi}_j$ might lead to a penetration, while the negative scaling $-\boldsymbol{\phi}_j$ leads to gaping of the surfaces. Consequently, a high contact stiffness or no additional stiffness occurs. Hence, for one mode shape $\boldsymbol{\phi}_i$ it is necessary to compute two trial vector derivatives with respect to ζ_j, namely $\frac{\partial \boldsymbol{\phi}_i}{\partial \zeta_j}$ and $\frac{\partial \boldsymbol{\phi}_i}{\partial(-\zeta_j)}$. According to that, for joint induced nonlinearities the number of all TVDs is $k = 2m^2$.

TVDs for the friction bar

To give an impression of TVDs, the friction bar introduced in chapter 1 is used. For the computation of TVDs the first three mode shapes (with a nonzero eigenfrequency) of the CMS reduction basis are considered. These orthogonalized free-free mode shapes are depicted in fig. 3.2.

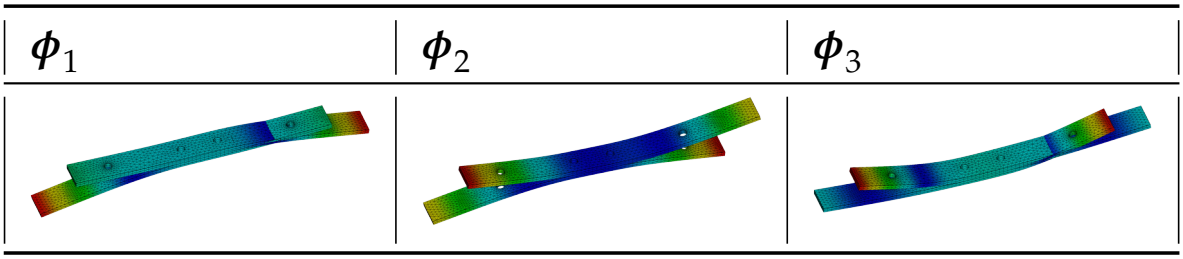

Figure 3.2: CMS mode shapes of the friction bar

For the considered $m = 3$ CMS mode shapes, overall $k = 2m^2 = 18$ TVDs are computed. These TVDs are depicted in fig. 3.3.

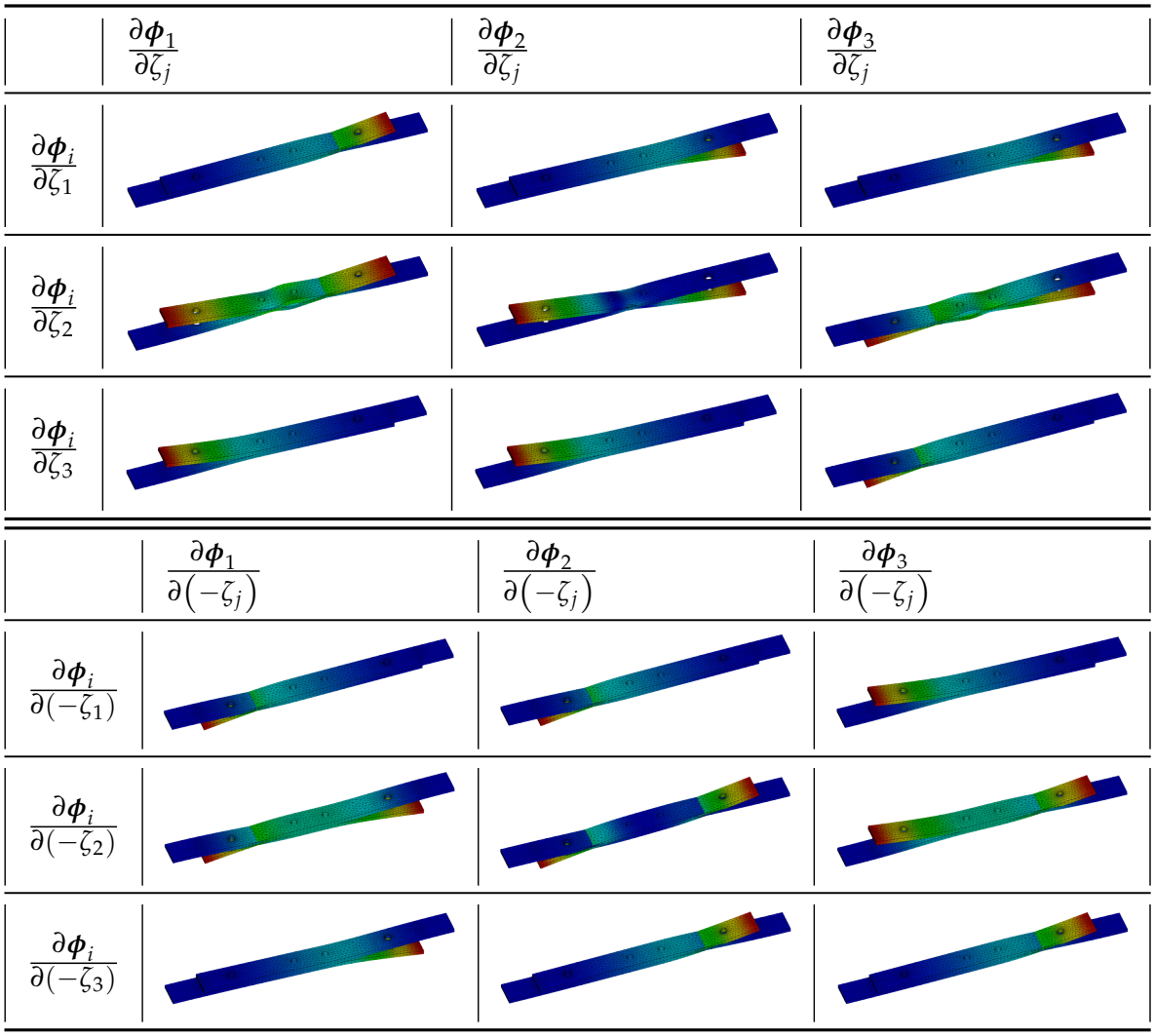

Figure 3.3: TVDs for the friction bar

It can be seen that the computed TVDs have similar deformation shapes, which means a redundant information content. For a CMS reduction basis with $m = 50$ trial vectors for instance, $k = 2m^2 = 5000$ TVDs can be computed. This is by far too high to use all TVDs directly for an extension of the reduction basis. Furthermore, the redundant information content of TVDs might lead to numerical problems.

3.2.2 Joint modes for arbitrary structures

To use TVDs for joint modes, a lower dimensional subspace which contains most of the information covered by the space spanned by all TVDs $\boldsymbol{\Phi}_\mathrm{T}$ has to be found. For this purpose proper orthogonal decomposition (POD) is used. POD can be either applied to the matrix

$\boldsymbol{\Phi}_\mathrm{T}$ containing all TVDs or to the matrix $\mathbf{F}$ containing all fictive forces. Both approaches can be used to compute joint modes. In the following sections, the advantages or disadvantages of these approaches are discussed on a theoretical basis.

Application of POD to TVDs

As a first approach POD is applied to the space spanned by all TVDs. Therefore, the $\left(n_\mathrm{FE} \times 2m^2\right)$ matrix of all TVDs $\boldsymbol{\Phi}_\mathrm{T}$ is considered. POD can be applied in its weighted and unweighted form to this matrix. From a mechanical point of view, the required characteristics of the weighting matrix are the same as the system's stiffness matrix $\mathbf{K_c}$, since this matrix is symmetric (for non sliding friction) and positive definite.

A characteristics of POD is that TVDs with a higher Euclidean norm find greater representation in the computed joint modes. For the computation of joint modes only the space spanned by the TVDs and not their Euclidean norm is of importance. Consequently, an appropriate normalization of TVDs has to be performed before the POD. Such a normalization can be computed by

$$\overline{\boldsymbol{\phi}}_{\mathrm{T},i} = \frac{1}{\sqrt{\boldsymbol{\phi}_{\mathrm{T},i}{}^\mathsf{T} \mathbf{A} \boldsymbol{\phi}_{\mathrm{T},i}}} \boldsymbol{\phi}_{\mathrm{T},i} \quad \text{for } i = 1, \ldots, 2m^2, \tag{3.47}$$

where $\boldsymbol{\phi}_{\mathrm{T},i}$ is the i-th TVD of the matrix $\boldsymbol{\Phi}_\mathrm{T}$, and $\overline{\boldsymbol{\phi}}_{\mathrm{T},i}$ is the corresponding normalized TVD. The normalized TVDs are collected in the columns of the $\left(n_\mathrm{FE} \times 2m^2\right)$ matrix $\overline{\boldsymbol{\Phi}}_\mathrm{T}$. For the unweighted POD the matrix $\mathbf{A}$ is replaced by the identity matrix $\mathbf{A} = \mathbf{I}$ and for the weighted POD $\mathbf{A} = \mathbf{K_c}$ is used.

According to the mathematical formulation of POD (eqs. (2.101) and (2.102)) the joint modes without inner weighting are computed along

$$\left(\overline{\boldsymbol{\Phi}}_\mathrm{T}{}^\mathsf{T} \overline{\boldsymbol{\Phi}}_\mathrm{T}\right) \hat{\boldsymbol{\phi}}_{\mathrm{J},i} = \lambda_{\mathrm{POV},i} \hat{\boldsymbol{\phi}}_{\mathrm{J},i} \quad \text{for } i = 1, \ldots, g, \tag{3.48}$$

and following

$$\boldsymbol{\phi}_{\mathrm{J},i} = \frac{1}{\sqrt{\lambda_{\mathrm{POV},i}}} \overline{\boldsymbol{\Phi}}_\mathrm{T} \hat{\boldsymbol{\phi}}_{\mathrm{J},i}. \tag{3.49}$$

In the case of inner weighting with respect to the stiffness matrix, the joint modes are computed along

$$\left(\overline{\boldsymbol{\Phi}}_\mathrm{T}{}^\mathsf{T} \mathbf{K_c} \overline{\boldsymbol{\Phi}}_\mathrm{T}\right) \hat{\boldsymbol{\phi}}_{\mathrm{J},i} = \lambda_{\mathrm{POV},i} \hat{\boldsymbol{\phi}}_{\mathrm{J},i} \quad \text{for } i = 1, \ldots, g \tag{3.50}$$

and following

$$\boldsymbol{\phi}_{\mathrm{J},i} = \frac{1}{\sqrt{\lambda_{\mathrm{POV},i}}} \overline{\boldsymbol{\Phi}}_\mathrm{T} \hat{\boldsymbol{\phi}}_{\mathrm{J},i}. \tag{3.51}$$

An algorithm summarizing the computation of joint modes based on TVDs is presented in section 3.3 (algorithm 3.2).

Application of POD to fictive forces

A different approach is to apply POD to the fictive forces collected in the $\left(n_{\mathrm{FE}} \times 2m^2\right)$ matrix $\mathbf{F}$ (see eq. (3.44)). Again POD can be applied in a weighted and unweighted version to this matrix. For POD with weighted inner product the positive definite and symmetric $(n_{\mathrm{FE}} \times n_{\mathrm{FE}})$ compliance matrix $\mathbf{C} = {\mathbf{K_c}}^{-1}$ is used. Also for this application of POD a normalization of all $2m^2$ fictive forces $\mathbf{f}_{i,j}$ in the form

$$\bar{\mathbf{f}}_{i,j} = \frac{1}{\sqrt{{\mathbf{f}_{i,j}}^{\mathsf{T}} \mathbf{A} \mathbf{f}_{i,j}}} \mathbf{f}_{i,j} \tag{3.52}$$

has to be performed. For the matrix $\mathbf{A}$ either the compliance matrix $\mathbf{C}$ (weighted POD) or the identity matrix $\mathbf{I}$ (unweighted POD) is used. The normalized fictive forces are subsequently collected as columns in the $\left(n_{\mathrm{FE}} \times 2m^2\right)$ matrix $\overline{\mathbf{F}}$.

POD without inner weighting of the fictive can be written according to eqs. (2.101) and (2.102) as

$$\left(\overline{\mathbf{F}}^{\mathsf{T}} \overline{\mathbf{F}}\right) \hat{\mathbf{f}}_{\mathrm{J},i} = \lambda_{\mathrm{POV},i} \hat{\mathbf{f}}_{\mathrm{J},i} \quad \text{for } i = 1, \ldots, g \tag{3.53}$$

and following

$$\mathbf{f}_{\mathrm{J},i} = \frac{1}{\sqrt{\lambda_{\mathrm{POV},i}}} \overline{\mathbf{F}} \hat{\mathbf{f}}_{\mathrm{J},i}. \tag{3.54}$$

If inner weighting of the fictive forces with respect to the compliance matrix is considered, the POD can be written according to eq. (2.104) as

$$\left(\overline{\mathbf{F}}^{\mathsf{T}} \mathbf{C} \overline{\mathbf{F}}\right) \hat{\mathbf{f}}_{\mathrm{J},i} = \lambda_{\mathrm{POV},i} \hat{\mathbf{f}}_{\mathrm{J},i} \quad \text{for } i = 1, \ldots, g \tag{3.55}$$

and following

$$\mathbf{f}_{\mathrm{J},i} = \frac{1}{\sqrt{\lambda_{\mathrm{POV},i}}} \overline{\mathbf{F}} \hat{\mathbf{f}}_{\mathrm{J},i}. \tag{3.56}$$

Due to the fact that forces are used for POD, the final computation of the g joint modes is performed by

$$\boldsymbol{\phi}_{\mathrm{J},i} = {\mathbf{K_c}}^{-1} \mathbf{f}_{\mathrm{J},i} \quad \text{for } i = 1, \ldots, g. \tag{3.57}$$

An algorithm for computing joint modes based on fictive forces is presented in section 3.3 (algorithm 3.3).

Equivalence of joint modes with inner weighting

It is noteworthy that joint modes computed with weighted POD of TVDs and weighted POD of fictive forces are equivalent. This can be easily shown by inserting the formula for computation of the TVDs (eq. (3.42)) into eq. (3.55) which leads to

$$\left(\boldsymbol{\Phi}_{\mathrm{T}}{}^{\mathsf{T}}\mathbf{K}_{\mathbf{c}}{}^{\mathsf{T}}\mathbf{C}\mathbf{K}_{\mathbf{c}}\boldsymbol{\Phi}_{\mathrm{T}}\right)\hat{\mathbf{f}}_{\mathrm{J},i} = \lambda_{\mathrm{POV},i}\hat{\mathbf{f}}_{\mathrm{J},i}. \tag{3.58}$$

With the properties of the stiffness matrix, namely $\mathbf{C} = \mathbf{K}_{\mathbf{c}}{}^{-1}$ and $\mathbf{K}_{\mathbf{c}} = \mathbf{K}_{\mathbf{c}}{}^{\mathsf{T}}$, this equation simplifies to

$$\left(\boldsymbol{\Phi}_{\mathrm{T}}{}^{\mathsf{T}}\mathbf{K}_{\mathbf{c}}\boldsymbol{\Phi}_{\mathrm{T}}\right)\hat{\mathbf{f}}_{\mathrm{J},i} = \lambda_{\mathrm{POV},i}\hat{\mathbf{f}}_{\mathrm{J},i}, \tag{3.59}$$

which is the same eigenvalue problem as in eq. (3.51) for computing weighted POD of TVDs. Following eq. (3.56) and eq. (3.57), the joint modes are finally computed along

$$\boldsymbol{\phi}_{\mathrm{J},i} = \frac{1}{\sqrt{\lambda_{\mathrm{POV},i}}}\mathbf{K}_{\mathbf{c}}{}^{-1}\mathbf{F}\hat{\mathbf{f}}_{\mathrm{J},i}, \tag{3.60}$$

which is equal to eq. (3.51) since $\mathbf{K}_{\mathbf{c}}{}^{-1}\mathbf{F} = \boldsymbol{\Phi}_{\mathrm{T}}$.

Usage of POVs to estimate the number of joint modes

The proper orthogonal values (POVs) $\lambda_{\mathrm{POV},i}$ computed by POD indicates the importance of a certain proper orthogonal mode (POM) $\mathbf{u}_i$ for the optimization problem defined by eq. (2.99). A large POV $\lambda_{\mathrm{POV},i}$ indicates an important POM $\mathbf{u}_i$. In the case of joint modes computed based on POD a ratio

$$w(g) = \frac{\sum_{i=1}^{g}\lambda_{\mathrm{POV},i}}{\sum_{i=1}^{2m^2}\lambda_{\mathrm{POV},i}} \tag{3.61}$$

can be defined. This ratio $w(g)$ can be used to estimate the number joint modes g required in the extended reduction basis. Similar ratios have already been used in combination with POD (see [133, 144]).

Summary on joint modes for arbitrary structures

Due to the connection with the stiffness matrix, joint modes computed with inner weighting optimally approximate the deformation energy caused by all TVDs. Hence, for POD with weighted inner product the ratio $w(g)$ provides an estimation of how much deformation energy represented by all TVDs is already covered by g joint modes. On the other, POD without inner weighting approximates the deformation space of all TVDs. From a mechanical point of view, the approximation of the deformation energy seems to be more meaningful.

The advantage of applying POD to the fictive forces is that the essential information are extracted before the (time consuming) computation of $2m^2$ TVDs. This leads to a lower

computational effort. On the other hand, the determination of the compliance matrix $\mathbf{C} = \mathbf{K_c}^{-1}$ is practically not possible for large FE structures with a high number of DOFs, since the solution of the nonlinear equation $\mathbf{K_c x} = \mathbf{f}$ does not deliver $\mathbf{C}$. Hence, for the computation of joint modes based on weighted POD the computational scheme considering TVDs is used.

From the theoretical considerations it is not clear which computation strategy for joint modes should be preferred. For the three computation strategies for joint modes, namely

a) joint modes based on weighted POD of TVDs (wPOD of TVDs),
b) joint modes based on unweighted POD of TVDs (POD of TVDs), and
c) joint modes based on unweighted POD of fictive forces (POD of forces),

five joint modes computed for the friction bar are visualized in fig. 3.4.

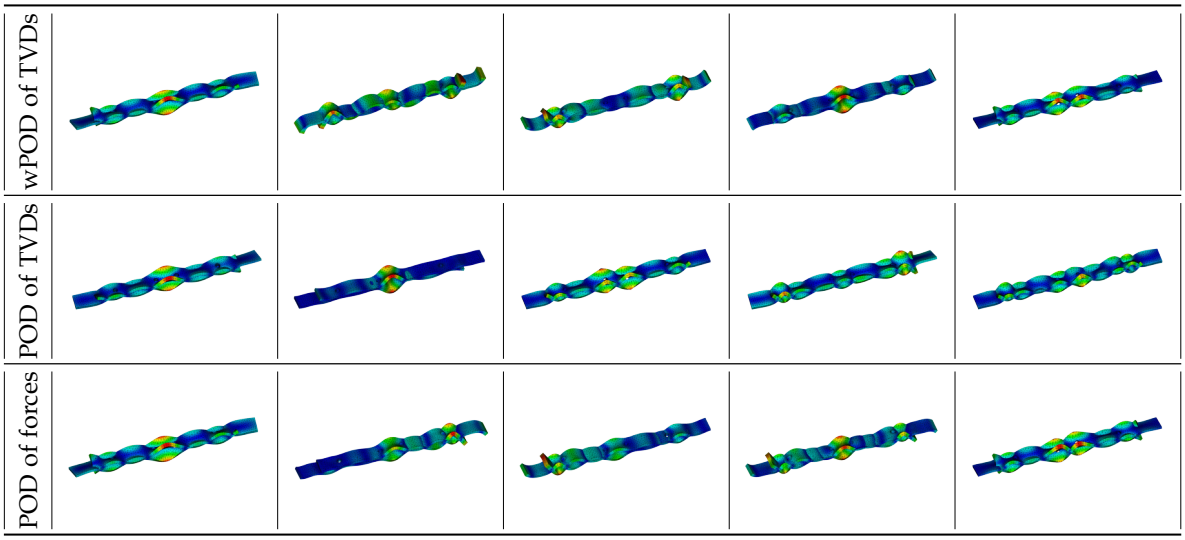

Figure 3.4: Joint modes for the friction bar

All three methods lead to similar looking joint modes. From the visual and theoretical comparison the quality of the different joint modes cannot be evaluated. Hence, these three joint mode methods are investigated on numerical examples in chapter 4. Furthermore, the application of the ratio $w(g)$ for the different joint mode methods is investigated.

3.2.3 Preloaded joint modes

In the previous sections joint modes based on TVDs which are universally usable for arbitrary jointed structures have been introduced. These joint modes are based on the computation of all possible TVDs via a series of static FE analyses. The number of static computations depends with $k = 2m^2$ on the square of the size of the CMS reduction basis m. For industrial applications with $m > 100$ the number of static computations can become quite huge

($k > 10^4$). This is a high computational effort which is only required for an intermediate step. The idea of preloaded joint modes is to alleviate this bottleneck by considering the information of the preload deformation.

The Taylor series expansion (eq. (2.89)) in the theory section of TVDs has been built around the undeformed state $\hat{\boldsymbol{\zeta}} = \mathbf{0}$ for general joint modes. This is a good choice if it can be assumed that the deformations are small around the undeformed state. For preloaded structures this assumption is no longer valid. Deformations of such structures cannot be assumed to be small around the undeformed state, but may be small around the preload deformation state, caused mainly by mounting forces. Hence, the Taylor series expansion has to be built around $\hat{\boldsymbol{\zeta}}_{\mathrm{PL}} = [\zeta_1(\mathbf{x}_{\mathrm{PL}}) \cdots \zeta_m(\mathbf{x}_{\mathrm{PL}})]^{\mathsf{T}}$

$$\boldsymbol{\phi}_i(\boldsymbol{\zeta}) = \boldsymbol{\phi}_i\big|_{\hat{\boldsymbol{\zeta}}_{\mathrm{PL}}} + \sum_{j=1}^{m} \left.\frac{\partial \boldsymbol{\phi}_i}{\partial \zeta_j}\right|_{\hat{\boldsymbol{\zeta}}_{\mathrm{PL}}} (\zeta_j - \zeta_j(\mathbf{x}_{\mathrm{PL}})) + \textit{terms of higher order}, \tag{3.62}$$

where $\zeta_j(\mathbf{x}_{\mathrm{PL}})$ denotes the j-th modal coordinate at the preload state $\mathbf{x}_{\mathrm{PL}}$. For the practical application of the Taylor series expansion around the preload state $\mathbf{x}_{\mathrm{PL}}$ some difficulties occur in combination with commercial FE software:

- The computation of the trial vectors of the CMS reduction basis at the preload state $\boldsymbol{\phi}_i\big|_{\hat{\boldsymbol{\zeta}}_{\mathrm{PL}}}$ is possible, but not a straight forward task.
- Inside the matrix $\mathbf{K_c} = \mathbf{K}(\boldsymbol{\Phi}\hat{\boldsymbol{\zeta}}_{\mathrm{PL}})$ a contact stiffness is considered for contacting nodes at the preload state. If these nodes are separating during the computation of TVDs (see matrix $\frac{\partial \mathbf{K_c}}{\partial \zeta_j}$ described in section 3.2.1) or the computation of contact forces in the MBS this contact stiffness has to be corrected. Hence, the used contact formulation and the implementation in the FE software must be known exactly.

These limitations make the approach of eq. (3.62) impracticable for industrial FE structures which require the usage of commercial FE software.

In order to obtain a special consideration of the preload state (like the deformation due to screw preload) in the reduction basis, so-called *preload modes* (PLMs) are introduced. The $(n_{\mathrm{FE}} \times 1)$ PLM $\boldsymbol{\phi}_{\mathrm{PL},i}$ is basically the static deformation shape due to the preload force $\mathbf{f}_{\mathrm{PL},i}$ considering full nonlinear contact

$$\mathbf{K}_{nl}(\mathbf{x})\boldsymbol{\phi}_{\mathrm{PL},i} = \mathbf{f}_{\mathrm{PL},i} \quad i = 1, \ldots, p. \tag{3.63}$$

These PLMs are collected in the $(n_{\mathrm{FE}} \times p)$ matrix $\boldsymbol{\Phi}_{\mathrm{PL}}$ and the $(n_{\mathrm{FE}} \times r)$ reduction basis with $r = m + p$ trial vectors can be written as

$$\boldsymbol{\Phi} = \begin{bmatrix} \boldsymbol{\Phi}_{\mathrm{CMS}} & \boldsymbol{\Phi}_{\mathrm{PL}} \end{bmatrix}. \tag{3.64}$$

The number p of considered PLMs depends on the design of the structure and the spatial distribution of the preloaded areas, such as the distance between preloaded bolts.

Assuming that only one $(p = 1)$ PLM $\boldsymbol{\phi}_{\mathrm{PL}}$ with the corresponding flexible coordinate ζ_{PL} is considered, the Taylor series expansion for the undeformed state eq. (2.89) can be written

as

$$\boldsymbol{\phi}_i(\zeta) = \boldsymbol{\phi}_i\big|_{\mathbf{0}} + \left(\sum_{j=1}^{m} \frac{\partial \boldsymbol{\phi}_i}{\partial \zeta_j}\bigg|_{\mathbf{0}} \zeta_j + \frac{\partial \boldsymbol{\phi}_i}{\partial \zeta_{\mathrm{PL}}}\bigg|_{\mathbf{0}} \zeta_{\mathrm{PL}} \right) + \textit{terms of higher order}. \tag{3.65}$$

In order to explain the proposed method, a nonlinear projection as mentioned in section 2.2.2 is presumed. By neglecting the higher order terms of eq. (3.65) and inserting this equation in the projection equation $\mathbf{x} \approx \boldsymbol{\Phi}\boldsymbol{\zeta}$ a nonlinear reduction is formed and the displacements can be approximated as

$$\begin{aligned} \mathbf{x} \approx & \sum_{i=1}^{m} \boldsymbol{\phi}_i \zeta_i + \boldsymbol{\phi}_{\mathrm{PL}} \zeta_{\mathrm{PL}} + \frac{\partial \boldsymbol{\phi}_{\mathrm{PL}}}{\partial \zeta_{\mathrm{PL}}} \zeta_{\mathrm{PL}} \zeta_{\mathrm{PL}} \\ & + \sum_{i=1}^{m} \frac{\partial \boldsymbol{\phi}_i}{\partial \zeta_{\mathrm{PL}}} \zeta_{\mathrm{PL}} \zeta_i + \sum_{i=1}^{m} \frac{\partial \boldsymbol{\phi}_{\mathrm{PL}}}{\partial \zeta_i} \zeta_i \zeta_{\mathrm{PL}} + \sum_{i=1}^{m} \sum_{j=1}^{m} \frac{\partial \boldsymbol{\phi}_i}{\partial \zeta_j} \zeta_j \zeta_i. \end{aligned} \tag{3.66}$$

Due to the definition of the PLM in eq. (3.63) the deformation at the preload state $\mathbf{x}_{\mathrm{PL}}$ can be written as

$$\mathbf{x}_{\mathrm{PL}} = \boldsymbol{\phi}_{\mathrm{PL}} \overline{\zeta_{\mathrm{PL}}}. \tag{3.67}$$

This implies that at the preload state $\zeta_{\mathrm{PL}} = \overline{\zeta_{\mathrm{PL}}}$, while all other scaling factors are zero $(\zeta_i = 0; i = 1, \ldots, m)$. Assuming that the displacements vary around the preload deformation allows to write the entire deformations in partitioned form as

$$\mathbf{x} = \mathbf{x}_{\mathrm{PL}} + \Delta\mathbf{x}. \tag{3.68}$$

Consequently, this leads for model reduction to partitioned scaling factors $(\zeta_i = 0 + \Delta\zeta_i; i = 1, \ldots, m)$ and $\zeta_{\mathrm{PL}} = \overline{\zeta_{\mathrm{PL}}} + \Delta\zeta_{\mathrm{PL}}$. In eq. (3.66) different multiplications of the scaling factors $(\zeta_i\zeta_j; \zeta_i\zeta_{\mathrm{PL}}; \zeta_{\mathrm{PL}}\zeta_{\mathrm{PL}})$ appear. Inserting the partitioned scaling factors into these multiplications and assuming that all variations $\Delta\zeta_i, \Delta\zeta_j, \Delta\zeta_{\mathrm{PL}}$ have approximately the same magnitude yields

$$\zeta_i\zeta_j < \zeta_i\zeta_{\mathrm{PL}} < \zeta_{\mathrm{PL}}\zeta_{\mathrm{PL}} \tag{3.69a}$$

$$(\Delta\zeta_i)(\Delta\zeta_j) < (\Delta\zeta_i)(\overline{\zeta_{\mathrm{PL}}} + \Delta\zeta_{\mathrm{PL}}) < (\overline{\zeta_{\mathrm{PL}}} + \Delta\zeta_{\mathrm{PL}})(\overline{\zeta_{\mathrm{PL}}} + \Delta\zeta_{\mathrm{PL}}). \tag{3.69b}$$

For these inequalities to be fulfilled, it has to be assumed that the amplitudes of all trial vectors $\boldsymbol{\phi}_i, i = 1, \ldots, m; \boldsymbol{\phi}_{\mathrm{PL}}$ are in the same range. This is normally guaranteed by a normalization of the trial vectors.

If the inequalities in eq. (3.69) are satisfied, not all TVDs in the nonlinear reduction defined by eq. (3.66) are of same relevance for the displacements. Hence, it is assumed that the TVDs within the double sum (last term) of eq. (3.66) can be neglected. Consequently, the POD based computation of joint modes can be performed using only TVDs related to the preload mode. These $k_{\mathrm{PL}} = 2(p^2 + 2pm)$ PLM related derivatives are collected as columns in the $(n_{\mathrm{FE}} \times k_{\mathrm{PL}})$ matrix

$$\Phi_{\mathrm{TVD,PL}} = \left[\frac{\partial \boldsymbol{\phi}_{\mathrm{PL}}}{\partial \zeta_{\mathrm{PL}}} \quad \cdots \quad \frac{\partial \boldsymbol{\phi}_i}{\partial \zeta_{\mathrm{PL}}} \quad \cdots \frac{\partial \boldsymbol{\phi}_{\mathrm{PL}}}{\partial \zeta_i} \quad \cdots \right] \; i = 1, \ldots, m. \tag{3.70}$$

Since the most important information should be covered by the derivatives in $\Phi_{\mathrm{TVD,PL}}$, the joint modes computed with PLM related derivatives should yield high quality results which are comparable to the results using all possible TVDs. Furthermore, it is assumed that the space spanned by the matrix $\Phi_{\mathrm{TVD,PL}}$ is more specific concerning the interesting joint deformation, and hence the specialized joint modes should lead to a faster convergence.

Moreover, this approach has the advantage that the number of TVDs which need to be computed is much lower compared to the joint modes for arbitrary structures ($2(p^2 + 2pm) << 2(m+p)^2$). This fact is of practical relevance since the computation of all TVDs is a time and memory consuming task for industrial applications with many trial vectors in the CMS reduction basis. Furthermore, the number of preload modes is much lower for most types of structures than the number of CMS trial vectors ($p << m$).

From an engineering point of view, it is easy to imagine that the derivatives $\frac{\partial \boldsymbol{\phi}_{\mathrm{PL}}}{\partial \zeta_i}$, $\frac{\partial \boldsymbol{\phi}_i}{\partial \zeta_{\mathrm{PL}}}$ are most important since they describe the change of a deformation according to the preload state, and the change of the preload state with respect to a dynamic deformation.

The inequalities (3.69) also indicate the limits of the proposed method. For dynamic simulations it is questionable whether PLM related TVDs form a valid reduction basis if the dynamic deformation state significantly differs from the preload deformations. Another influencing factor might be the spatial distribution of the joint and the surface ratio of the preload area compared to the area of the entire joint.

The method described for preloaded joint modes and the influence of the possible limitations are investigated in chapter 4. An algorithm summarizing the procedure for computing the specialized joint modes for preloaded structures is shown in section 3.3 (algorithm 3.4).

3.3 Implementation details of the presented approach

In the previous sections the efficient consideration of jointed flexible structures in an MBS has been discussed on a theoretical basis. To make the theory of joint modes and the computation of joint forces in flexible multibody systems usable for industrial applications, it is necessary to embed the method into the simulation process.

The simulation process can be divided into three main tasks, namely:

a) preprocessing,
b) multibody simulation including contact and friction forces, and
c) postprocessing.

The workflow of the entire simulation process is visualized in fig. 3.5.

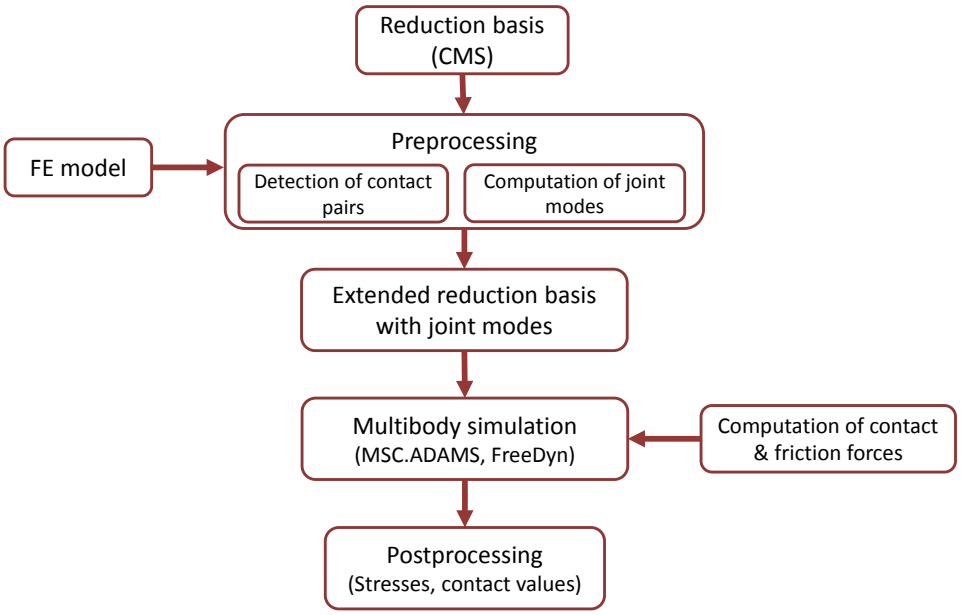

Figure 3.5: Simulation workflow

The pre- and postprocessing steps are performed by a self written software called *ContactDefiner*. The *ContactDefiner* utilizes the open-source visualization toolkit *VTK* [107] for visualization and for standard operations on the FE mesh. The computation of the nonlinear forces is embedded in the free MBS solver *FreeDyn* [132] directly, or via a subroutine in *MSC.ADAMS* [73].

The computation of nonlinear joint forces is based on a master-slave node-to-segment formulation. For this formulation the FE nodes of the slave surface are directly used, and on the master surface virtual contact points (intersection points) are identified. Details on the considered node-to-segment formulation can be found in the textbook of Wriggers [146].

The implementation of the contact computation is described for a uniform FE mesh consisting of isoparametric solid elements in the following sections. An extension towards isoparametric shell elements and non uniform meshes is implemented, but not described in this thesis. Moreover, theoretical basics of isoparametric finite elements are used in the following sections without discussing the details. Detailed insight into isoparametric finite elements can be found in many FEM textbooks, for instance in [7, 53, 146, 149].

3.3.1 Preprocessing

The main tasks of the preprocessing module are a) detection of contact pairs, and b) computation of joint modes. The necessary steps to detect the contact pairs for the node-to-segment contact elements are discussed in the following paragraphs. The implementation for the computation of joint modes is presented in form of pseudo-code algorithms.

Determination of exterior surfaces Contact and friction forces act only on the exterior surfaces of the contacting bodies. Hence, only the finite elements located on exterior surfaces are of relevance for the determination of node-to-segment contact pairs. For the detection of these surfaces the master and slave surfaces involved in the contact are marked via sets with different properties in the FE model. The detection of finite elements on the exterior surface can be in general performed based on the connectivity of the finite elements and the corresponding FE nodes. For the practical implementation of this task the functionality of *VTK* is used.

Computation of a local coordinate system The contact pressure $p_{N,i}$ and frictional stress $\tau_{F,i}$ of each contact pair are defined as a function of the local normal gap $g_{N,i}$ and the tangential displacement s_i. Hence, each contact pair requires a local coordinate system $C_i\{\vec{n}, \vec{t}_i^{\,1}, \vec{t}_i^{\,2}\}$ to describe the local normal and tangential displacement. Furthermore, the normal vectors of the master surface are required to determine the intersection point for the node-to-segment contact element.

In appendix D.1 it is described how a local coordinate system can be computed at any point $\vec{X}$ of a finite element. This leads to a local coordinate system which can be evaluated based on the isoparametric coordinates ξ, η using the finite element shape functions $N_i = N_i(\xi, \eta)$. Exemplary, local coordinate systems at different locations of an isoparametric quadratic triangle are depicted in fig. 3.6.

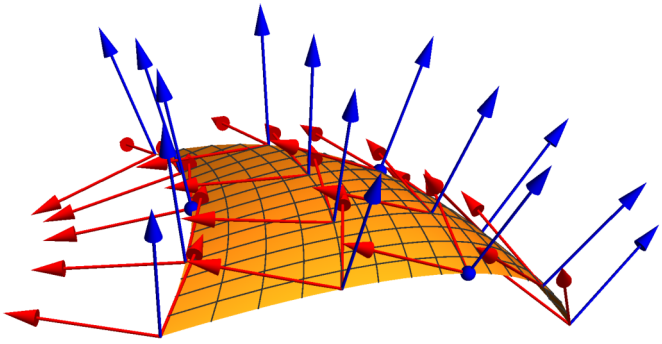

Figure 3.6: Local coordinate systems for six-node isoparametric triangle

Detection of an intersection point In the considered node-to-segment contact formulation each slave node requires a unique intersection point on the master surface. In fig. 3.7a the detection of the intersection point $\vec{\overline{X}}^M(\overline{\xi}, \overline{\eta})$ on the master surface is shown for a three-node isoparametric triangle.

In general the intersection point $\vec{\overline{X}}^M(\overline{\xi}, \overline{\eta})$ can be found with the condition that the vector between the slave node $\vec{X}^S$ and $\vec{\overline{X}}^M(\overline{\xi}, \overline{\eta})$ is coincident with the normal vector of the master surface $\vec{n}^M(\overline{\xi}, \overline{\eta})$. A mathematical description of this condition is outlined in appendix D.1.

For the practical computation of an intersection point $\vec{\overline{X}}^M\left(\overline{\xi},\overline{\eta}\right)$, the functionality of *VTK* is used. In fig. 3.7b the intersection points with the assigned local coordinate systems are visualized for an arbitrary structure.

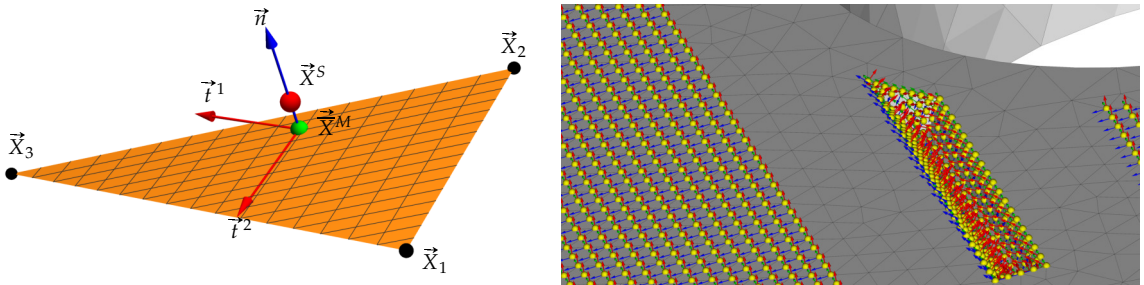

(a) Intersection point for three-node isoparametric triangle

(b) Intersection points for arbitrary sturcture

Figure 3.7: Intersection points for node-to-segment contact

Computation of joint modes All presented approaches for joint modes are based on the use of TVDs. The computation of all TVDs can be interpreted as a series of static FE computations with different loadings. In algorithm 3.1 the computation procedure for TVDs in combination with an FE software is summarized. For initially opened joints an initial gap and furthermore

different scaling values of the deflection directions need to be considered in algorithm 3.1.

input : FE model
output: $\mathbf{\Phi}_\mathrm{T}$
initialization ;
compute CMS reduction basis $\mathbf{\Phi}_\mathrm{CMS}$;
Find contact pairs ;
// m being the number of mode shapes in $\mathbf{\Phi}_\mathrm{CMS}$
// k being the deflection direction of the mode shape
// n_CP being the number of contact pairs
for $j = 1 : m$ **do**
  for $k = -1 : 2 : 1$ **do**
    for $i = 1 : n_{CP}$ **do**
      compute $g_{N,i}$ due to $k\boldsymbol{\phi}_j$;
      if $g_{N,i} < 0$ **then**
        add ε_N in the matrix $\frac{\partial \mathbf{K_c}}{\partial \zeta_{k \cdot j}}$ (corresponding to DOFs of contact pair i)
      end
    end
    for $i = 1 : m$ **do**
      $\mathbf{f}_{i,k \cdot j} = \frac{\partial \mathbf{K_c}}{\partial \zeta_{k \cdot j}} \boldsymbol{\phi}_i$;
      $\mathbf{F} = \begin{bmatrix} \mathbf{F} & \mathbf{f}_{i,k \cdot j} \end{bmatrix}$;
    end
  end
end
compute TVDs with FE software based on $\mathbf{K_c}\mathbf{\Phi}_\mathrm{T} = \mathbf{F}$

Algorithm 3.1: Computation of TVDs with FE software

The computation scheme for the joint mode approaches which use TVDs directly (wPOD of TVDs, POD of TVDs) is presented in algorithm 3.2. The algorithm for computing joint modes based on POD of fictive forces (POD of forces) is summarized in algorithm 3.3.

In these algorithms the stiffness matrix of the FE model $\mathbf{K_c}$ is used in the formulas in order to keep the notation consistent with the theory described in section 3.2. For the practical computation the stiffness matrix is not required since the equality $\mathbf{K_c}\mathbf{\Phi}_\mathrm{T} = \mathbf{F}$ respectively $\mathbf{K_c}\frac{\partial \boldsymbol{\phi}_i}{\partial \zeta_j} = \mathbf{f}_{i,j}$ can be used.

The computation scheme for preloaded joint modes is summarized in algorithm 3.4 for the case that one PLM is considered.

input : FE model, $\mathbf{K_c}$, POD with inner weighting (true or false)
output: extended reduction basis $\mathbf{\Phi} = \begin{bmatrix}\mathbf{\Phi}_{\text{CMS}} & \mathbf{\Phi}_{\text{J}}\end{bmatrix}$

1 initialize ;
2 compute CMS reduction basis $\mathbf{\Phi}_{\text{CMS}}$;
3 compute $\mathbf{\Phi}_{\text{T}}$ based on $\mathbf{K_c}\mathbf{\Phi}_{\text{T}} = \mathbf{F}$ with FE software (see algorithm 3.1) ;
`// compute POD`
4 **if** *POD with inner weighting* **then**
5 | normalize each $\boldsymbol{\phi}_{\text{T},i}$ with respect to $\mathbf{K_c}$;
6 | solve eigenvalue problem $\left(\overline{\mathbf{\Phi}}_{\text{T}}{}^{\mathsf{T}}\mathbf{K_c}\overline{\mathbf{\Phi}}_{\text{T}}\right)\hat{\boldsymbol{\phi}}_{\text{J},i} = \lambda_{\text{POV},i}\hat{\boldsymbol{\phi}}_{\text{J},i}$
7 **else**
8 | normalize each $\boldsymbol{\phi}_{\text{T},i}$ with respect to $\mathbf{I}$;
9 | solve eigenvalue problem $\left(\overline{\mathbf{\Phi}}_{\text{T}}{}^{\mathsf{T}}\overline{\mathbf{\Phi}}_{\text{T}}\right)\hat{\boldsymbol{\phi}}_{\text{J},i} = \lambda_{\text{POV},i}\hat{\boldsymbol{\phi}}_{\text{J},i}$
10 **end**
11 determine number of joint modes g ;
12 **for** $i = 1 : g$ **do**
13 | $\boldsymbol{\phi}_{\text{J},i} = \frac{1}{\sqrt{\lambda_{\text{POV},i}}}\overline{\mathbf{\Phi}}_{\text{T}}\hat{\boldsymbol{\phi}}_{\text{J},i}$
14 **end**
`// extended reduction basis`
15 $\Phi = \left[\mathbf{\Phi}_{\text{CMS}} \quad \boldsymbol{\phi}_{\text{J},1}, \ldots, \boldsymbol{\phi}_{\text{J},g}\right] = \begin{bmatrix}\mathbf{\Phi}_{\text{CMS}} & \mathbf{\Phi}_{\text{J}}\end{bmatrix}$;

Algorithm 3.2: Reduction basis with joint modes based on POD of TVDs

input : FE model, $\mathbf{K_c}$
output: extended reduction basis $\mathbf{\Phi} = \begin{bmatrix}\mathbf{\Phi}_{\text{CMS}} & \mathbf{\Phi}_{\text{J}}\end{bmatrix}$

1 initialize ;
2 compute CMS reduction basis $\mathbf{\Phi}_{\text{CMS}}$;
3 compute fictive forces $\mathbf{F}$ for TVDs along algorithm 3.1 (lines 2–17) ;
`// compute POD`
4 normalize each $\mathbf{f}_{i,j}$ with respect to or $\mathbf{I}$;
5 solve eigenvalue problem $\left(\overline{\mathbf{F}}^{\mathsf{T}}\overline{\mathbf{F}}\right)\hat{\mathbf{f}}_{\text{J},i} = \lambda_{\text{POV},i}\hat{\mathbf{f}}_{\text{J},i}$;
6 determine number of joint modes g ;
7 **for** $i = 1 : g$ **do**
8 | solve $\mathbf{K_c}\ \boldsymbol{\phi}_{\text{J},i} = \frac{1}{\sqrt{\lambda_{\text{POV},i}}}\overline{\mathbf{F}}\hat{\mathbf{f}}_{\text{J},i}$
9 **end**
`// extended reduction basis`
10 $\Phi = \left[\mathbf{\Phi}_{\text{CMS}} \quad \boldsymbol{\phi}_{\text{J},1}, \ldots, \boldsymbol{\phi}_{\text{J},g}\right] = \begin{bmatrix}\mathbf{\Phi}_{\text{CMS}} & \mathbf{\Phi}_{\text{J}}\end{bmatrix}$;

Algorithm 3.3: Reduction basis with joint modes based on POD of fictive forces

input : FE model
output: extended reduction basis $\boldsymbol{\Phi} = \begin{bmatrix} \boldsymbol{\Phi}_{\mathrm{CMS}} & \boldsymbol{\Phi}_{\mathrm{PL}} & \boldsymbol{\Phi}_{\mathrm{J}} \end{bmatrix}$

1 initialize ;
2 compute CMS reduction basis $\boldsymbol{\Phi}_{\mathrm{CMS}}$;
3 compute preload mode $\boldsymbol{\phi}_{\mathrm{PL}}$ along $\mathbf{K}_{nl}(\mathbf{x})\boldsymbol{\phi}_{\mathrm{PL}} = \mathbf{f}_{\mathrm{PL}}$ (see eq. (3.63)) ;
4 compute PLM related trial vector derivatives $\begin{bmatrix} \frac{\partial \boldsymbol{\phi}_{\mathrm{PL}}}{\partial \zeta_{\mathrm{PL}}} & \cdots & \frac{\partial \boldsymbol{\phi}_i}{\partial \zeta_{\mathrm{PL}}} & \cdots \frac{\partial \boldsymbol{\phi}_{\mathrm{PL}}}{\partial \zeta_i} & \cdots \end{bmatrix}$ with FE software (see algorithm 3.1) ;
5 compute joint modes based on POD (with inner weighting) along algorithm 3.2 (lines $4-14$) ;
// extended reduction basis
6 $\boldsymbol{\Phi} = \begin{bmatrix} \boldsymbol{\Phi}_{\mathrm{CMS}} & \boldsymbol{\Phi}_{\mathrm{PL}} & \boldsymbol{\phi}_{\mathrm{J},1}, \ldots, \boldsymbol{\phi}_{\mathrm{J},g} \end{bmatrix} = \begin{bmatrix} \boldsymbol{\Phi}_{\mathrm{CMS}} & \boldsymbol{\Phi}_{\mathrm{PL}} & \boldsymbol{\Phi}_{\mathrm{J}} \end{bmatrix}$;

Algorithm 3.4: Joint modes for preloaded structures (for one PLM)

3.3.2 MBS including contact and friction forces

For the computation of nonlinear contact and friction forces the relative displacements between the master and slave surface are required. In the following sections it is described how these relative displacements can be computed efficiently for reduced structures in a multibody simulation. Furthermore, the computation of the nonlinear forces on the master and slave surface and the computation of the resulting modal forces is described.

Relative master-slave displacements

An efficient computation of the relative displacement between the slave node and the intersection point on the master surface ${}^{C_i}\vec{y}_i^{MS}$ as a function of the flexible coordinates $\boldsymbol{\zeta}$ is outlined in this section. For better readability only one contact pair i is considered. An extension of the formulas to all n_{CP} contact pairs can be found in appendix D.2.

For the contact pair i, the relative displacement can be written as

$$ {}^{C_i}\vec{y}_i^{MS} = {}^{C_i}\vec{x}_i^{M} - {}^{C_i}\vec{x}_i^{S}, \tag{3.71} $$

where ${}^{C_i}\vec{x}_i^{M}, {}^{C_i}\vec{x}_i^{S}$ are the (3×1) displacement vectors of the intersection point and the slave node, respectively. The quantities of the latter equation are described in the local coordinate system C_i of the contact pair.

A transformation of displacements between the body reference coordinate system $B\{\tilde{\mathbf{e}}_1^i, \tilde{\mathbf{e}}_2^i, \tilde{\mathbf{e}}_3^i\}$ and the local coordinate system C_i is given by

$$ {}^{B}\vec{x}_i = \mathbf{Q}_i \, {}^{C_i}\vec{x}_i = \begin{bmatrix} {}^{B}\vec{t}_i^{\,1} & {}^{B}\vec{t}_i^{\,2} & {}^{B}\vec{n}_i \end{bmatrix} {}^{C_i}\vec{x}_i, \tag{3.72} $$

where $\mathbf{Q}_i$ denotes a (3×3) orthogonal transformation matrix with the property $\mathbf{Q}_i^{-1} = \mathbf{Q}_i^{\mathrm{T}}$. Hence, the inverse transformation is given by

$$ {}^{C_i}\vec{x}_i = \mathbf{Q}_i^{-1} \, {}^{B}\vec{x}_i = \mathbf{Q}_i^{\mathrm{T}} \, {}^{B}\vec{x}_i. \tag{3.73} $$

The normal and tangential vectors describing the matrix $\mathbf{Q}_i$ are computed as described in section 3.3.1.

The displacement of the slave node in the body coordinate system ${}^B\vec{x}_i^S$ is identical with the displacement of the associated FE node. Hence, ${}^B\vec{x}_i^S$ can be directly computed with the flexible coordinates along

$$ {}^B\vec{x}_i^S = \mathbf{\Phi}_i^S \boldsymbol{\zeta}, \tag{3.74} $$

where the $(3 \times r)$ matrix $\mathbf{\Phi}_i^S$ contains the components of all trial vectors corresponding to the slave node. Applying the transformation described by eq. (3.73), the displacement of the slave node in the local coordinate system can be written as

$$ {}^{C_i}\vec{x}_i^S = \mathbf{Q}_i^{\mathsf{T}} {}^B\vec{x}_i^S = \mathbf{Q}_i^{\mathsf{T}} \mathbf{\Phi}_i^S \boldsymbol{\zeta}. \tag{3.75} $$

Contrary to the salve node, the intersection point on the master surface is in general not coincident with an FE node. Hence, the displacement of the intersection point can be written as

$$ {}^B\vec{x}_i^M = \overline{\mathbf{N}}_i^e \mathbf{x}_i^e, \tag{3.76} $$

where the $(3 \times 3n_{\mathrm{FE}}^e)$ matrix $\overline{\mathbf{N}}_i^e$ (defined by eq. (D.2)) contains the finite element shape functions evaluated at the isoparametric coordinates of the intersection point $(\overline{\mathbf{N}}_i^e = \mathbf{N}^e\left(\overline{\xi}_i, \overline{\eta}_i\right))$. The $(3n_{\mathrm{FE}}^e \times 1)$ vector $\mathbf{x}_i^e$ contains the nodal displacements of the finite element on which the intersection point is located, and can be written in terms of model order reduction as

$$ \mathbf{x}_i^e = \mathbf{\Phi}_i^e \boldsymbol{\zeta}, \tag{3.77} $$

where the $(3n_{\mathrm{FE}}^e \times r)$ matrix $\mathbf{\Phi}_i^e$ contains in its columns the components of all trial vectors corresponding to the FE nodes of the element. Combining eqs. (3.76) and (3.77) and the coordinate transformation described by eq. (3.73), the displacement of the intersection point in the local coordinate system can be computed along

$$ {}^{C_i}\vec{x}_i^M = \mathbf{Q}_i^{\mathsf{T}} {}^B\vec{x}_i^M = \mathbf{Q}_i^{\mathsf{T}} \overline{\mathbf{N}}_i^e \mathbf{x}_i^e = \mathbf{Q}_i^{\mathsf{T}} \overline{\mathbf{N}}_i^e \mathbf{\Phi}_i^e \boldsymbol{\zeta}. \tag{3.78} $$

Inserting the results of eqs. (3.75) and (3.78) into the definition of the relative displacement between the slave node and the intersection point ${}^{C_i}\vec{y}_i^{MS}$ given by eq. (3.71) yields

$$ {}^{C_i}\vec{y}_i^{MS} = \mathbf{Q}_i^{\mathsf{T}} \overline{\mathbf{N}}_i^e \mathbf{\Phi}_i^e \boldsymbol{\zeta} - \mathbf{Q}_i^{\mathsf{T}} \mathbf{\Phi}_i^S \boldsymbol{\zeta} = \mathbf{Q}_i^{\mathsf{T}} \left[\overline{\mathbf{N}}_i^e \mathbf{\Phi}_i^e - \mathbf{\Phi}_i^S \right] \boldsymbol{\zeta} = \mathbf{\Phi}_i^{MS} \boldsymbol{\zeta}. \tag{3.79} $$

With this equation the relative displacement ${}^{C_i}\vec{y}_i^{MS}$ can be computed with one matrix vector multiplication since all components of the $(3 \times r)$ matrix $\mathbf{\Phi}_i^{MS} = \mathbf{Q}_i^{\mathsf{T}} \left[\overline{\mathbf{N}}_i^e \mathbf{\Phi}_i^e - \mathbf{\Phi}_i^S \right]$ are constant and can be evaluated before the multibody simulation.

For the computation of the contact pressure $p_{N,i}$ and friction stress $\tau_{F,i}$ the total relative displacement vector ${}^{C_i}\vec{y}_i^{MS}$ cannot be used directly. In fact, the initial gap in normal direction ${}^{C_i}g_{N,i,0}$ and relative tangential displacements which occur before the surfaces are in contact

${}^{C_i}s_{1,i,t^*}, {}^{C_i}s_{2,i,t^*}$, need to be considered. Hence, the required displacement for the contact pair can be written in a (3×1) vector as

$$ {}^{C_i}\vec{z}_i = \begin{bmatrix} s_{1,i} \\ s_{2,i} \\ g_{N,i} \end{bmatrix} = {}^{C_i}\vec{y}_i^{MS} + \begin{bmatrix} 0 \\ 0 \\ {}^{C_i}g_{N,i,0} \end{bmatrix} - \begin{bmatrix} {}^{C_i}s_{1,i,t^*} \\ {}^{C_i}s_{2,i,t^*} \\ 0 \end{bmatrix}, \tag{3.80} $$

with $g_{N,i}$ being the normal gap considering the initial gap, and $s_{1,i}, s_{2,i}$ being the tangential relative displacement occurring after the contact closure at time t^*. Finally, the values $s_{1,i}, s_{2,i}, g_{N,i}$ are required for the computation of the contact pressure and friction stress as described in sections 3.1.1 and 3.1.2.

Nonlinear modal force

As described in section 3.1 a modal representation of the nonlinear contact and friction forces is required for the multibody simulation. Hence, an efficient computation of the resulting nonlinear modal force based on the nonlinear forces acting on the master and slave surface is described in the following subsections.

Nonlinear forces on slave surface For each contact pair the contact pressure $p_{N,i}$ and frictional stress components in the principal directions $\tau_{F,i,1}, \tau_{F,i,2}$ can be combined in one (3×1) vector

$$ {}^{C_i}\vec{v}_i = \begin{bmatrix} {}^{C_i}\tau_{F,i,1} & {}^{C_i}\tau_{F,i,2} & {}^{C_i}p_{N,i} \end{bmatrix}^{\mathsf{T}}, \tag{3.81} $$

where all components are described in the local coordinate system C_i of the contact pair.

For a consistent force analogy in terms of the FE shape functions it is necessary to compute a consistent nodal force from the vector ${}^{C_i}\vec{v}_i$. The nodal force on the slave node described in the body coordinate system can be written in a (3×1) vector as

$$ {}^{B}\vec{f}_i^{S} = \mathbf{A}_i \, {}^{B}\boldsymbol{\nu}_i = \mathbf{A}_i \mathbf{Q}_i \, {}^{C_i}\boldsymbol{\nu}_i, \tag{3.82} $$

where the (3×3) matrix $\mathbf{A}_i$ holds the surface integrals of the finite elements connected to the slave node. A detailed derivation of the matrix $\mathbf{A}_i$ is out of the scope of this thesis since the integration over element surfaces and assembling the corresponding matrices is a well-known task in the theory of finite element analysis.

Modal force on slave surface The nodal force on the slave surface has to be projected on the subspace spanned by the trial vectors. For this purpose, eq. (3.82) is pre-multiplied with $\boldsymbol{\Phi}_i^{S\mathsf{T}}$ to get a modal representation of ${}^{B}\vec{f}_i^{S}$. Applying this multiplication yields the $(r \times 1)$ vector of modal slave forces

$$ \mathbf{f}_i^{m,S} = \boldsymbol{\Phi}_i^{S\mathsf{T}} \, {}^{B}\vec{f}_i^{S} = \boldsymbol{\Phi}_i^{S\mathsf{T}} \mathbf{A}_i \mathbf{Q}_i \, {}^{C_i}\vec{v}_i, \tag{3.83} $$

where the $(3 \times r)$ matrix $\mathbf{\Phi}_i^S$ contains the components of all trial vectors corresponding to the slave node.

The previous equation can be written in a more compact form along

$$\mathbf{f}_i^{m,S} = \mathbf{\Theta}_i^S \, {}^{C_i}\vec{v}_i, \tag{3.84}$$

with the $(r \times 3)$ matrix $\mathbf{\Theta}_i^S = \mathbf{\Phi}_i^{S\mathsf{T}} \mathbf{A}_i \mathbf{Q}_i$.

Nonlinear forces on master surface To achieve a local equilibrium between the nodal forces acting on the slave node and the intersection point on the master surface, the force vector ${}^B\vec{f}_i^M = -{}^B\vec{f}_i^S = -\mathbf{A}_i \mathbf{Q}_i \, {}^{C_i}\vec{v}_i$ is applied on the intersection point. For consistent nodal forces on the finite element corresponding to the intersection point the FE shape functions are used. This yields the $(3n_{\mathrm{FE}}^e \times 1)$ vector

$${}^B\mathbf{f}_i^e = \begin{bmatrix} {}^B\vec{f}_1^{\,e} \\ \vdots \\ {}^B\vec{f}_{n_{\mathrm{FE}}^e}^{\,e} \end{bmatrix} = \left[\mathbf{N}^e\left(\overline{\xi}_i, \overline{\eta}_i\right)\right]^{\mathsf{T}} \, {}^B\vec{f}_i^M = \widetilde{\mathbf{N}}_i^e \mathbf{A}_i \mathbf{Q}_i \, {}^{C_i}\vec{v}_i, \tag{3.85}$$

where the $(3n_{\mathrm{FE}}^e \times 3)$ matrix $\widetilde{\mathbf{N}}_i^e$ is defined as $\widetilde{\mathbf{N}}_i^e = -\left[\mathbf{N}^e\left(\overline{\xi}_i, \overline{\eta}_i\right)\right]^{\mathsf{T}}$.

Modal force on master surface The vector ${}^B\mathbf{f}_i^e$ has to be projected on the subspace spanned by the trial vectors, and hence eq. (3.85) is pre-multiplied with the transposed $(3n_{\mathrm{FE}}^e \times r)$ matrix $\mathbf{\Phi}_i^e$. This matrix contains the trial vectors corresponding to the FE nodes of the element on which the intersection point is located. The $(r \times 1)$ vector of modal master forces can be computed along

$$\mathbf{f}_i^{m,M} = \left[\mathbf{\Phi}_i^e\right]^{\mathsf{T}} \, {}^B\mathbf{f}_i^e = \left[\mathbf{\Phi}_i^e\right]^{\mathsf{T}} \, \widetilde{\mathbf{N}}_i^e \mathbf{A}_i \mathbf{Q}_i \, {}^{C_i}\vec{v}_i = \mathbf{\Theta}_i^M \, {}^{C_i}\vec{v}_i, \tag{3.86}$$

with the $(r \times 3)$ matrix $\mathbf{\Theta}_i^M = \left[\mathbf{\Phi}_i^e\right]^{\mathsf{T}} \widetilde{\mathbf{N}}_i^e \mathbf{A}_i \mathbf{Q}_i$.

Computation of overall modal force The overall modal forces due to the slave nodes (see eq. (3.84)) and due to the master surface (see eq. (3.86)) can be combined in the $(r \times 1)$ vector

$$\mathbf{f}_i^m = \mathbf{f}_i^{m,S} + \mathbf{f}_i^{m,M} = \mathbf{\Theta}_i^S \, {}^{C_i}\vec{v}_i + \mathbf{\Theta}_i^M \, {}^{C_i}\vec{v}_i = \mathbf{\Theta}_i \, {}^{C_i}\vec{v}_i. \tag{3.87}$$

The $(r \times 3)$ matrix $\mathbf{\Theta}_i = \mathbf{\Theta}_i^S + \mathbf{\Theta}_i^M$ can be computed before the actual MBS. Hence, with the previous defined equation the resulting modal force for the MBS can be computed based on the contact pressure and friction stress via one simple matrix vector multiplication.

3.3.3 Postprocessing

To evaluate and analyze the contact situation after an MBS, a postprocessing toolbox was embedded in the *ContactDefiner*. This postprocessing toolbox enables a better insight into the dynamic behavior of the jointed structure and the contact situation. The tool visualizes the values of

- normal gap $g_{N,i}$,
- contact pressure $p_{N,i}$,
- contact status (gaping or penetrating; sticking or sliding),
- tangential displacement in first principal direction $s_{1,i}$,
- tangential displacement in second principal direction $s_{2,i}$, and
- frictional stress $\tau_{F,i}$

on the slave nodes of each contact pair at different instances of time. In fig. 3.8 the toolbox and the normal gaps for a bolted connection rod (see section 4.2) are visualized for the sake of demonstration. Furthermore, the toolbox gives the opportunity for an animation of the selected value and an export to an image file.

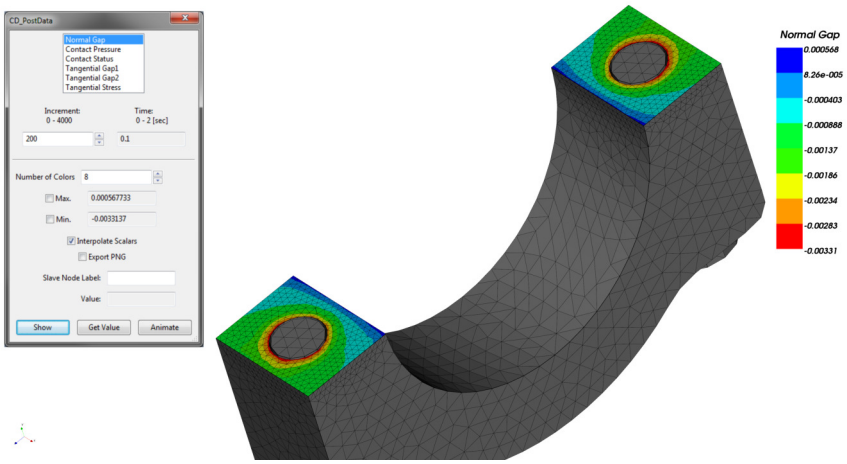

Figure 3.8: Postprocessing toolbox

4 Examples and evaluation

The general joint mode methods for arbitrary structures (wPOD of TVDs, POD of TVDs, POD of forces) are investigated using two numerical examples in the following sections. In section 4.1.1 an academic example of a friction bar is used, while in section 4.2.1 an industrial application of a bolted connection rod bearing cap is investigated. For both examples, the intention is to compare the different computation methods for joint modes with respect to their convergence behavior in terms of displacements, stresses and normal gaps. For this purpose static and dynamic computations are performed.

Furthermore, the theory of preloaded joint modes is investigated using numerical examples. The considered structures are basically identical with the examples used for the numerical evaluation of general joint modes. The friction bar is slightly modified in order to introduce preloaded areas. The aim of these studies is to compare the preloaded joint modes with respect to the general joint modes. The numerical investigations focus on whether the exclusive use of PLM related TVDs for the computation of joint modes leads to good convergence, as suggested in section 3.2.3. Furthermore, possible limitations and influence parameters are analyzed. The robustness of different reduction bases is examined and the following points are considered in detail:

- Are joint modes based on PLM derivatives suitable for large-area joints with a very localized preload area?
- How is the convergence rate of the different reduction bases influenced by the level of system dynamics?
- Are PLMs able to capture diverging contact parameters?

For all examples the Craig-Bampton reduction basis [22] with subsequent mode shape orthogonalization [37] was computed with the FE solver *MSC.NASTRAN* [74]. The static and dynamic computations were performed within *MSC.ADAMS* [73], whereby the nonlinear contact and friction forces were computed via a subroutine as described in section 3.3. The contact subroutine was enabled for all simulations, even if the investigated reduction basis does not include joint modes. For the computation of the contact forces a simple linear penalty model (see section 2.4.2) is used and *small sliding* is assumed. Friction forces were only considered in dynamic simulations via a three-parameter Coulomb-type friction model (see section 2.4.1).

For the static computations, the error of the static equilibrium solver was set to $e = 1\mathrm{e}-4$. For the dynamic simulations an HHT solver [52, 75] with the settings $e = 1\mathrm{e}-8, h_{max} = 5\mathrm{e}-4\,\mathrm{s}$, and $\alpha = -0.3$ was used.

4.1 Academic example of a friction bar

4.1.1 Verification of general joint modes

A schematic draft of the friction bar with the applied loads and mounting is depicted in fig. 4.1. The model consists of two metallic sheets of size 200 mm × 20 mm × 3 mm with four holes. The two middle holes are used to connect the metal sheets via beam elements. The total length of the structure is indicated in fig. 4.1 with $l_{FB} = 225\,\text{mm}$. The joint area itself is highlighted in this figure with a thick red line. The structure was fixed on one side, while on the free end the external loads $\vec{f}_e, M_x$ were applied. In order to apply the force and mounting all nodes of the end faces were coupled to one middle node in the FE model. For the investigation of general joint modes no preload forces were applied.

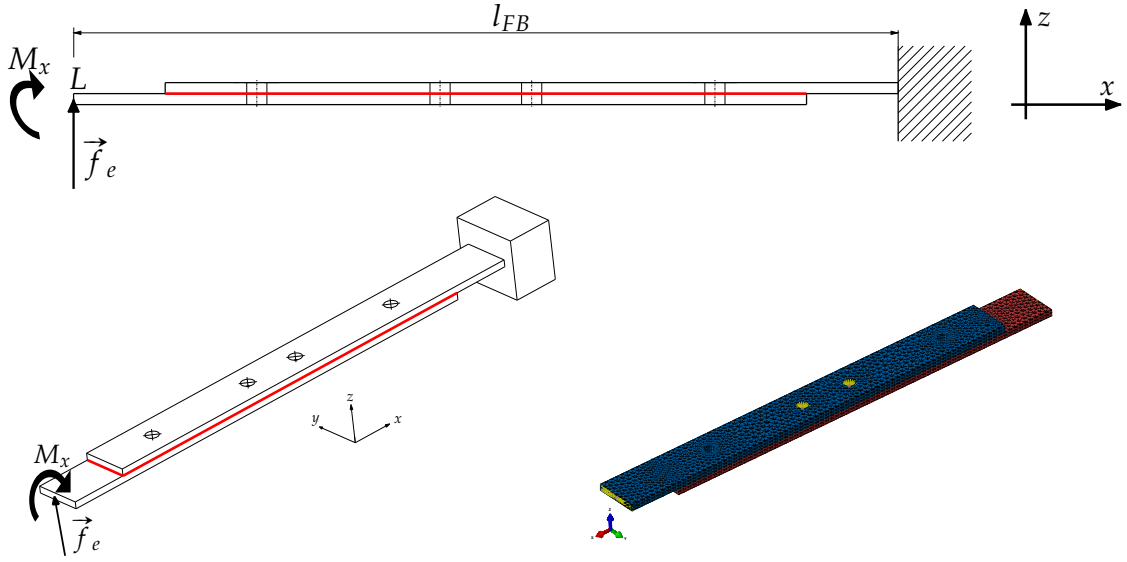

Figure 4.1: Schematic draft and FE model of the friction bar

The FE model of the structure is also depicted in fig. 4.1. The model consists of 38162 FE nodes and 22060 quadratic tetrahedron elements. The two metal sheets and the beam elements were modeled out of steel. This yields an overall mass of $m_{FB} = 0.185\,\text{kg}$. The joint area was not modeled with coincident meshes. Hence, inside the joint area $n_{\text{CP}} = 3055$ node-to-node and node-to-segment contact pairs were considered.

The CMS reduction basis of the friction bar was computed with $v = 10$ vibration modes and $s = 12$ constraint modes according to the mounting and load application points. Hence, after mode shape orthogonalization $m = 16$ trial vectors with a nonzero eigenfrequency remained in the CMS reduction basis. For the joint modes based on TVDs this leads to $k = 2m^2 = 512$ static FE analysis required for the computation of all TVDs.

Static convergence study

The static convergence study was performed with two different load cases. For both load cases the convergence of the three different joint mode methods (wPOD of TVDs, POD of TVDs, POD of forces) and the convergence of additional vibration modes of the CMS reduction basis was investigated. Vibration modes are not specialized for considering contact but nevertheless the contact subroutine was enabled for all reduction basis. In order to evaluate the quality of the extension strategies, different convergence criteria were evaluated with respect to the number of additional trial vectors. For this study the contact stiffness for the linear penalty model was set to $\varepsilon_{\mathrm{N}} = 50000\,\mathrm{N/mm^3}$.

Load case $\mathbf{f}_e$ For the first load case only the external force with $\vec{f}_e = \begin{bmatrix}0 & 0 & 100\,\mathrm{N}\end{bmatrix}^{\mathsf{T}}$ and no torsional torque was applied. The absolute value of the static deflection of the load application point $|z_L|$ and the Euclidean norm of the vector containing the normal gaps of all contact pairs $\|\mathbf{g}_N\|_2$ were considered as convergence criteria. Beside the absolute values of these criteria also a relative error defined as

$$e(g) = \frac{u(100) - u(g)}{u(100)} \tag{4.1}$$

is evaluated. In the previous definition $u(100)$ denotes the solution of either $u = |z_L|$ or $u = \|\mathbf{g}_N\|_2$ with $g = 100$ joint modes. The solution with $g = 100$ joint modes is considered as reference solution since all joint mode methods reach this solution with a variance below 1 %.

In fig. 4.2 the convergence criterion $|z_L|$ and in fig. 4.3 the convergence criterion $\|\mathbf{g}_N\|_2$ with respect to the number of joint modes are depicted.

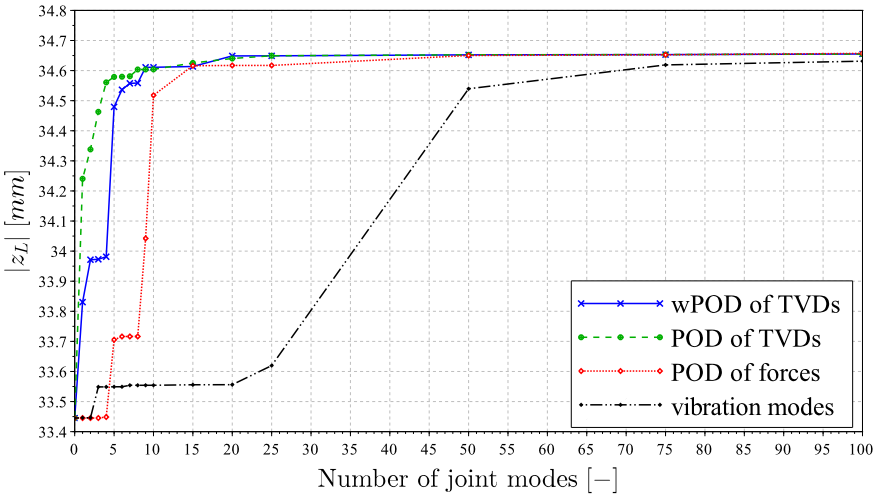

Figure 4.2: Static convergence of $|z_L|$ for load case force $\mathbf{f}_e$

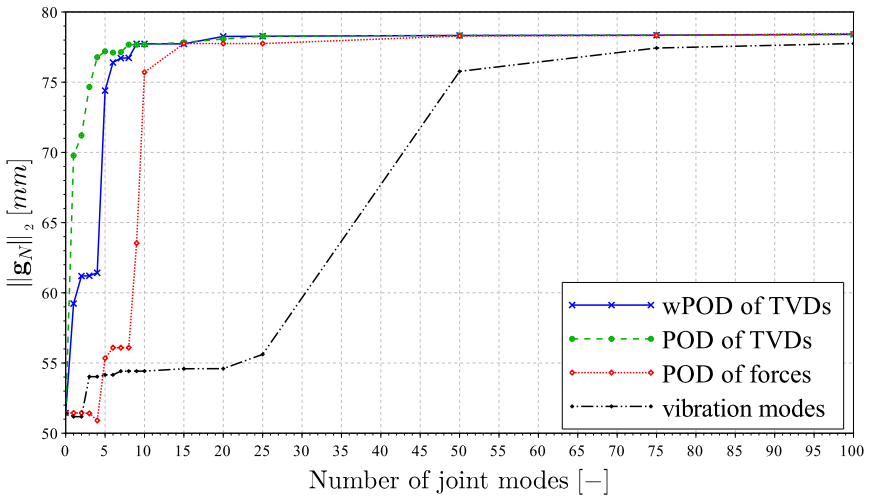

Figure 4.3: Static convergence of $\|\mathbf{g}_N\|_2$ for load case $\mathbf{f}_e$

For this load case both criteria show nearly the same convergence rate. Comparing the different joint mode methods, the method POD of TVDs shows the fastest convergence. Joint modes computed by wPOD of TVDs have also a faster convergence than the joint modes computed by POD of forces. On the contrary, the converged results cannot be achieved with 100 additional vibration modes. This fact confirms the importance of joint modes and shows that the vibration modes of the CMS reduction basis are not suitable for considering contact.

Load case M_x For the second load case an external torsional torque around the x-axis with $M_x = 20\,\text{Nm}$ was applied. For this load case the twist angle around the x-axis θ_x and the Euclidean norm of the vector containing the normal gaps of all contact pairs $\|\mathbf{g}_N\|_2$ were used as convergence criteria. The convergence rate of these criteria with respect to the number of additional trial vectors are depicted in fig. 4.4 and fig. 4.5.

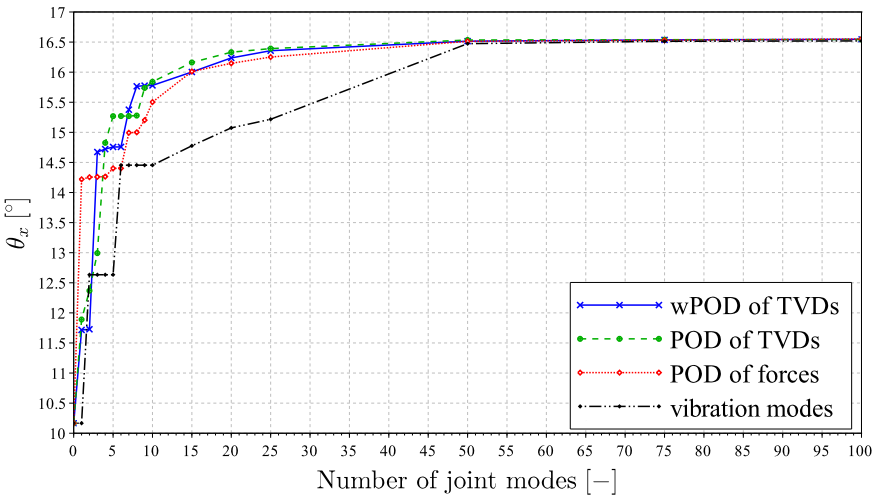

Figure 4.4: Static convergence of θ_x for load case M_x

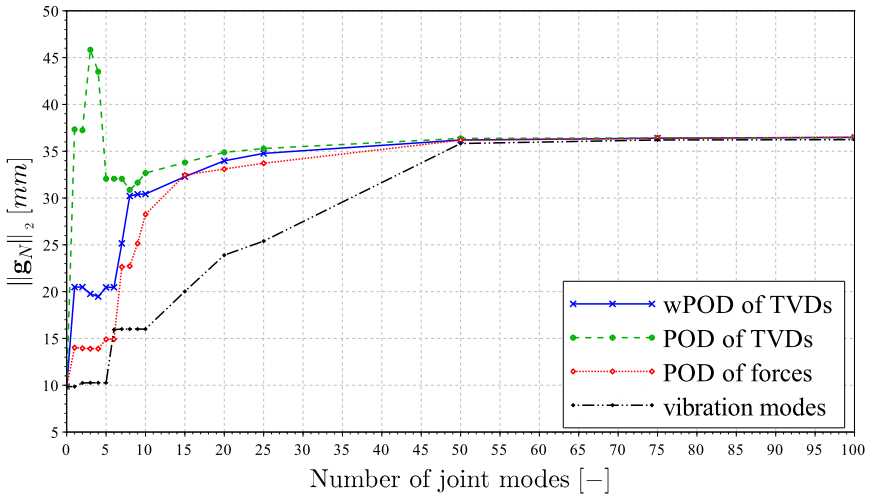

Figure 4.5: Static convergence of $\|\mathbf{g}_N\|_2$ for load case M_x

The evaluation of the twist angle θ_x (depicted in fig. 4.4) shows for all joint mode methods a very similar convergence rate. Again, in the case of additional vibration modes a much slower convergence can be seen. On the other hand, the convergence behavior of the criterion $\|\mathbf{g}_N\|_2$ is quite different for the three joint mode method (see fig. 4.5). Joint modes computed by wPOD of TVDs and POD of forces show a smooth convergence behavior. The method using unweighted POD of TVDs shows a rather unsteady convergence rate.

In general, for the torsional load case a slightly slower convergence rate can be noticed compared to the bending load case. One possible reason for this fact can be found in the original reduction basis which is the foundation for the computation of TVDs and fictive forces. In the original reduction basis nine trial vectors showing a bending deformation

(around the y-axis) are included, whereas only four trial vectors representing a torsional vibration (around the x-axis) can be found. The remaining three trial vectors do not show a clear deformation in any of these two directions. This fact consequently leads to a greater appearance of the bending direction in the joint modes.

Dynamic convergence study

In the dynamic convergence study it was investigated if the convergence criteria show the same convergence behavior for dynamic simulations. For this purpose the friction bar was excited with load case $\mathbf{f}_e$ considering a smoothed step load using a Haversine function. The final values of $\vec{f}_e = \begin{bmatrix} 0 & 0 & 50\,\mathrm{N} \end{bmatrix}^\mathsf{T}$ are thereby reached after 0.01 s. The motion of the friction bar was investigated for $T = 0.1\,\mathrm{s}$. For the linear penalty model the contact stiffness was set to $\varepsilon_\mathrm{N} = 50000\,\mathrm{N/mm^3}$. The parameters of the used Coulomb friction model were set to: friction coefficient $\mu = 0.15$, sticking stiffness $\varepsilon_\mathrm{T,st} = 10000\,\mathrm{N/mm^3}$, and sliding stiffness $\varepsilon_\mathrm{T,sl} = 500\,\mathrm{N/mm^3}$. For the dynamic convergence study only the three joint mode methods are compared. A comparison with additional vibration modes (black curves in the previous figures) is omitted due to the clear slower convergence in the static convergence study.

In fig. 4.6 the absolute value of the tip deflection is shown for the three joint mode methods. The figure shows, that not only the amplitude but also the frequency of the oscillation is different if no joint modes are considered.

In fig. 4.7 the dynamic evaluation of the error e for the criterion $|z_L|$ is depicted. In these figures the curves for $g = 0$ joint modes are omitted for better readability. As in the static convergence study the methods wPOD of TVDs (fig. 4.7a) and POD of TVDs (fig. 4.7b) show a very similar convergence rate . For these two methods the maximum error of the tip deflection is for $g = 5$ joint modes $e(5) \approx 5\%$, and with $g = 20$ joint modes $e(20) < 1\%$. The dynamic convergence for joint modes computed by POD of forces is shown in fig. 4.7c. These joint modes show clearly a slower convergence with an error $e(5) > 30\%$ using $g = 5$ joint modes. An error below $e(g) < 5\%$ can be first achieved by using at least $g = 50$ joint modes.

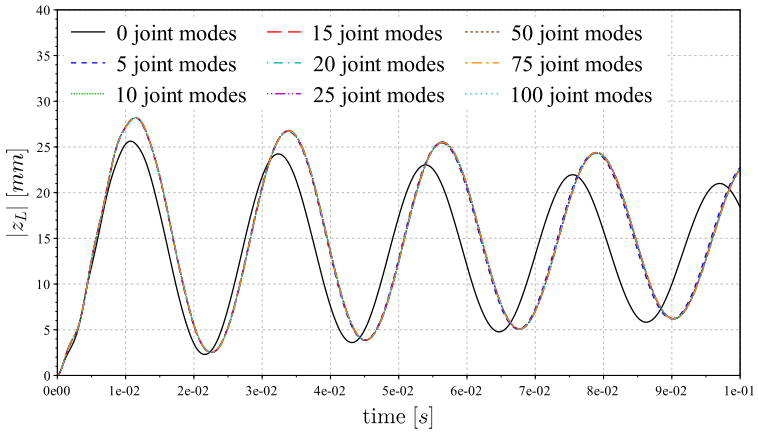

(a) wPOD of TVDs

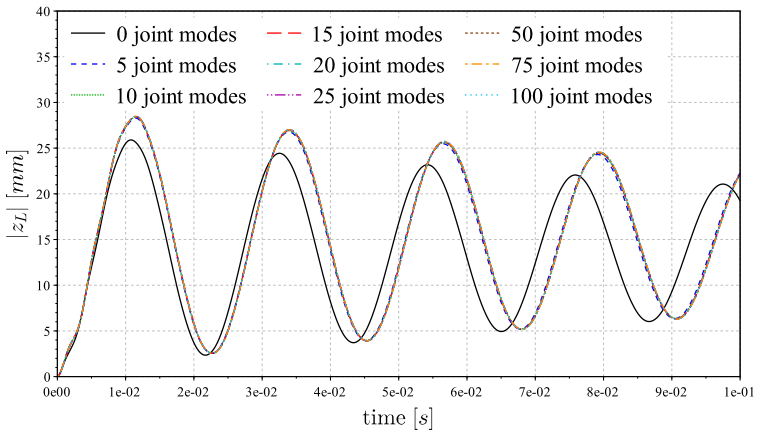

(b) POD of TVDs

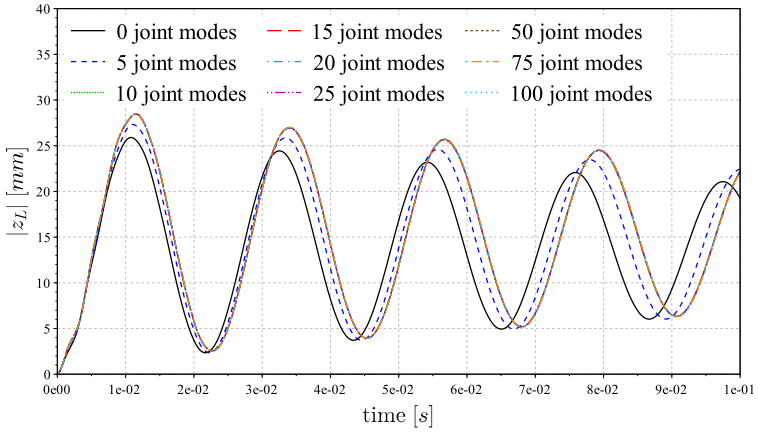

(c) POD of forces

Figure 4.6: Dynamic convergence of $|z_L|$

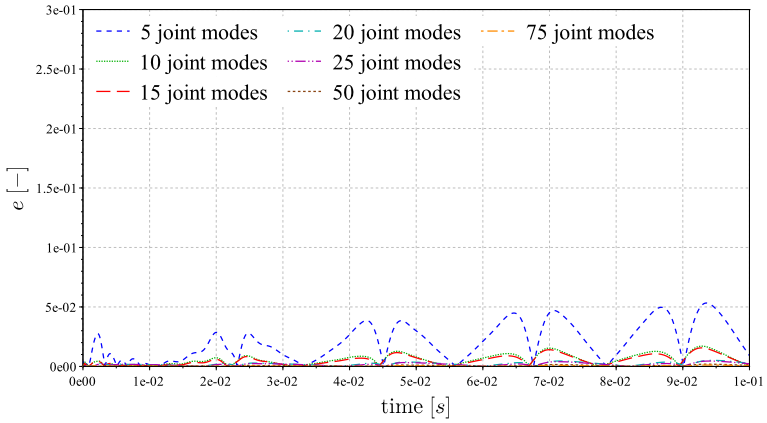

(a) wPOD of TVDs

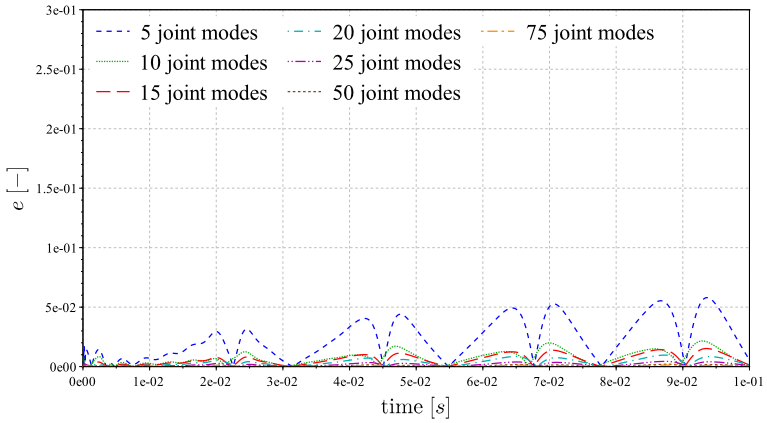

(b) POD of TVDs

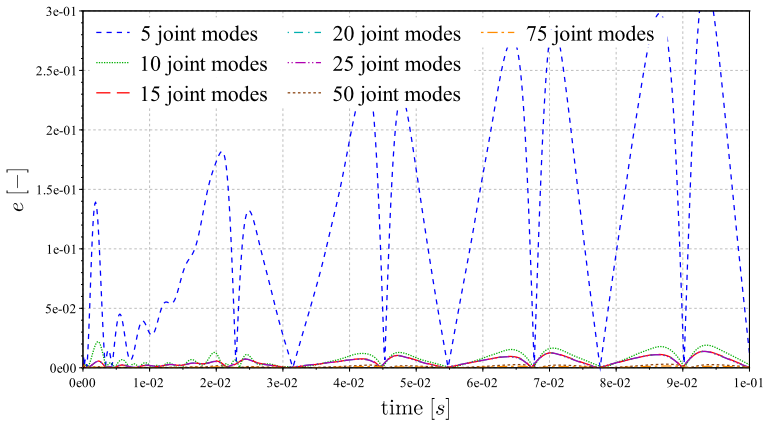

(c) POD of forces

Figure 4.7: Dynamic convergence of error of $|z_L|$, $e\left(|z_L|\right)$

For the second criterion $\|\mathbf{g}_N\|_2$ the corresponding error e is depicted for approximately two oscillations in fig. 4.8. Again the error for $g = 0$ joint modes is omitted.

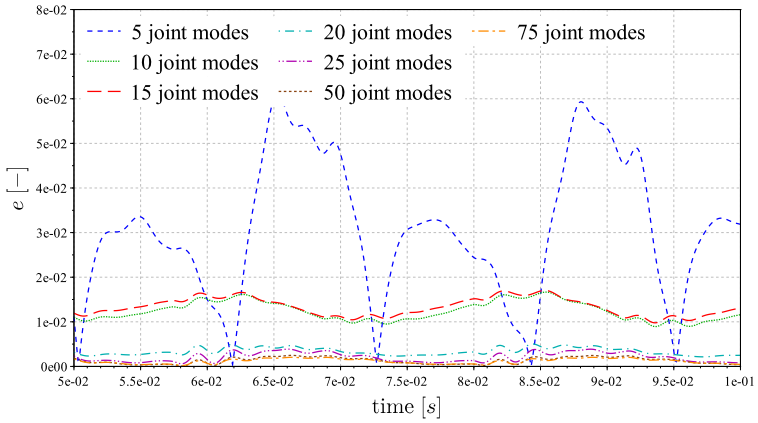

(a) wPOD of TVDs

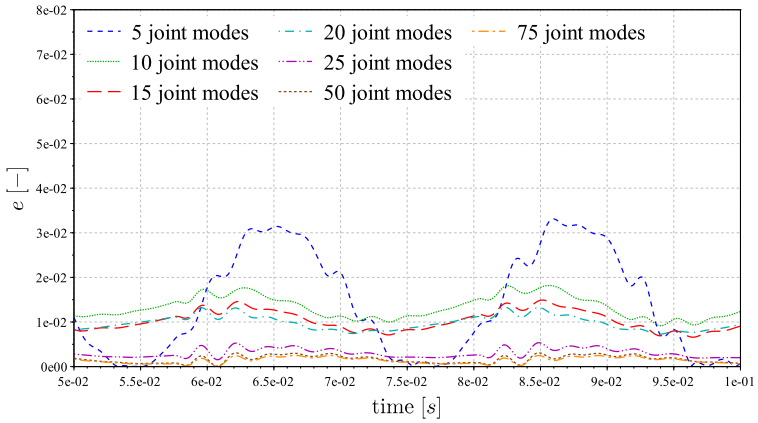

(b) POD of TVDs

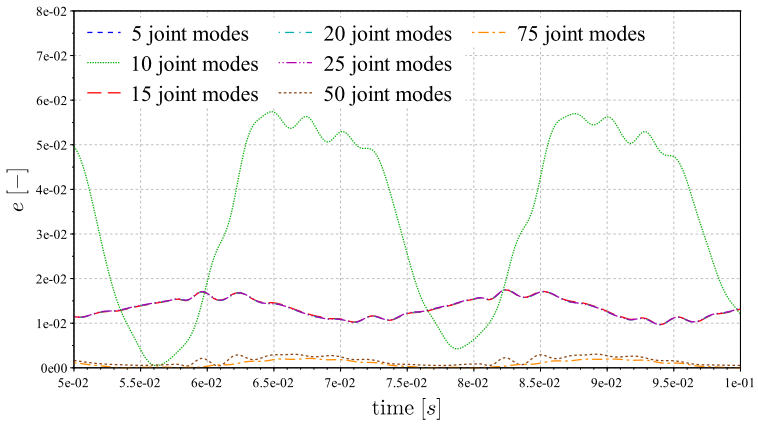

(c) POD of forces

Figure 4.8: Dynamic convergence of error of $\|\mathbf{g}_N\|_2$, $e\left(\|\mathbf{g}_N\|_2\right)$

Figure 4.8 confirms the faster convergence of joint modes based on wPOD of TVDs and POD of TVDs compared to joint modes based on POD of forces. This can be seen especially

in the error for $g = 5$ joint modes. The error is up to $e(5) = 30\%$ (out of the range of the chart) for joint modes based on POD of forces. On the other hand, for the methods wPOD of TVDs and POD of TVDs the error is in the range of $e(5) \approx 5\%$. An error $e(g) < 1\%$ can be achieved by wPOD of TVDs and POD of TVDs at $g = 20$ joint modes and for the method POD of forces at $g = 50$ joint modes.

In general, the dynamic convergence study confirms the results of the static investigations in section 4.1.1.

Estimation of required joint modes

In fig. 4.9a the ratio $w(g)$ defined by eq. (3.61) is depicted for the different joint mode methods. In section 3.2.2 it has been mentioned that this ratio can be used as an estimator for the number of required joint modes g. In order to approve this assumption, in fig. 4.9b the averaged error of the criteria $|z_L|$, $\|\mathbf{g}_N\|_2$ for all considered load cases in the static convergence study is depicted.

Comparing the two charts of fig. 4.9 shows, that the sequence of convergence coincides with the sequence of the ratio w for all methods. Joint modes computed by POD of TVDs show the fastest increase of the ratio and reach $w(g) > 98\%$ with already $g = 4$ joint modes. With $e(g = 4) \approx 8\%$ the error for this number of joint modes still relative high. Furthermore, the increase of the error at $g = 3$ joint modes is not in consensus with the ratio curve. The joint modes computed by wPOD of TVDs show a very smooth curves for the ratio and the convergence rate. A ratio of $w(g) \approx 98\%$ is reached with $g = 10$ joint modes which corresponds to an error of $e(g = 10) \approx 5\%$. The joint modes computed by POD of forces show the slowest increase in the ratio and a slow and unsteady convergence of the error. Hence, for the friction bar it can be stated that the convergence behavior seems to be only connected to the ratio for the joint modes computed by wPOD of TVDs.

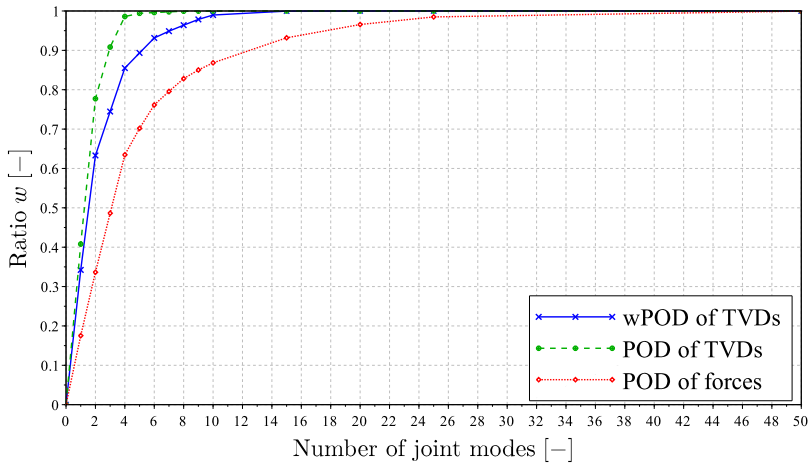

(a) Ratio w

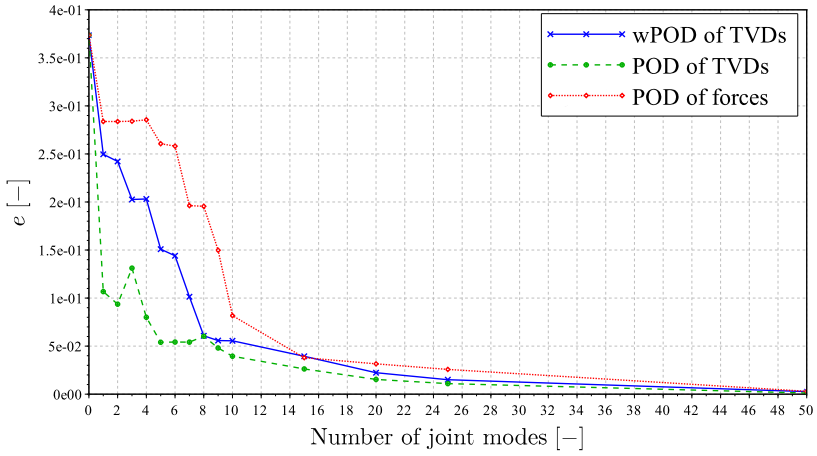

(b) Avaraged error e

Figure 4.9: Estimation of the number of required joint modes for the friction bar

4.1.2 Verification of preloaded joint modes

The preloaded friction bar is basically identical with the example used in previous section. Additionally to the original friction bar two preload areas at the outer two holes of the structure are considered. These preload areas (PL1, PL2) are marked with red color in fig. 4.10. The preload forces $\vec{f}_{\mathrm{PL1}} = \vec{f}_{\mathrm{PL2}} = \begin{bmatrix} 0 & 0 & \pm 6000\,\mathrm{N} \end{bmatrix}^{\mathsf{T}}$ were applied to one center node of the drilling which was coupled to the marked area around the hole with distributing coupling elements.

Based on the results of the previous section, the general joint modes based on wPOD of TVDs were used for a comparison and as reference.

The CMS reduction basis was computed with $v = 20$ vibration modes and $s = 16$ constraint

modes according to the mounting and force application points. This leaded to $m = 36$ trail vectors. The increase from $v = 10$ to $v = 20$ vibration modes compared to the previous section was chosen to demonstrate the benefit of the method using only PLM related derivatives. Optionally, one PLM $(p = 1)$ was included in the reduction basis. If all first order TVDs are used for the computation of the joint modes, $k = 2(m + p)^2 = 2738$ static load cases have to be computed. Alternatively, if only PLM related TVDs are used, only $k_{\mathrm{PL}} = 2(p^2 + 2pm) = 146$ static load cases have to be computed.

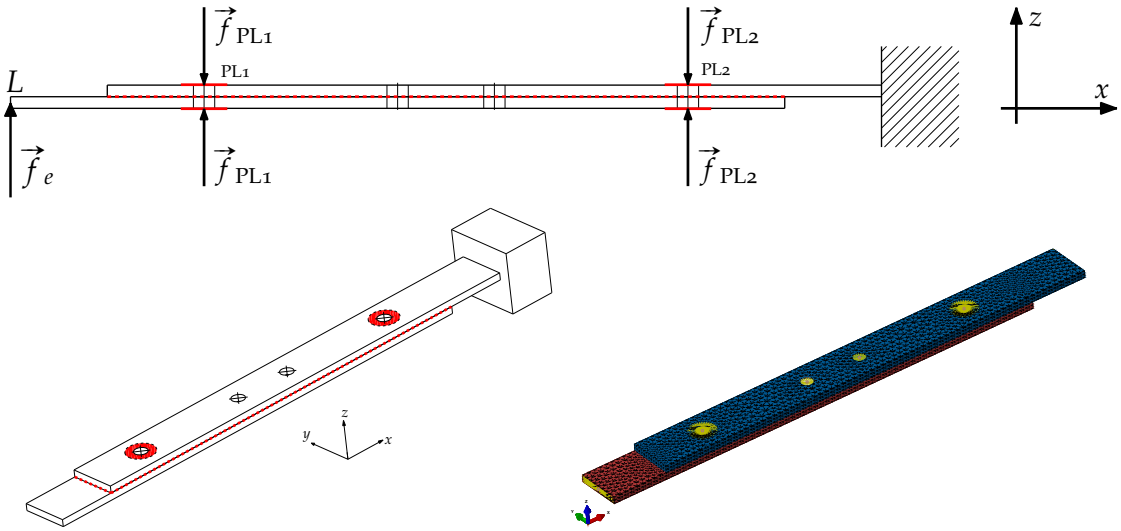

Figure 4.10: Schematic draft and FE model of the preloaded friction bar

Evaluation of the preload mode

In this first investigation, only the preload forces were applied in order to investigate the convergence in case a PLM is included in the reduction basis. The PLM corresponds to the deformation of the structure due to preload forces and full consideration of nonlinear contact. For the friction bar, one PLM is computed with the nonlinear FE solver *MSC.NASTRAN* [74]. This PLM is depicted in fig. 4.11 (with 2000 scaling).

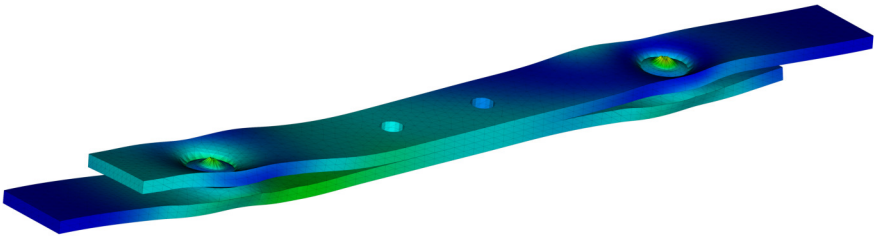

Figure 4.11: Deformation shape of preload mode for the friction bar

Figure 4.12 shows a comparison of the contact pressure distribution around one preload area

(PL1) for different reduction bases. For all computations the contact subroutine was enabled. The figure indicates that with the PLM, the contact pressure due to preload forces, can be computed nearly identically to the contact pressure achieved by a full nonlinear FE analysis (performed with *Abaqus* [26]). On the other hand, fig. 4.12a shows that without the PLM the contact situation cannot be reproduced by the CMS reduction basis. This demonstrates the importance of the PLM in case local effects around the preload area are of interest.

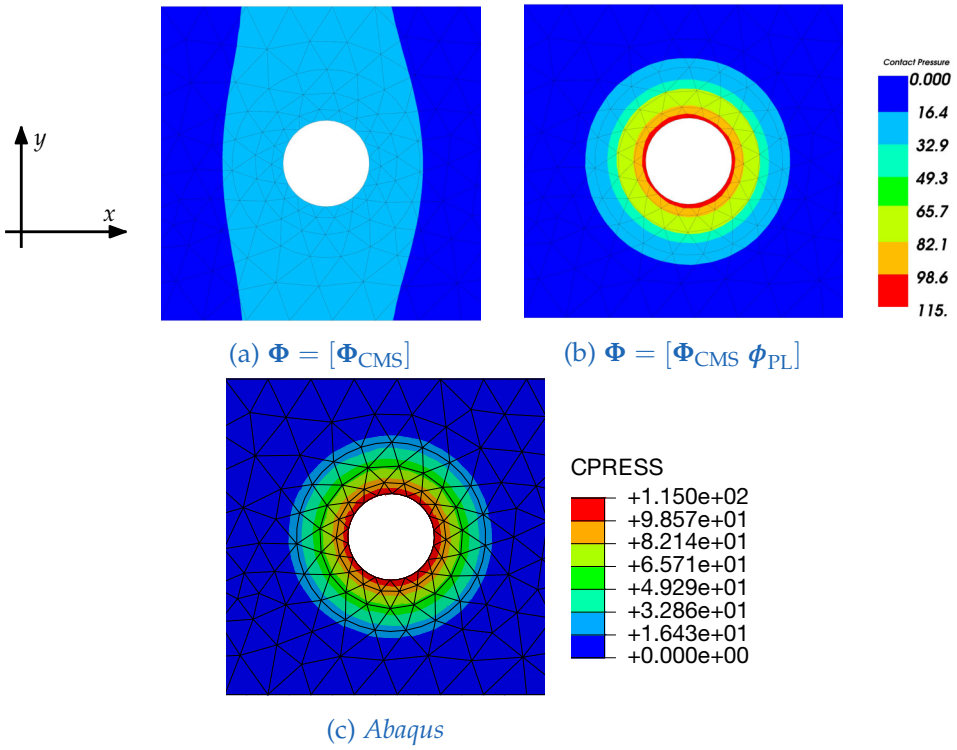

(a) $\mathbf{\Phi} = [\mathbf{\Phi}_{\mathrm{CMS}}]$ (b) $\mathbf{\Phi} = [\mathbf{\Phi}_{\mathrm{CMS}}\ \boldsymbol{\phi}_{\mathrm{PL}}]$

(c) *Abaqus*

Figure 4.12: Contact pressure p_N ($^{\mathrm{N}}/_{\mathrm{mm}^2}$) due to preload at PL1

Static convergence study

For this static analysis the friction bar was excited with $\vec{f}_e = \begin{bmatrix} 0 & 0 & \pm 100\,\mathrm{N} \end{bmatrix}^{\mathsf{T}}$ and the preload forces were applied. In order to validate the convergence of joint modes, the static deflection of the force application point z_L is analyzed for both bending directions.

The deflection z_L is depicted in fig. 4.13. The figure shows a faster and more straight convergence if only PLM related derivatives are used (for both bending directions). Using this method, a converged deflection can be achieved with $g = 25$ joint modes. Surprisingly, the convergence of joint modes based on all possible TVDs is nearly equivalent for considering or omitting the PLM. This indicates that for this structure the global deformation can be accurately considered without a PLM while the local effects (like contact pressure distribution)

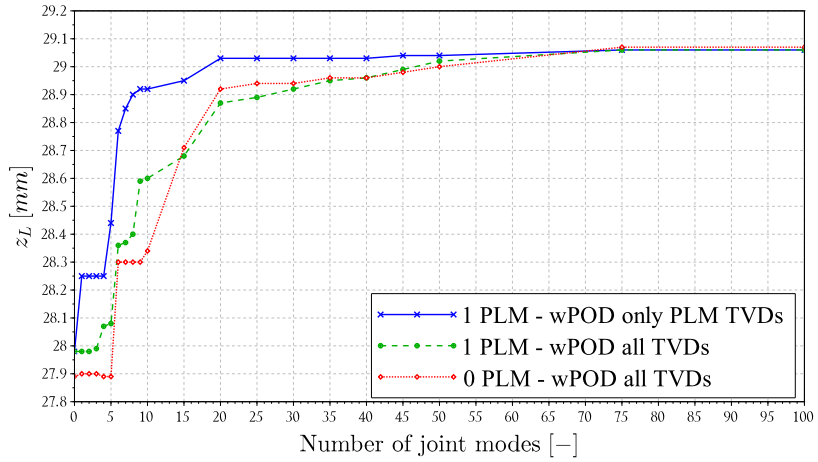

(a) Loadcase $\mathbf{f}_e^+$

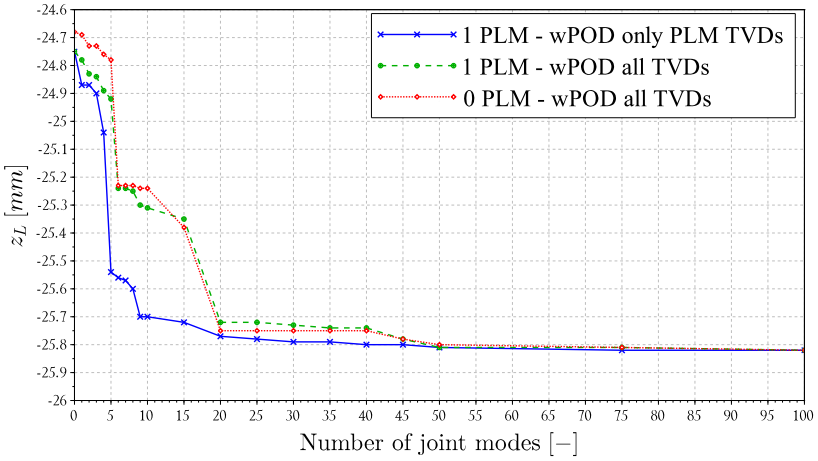

(b) Loadcase $\mathbf{f}_e^-$

Figure 4.13: Static convergence of z_L for preloaded friction bar

cannot. For the general joint modes (using all TVDs) at least $g = 50$ joint modes are required for a converged solution.

The contact pressure around the area of PL1 in the positive bending direction is shown in fig. 4.14. This figure shows that the local effects inside the preload area can be considered as good quality when using only $g = 25$ joint modes based on PLM derivatives (fig. 4.14a). The use of $p = 1$ PLM and $g = 25$ general joint modes based on all TVDs (fig. 4.14b) leads to a good detection of the contacting area but to some differences in the distribution of the contact pressure. If no PLM is included in the reduction basis $g = 25$ general joint modes (fig. 4.14c) are insufficient to represented the contact pressure with good quality compared to the full nonlinear FE analysis (fig. 4.14d).

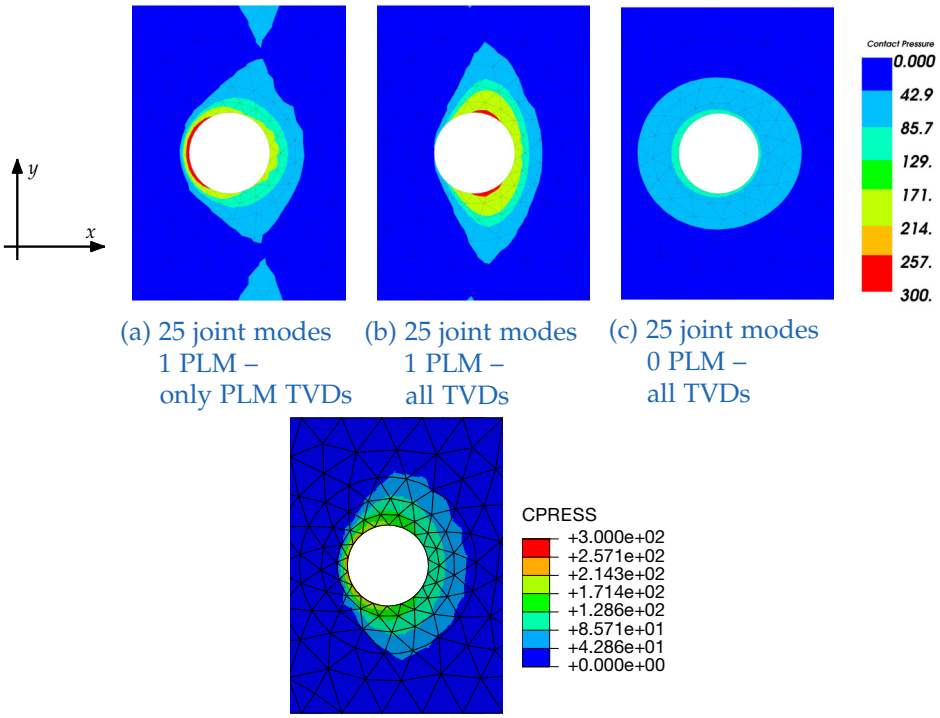

(a) 25 joint modes 1 PLM – only PLM TVDs

(b) 25 joint modes 1 PLM – all TVDs

(c) 25 joint modes 0 PLM – all TVDs

(d) *Abaqus*

Figure 4.14: Contact pressure p_N (N/mm^2) at PL1 due to $\mathbf{f}_e^+$

4.1.3 Study on the limitations of preloaded joint modes

Friction bar with only one preload area

On the preloaded friction bar it was investigated if joint modes based on PLM derivatives suitable for large-area joints with a very localized preload area. For this purpose, a slightly modified friction bar was investigated. Instead of considering two preload areas, only the preload force at PL1 was applied and the metal sheets are not connected at PL2. Hence, a structure with a ratio between preload area and overall joint area was constructed, which might be adverse for the use of joint modes based on PLM derivatives.

Again the static deflection z_L was considered as convergence criterion. For both bending directions, these deflections are plotted in fig. 4.15. Again the structure was excited with an external load of $\vec{f}_e = \begin{bmatrix} 0 & 0 & \pm 100\,\mathrm{N} \end{bmatrix}^\mathsf{T}$. The preload forces were set to $\vec{f}_{\mathrm{PL1}} = \begin{bmatrix} 0 & 0 & \pm 6000\,\mathrm{N} \end{bmatrix}^\mathsf{T}$ and $\vec{f}_{\mathrm{PL2}} = \begin{bmatrix} 0 & 0 & 0 \end{bmatrix}^\mathsf{T}$.

The convergence of joint modes based on all TVDs is with and without the PLM again very similar for the displacements. On the other hand, the convergence for joint modes based on PLM derivatives is slower for both bending directions. Moreover, the converged solution cannot be reached even with a high number of joint modes. This is partly caused by the adverse surface ratio mentioned previously. Moreover, the fact that the entire area around

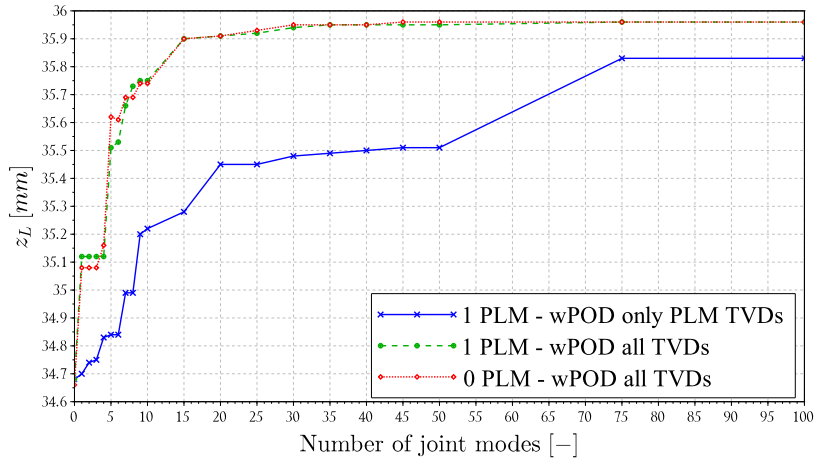

(a) Loadcase $\mathbf{f}_e^+$

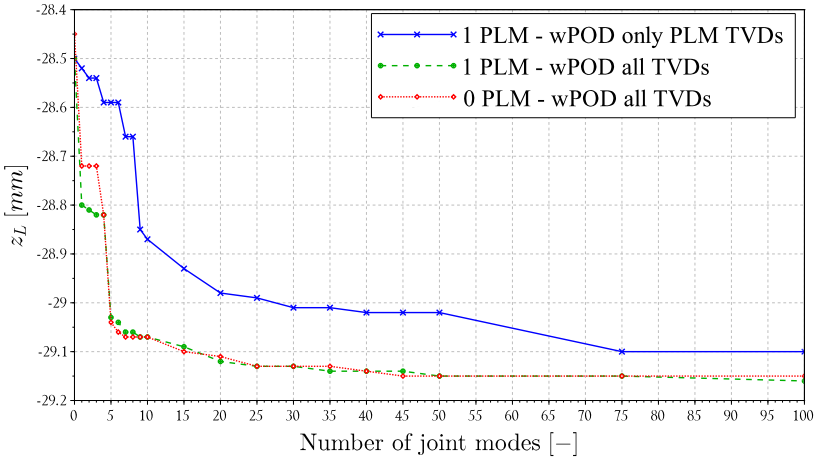

(b) Loadcase $\mathbf{f}_e^-$

Figure 4.15: Static convergence of z_L for friction bar with PL1 only

PL2 is unreachable for the PLM and the associated derivatives computed only with $\vec{f}_{\text{PL1}}$ might be the more important reason. This means that no flexibility is added around PL2 through the joint modes since this part of the structure is separated from PL1 with the two beams in the middle. Hence, this type of structure is not suitable for analysis with joint modes based on PLM derivatives only.

4.2 Bolted bearing cap of an engine connection rod

4.2.1 Verification of general joint modes

As a second example the bolted bearing cap of an engine connection rod from a single cylinder engine is considered. A schematic draft of the multibody system is depicted in fig. 4.16a. The model consists of a crankshaft, a piston and a flexible connection rod with a bolted bearing cap. The multibody system was excited with a prescribed rotation of the crankshaft. The parameters of the model are summarized in table 4.1. The FE model of the flexible connection rod is depicted in fig. 4.16b. The FE model consists of 11617 nodes and 51702 linear tetrahedron elements. In the contact region of the big end bearing $n_{\mathrm{CP}} = 631$ contact pairs were considered. The meshes at the contact area are not modeled with coincident nodes. The big and small end bearing holes of the connection rod were coupled with *MSC.NASTRAN* RBE3 constraint elements to the center nodes of the bearings. These RBE3 elements distribute the force, but allow deformation of the bearing hole. To apply the screw preload, the screw shaft was cut through, and the FE nodes at the intersection were coupled to one center node on which the screw preload forces $\vec{f}_{\mathrm{PL}}$ were applied (see fig. 4.16c). For the CMS reduction basis of the connection rod, $v = 20$ vibration modes and $s = 16$ constraint modes (4 due to preload nodes, 12 due to bearing middle nodes) were considered.

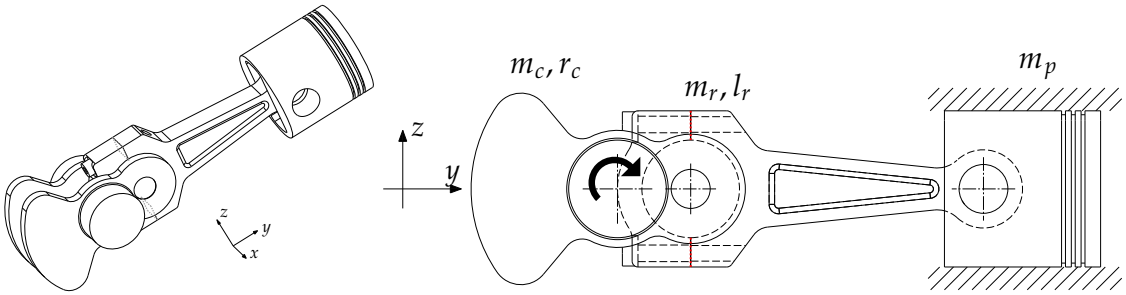

(a) Schematic draft of single cylinder MBS model

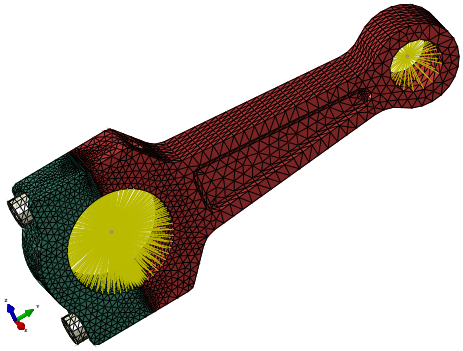

(b) FE model of the connection rod

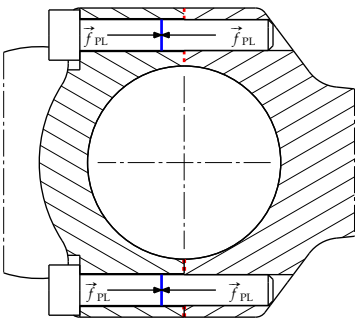

(c) Screw preload modeling

Figure 4.16: Single cylinder with flexible bolted connection rod

Table 4.1: Parameters of the MBS single cylinder engine model

crank shaft mass	$m_c = 2.07\,\mathrm{kg}$	connection rod mas	$m_r = 1.03\,\mathrm{kg}$
crank length	$r_c = 37.5\,\mathrm{mm}$	connection rod length	$l_r = 150\,\mathrm{mm}$
piston mass	$m_p = 0.71\,\mathrm{kg}$	preload force	$\vec{f}_{\mathrm{PL}} = \begin{bmatrix} 0 & \pm 16500 & 0 \end{bmatrix}^{\mathrm{T}}\mathrm{N}$

The contact stiffness was set to $\varepsilon_{\mathrm{N}} = 50000\,\mathrm{N/mm^3}$ and for dynamic simulations the friction parameters were set to: friction coefficient $\mu = 0.2$, sticking stiffness $\varepsilon_{\mathrm{T,st}} = 10000\,\mathrm{N/mm^3}$, and sliding stiffness $\varepsilon_{\mathrm{T,sl}} = 500\,\mathrm{N/mm^3}$.

The example of the bolted bearing cap was inspired by an practical application. It has to be mentioned that the used modeling approach is only valid to demonstrate and verify the presented joint modes. This is because no gas forces are considered and furthermore the force transmission in the bearing cap is not modeled realistic with the used RBE3 elements. A realistic distribution of the forces could be achieved with the modeling of an elastohydrodynamic contact. Nevertheless the principal behavior inside the considered joint is basically the same whereas the absolute physical values are not realistic.

Static convergence study

For the static convergence study the connection rod was statically loaded with the screw preload force $\vec{f}_{\mathrm{PL}}$. The Euclidean norm of the gap vector $\|\mathbf{g}_N\|_2$ was considered as convergence criterion. Additionally, the normal stresses (S_{yy}) inside the joint area were evaluated. The stresses were analyzed using modal stresses and modal coordinates (see [109]).

In fig. 4.17 the absolute value of $\|\mathbf{g}_N\|_2$ and the error e defined by eq. (4.1) are depicted.

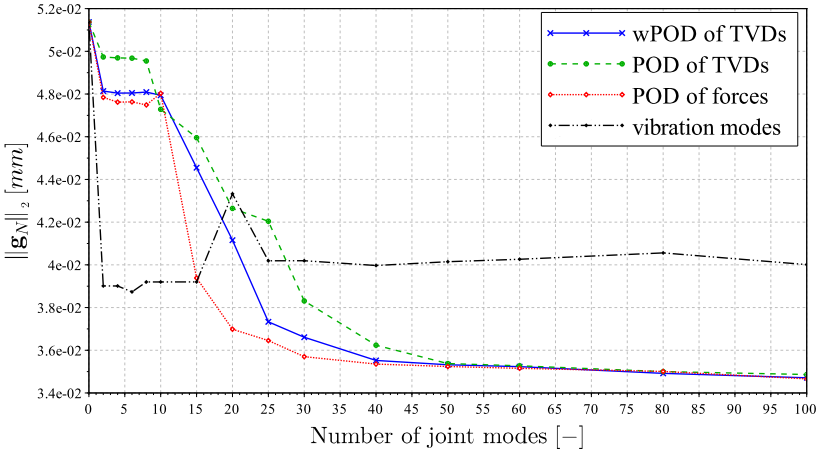

(a) Absolute value

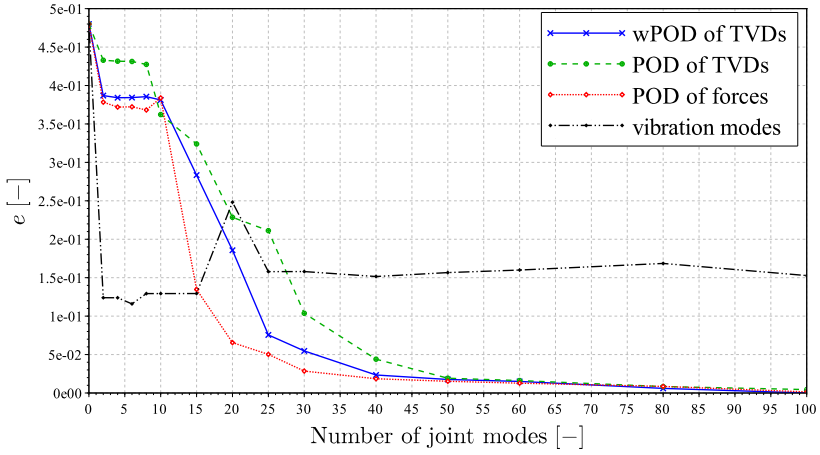

(b) Error e

Figure 4.17: Static convergence of $\|\mathbf{g}_N\|_2$ due to screw preload

Figure 4.17 indicates that using additional vibration modes (of the CMS reduction basis) does not lead to the converged solution for this example. On the other hand, all joint mode methods converge to the same value at $g > 50$ joint modes. Joint modes computed by POD of forces show the fastest convergence. This method reaches an error of $e \approx 5\%$ with $g = 25$ joint modes. Joint modes computed by wPOD of TVDs reach an error of $e \approx 5\%$ with $g = 30$ and show thereby an intermediate convergence rate. The slowest convergence is achieved by joint modes computed by POD of TVDs. For this method $g = 40$ joint modes are required to reach an error of $e \approx 5\%$.

The normal stresses (S_{yy}) inside the joint are depicted in fig. 4.18. In this figure each row corresponds to one extension strategy, while each column represents the results for a specific number of additional trial vectors. The illustrations in the right column are the stresses computed with a full nonlinear FE analysis using the commercial software *Abaqus* [26].

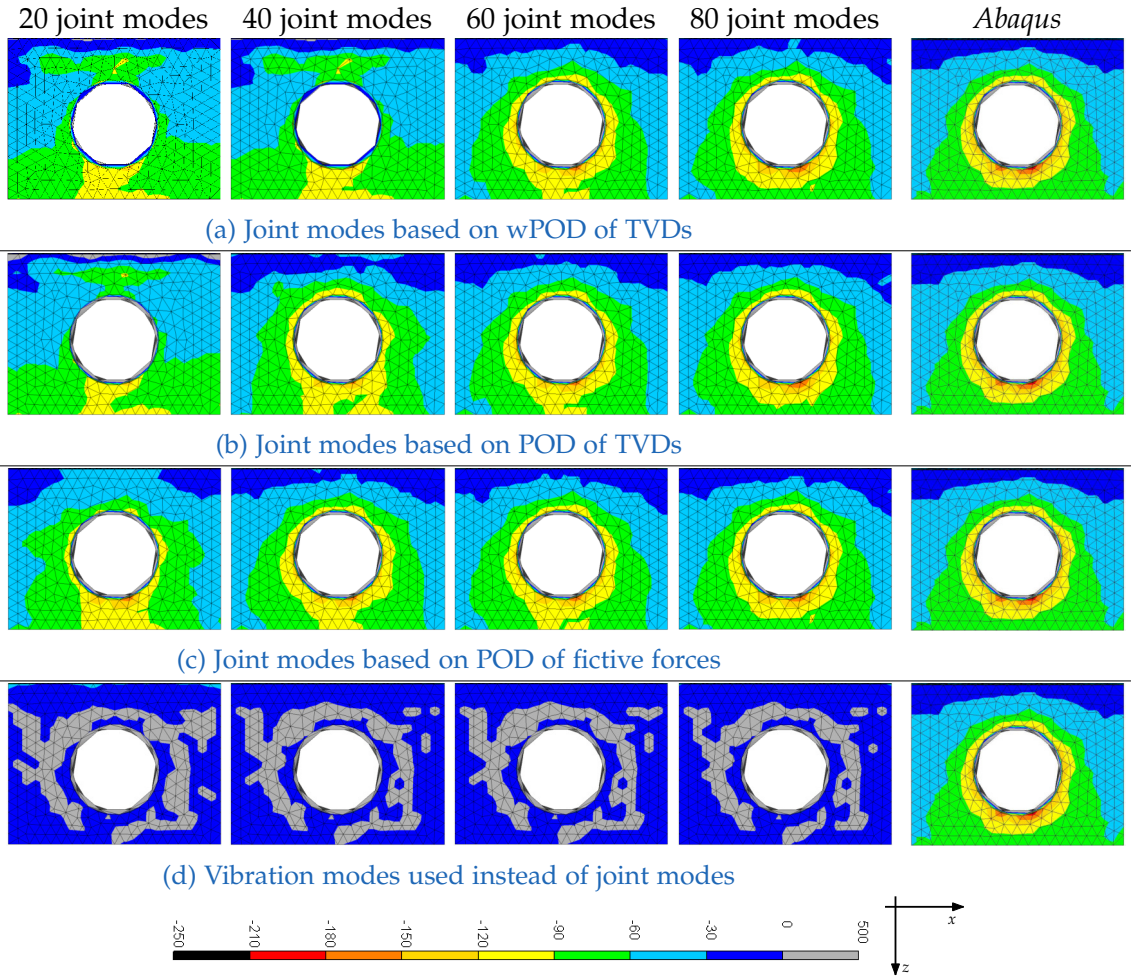

(a) Joint modes based on wPOD of TVDs

(b) Joint modes based on POD of TVDs

(c) Joint modes based on POD of fictive forces

(d) Vibration modes used instead of joint modes

Figure 4.18: Static convergence of normal stress S_{yy} (N/mm^2) in the joint area

The analysis of the stresses confirms the convergence behavior derived from the evaluation of $\|\mathbf{g}_N\|_2$. All joint mode methods show with $g = 60$ respectively $g = 80$ joint modes results which are very similar to the stress distribution computed with a full nonlinear FE analysis. Furthermore, fig. 4.18 confirms that the use of additional vibration modes (see fig. 4.18d) does not lead to a converged solution. In case of additional vibration modes the stress distribution is completely inappropriate for further analyses, like a fatigue computation.

From fig. 4.17b, for each joint mode method a specific number of joint modes can be identified which is required to reach an error of $e \approx 5\%$. In fig. 4.19 the normal stresses for the according number of joint modes are depicted. The legend and color-bar for the stresses is the same as in fig. 4.18. Figure 4.19 shows, that all methods deliver comparable results in terms of stresses at the same level of the error. This fact confirms that the Euclidean norm of the gap vector $\|\mathbf{g}_N\|_2$ and the thereof derived error are a robust convergence criteria.

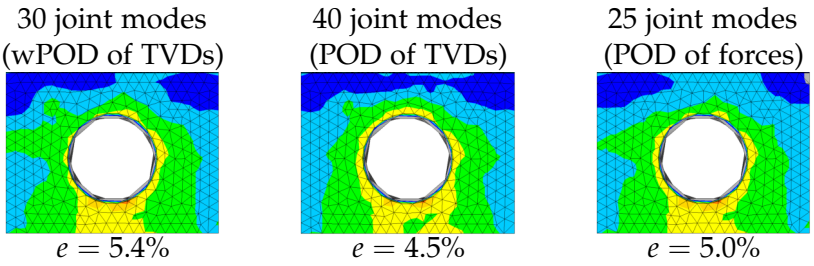

Figure 4.19: Normal stress (S_{yy}) for different joint mode methods at 5% error of $\|\mathbf{g}_N\|_2$

Dynamic convergence study

The convergence of the different joint mode methods was investigated on the rotating single cylinder engine without gas forces. For this purpose, the crankshaft was actuated by a prescribed motion and the system was simulated for $T = 0.3\,\mathrm{s}$. The motion was prescribed with a smoothed step using a Haversine function where the rotational end speed of $n_c = 10000\,\mathrm{min}^{-1}$ was reached after 0.25 s.

The Euclidean norm of the vector containing the normal gaps of all contact pairs $\|\mathbf{g}_N\|_2$ was used as convergence criterion. The corresponding errors e for the different joint mode methods are depicted in figs. 4.20 to 4.22. The absolute values of $\|\mathbf{g}_N\|_2$ are depicted in appendix F.1, figs. F.1 to F.3

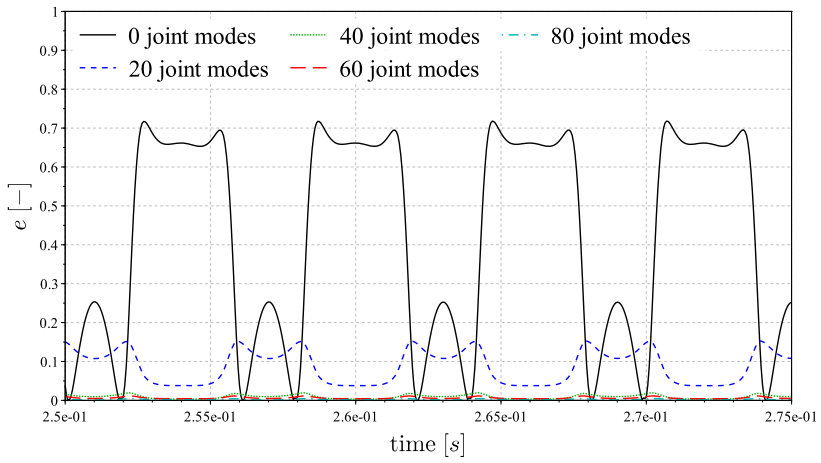

Figure 4.20: Dynamic convergence of $e(\|\mathbf{g}_N\|_2)$ for joint modes based on wPOD of TVDs

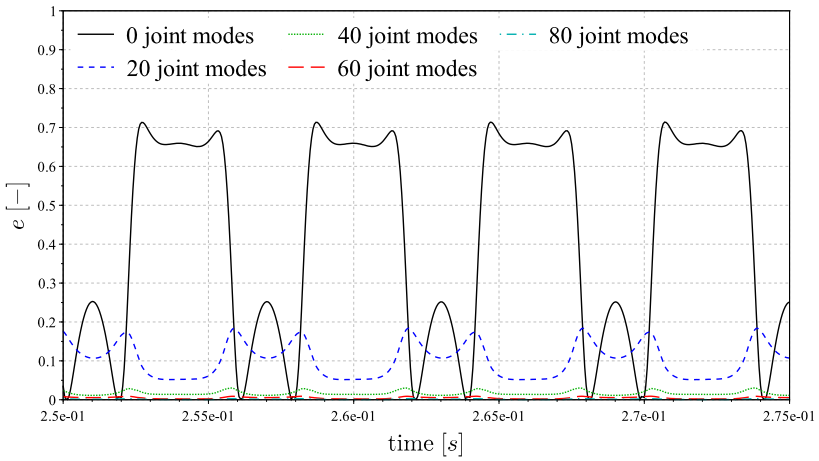

Figure 4.21: Dynamic convergence of $e(\|\mathbf{g}_N\|_2)$ for joint modes based on POD of TVDs

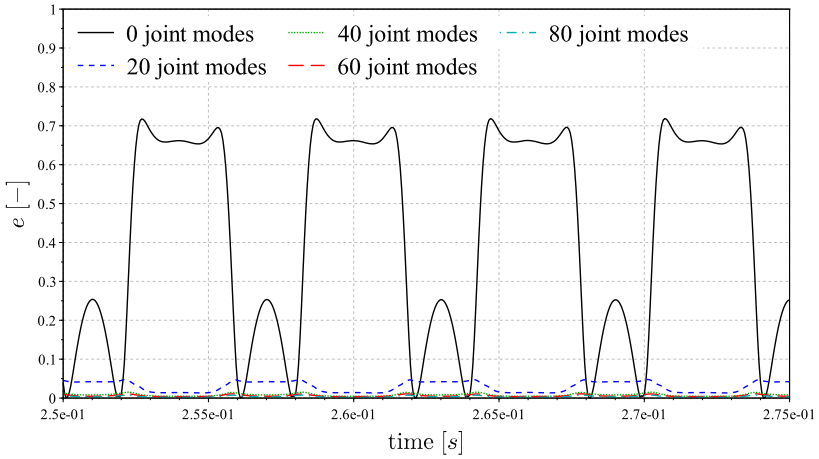

Figure 4.22: Dynamic convergence of $e(\|\mathbf{g}_N\|_2)$ for joint modes based on POD of forces

In terms of convergence order the same results as obtained from the static convergence analysis are achieved. The joint modes computed by POD of forces show the fastest convergence with an error $e < 5\%$ at $g = 20$ joint modes. The methods using wPOD of TVDs and POD of TVDs show both at $g = 20$ an error of $e \approx 20\%$ and reach an error $e < 5\%$ first at $g = 40$ additional joint modes.

For the sake of completeness the contact pressure over one operation cycle is depicted in fig. 4.23. For this figure a converged solution considering $g = 40$ joint modes computed by wPOD of TVDs was used. The first sub-figure ($t = 0.2570\,\mathrm{s}$) corresponds to the top dead center of the single cylinder engine. In the different distribution of the contact pressure the dynamic loading of the joint area due to inertia forces and due to the bending of the flexible connection rod can bee seen.

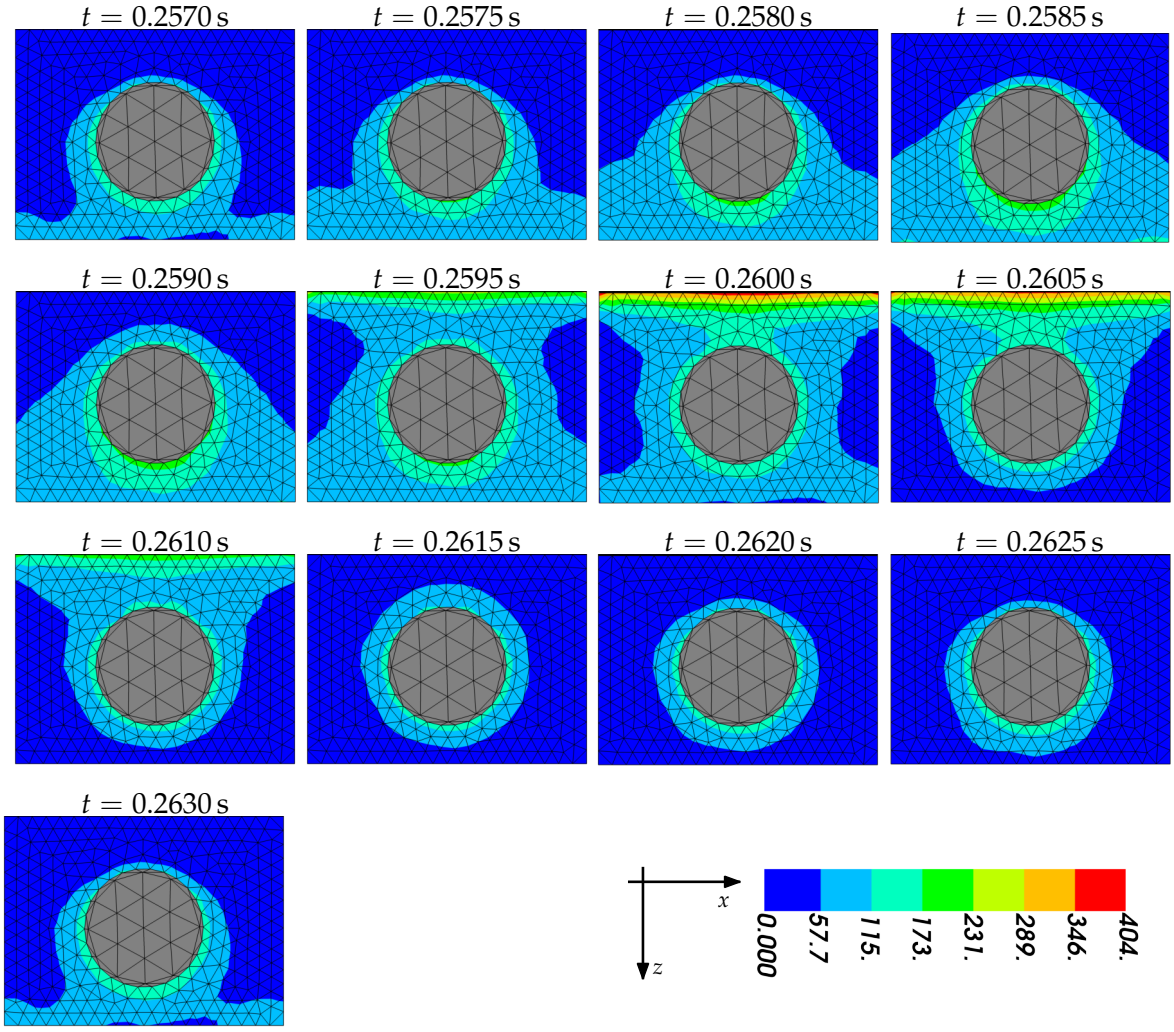

Figure 4.23: Contact pressure p_N (N/mm^2) in the joint area at different time steps

Estimation of required joint modes

The ratio $w(g)$ for the three different joint mode methods is depicted in fig. 4.24. The method POD of TVDs shows the fastest increase in the ratio, whereas the ratio for the joint modes using POD of forces shows the slowest increase.

The number of required joint modes g to reach an error of $e \approx 5\%$ for the different joint mode methods are listed in table 4.2. Additionally the corresponding ratios $w(g)$ are given. From this table it can be seen, that for joint modes computed by POD of TVDs $g = 40$ joint modes are required to reach an error of $e = 4.5\%$ whereby the ratio is $w(40) \approx 100\%$. For the joint modes computed with wPOD of TVDs an error of $e = 5.4\%$ corresponds to $g = 30$ joint modes which leads to a ratio of $w(30) = 99.897\%$. Joint modes based on POD of forces only require $g = 25$ joint modes which implies a ratio of $w(25) = 98.504\%$ for an error of $e = 5.0\%$.

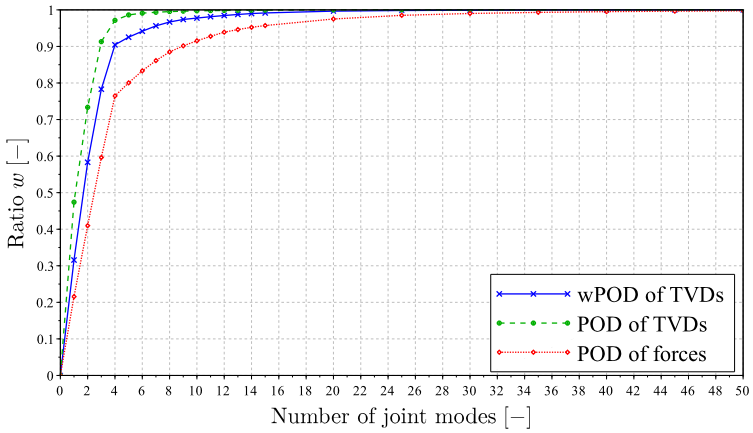

Figure 4.24: Estimation of the number of required joint modes for the connection rod

Table 4.2: Comparison of ration w and error e

method	g	ratio w	error e
wPOD of TVDs	30	99.897%	5.4%
POD of TVDs	40	99.999%	4.5%
POD of forces	25	98.504%	5.0%

For the connection rod, the order of the ratios does not coincide with the convergence order obtained by the static convergence study (see fig. 4.17). While joint modes computed based on POD of forces show the fastest convergence, this method shows the slowest increase in the ratio. Furthermore, table 4.2 indicates that the values of the ratio for a converged solution are at high level nearly to 100%.

4.2.2 Verification of preloaded joint modes

Additionally, the bolted connection rod bearing cap is used to evaluate the preloaded joint modes. For these investigations the reduction basis including the PLM were compared to the reduction basis without the PLM. Furthermore, the convergence of joint modes computed with PLM related TVDs was compared to the convergence of joint modes computed with all TVDs. The considered multibody system of a single cylinder engine is identical to the system described in the previous section and depicted in fig. 4.16a.

Static convergence study

For the preloaded joint modes the static convergence study concerning the number of joint modes was performed considering the normal stress distribution S_{yy} in the joint area. For this study, only the preload forces acted on the connection rod. In fig. 4.25 the distribution of the normal stress on one side of the bearing cap for different computation methods and different

numbers of joint modes is depicted. Like in the previous section, the stresses were analyzed using modal stresses and modal coordinates (see [109]). The normal stresses computed with full nonlinear analysis performed with *Abaqus* [26] are also shown as reference solution.

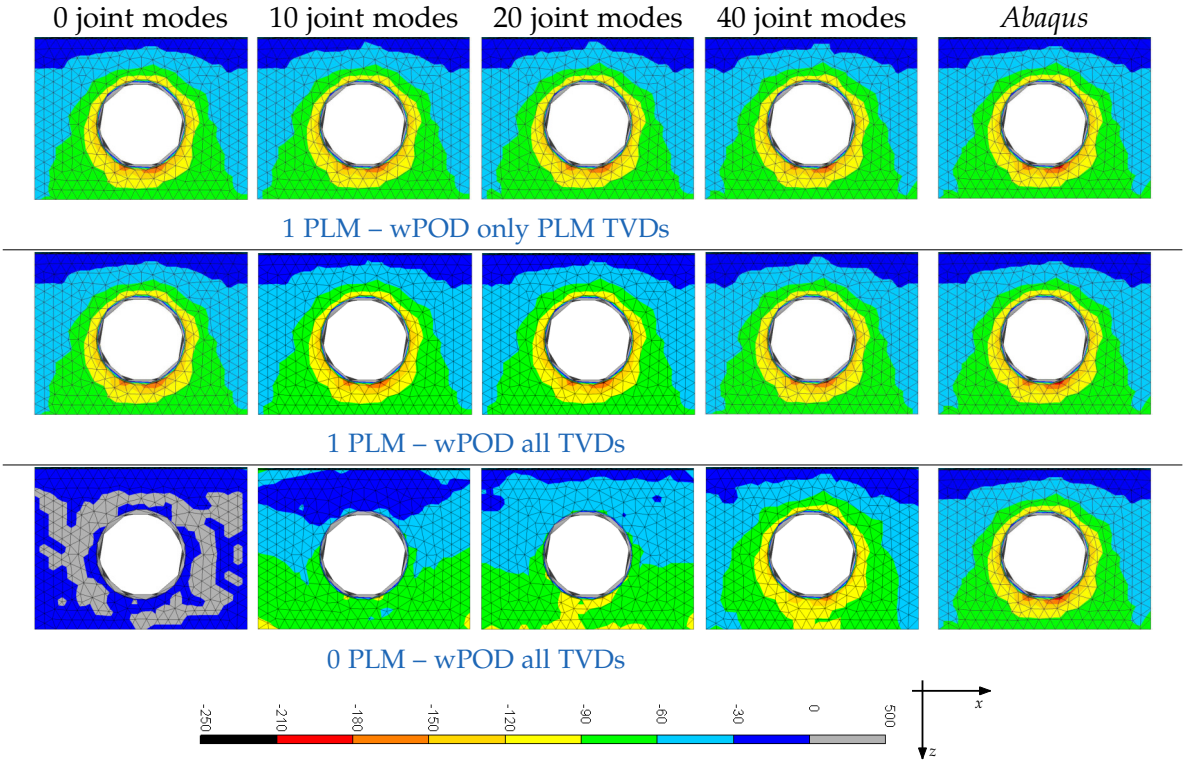

Figure 4.25: Static convergence of normal stress (S_{yy} N/mm^2) in the joint area

For both reduction bases which include a PLM, it can be seen that the results with $g = 0$ joint modes are already identical to the reference solution. Hence, no conclusion about the convergence behavior of the methods considering only PLM derivatives and all TVDs can be drawn from this analysis. If no PLM is used, at least $g = 40$ joint modes are required to reach a stress distribution which is similar to the reference solution.

Dynamic convergence study

Additionally to the static convergence study, the dynamic convergence of preloaded joint modes was investigated. As convergence criterion $\|\mathbf{g}_N\|_2$ was considered. In figs. 4.26 to 4.28, the error curves for the three compared extension strategies are shown. The curves of the absolute values are depicted in appendix F.1, figs. F.4 to F.6.

The figure shows that even under high dynamical loads, the use of the PLM leads to substantially better convergence. Alike the static analysis, without the PLM at least $g = 40$ joint modes are required to reach a converged solution. In case the PLM is considered, the methods considering only PLM derivatives or all TVDs lead to the same convergence. For

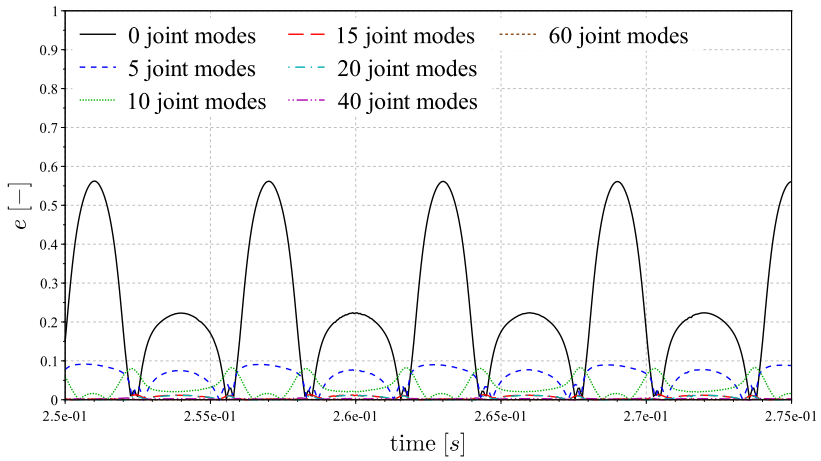

Figure 4.26: Dynamic convergence of $e(\|\mathbf{g}_N\|_2)$: 1 PLM – wPOD only PLM TVDs

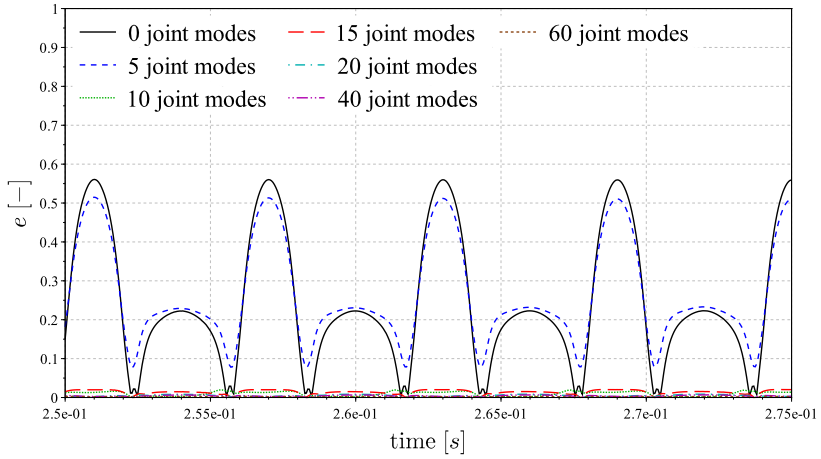

Figure 4.27: Dynamic convergence of $e(\|\mathbf{g}_N\|_2)$: 1 PLM – wPOD all TVDs

both methods the solution shows a high level of accuracy at $g = 15$ joint modes, since the error stays below $e < 4\,\%$. Without the PLM this $e < 4\,\%$ limit is reached at $g = 40$ joint modes.

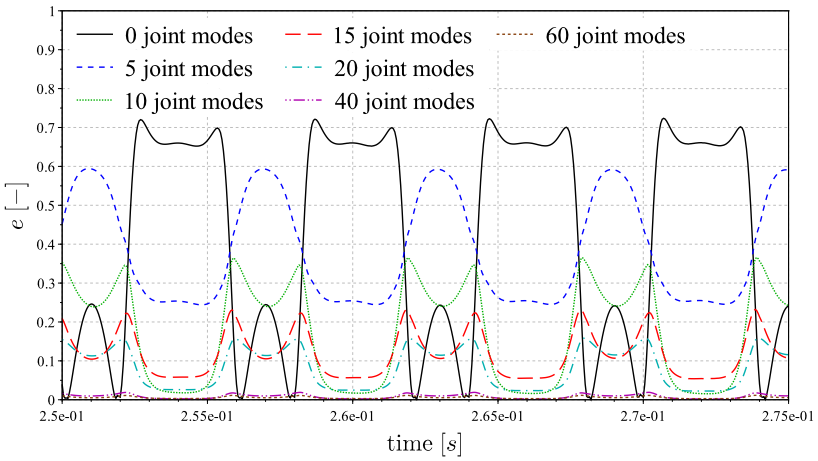

Figure 4.28: Dynamic convergence of $e(\|\mathbf{g}_N\|_2)$: 0 PLM – wPOD all TVDs

4.2.3 Study on the limitations of preloaded joint modes

Connection rod excited at different dynamic levels

For the following investigation the single cylinder engine (see fig. 4.16) was investigated at a fast $n_c = 10000\,\mathrm{min}^{-1}$ and slow $n_c = 1000\,\mathrm{min}^{-1}$ rotational speed. At a slow rotational speed ($n_c = 1000\,\mathrm{min}^{-1}$) it was expected that the deformation state remains close to the preload state. Hence, the reduction basis including the PLM and joint modes computed with PLM related TVDs should lead to a good convergence rate. At a high rotational speed (including high inertia forces) the deformations might be different to the preload state, and hence the convergence of joint modes computed with PLM related TVDs might be slower. The aim was to determine how the level of system dynamics influences the convergence rate of the different extension strategies. For this study the maximum value of the error $e\left(\|\mathbf{g}_N\|_2\right)$ reached during dynamic the simulations was considered.

In fig. 4.29a the convergence of this error is shown for low rotational speed. As in the previous investigations, the excellent convergence of the methods using the PLM can be seen since the system remains confined to the preload state. The maximum error with the PLM is $e \approx 1\,\%$ which is fifty times lower than without the PLM. On the other hand, the convergence at high rotational speed (depicted in fig. 4.29b) looks quite different. As expected, the error is at high dynamics with the PLM in the same range as the error without the PLM. Nevertheless, the convergence rate in terms of additional joint modes is still better, if a PLM is used.

This investigation reveals that the convergence rate of the methods considering a PLM is strongly dependent on the dynamics of the system. At high dynamics the deformations are no longer dominated by the preload state. On the other hand, the convergence of the joint modes without a PLM seems to be nearly independent on the dynamic level.

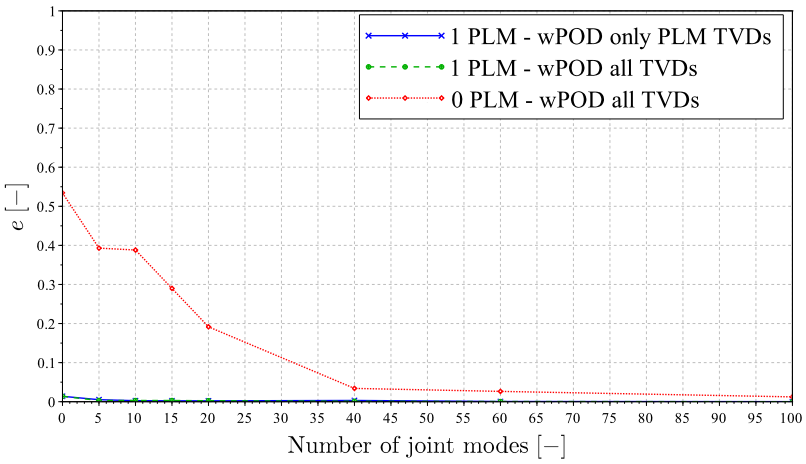

(a) $n_c = 1000\,\mathrm{min}^{-1}$

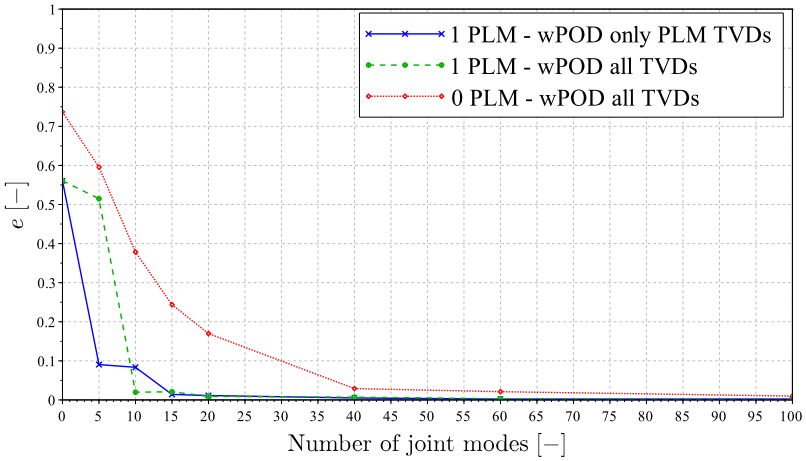

(b) $n_c = 10000\,\mathrm{min}^{-1}$

Figure 4.29: Convergence of $e\left(\|\mathbf{g}_N\|_2\right)$ at different dynamic levels

Connection rod with different contact parameters

For the FE computation of the PLM, a contact formulation and contact parameters have to be specified. In the following investigations it was examined whether the computed PLM is able to deliver accurate results if the parameters of the contact model in the dynamic simulation differ from the parameters used for the PLM computation.

The original PLM was computed with a linear penalty contact model with a contact stiffness of $\varepsilon_\mathrm{N} = 50000\,\mathrm{N/mm^3}$. As shown in previous section in fig. 4.25, the PLM delivers accurate results, if the same contact parameters were used in the MBS. In the following computations the contact stiffness was reduced to $\varepsilon_\mathrm{N} = 10000\,\mathrm{N/mm^3}$. The resulting distribution of the normal stress in the joint area is visualized in fig. 4.30.

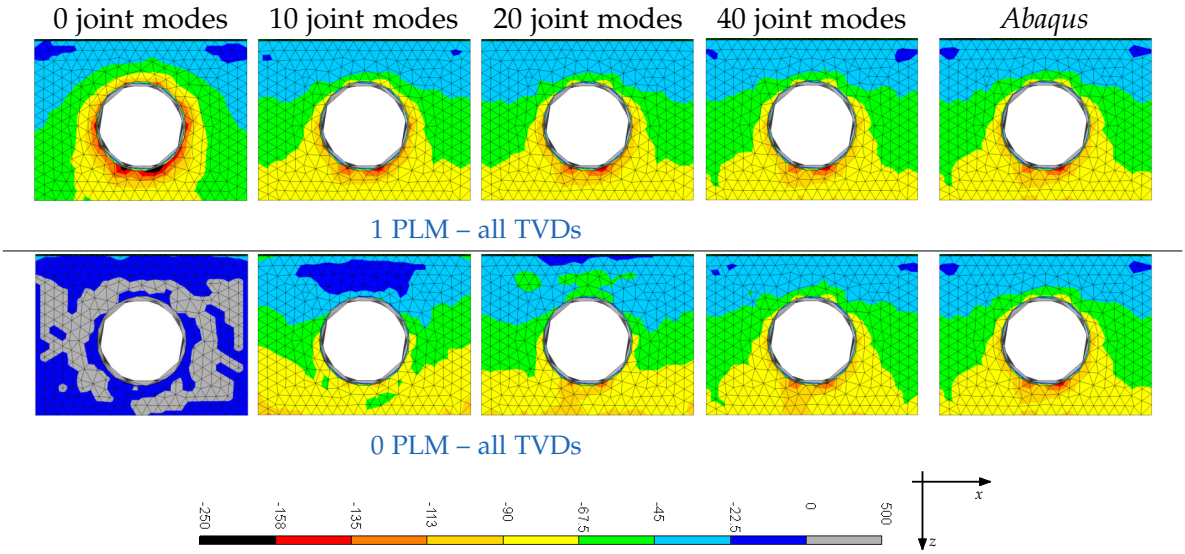

Figure 4.30: Convergence of normal stress S_{yy} (N/mm^2) in the joint area with modified contact parameters

Figure 4.30 shows, that with modified contact parameters the PLM is not able to produce completely accurate results. Nevertheless the overall stress distribution can still be captured. With $g = 10$ joint modes, the results can already be considered as a converged solution. As in the previous investigations, without the PLM at least $g = 40$ joint modes are required to reach accurate results. In general, the change of the contact stiffness leads to a slight change in the amplitudes of the stresses, but the stress distribution is very similar to the original.

4.3 Conclusion on general joint modes and preloaded joint modes

4.3.1 General joint modes

The two numerical examples confirm that all presented joint modes show an excellent convergence behavior with respect to all defined criteria. The investigations indicate that a static convergence study, with proper loading, is for the considered type of structures sufficient to determine the number of required joint modes for dynamic simulations. Moreover, the examples confirmed that the use of additional vibration modes does not lead to accurate results with an acceptable number of additional trial vectors. This can be especially seen on the example of the bolted connection rod. For this example the use of additional vibration modes does not lead to acceptable result quality in terms of stresses in the contact area (see fig. 4.18).

An interesting insight of the numerical investigation is that the convergence order of the investigated joint mode methods is not identical for the two examples. Joint modes based on POD of forces show the slowest convergence for the friction bar while these joint modes show the best convergence for the bolted connection rod. On the other hand, joint modes

computed with POD of TVDs show the opposing convergence behavior. An intermediate and consistent convergence rate is achieved by the joint modes computed by wPOD of TVDs for both examples.

The evaluation of the ratios $w(g)$ delivers inconsistent results for the examples. For the friction bar the ratios for different joint mode methods correspond to their convergence order, while for the bolted connection rod they do not. The results indicate that the defined ratio $w(g)$ can be used as estimator for the number of required joint modes. The specific value for a converged solution depends on the considered structure and the joint mode method.

Considering the convergence rate and the value of the ratio for both examples, the joint modes computed with wPOD of TVDs seem to be the most stable and robust method for different type of applications. With their connection to the deformation energy (see section 3.2.2) these joint modes are also the most reasonable choice from the theoretical point of view. For this reason joint modes computed by wPOD of TVDs are used for the following investigations of contact models (see section 4.4) and for the practical applications in section 4.5.

4.3.2 Preloaded joint modes

The numerical examples confirm the excellent convergence for the preload state due to the inclusion of a PLM. Furthermore, a straighter convergence of the joint modes based on PLM derivatives was observed.

Moreover, the limitations of the method were investigated. These investigations show that the use of only PLM derivatives can be problematic if the structure contains contact relevant joint regions which are separated from the preload area. Nevertheless, joint modes based on PLM derivatives showed a robust convergence under different dynamic loads (different level of inertia forces) or varied contact parameters, although the number of required joint modes varied. This variance in the number of joint modes is a result of the reduced influence of the preload at high dynamics.

In general, preloaded joint modes are a promising strategy for forming an efficient reduction basis for preloaded structures. For practical application of the method, the discussed limitations need to be considered in order to avoid poor quality results.

4.4 Evaluation of contact and friction models

Joint modes show an efficient way to get an accurate representation of the local deformations inside a joint. These local deformations allow contact and friction models to capture the physical characteristics of the joint. To ensure low computational effort for the entire computation process it is important that the used contact and friction models are numerically efficient.

Based on the review of contact and friction models presented in section 2.4, the physical requirements on friction models have been defined. In the following subsections different contact models and friction models are compared and investigated concerning numerical criteria. Furthermore, a recommendation for a contact and friction model in the context of MBS is given.

4.4.1 Contact models

Contact models should give a realistic representation of the contact mechanics and the contact pressure with (few) physically meaningful parameters. Furthermore, the continuity of the model and the simplicity of the mathematical description are considered. In the following subsections, different penalty contact models are compared and investigated on a numerical example. The contact models reviewed in section 2.4.2, namely (A) linear, (B) multi-stage linear, (C) power-function-based, (D) exponential, (E) quadratic-linear, and (F) joint-adapted exponential penalty model are evaluated in this section.

Comparison of contact models

In order to compare the different contact models, the parameters for the models are chosen in a way that they lead to the same contact pressure for a defined penetration ($g_N = -2.5\,\mu$m). In fig. 4.31 the pressure-gap relationship for all discussed contact models is plotted, and in table 4.3 their properties are summarized and rated.

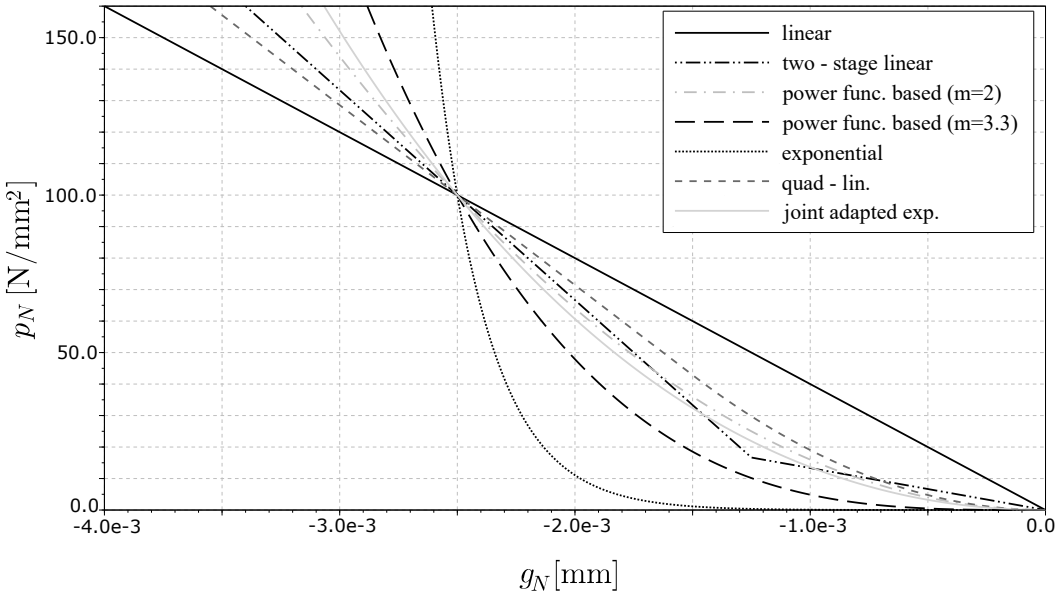

Figure 4.31: Pressure-gap relationship for different penalty models

In terms of simplicity, it can be stated that the linear penalty model is clearly the simplest model. The multi-stage penalty model is also rather simple but requires additional distinction

Table 4.3: Comparison of contact models
(A) linear (B) multi-stage linear (C) power-function-based
(D) exponential (E) quadratic-linear (F) joint-adapted exp.

	(A)	(B)	(C)	(D)	(E)	(F)
simplicity of mathematical description	+	○	+	−	○	○
number of parameters	1	≥ 3	2	2	3	3
physical interpretation of parameters	+	+	−	○	○	○
contact mechanical interpretation	-	-	+	+	○	+
continuity of slope	-	-	+	+	+	+

in the pressure-gap relationship. This additional distinction is also needed for the quadratic-linear model. The power-function-based model and the exponential models do not include additional case distinction but have a more complicated (time consuming) mathematical description and require a higher number of floating-point operations.

For the linear and multi-stage linear models, a step in the slope of the pressure-gap relationship at $g_N = 0$ occurs, whereas all other penalty models show a continuous transition in the pressure-gap relationship between gaping and penetration.

Concerning the contact mechanical interpretation the following points can be stated. The exponential and the power-function-based pressure-gap relationship can be associated with the Hertzian contact theory by using statistical models for the roughness of the surfaces. For all other models, such a contact mechanical interpretation is not available.

Numerical evaluation of contact models

A 2D car pendulum model including an additional point mass at one end of the pendulum, as shown in fig. 4.32, is used to investigate the numerical efficiency of the discussed contact models. The pendulum was designed as a flexible multilayer sheet structure with three metal sheets rotationally fixed to the car. The two outer metal sheets (300 mm × 20 mm × 1 mm) were connected via beam elements at two locations. The central metal sheet (400 mm × 20 mm × 1 mm) was not directly connected to the outer sheets but interacts via contact forces with the outer sheets. The flexible structure was modeled out of steel and planar stress elements in the FE software *Abaqus* [26] and the resulting mass and stiffness matrices were imported into *Scilab* [110] for all following computations. The entire model of the structure had $n_{\mathrm{FE}} = 3009$ DOFs whereof 2709 DOFs were involved in the joint. The mesh was designed as a regular mesh with coincident nodes in the joint area. The system was excited either by an external force at the point mass (see fig. 4.33 and table 4.4) or by gravity (see table 4.5). The external force f_{ext} was applied in two different ways as a smoothed step function (force0) using a half-wave cosine with a short period of $T = 0.05\,\mathrm{s}$ as shown in fig. 4.33.

The differential algebraic equations describing the flexible multibody system were solved with a modified HHT solver (see section 2.1.2) written in *Scilab* [110].

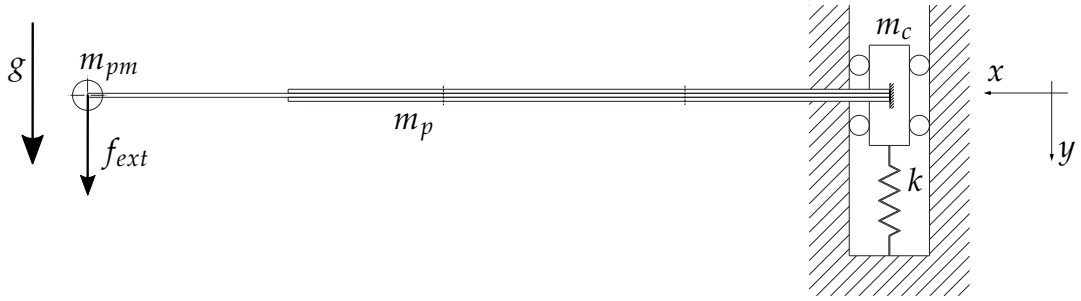

Figure 4.32: Schematic draft of 2D car pendulum model

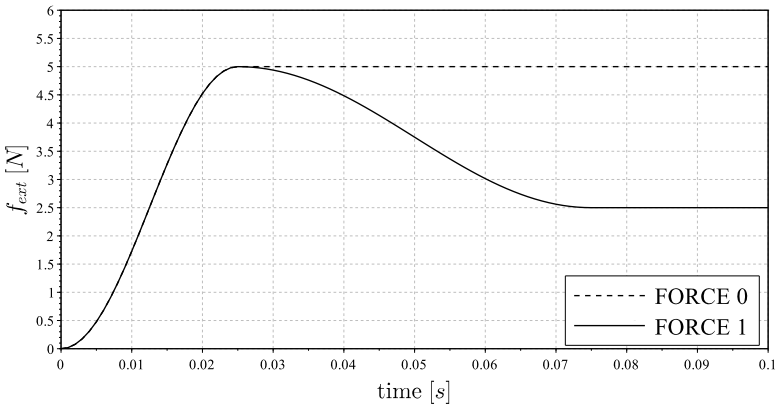

force0:

$$f_{ext}(t) = \begin{cases} -\frac{f_0}{2}\cos\left(\frac{2\pi}{T}t\right) + \frac{f_0}{2} & \text{if } t \leq \frac{T}{2}, \\ f_0 & \text{if } t > \frac{T}{2}. \end{cases}$$

force1:

$$f_{ext}(t) = \begin{cases} -\frac{f_0}{2}\cos\left(\frac{2\pi}{T}t\right) + \frac{f_0}{2} & \text{if } t \leq \frac{T}{2}, \\ -\frac{f_0}{3}\cos\left(\frac{2\pi}{T}t\right) + \frac{2f_0}{3} & \text{if } \frac{T}{2} < t \leq T, \\ \frac{f_0}{3} & \text{if } t > T. \end{cases}$$

Figure 4.33: Description of applied external force

Table 4.4: Model parameters: case FORCE

$m_c = 0.95\,\text{kg}$	$m_{pm} = 0.2\,\text{kg}$
$m_p = 0.157\,\text{kg}$	$k = 1000\,\text{N/m}$
$f_0 = 5\,\text{N}$	$g = 0\,\text{kg m/s}^2$

Table 4.5: Model parameters: case GRAVITY

$m_c = 0.95\,\text{kg}$	$m_{pm} = 0.2\,\text{kg}$
$m_p = 0.157\,\text{kg}$	$k = 1000\,\text{N/m}$
$f_0 = 0\,\text{N}$	$g = 9.81\,\text{kg m/s}^2$

The flexible pendulum was included in the MBS using the CMS reduction basis containing

$v = 5$ bending vibration modes and $s = 6$ static deformation modes. Moreover, the reduction basis was extended with $g = 60$ joint modes based on wPOD of TVDs for an accurate representation of the joint deformation. A convergence study on the number of required joint modes can be found in appendix F.2.

The 2D car pendulum model was simulated for the three described load cases (case gravity, case force0, case force1) over a period of $T_{sim} = 2.5\,\mathrm{s}$. For a fair comparison of the different penalty models, the contact parameters were chosen in a way that the maximal penetration is approximately equal. The parameters given in table 4.6 lead to a maximal penetration of $g_{Nmax} \approx -3\,\mu\mathrm{m}$. Clearly, for penalty models with more than one parameter, different combinations of the parameters are possible to achieve this maximal penetration. The parameters listed in table 4.6 lead to a similar pressure-gap relationship as shown in fig. 4.31.

Table 4.6: Penalty parameters

(A) linear; (B) two-stage linear; (C1) power-func.-based $(m = 2)$; (C2) power-func.-based $(m = 3.3)$; (D) exponential; (E) quadratic-linear; (F) joint-adapted exp.

(A)	$\varepsilon_N = 400\,\mathrm{N/mm^3}$		
(B)	$\varepsilon_{N1} = 667\,\mathrm{N/mm^3}$ $\varepsilon_{N0} = 133\,\mathrm{N/mm^3}$	$g_{N0} = 0\,\mu\mathrm{m}$	$g_{N1} = -1.25\,\mu\mathrm{m}$
(C1)	$\varepsilon_N = 0.16\,\mathrm{N/mm^2(\mu m)^2}$	$m = 2$	
(C2)	$\varepsilon_N = 4.86\mathrm{e}^{-2}\,\mathrm{N/mm^2(\mu m)^{3.3}}$	$m = 3.3$	
(D)	$p_{N0} = 1.23\mathrm{e}^{-4}\,\mathrm{N/mm^2}$	$g_{N0} = 0.4\,\mu\mathrm{m}$	
(E)	$\varepsilon_N = 5.7\mathrm{e}^{-1}\,\mathrm{N/mm^2(\mu m)}$	$g_{N0} = 0\,\mu\mathrm{m}$	$g_{N1} = -1.5\,\mu\mathrm{m}$
(F)	$\epsilon_N = 617\,\mathrm{N/mm^3}$	$g_{N0} = 0\,\mu\mathrm{m}$	$\lambda_N = 200\,\mathrm{1/mm}$

The required computational time, the number of time steps, and the number of Jacobian updates were used as criteria to benchmark the numerical efficiency of the different contact models. These criteria are plotted for the different load cases in fig. 4.34. In this figure the results are presented in a normalized form with the linear penalty model denoting a reference value of 100%.

The results depicted in fig. 4.34b show that for the excitation with force0, the linear penalty model leads to the lowest computational effort, whereby the number of time steps and Jacobian updates is at the same level for all models. For the excitation with force1 (fig. 4.34c) or with gravity (fig. 4.34d), the numerical investigations showed quite different results. For these two cases, the linear penalty model shows clearly the highest computational effort. The reason for the difference between the results might be in the different bending of the flexible structure for the different cases. The excitation with force0 only leads to bending in one direction, whereas the bending direction changes for the other two cases. Hence, it seems that contact models with a quite smooth transition in the pressure-gap relationship

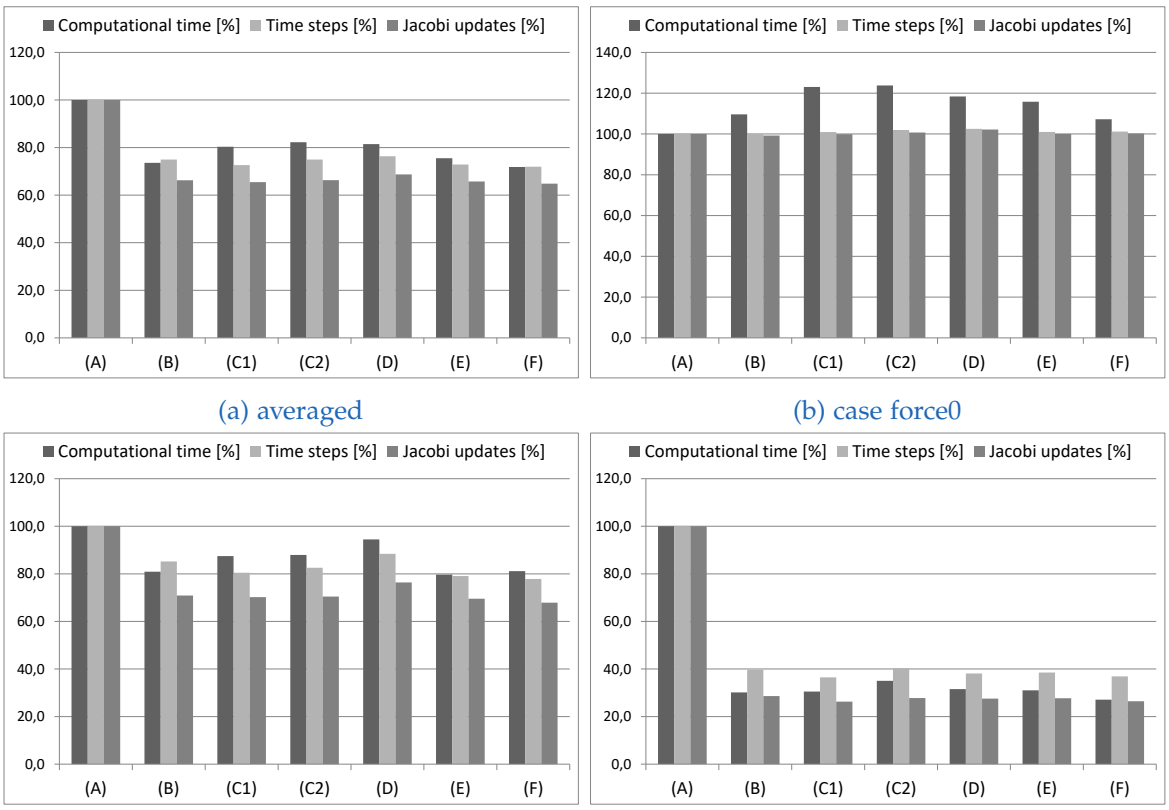

(a) averaged

(b) case force0

(c) case force1

(d) case gravity

(A) linear; (B) two-stage linear; (C1) power-func.-based ($m = 2$); (C2) power-func.-based ($m = 3.3$); (D) exponential; (E) quadratic-linear; (F) joint-adapted exp.

Figure 4.34: Comparison of numerical efficiency of contact models

between gapping and penetration have numerical advantages in case it comes to qualitative changes in the deformation state during the dynamic simulation. Beside the linear model, all penalty models show a numerical performance that is approximately at one level for the cases force0 and gravity.

4.4.2 Friction models

Based on the insights of the literature review in section 2.4.1 and especially the work of Gaul and his associates [40, 42, 61, 62], the defined requirements for a friction model characterizing dry fiction in the microslip regime (small sliding) are:

- Two different nonzero slopes (frictional stress over relative displacement) for the stick and slip regime.
- No energy dissipation in case of sticking.
- Frequency-independent energy dissipation in case of sliding.
- Physically reasonable parameters (as few as possible).

In the following subsections different friction models, namely a) Three-parameter Coulomb-type friction model (see fig. 2.4, denoted as reference model), b) Adapted Dahl friction model, c) Valanis friction model, d) Bouc–Wen friction model, and e) Viscous damping model (Kelvin–Voigt element) are rated based on these criteria. Furthermore, the numerical efficiency of the friction models was evaluated on a multi-mass oscillator. Finally, a decision matrix with a comprehensive evaluation is presented.

Comparison of the friction models

In order to compare the mentioned friction models, the hysteresis curves for sticking/sliding and for pure sticking are considered. To determine these curves the force elements describing the friction stresses were excited with a prescribed sinusoidal relative tangential displacement s and a corresponding tangential slip velocity $\dot{s}$. The values for the tangential displacement s were chosen in a range for which either pure sticking $(-8e-6\,\mathrm{m} < s < 8e-6\,\mathrm{m})$ or a switching between sticking and sliding was expected $(-2e-5\,\mathrm{m} < s < 2e-6\,\mathrm{m})$ for the considered friction parameters. In fig. 4.35 the resulting hysteresis curves for the investigated models are plotted.

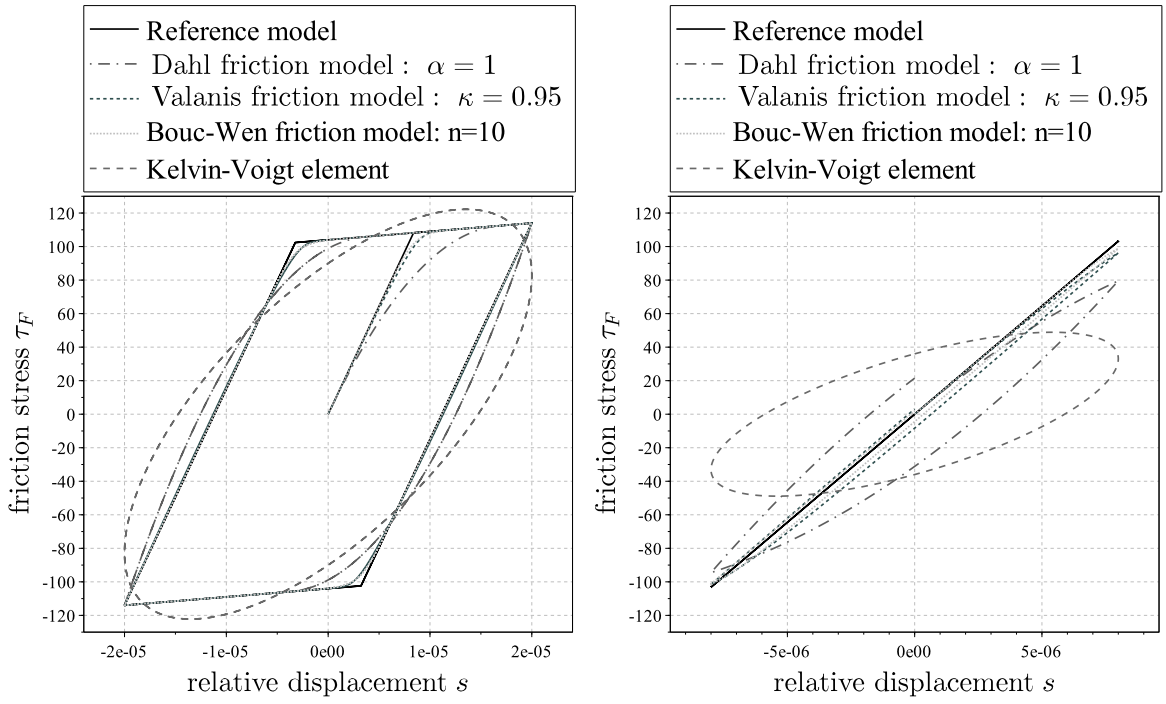

(a) sticking/sliding (b) pure sticking

Figure 4.35: Hysteresis of different friction models

Figure 4.35a shows that the reference model, the Valanis model, and the Bouc–Wen model are able to represent two different slopes for sticking and sliding. For the Dahl friction model

with $\alpha = 1$, the two slopes are not clearly separated, and for viscous damping the sticking and slipping slopes cannot be seen at all.

In fig. 4.35b the curves for pure sticking are plotted. Only the reference model shows real zero energy dissipation during sticking. For the Valanis model and the Bouc–Wen model, the hysteresis for pure sticking is very small and seems to give a good representation of the real physical behavior. The Dahl friction model and viscous damping clearly show a hysteresis, and hence energy dissipation during sticking.

To investigate the frequency dependency of the models, the frequency of the prescribed motion was increased. The resulting hysteresis curves are plotted in fig. 4.36.

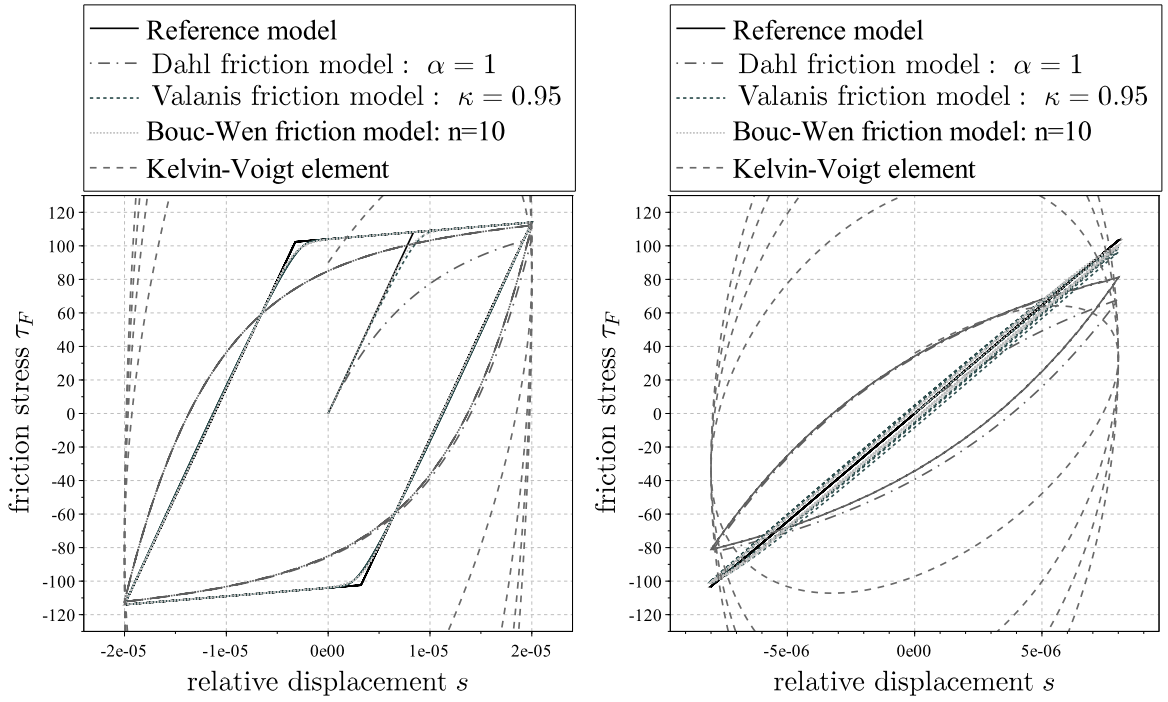

(a) sticking/sliding

(b) pure sticking

Figure 4.36: Hysteresis of different friction models: frequency sweep

Figure 4.36 shows for both cases (sticking/sliding and pure sticking) that only the viscous damping model is frequency-dependent. For all other models the shape of the hysteresis remains constant which implies that the friction models are frequency independent.

In table 4.7 the parameters of the friction models are summarized and distinguished in physical parameters and model parameters which are required for the mathematical description of the model. Comparing the parameters of the friction models in table 4.7 shows that for all parameters of the reference model a physical interpretation can be found. All other models have at least one parameter that has no clear physical meaning but is necessary for the mathematical description.

Table 4.7: Comparison of Friction parameters

	Reference	Dahl	Valanis	Bouc–Wen	Viscous
physical parameters	R_G, c_1, c_2	R_G, σ_0, c_2	E_t, E_0, λ_0	A	-
model parameters	-	α	κ	B, γ, n	$d, c_1, (c_2)$

In table 4.8 the characteristics of the investigated friction models with respect to the defined criteria are summarized. Drawing a conclusion from table 4.8, it can be stated that viscous

Table 4.8: Comparison of Friction models

	Reference	Dahl	Valanis	Bouc–Wen	Viscous
simplicity of mathematical description	○	○	-	-	+
sticking/sliding	+	○	+	+	-
no energy dissipation during sticking	+	-	○	○	-
frequency-independent	+	+	+	+	-
few physically parameters	+	○	○	-	-

damping is not able to fulfill any of the defined criteria to model dry friction inside joints. Hence, viscous damping is not included in the numerical study.

Applying an implicit Euler scheme to discretize the differential equations of the simplified Dahl friction model (eq. (2.118)) and Valanis friction (eq. (2.119)) leads for both to an equation that can be solved explicitly. On the other hand, the differential equation of the Bouc–Wen model (eq. (2.122)) can only be solved iteratively.

Numerical evaluation of friction models

The four friction models (three-parameter Coulomb model, Dahl, Valanis, Bouc–Wen) which fulfill (most of) the defined criteria are investigated in terms of numerical efficiency in this section. For this purpose, a multi-mass oscillator as shown in fig. 4.37 is used, where each mass is connected to ground with a friction element. For the investigations the multi-mass oscillator was simulated with 100 masses and the parameters were set to $k = 100\,\mathrm{N/m}, m = 0.1\,\mathrm{kg}, f_{ext}(t) = 0.2\sin(2\pi t)\,\mathrm{N}$. The friction parameters for different friction models are represented by the vector $\mathbf{c}$, and the particular parameters are defined in table 4.7.

In order to achieve approximately the same behavior as in a real joint, different cases were simulated. The sticking limit R_G was varied as described in table 4.9 since it is an influence factor for all friction models. For the case where gaping is simulated a negative value R_G was interpreted as gaping. Furthermore, the number of excited masses and the sticking stiffness of the friction models was varied. The system was simulated with all masses or only

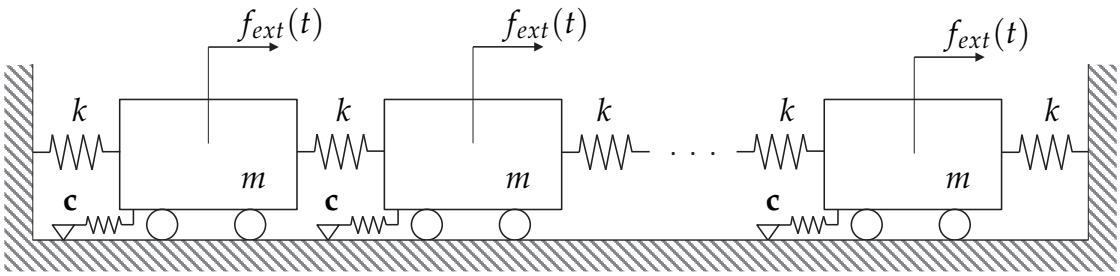

Figure 4.37: Multi-mass oscillator

ten masses ($m_i,\ i = 1, 10, 15, 25, 50, 65, 80, 85, 90, 99$) being excited. As a consequence, some masses switch between sticking and slipping, whereas other masses show pure sticking.

The three-parameter Coulomb model was implemented as discussed in [39] by decomposing the tangential displacement into elastic (reversible) and plastic (irreversible) components. The differential equations describing the Dahl, Valanis and Bouc–Wen friction model were evaluated based on a discretization with an implicit Euler scheme.

Table 4.9: Cases multi-mass oscillator

gaping	varying R_G	sticking/sliding	pure sticking
$R_G^* = \frac{R_{G0}}{2}\cos\left(\frac{3\pi}{2}t\right)$ $R_G = \begin{cases} R_G^* & \text{if } R_G^* > 0 \\ 0 & \text{if } R_G^* \leq 0 \end{cases}$	$R_G = \frac{R_{G0}}{2}\cos\left(\frac{3\pi}{2}t\right) + R_{G0}$	$R_G = R_{G0}$	$R_G = R_{G0}$
$R_{G0} = 0.15\,\mathrm{N}$	$R_{G0} = 0.15\,\mathrm{N}$	$R_{G0} = 0.15\,\mathrm{N}$	$R_{G0} = 5\,\mathrm{N}$

Exemplary for the different variations in the model parameters, the displacements (fig. 4.38), and the resulting hysteresis curves (fig. 4.39) of mass m_{25} for varying R_G and only ten masses excited are plotted.

It can be seen in fig. 4.38 that the reference model, the Valanis model, and the Bouc–Wen model produce nearly the same displacements. The Dahl friction model matches the displacement curves quite well in the time periods of sliding, whereas in the periods of sticking a deviation from the other friction models can be seen. The comparison of the hysteresis curves in fig. 4.39 shows again a divergence of the Dahl friction model compared to all other models.

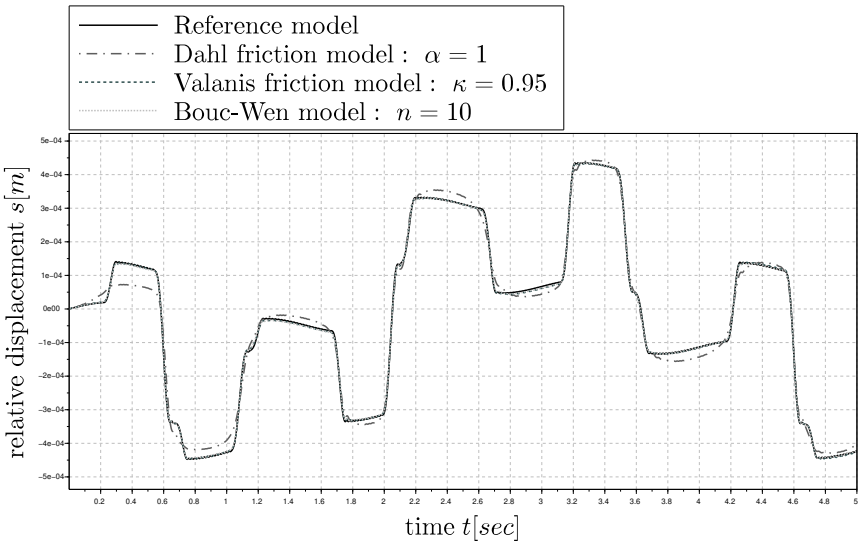

Figure 4.38: Displacement of mass m_{25}

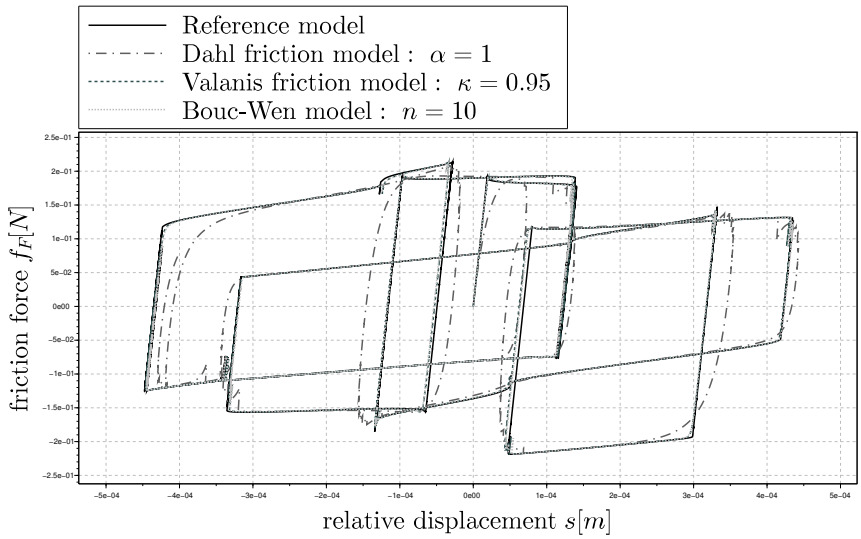

Figure 4.39: Hysteresis of mass m_{25}

In order to evaluate the numerical efficiency of the four friction models, the computational time, the number of time steps, and the number of Jacobian updates during the time integration are used as criteria. Averaged over all parameter variations, the results are shown in fig. 4.40. None of the investigated cases shows a qualitatively different result in terms of numerical efficiency than the averaged results shown in fig. 4.40.

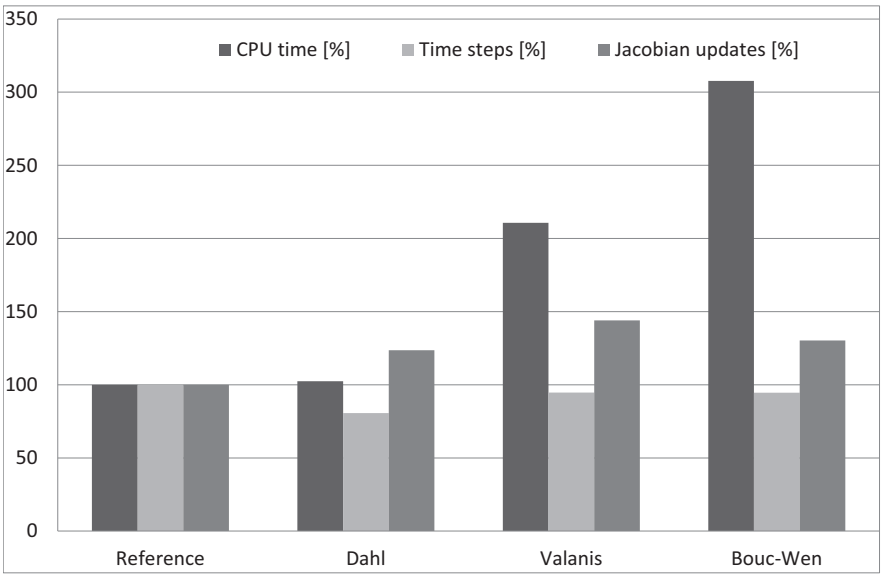

Figure 4.40: Comparison of numerical efficiency of friction models

The results show that the reference model and the Dahl friction model are at the same level in terms of the computational time, whereas the computational time for the Valanis and the Bouc–Wen model is much higher. A possible reason might be the higher number of floating-point operations for the computation of the friction force and the Jacobian. The required time steps for all models are a little lower than the reference model, whereas the number of the required Jacobian updates is higher.

4.4.3 Conclusions on contact and friction models

The results of the numerical investigations on contact models indicate that all models with a smooth transition in the pressure-gap relationship tend to have a lower computational effort. Together with the theoretical comparison of table 4.3, the joint-adapted exponential model seems to be the best choice for computing contact pressure within an MBS. Moreover, this model has the advantage that it can be derived from some contact physical background.

Different friction models that capture the defined characteristics of dry friction (see section 4.4.2) have been evaluated. The defined requirements for the friction models are simplified specifications which are only valid for the microslip regime. As a result of the findings summarized in table 4.8 and the numerical investigations on the multi-mass oscillator, the three-parameter Coulomb-type friction model (reference model) seems to be the best choice for the modeling of dry friction inside jointed structures although it is not continuous.

4.5 Industrial applications

Two industrial problems, which were analyzed with the use of general joint modes, are presented in this chapter . Both examples are from the field of automotive engineering and were processed in cooperation with a well known combustion engine manufacturer. The implementation discussed in section 3.3 together with the MBS software *MSC.ADAMS* [73] was used to analyze these problems.

The aim of this section is to demonstrate the applicability of the presented approach for industrial applications. It should be demonstrated that full dynamic simulations considering nonlinear contact of jointed structures are possible for industrial examples with the presented method. This includes the consideration of large mechanical structures with complex joint geometry and the inclusion of the method into existing and sophisticated multibody simulation models. Due to the obligation to maintain confidentiality no detailed results of the investigated projects can be revealed.

The first industrial application, presented in section 4.5.1, deals with the analysis of the dynamic behavior and the damping properties of a dual mass flywheel. The goal of this project was to evaluate if the used (and estimated) modal damping values of the dual mass flywheel are realistic or not.

In section 4.5.2 a second industrial application of joint modes is presented. In this application the contact situation between the engine block and the crankshaft bearing cap was analyzed. One goal of this project was to achieve a realistic representation of the stresses in the involved components during a full dynamic engine speed up. Based on these stresses, a more accurate fatigue prediction in the area of the joint is possible.

4.5.1 Modal damping of a dual mass flywheel

Problem description

A dual mass flywheel is part of the powertrain of modern vehicles. The main purpose of the dual mass flywheel is to reduce the torsional oscillations and to provide a more continuous rotational energy for the powertrain. Furthermore, inside the dual mass flywheel three thin metal sheets, so-called flex plates, ensure that the bending vibrations of the crankshaft are not transferred to the following components of the powertrain.

The cooperation partner considered the dual mass flywheel as flexible body in the MBS model of an combustion engine, whereby the damping properties for the bending direction were unknown. For a stable numerical simulation of an engine speed up high values of modal damping ($> 20\%$) for the bending vibration modes of the dual mass flywheel were necessary. Hence, it was assumed that the friction between the flex plates leads to the high values of damping required for the numerical simulation.

The purpose of the project was to investigate if it is realistic that friction between the flex plates causes the high values of modal damping of the flex plate's bending vibration modes.

Methods of analysis

For the numerical investigations and the investigations on a test rig a simplified model containing only the isolated flex plates (as depicted in fig. 4.41a) was used. The isolated flex plates form a triple-layered sheet metal structure and the corresponding FE model is depicted in fig. 4.41b.

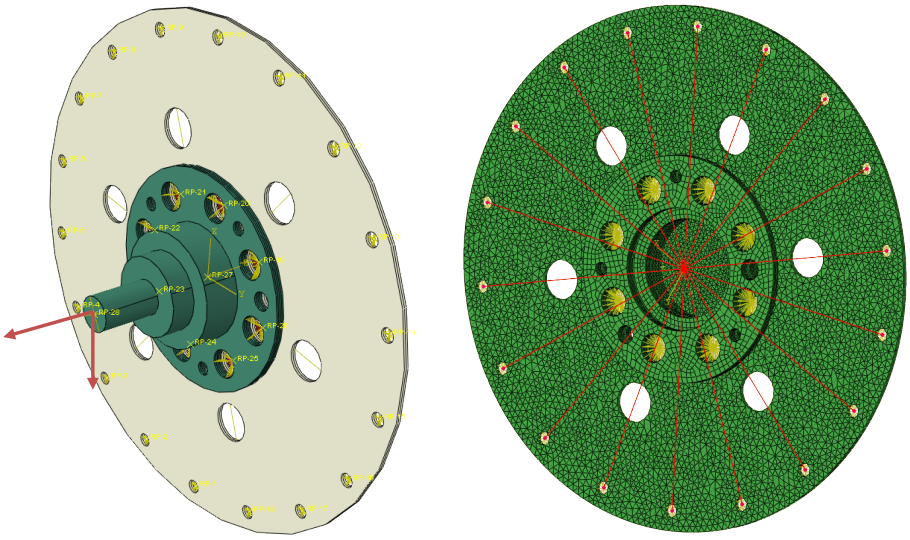

(a) Model of isolated flex plates (b) FE model of isolated flex plates

Figure 4.41: Schematic draft of isolated flex plates

Evaluation of modal damping with joint modes In fig. 4.42 the joint surfaces between the flex plates are marked with colored dotted lines. Altogether, $n_{CP} = 12572$ contact pairs were considered inside the four joint areas. Based on static convergence studies with different loadings and a comparison with a full nonlinear FE simulation, $g = 250$ joint modes were used for the dynamic simulations.

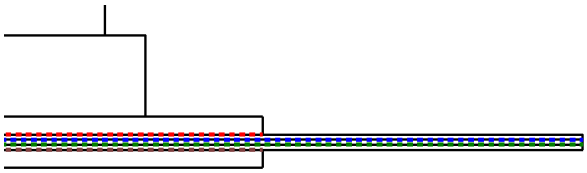

Figure 4.42: Joint areas between flex plates

For the numerical evaluation of the modal damping values the isolated flex plates were loaded with preload forces and a smoothed force impulse in axial or radial direction (see fig. 4.41a). Hence, the first axial and the first bending vibration mode were exited separately. During the dynamic simulation full nonlinear contact and friction forces between the flex plates were considered.

Since mainly one bending vibration mode was exited with the force impulse, the dynamic response of the force application point was compared to a damped single mass oscillator. Based on the equation of motion of the single mass oscillator a comparable modal damping value was identified. In fig. 4.43 the normalized damping values for one axial vibration mode are compared. The identified damping value is only $\approx 1\%$ of the originally used value. It can be reported that for all applied loadings the identified damping values were much lower than the damping values used for the original dual mass flywheel. This fact indicates that the influence of friction between the flex plates is much lower than assumed.

Evaluation of modal damping on a test rig In order to assess the results obtained from the numerical analysis, an experimental modal analysis (EMA) was performed on the isolated flex plates. For the EMA the flex plates were mounted in the same way as in the simulation model. The plates were excited with an impact hammer and the accelerations of the force application point were recorded.

The results of the EMA confirmed that the damping of the flex plates is much lower than the values used in the original model. In fig. 4.43 it can be seen that the by EMA determined Lehr's damping value is $\approx 3\%$ of the originally used value for the axial bending mode.

Conclusion

Based on the numerical investigations with general joint modes and the EMA, it was pointed out that the high modal damping values used for the bending vibration modes dual mass flywheel are not caused by the friction between the flex plates.

An important result of this project is that joint modes are able to deliver realistic contact and friction behavior as the numerical results are in good accordance with the results of the EMA. The four times lower damping identified in the numerical analysis (only friction considered) is in a realistic range in comparison to all surrounding effects (test rig, material damping,...) measured during the EMA and the general uncertainties for estimating damping.

Note once again that only $g = 250$ joint modes have been considered for the dynamic simulations instead of 37716 DOFs inside the joint areas. Only due to this reduction of DOFs the example could be solved with acceptable computational effort.

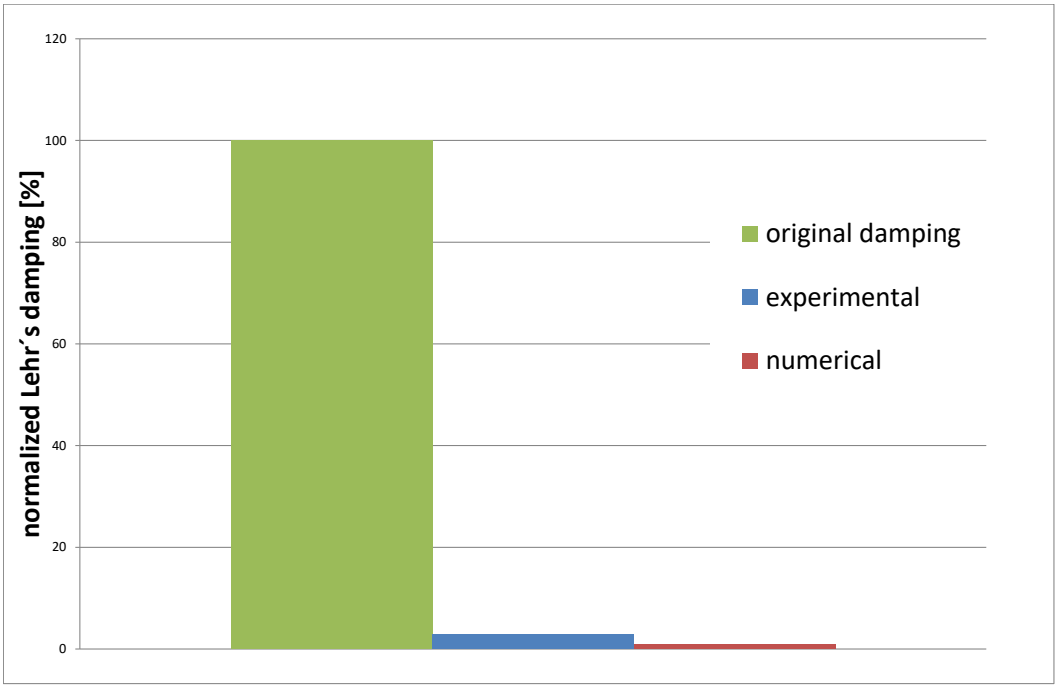

Figure 4.43: Normalized Lehr's damping values for one mode shape

4.5.2 Evaluation of the engine block–crankshaft bearing cap contact

In this industrial example full nonlinear contact between the engine block and the crankshaft bearing cap during an engine speed up was considered. Therefore, joint modes were included in the reduction basis of the engine transition unit. With this model a flexible MBS of a full engine speed up was performed.

An exemplary illustration of an engine block–crankshaft bearing cap joint is depicted in fig. 4.44, where the joint area is highlighted with a red line.

Problem description

So far, the contact between the engine block and the bearing cap was modeled with a tied contact formulation. This tied contact effects that the contacting surfaces cannot deform with respect to each other. This implies that the surfaces cannot separate from each other (gapping) and that no relative tangential motion occurs. Hence, the computed stresses inside the joint and in the surrounding area are not realistic. Based on these unrealistic stresses a meaningful fatigue computation in the area of the joint is not possible.

The main goal of this project was the accurate consideration of full nonlinear contact and friction forces during an engine speed up. Besides the dynamics of the crank drive also forces due to screw preloads were considered. Based on more realistic stresses a more accurate fatigue prediction in the area of the bearing block is expected.

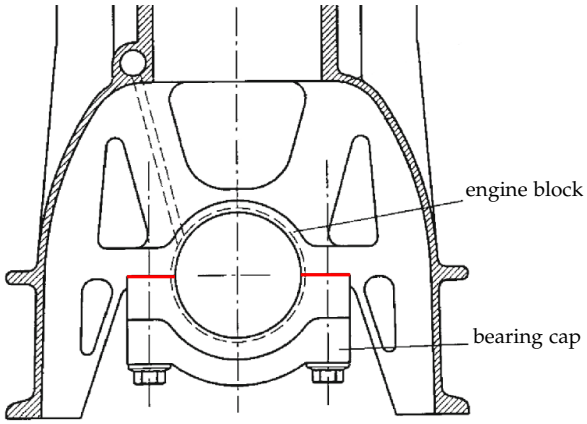

Figure 4.44: Exemplary illustration of the considered engine block–bearing cap contact (original figure from [6])

Methods of analysis

The FE mesh of the engine transition unit contains $\approx 4\ 10^6$ elements and $> 6\ 10^6$ FE nodes. Especially the area around the considered joint was fine meshed, and hence $n_{\mathrm{CP}} = 10691$ contact pairs were considered between the surfaces.

On an isolated model of the considered bearing block a static convergence analysis in terms of normal stresses and normal gaps inside the joint was performed. For this static analysis only the screw preload forces were applied. The computed stresses and normal gaps were compared to the results of a full nonlinear FE simulation of the isolated bearing block. A result of this convergence study was that with $g = 80$ joint modes the stresses and the normal gaps are in good conformance with the results of the full FE simulation. A comparison of the normal stresses computed with $g = 80$ joint modes and the full FE simulation is shown in fig. 4.45. In this figure only one side of the bearing cap with a simplified mesh is depicted.

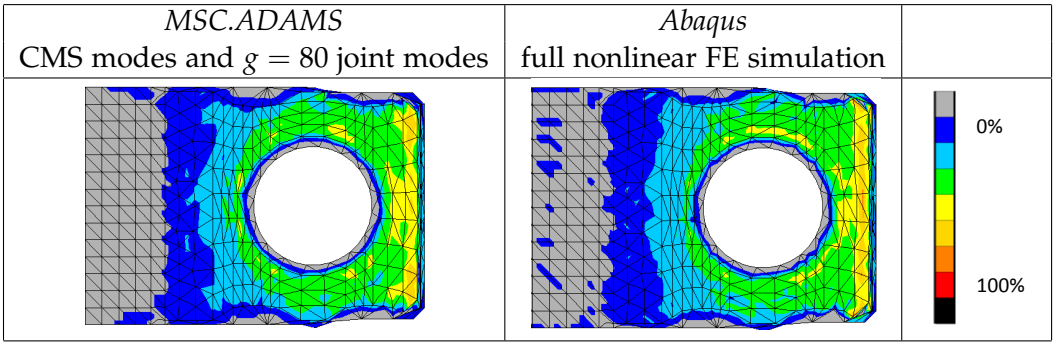

Figure 4.45: Comparison of preload induced normal stresses in the joint (simplified mesh)

In the MBS $g = 80$ joint modes were used for the consideration of full nonlinear contact. Furthermore, the interaction with the elastohydrodynamic contact inside the crankshaft bearing was considered during the dynamic engine speed up. For the elastohydrodynamic contact an existing subroutine for *MSC.ADAMS* was used. Based on the results of the flexible

MBS a fatigue analysis was performed. In fig. 4.46 the lowest safety factors in the joint region obtained by fatigue analysis of the original model and the simulation considering joint modes are depicted. For this figure the lowest calculated safety factor was considered as 100%. It should be noted that not only the values of the safety factors differ, but also the location where these lowest safety factors appear were different.

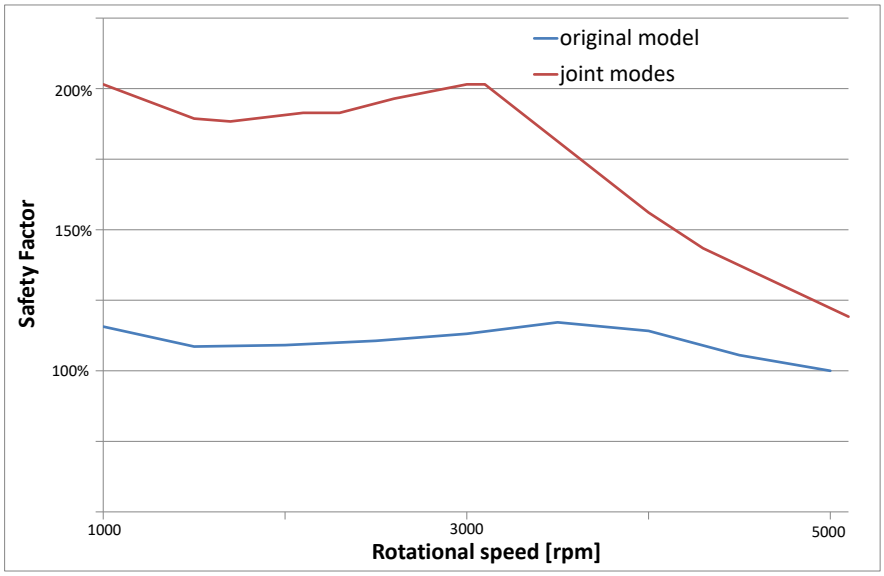

Figure 4.46: Safety factors in the joint region during engine speed up

Conclusion

With the stress data obtained from the engine speed up considering joint modes, an improved fatigue computation was possible. As expected, different stress distributions and safety factors appear in the joint area compared to the so far used simplified contact formulation.

Furthermore, the postprocessing toolbox (see section 3.3.3) allowed detailed insight into the contact situation (possible gaping, sticking or sliding) at different dynamic loads.

It should be mentioned that with common computation strategies a full engine speed up considering nonlinear contact between the engine block and the crankshaft bearing cap is not possible. Simplified computations could be performed with a quasi-static finite element simulation and/or a reduced number of degrees of freedom in the joint area.

5 Outlook

In this chapter two possible research topics for further improvement of the presented strategy are shortly outlined and discussed. Both presented topics deal with the reduction of computational effort for numerical time integration and not with the improvement of joint modes.

Section 5.1 focuses on the efficient computation of the reduced nonlinear forces $\mathbf{f}_{nl}^{m}$ and how these forces can be approximated. Hence, different methods, so-called hyper-reduction strategies, found in literature are reviewed and their possible application on contact and friction forces is discussed.

In section 5.2 an approach for separated time integration of low and high frequency modes is reviewed and its usability for joint modes is discussed. Furthermore, some possible improvements of this separated time integration are outlined.

5.1 Computation of reduced nonlinear forces

In section 2.2 the reduction of the number of FE DOFs (n_{FE}) via projective model order reduction techniques has been reviewed. The number of unknowns for time integration is thereby reduced to $r << n_{\mathrm{FE}}$. Nevertheless, the evaluation of the nonlinear forces still has to be performed in the physical DOFs of order n_{FE}. This requires the computation of the physical DOFs inside the joint ($\mathbf{x} = \mathbf{\Phi}\boldsymbol{\zeta}$) and a re-projection of the nonlinear forces ($\mathbf{f}_{nl}^{m} = \mathbf{\Phi}^{\mathsf{T}}\mathbf{f}_{nl}$) at every iteration of every time step.

In order to alleviate this bottleneck and to reduce the computational effort, a second reduction (also called hyper-reduction) might be employed. Different hyper-reduction strategies, like

- matrix expansion [71, 147],
- discrete empirical interpolation method (DEIM)[15, 18, 63, 130]
- a priori hyper-reduction (APHR) [101, 102] , and
- energy-conserving (mesh) sampling and weighting (ECSW) [31, 33, 63]

are discussed in the following in the context of contact and friction forces. A good overview of these methods can be found in the lecture notes of Rixen [97], from which also parts of the following subsections are taken.

5.1.1 Matrix expansion

Matrix expansion (see [71, 147]) allows an efficient computation of the nonlinear forces in the reduced coordinates in case the nonlinear forces can be computed by a tensor expansion in the physical DOFs. This is for example the case in structural dynamics with geometrical nonlinearities since the nonlinear elastic forces can be written as

$$\mathbf{f}_{nl} = \mathbf{K}^{\{1\}}\mathbf{x} + \mathbf{K}^{\{2\}}\mathbf{x}\mathbf{x} + \mathbf{K}^{\{3\}}\mathbf{x}\mathbf{x}\mathbf{x}, \tag{5.1}$$

with constant second order, third order and fourth order tensors $\mathbf{K}^{\{1\}}, \mathbf{K}^{\{2\}}, \mathbf{K}^{\{3\}}$. Consequently, the reduced nonlinear forces can be written as cubic polynomial in the reduced coordinates in the form

$$\mathbf{f}_{nl}^{m} = \tilde{\mathbf{K}}^{\{1\}}\boldsymbol{\zeta} + \tilde{\mathbf{K}}^{\{2\}}\boldsymbol{\zeta}\boldsymbol{\zeta} + \tilde{\mathbf{K}}^{\{3\}}\boldsymbol{\zeta}\boldsymbol{\zeta}\boldsymbol{\zeta}. \tag{5.2}$$

The tensors $\tilde{\mathbf{K}}^{\{1\}}, \tilde{\mathbf{K}}^{\{2\}}, \tilde{\mathbf{K}}^{\{3\}}$ can be computed by training configurations with commercial FE codes using a number of nonlinear static solutions.

This approach is not suitable for contact and friction forces, since the strong nonlinear and asymmetric characteristics of contact and friction forces does not allow a tensor expansion as described by eq. (5.1).

5.1.2 Discrete empirical interpolation method (DEIM)

The basic idea behind DEIM [15, 18, 130] is to approximate the nonlinear forces $\mathbf{f}_{nl}$ by

$$\mathbf{f}_{nl} \approx \mathbf{T}_c\boldsymbol{\gamma}, \tag{5.3}$$

where the $(n_{\mathrm{FE}} \times k)$ basis $\mathbf{T}_c$ contains $k < n_{\mathrm{FE}}$ force trial vectors $\mathbf{t}_{c,i}$, and $\boldsymbol{\gamma}$ is the $(k \times 1)$ vector of unknown amplitudes. The force trial vectors $\mathbf{t}_{c,i}$ are obtained via POD of a set of appropriate snapshots of nonlinear forces. The force snapshots are computed based on different loading conditions of the full system.

To solve the overdetermined eq. (5.3) for the unknown amplitudes $\boldsymbol{\gamma}$, this equation can be pre-multiplied with the transpose of a $(n_{\mathrm{FE}} \times k)$ boolean selection matrix $\mathbf{P}$, which yields

$$\mathbf{P}^{\mathsf{T}}\mathbf{f}_{nl} = \mathbf{P}^{\mathsf{T}}\mathbf{T}_c\boldsymbol{\gamma}. \tag{5.4}$$

With the multiplication $\mathbf{P}^{\mathsf{T}}\mathbf{f}_{nl}$, certain entries of the nonlinear force vector are specified and the nonlinear forces are exact at these specified nodes. An algorithm for the selection of these nodes is given in [18].

If $\mathbf{P}^{\mathsf{T}}\mathbf{T}_c$ is non-singular, the amplitudes $\boldsymbol{\gamma}$ can be computed along

$$\boldsymbol{\gamma} = \left[\mathbf{P}^{\mathsf{T}}\mathbf{T}_c\right]^{-1}\mathbf{P}^{\mathsf{T}}\mathbf{f}_{nl}, \tag{5.5}$$

and the nonlinear force approximation defined by eq. (5.3) can be written as

$$\mathbf{f}_{nl} \approx \underbrace{\mathbf{T}_c\left[\mathbf{P}^{\mathsf{T}}\mathbf{T}_c\right]^{-1}}_{\mathbf{E}}\underbrace{\mathbf{P}^{\mathsf{T}}\mathbf{f}_{nl}}_{\tilde{\mathbf{f}}_{nl}}. \tag{5.6}$$

The term $\mathbf{E} = \mathbf{T}_c \left[\mathbf{P}^\mathsf{T}\mathbf{T}_c\right]^{-1}$ provides an extrapolation of the exact forces on some nodes $\tilde{\mathbf{f}}_{nl} = \left(\mathbf{P}^\mathsf{T}\mathbf{f}_{nl}\right)$ to all other nodes.

Inserting this approach in the reduced equation of motion yields

$$\left(\mathbf{\Phi}^\mathsf{T}\mathbf{M}\mathbf{\Phi}\right)\ddot{\boldsymbol{\zeta}} + \left(\mathbf{\Phi}^\mathsf{T}\mathbf{K}\mathbf{\Phi}\right)\boldsymbol{\zeta} + \mathbf{\Phi}^\mathsf{T}\mathbf{E}\tilde{\mathbf{f}}_{nl}(\mathbf{\Phi}\boldsymbol{\zeta}) = \mathbf{\Phi}^\mathsf{T}\mathbf{f}. \tag{5.7}$$

With the unassembled DEIM (UDEIM) Tiso presented in [130] a modification of the DEIM. This leads to fewer evaluations of the nonlinear forces and to better localization of the nonlinearities for an FE discretization.

The DEIM is mainly applied for nonlinear forces which show a smooth spatial distribution. This is in general not the case for contact and friction forces, where regions next to each other can show complete different behavior like gapping, sticking or sliding. Furthermore, the location of these regions might change during a dynamic simulation. These facts make the selection of points on which the forces are evaluated exactly and their extrapolation to other regions difficult. Nevertheless, Breitfuss [15] applied the DEIM for the computation of contact stresses. In the latter mentioned work it is noted that the DEIM might lead to wrong results if a loading occurs during the dynamic simulation which is not considered for the computation of the force trial vectors.

5.1.3 A priori hyper-reduction (APHR)

The idea APHR was first introduced by Ryckelynck [101] for analyzing transient nonlinear thermal problems. In [72, 102, 103] the APHR was extended to viscoelastic-viscoplastic problems including internal variables.

In the APHR the nonlinear forces are only computed on some nodes selected by the boolean selection matrix $\mathbf{P}^\mathsf{T}$. Contrary to the previous mentioned DEIM, no extrapolation of these forces is performed. Instead, the equilibrium conditions are only checked to be fulfilled at this reduced set of nodes, yielding

$$\mathbf{P}^\mathsf{T}\left(\mathbf{M}\mathbf{\Phi}\ddot{\boldsymbol{\zeta}} + \mathbf{K}\mathbf{\Phi}\boldsymbol{\zeta} + \mathbf{f}_{nl}\left(\mathbf{\Phi}\boldsymbol{\zeta}\right) = \mathbf{f} + \mathbf{res}\right). \tag{5.8}$$

The matrix $\mathbf{P}^\mathsf{T}$ selects more equations than unknowns in $\boldsymbol{\zeta}$, and therefore the residual vector does not vanish. Hence, it is required that the selected residual $\left(\mathbf{P}^\mathsf{T}\mathbf{res} \neq \mathbf{0}\right)$ is zero in the reduction subspace

$$\left(\mathbf{P}^\mathsf{T}\mathbf{\Phi}\right)^\mathsf{T}\left(\mathbf{P}^\mathsf{T}\mathbf{res}\right) = \mathbf{0}. \tag{5.9}$$

The reduced equation of motion can finally be written as

$$\mathbf{\Phi}^\mathsf{T}\mathbf{P}\mathbf{P}^\mathsf{T}\left(\mathbf{M}\mathbf{\Phi}\ddot{\boldsymbol{\zeta}} + \mathbf{K}\mathbf{\Phi}\boldsymbol{\zeta} + \mathbf{f}_{nl}\left(\mathbf{\Phi}\boldsymbol{\zeta}\right) = \mathbf{f}\right). \tag{5.10}$$

Since the selection of nodes might be difficult (as already mentioned for the DEIM in the previous section), the APHR seems to be not a promising strategy for the reduced computation of contact and friction forces.

5.1.4 Energy-conserving (mesh) sampling and weighting (ECSW)

The energy-conserving (mesh) sampling and weighting (ECSW) method was recently developed by Farhat [31, 33]. The main difference of the ECSW compared to other hyper-reduction methods is that energy-like quantities of the reduced forces $\mathbf{f}_{nl}^{m}$ are approximated directly. Hence, this methods avoids approximating first the nonlinear forces $\mathbf{f}_{nl}$ and projecting these approximations onto the subspace $\mathbf{\Phi}^{\mathsf{T}}$.

In an FE model the reduced nonlinear forces $\mathbf{f}_{nl}^{m}$ can be written at finite element level in the form

$$\mathbf{f}_{nl}^{m}(\zeta) = \sum_{e=1}^{n_e} \mathbf{\Phi}_e^{\mathsf{T}} \mathbf{f}_{nl}^{e}\left(\mathbf{\Phi}_e \zeta\right), \tag{5.11}$$

where the $(N_e \times r)$ matrix $\mathbf{\Phi}_e$ holds the components of the matrix $\mathbf{\Phi}$ associated with the N_e DOFs of the element e, n_e is the number of elements in the FE model, and the $(N_e \times 1)$ vector $\mathbf{f}_{nl}^{e}$ being the element level nonlinear forces from the element e.

According to [33], the basic idea behind ECSW is that each column of $\mathbf{\Phi}_e$ can be interpreted as virtual displacement. Hence, each row of $\mathbf{f}_{nl}^{m}$ defined by eq. (5.11) represents a virtual work along this virtual displacement performed by the forces $\mathbf{f}_{nl}$. Consequently, approximating the vector $\mathbf{f}_{nl}^{m}$ can be interpreted as approximating a set of energies associated with the full FE model. Hence, a small subset $\tilde{E}$ (also called reduced mesh) of the n_e elements of the full FE model and corresponding specific weighting coefficients ζ_e have to be identified in a way that the approximation

$$\mathbf{f}_{nl}^{m}(\zeta) \approx \tilde{\mathbf{f}}_{nl}^{m}(\zeta) = \sum_{\tilde{E}} \zeta_e \mathbf{\Phi}_e^{\mathsf{T}} \mathbf{f}_{nl,e}\left(\mathbf{\Phi}_e \zeta\right) \tag{5.12}$$

preserves the virtual work performed by the full FE model. The selection of elements in the reduced mesh and the computation of the weighting factors can be performed off-line based on training configurations solving a non-negative least-square problem. More details on this algorithm can be found in [31, 33].

For the application to nonlinear contact and friction forces, again the question arises if the selected elements (reduced mesh) are valid to describe the very local and time varying nonlinear behavior.

5.2 Separated time integration of low and high frequency modes

Although the number of necessary joint modes for accurate results is much smaller than the number of FE DOFs in the joint are, the resulting number of equations for a flexible multibody system can be still large.

It has been demonstrated in the work of Sherif [116, 119] that a reduction basis consisting of global and local modes can be separated into two groups of low and high frequency modes, respectively. The low frequency modes (LFM) usually describe the global deformation of the body, while the high frequency modes (HFM) mostly represent local deformations which

play an indispensable role in contact problems. In the context of this thesis, the presented joint modes are such HFM. Using a quasi-static approach by neglecting the inertia forces associated with the HFM, was found to lead to a significant reduce in CPU time. Moreover, according to [116, 119], a quasi-static consideration of HFM does not have a notable influence on the resulting quality.

By applying the simplifications of the mass matrix as discussed in section 2.1.1 (using *free-free modes* and setting the body coordinate system to the center of mass), the equations of motion of a single body can be written in the following form

$$\begin{bmatrix} \boldsymbol{\mathcal{M}}_{RR} & \mathbf{0} & \mathbf{0} & \mathbf{0} \\ & \boldsymbol{\mathcal{M}}_{\theta\theta} & \boldsymbol{\mathcal{M}}_{\theta 1} & \boldsymbol{\mathcal{M}}_{\theta 2} \\ & & \boldsymbol{\mathcal{M}}_{11} & \mathbf{0} \\ \text{sym.} & & & \boldsymbol{\mathcal{M}}_{22} \end{bmatrix} \begin{bmatrix} \ddot{\mathbf{R}} \\ \ddot{\boldsymbol{\theta}} \\ \ddot{\boldsymbol{\zeta}}_1 \\ \ddot{\boldsymbol{\zeta}}_2 \end{bmatrix} + \begin{bmatrix} \mathbf{0} & \mathbf{0} & \mathbf{0} & \mathbf{0} \\ & \mathbf{0} & \mathbf{0} & \mathbf{0} \\ & & \boldsymbol{\mathcal{K}}_{11} & \mathbf{0} \\ \text{sym.} & & & \boldsymbol{\mathcal{K}}_{22} \end{bmatrix} \begin{bmatrix} \mathbf{R} \\ \boldsymbol{\theta} \\ \boldsymbol{\zeta}_1 \\ \boldsymbol{\zeta}_2 \end{bmatrix} = \begin{bmatrix} \mathbf{Q}_R \\ \mathbf{Q}_\theta \\ \mathbf{Q}_1 \\ \mathbf{Q}_2 \end{bmatrix} - \begin{bmatrix} \mathbf{C}_\mathbf{R}^\mathsf{T} \\ \mathbf{C}_\theta^\mathsf{T} \\ \mathbf{C}_1^\mathsf{T} \\ \mathbf{C}_2^\mathsf{T} \end{bmatrix} \boldsymbol{\lambda}. \tag{5.13}$$

In this equation the flexible coordinates $\boldsymbol{\zeta}$ are split into $\boldsymbol{\zeta}_1, \boldsymbol{\zeta}_2$ being the flexible coordinates of the bodies low and high frequency modes, respectively. Furthermore, the quadratic velocity vector $\mathbf{Q}_v$, the vector of generalized external forces $\mathbf{Q}_e$, and the generalized nonlinear forces $\mathbf{Q}_{nl}$ are combined in one vector $\mathbf{Q} = \mathbf{Q}_v + \mathbf{Q}_e + \mathbf{Q}_{nl}$.

In eq. (5.13), the mass coupling of all flexible coordinates to the rigid body motion and the mass orthogonality of the LFM and HFM has to be mentioned. In [119] it was demonstrated that inertia forces related to the HFM can be excluded from time integration of eq. (5.13) (setting $\boldsymbol{\mathcal{M}}_{\theta 2} = \mathbf{0}, \boldsymbol{\mathcal{M}}_{22} = \mathbf{0}$). This leads to a simplification of eq. (5.13), and hence the equation of motion can be written the following form

$$\begin{bmatrix} \boldsymbol{\mathcal{M}}_{RR} & \mathbf{0} & \mathbf{0} \\ & \boldsymbol{\mathcal{M}}_{\theta\theta} & \boldsymbol{\mathcal{M}}_{\theta 1} \\ \text{sym.} & & \boldsymbol{\mathcal{M}}_{11} \end{bmatrix} \begin{bmatrix} \ddot{\mathbf{R}} \\ \ddot{\boldsymbol{\theta}} \\ \ddot{\boldsymbol{\zeta}}_1 \end{bmatrix} + \begin{bmatrix} \mathbf{0} & \mathbf{0} & \mathbf{0} \\ & \mathbf{0} & \mathbf{0} \\ \text{sym.} & & \boldsymbol{\mathcal{K}}_{11} \end{bmatrix} \begin{bmatrix} \mathbf{R} \\ \boldsymbol{\theta} \\ \boldsymbol{\zeta}_1 \end{bmatrix} + \begin{bmatrix} \mathbf{C}_\mathbf{R}^\mathsf{T} \\ \mathbf{C}_\theta^\mathsf{T} \\ \mathbf{C}_1^\mathsf{T} \end{bmatrix} \boldsymbol{\lambda} = \begin{bmatrix} \mathbf{Q}_R \\ \mathbf{Q}_\theta \\ \mathbf{Q}_1(\boldsymbol{\zeta}_1, \boldsymbol{\zeta}_2) \end{bmatrix} \tag{5.14a}$$

$$\boldsymbol{\mathcal{K}}_{22}\boldsymbol{\zeta}_2 = \mathbf{Q}_2(\boldsymbol{\zeta}_1, \boldsymbol{\zeta}_2) - \mathbf{C}_2^\mathsf{T}\boldsymbol{\lambda}. \tag{5.14b}$$

The key point of Sherif [116, 119] was that the dimension of the differential equation (eq. (5.14a)) for numerical time integration is thereby reduced compared to the original formulation. On the other hand, an additional set of algebraic equations (eq. (5.14b)) has to be solved in each time step. For the consideration of contact and friction forces, the two equations eqs. (5.14a) and (5.14b) are coupled via the state dependent generalized force vector $\mathbf{Q}(\boldsymbol{\theta}, \boldsymbol{\zeta}_1, \boldsymbol{\zeta}_2)$.

The time integration of eq. (5.14a) can be performed with commercial or free multibody simulation packages if $\boldsymbol{\zeta}_2$ is computed from eq. (5.14b) and inserted into eq. (5.14a). The computation of eq. (5.14b) and the right-hand side of eq. (5.14a) is performed by a user subroutine which communicates with the time integration of eq. (5.14a). This reduces the computational effort while at the same time the result quality should not change significantly.

Concerning the separated time integration proposed by [116, 119] the following questions arise for further research on this topic:

a) The subdivision of all modes into LFM and HFM leads to the decoupling outlined above and shown in detail in [116]. Herein an important assumption is that the inertia forces caused by $\boldsymbol{\mathcal{M}}_{\theta 2}$ can be omitted. Another issue is that the approximation $\mathbf{C}\left(\ldots, \boldsymbol{\zeta}_1, \boldsymbol{\zeta}_2\right) \approx \mathbf{C}\left(\ldots, \boldsymbol{\zeta}_1\right)$ is assumed. Hence, the question arises whether these two assumptions are valid with respect to a predefined result quality. Therefore, an algorithm to check particular simulation results with respect to these two assumptions might be a possible approach.
b) Due to the transformation of all trail vectors (Craig-Bampton modes and joint modes) into free-free modes the separation of LFM and HFM is not obvious. Hence, it is necessary to derive an a priori selection criterion for the subdivision into LFM and HFM.
c) The pure static consideration of HFM leads to a system with an unsteady step response due to the absence of mass. This might lead to numerical problems. Hence, another research question might be the extension of the pure static consideration of HFM to a dynamic problem including the mass matrix $\boldsymbol{\mathcal{M}}_{22}$ and a modal damping matrix $\boldsymbol{\mathcal{D}}_{22}$. In this case, eq. (5.14b) is extended to

$$\boldsymbol{\mathcal{M}}_{22}\ddot{\boldsymbol{\zeta}}_2 + \boldsymbol{\mathcal{D}}_{22}\dot{\boldsymbol{\zeta}}_2 + \boldsymbol{\mathcal{K}}_{22}\boldsymbol{\zeta}_2 = \mathbf{Q}_2(\boldsymbol{\zeta}_1, \boldsymbol{\zeta}_2) - \mathbf{C}_2^{\mathsf{T}}\boldsymbol{\lambda}, \tag{5.15}$$

where the left-hand side of eq. (5.15) consists of diagonal and time invariant matrices.

6 Summary and conclusions

The intention of the present dissertation was to develop a complete strategy for efficient and accurate consideration of contact and friction inside jointed flexible structures within multibody simulations. For this purpose the thesis has focused on

a) the inclusion of nonlinear joint forces in the equations of motion,
b) the accurate representation of joint deformations via joint modes,
c) the efficient computation of contact pressure, and
d) the efficient modeling of dry friction characteristics.

Inside the multibody system the jointed structure has been considered as one flexible body which includes the joint area. Thereby it has been avoided to model the joint between two flexible bodies in the multibody formulation. The equations of motion for a flexible multibody system (derived by a floating frame of reference formulation) have been extended with respect to nonlinear joint forces within the flexible body. For this purpose the vector of generalized nonlinear joint forces has been derived from the virtual work of the nonlinear joint forces. This leads to the conclusion that the nonlinear joint forces are self-equilibrated forces which have no contribution to the rigid body components of the generalized forces. Moreover, an efficient computation of the contact pressure, the frictional stress and the corresponding terms of the system's Jacobian using only the flexible coordinates has been formulated based on this insight.

Three novel strategies for the computation of general joint modes have been introduced. These general joint modes are used for a problem-oriented extension of a common reduction basis and enable an accurate representation of the local joint deformations. All joint mode methods, namely

a) joint modes based on weighted POD of TVDs (wPOD of TVDs),
b) joint modes based on unweighted POD of TVDs (POD of TVDs), and
c) joint modes based on unweighted POD of fictive forces (POD of forces),

are based on the use of trial vector derivatives of the reduction basis of the linear structure. To compute the joint modes, proper orthogonal decomposition has been applied with and without inner weighting to these trial vector derivatives and the corresponding fictive forces. For the required number of joint modes an a-priori estimator has been introduced, which is a by-product of the proper orthogonal decomposition. The three joint mode methods have been compared to each other on two numerical examples in terms of convergence rate and the usability of the estimator.

The numerical investigations indicate that for all presented general joint mode methods the joint nonlinearities in terms of contact forces can be considered with an accuracy which is comparable to the finite element method. The number of joint modes is up to 95% lower than the number of nodal degrees of freedom inside the joint area whereby the achieved results in terms of stresses and displacements are comparable to a full finite element simulation. In conclusion, the general joint modes computed by a stiffness weighted proper orthogonal decomposition (wPOD of TVDs) are recommended for practical application. This recommendation is based on the connection of these joint modes to the deformation energy covered by all trial vector derivatives and the best correlation to the a-priori estimator.

Beside the general joint modes, a specialized extension of a common reduction basis for preloaded structures has been presented. For such preloaded structures, like clamped joints, the deformations and stresses can be dominated by the preload state even during a dynamic simulation. Hence, so-called preload modes which consider the deformations due to preload forces have been included in the reduction basis. Moreover, a specialized computation method for preloaded joint modes has been introduced. The method assumes that the trial vector derivatives corresponding to the preload modes are significant for the computation of joint modes since these preload modes cover the dominating deformations. This method leads to a major reduction of the computational effort for joint modes.
Two numerical investigations confirmed the excellent convergence of preloaded joint modes for preload deformations due to the inclusion of preload modes. The joint forces due to preload deformations can be captured with the inclusion of the preload modes only. For both investigated examples a straighter convergence of the preloaded joint modes considering only preload mode derivatives has been observed. The number of joint modes computed with preload mode derivatives only is up to 50% lower than the number of general joint modes. Nevertheless, for the practical application of these preloaded joint modes some limitations have to be considered in order to avoid poor quality results. The limitations are mainly caused by the fact that the preload deformations are no longer dominating in case of high dynamics of the structure.

Different contact and friction models for dry friction found in literature have been reviewed and rated. The defined physical characteristics and numerical efficiency have been considered as criteria for this rating. For the efficient computation of the contact pressure an adaption of an exponential penalty model is recommended. This model is based on some contact physical background and requires low computational effort. The three-parameter Coulomb-type friction model turned out to be the best choice for computing the frictional stress. This model reproduces the characteristics of dry friction well, and is also numerically very efficient, although it is not continuous.

The presented strategy for considering jointed structures inside a flexible multibody system has been implemented in the free multibody software *FreeDyn* and is also available via a subroutine for *MSC.ADAMS*. Based on this implementation, it was possible to analyze two industrial applications from automotive engineering with the presented strategy.

In conclusion, the proposed method allows efficient computation of the dynamics of jointed structures within flexible multibody simulations. Due to the used joint modes, the result

quality of the computed joint forces and joint deformations is thereby comparable to the finite element method with only a few additional degrees of freedom.

Bibliography

[1] F. M. L. Amirouche. *Fundamentals of multibody dynamics: Theory and applications*. Boston: Birkhäuser, 2006. ISBN: 978-0-8176-4236-5.

[2] B. Armstrong-Hélouvry, P. Dupont, and C. C. De Wit. "A survey of models, analysis tools and compensation methods for the control of machines with friction." In: *Automatica* 30.7 (1994), pp. 1083–1138. ISSN: 0005-1098. DOI: 10.1016/0005-1098(94)90209-7.

[3] U. M. Ascher and L. R. Petzold. *Computer Methods for Ordinary Differential Equations and Differential-Algebraic Equations*. SIAM: Society for Industrial and Applied Mathematics, 1998. ISBN: 0898714125.

[4] K. Atkinson. *An Introduction to Numerical Analysis*. John Wiley & Sons, Inc., 1989. ISBN: 0471624896.

[5] E. Balmès. "Use of Generalized Interface Degrees of Freedom in Component Mode Synthesis." In: *Proceedings of the IMAC XIV*. Dearborn, Michigan, USA, 1996, pp. 1–7.

[6] R. van Basshuysen and F. Schäfer, eds. *Handbuch Verbrennungsmotor*. Springer Fachmedien Wiesbaden, 2017. DOI: 10.1007/978-3-658-10902-8.

[7] K.-J. Bathe. *Finite Element Procedures*. Upper Saddle River, New Jersey: Prentice Hall, 1996. ISBN: 0-13-301458-4.

[8] O. A. Bauchau. *Flexible Multibody Dynamics*. Vol. 176. Solid Mechanics and Its Applications. Springer Netherlands, 2011. ISBN: 978-94-007-0335-3. DOI: 10.1007/978-94-007-0335-3.

[9] O. A. Bauchau, C. L. Bottasso, and L. Trainelli. "Robust integration schemes for flexible multibody systems." In: *Computer Methods in Applied Mechanics and Engineering* 192.3–4 (2003), pp. 395–420. ISSN: 0045-7825. DOI: 10.1016/S0045-7825(02)00519-4.

[10] J. Becker and L. Gaul. "CMS Methods for Efficient Damping Prediction for Structures with Friction." In: *Proceedings of the IMAC - XXVI*. 2008.

[11] S. Bograd et al. "Modeling the dynamics of mechanical joints." In: *Mechanical Systems and Signal Processing* 25.8 (2011), pp. 2801–2826. ISSN: 0888-3270. DOI: 10.1016/j.ymssp.2011.01.010.

[12] F. Bourquin and F. d'Hennezel. "Intrinsic component mode synthesis and plate vibrations." In: *Computers & Structures* 44.1-2 (1992), pp. 315–324. ISSN: 0045-7949. DOI: 10.1016/0045-7949(92)90250-4.

[13] K. Brahmi and N. Bouhaddi. "Improved Component Mode Synthesis Based on Double Condensation Method." In: *Proceedings of the IMAC XV*. Orlando, Florida, USA, 1997, pp. 1469–1475.

[14] M. Breitfuss and H. J. Holl. "Numerical Studies on the Reduced Order Modeling of Frictionless Joint Contact Interfaces." In: *Shock & Vibration, Aircraft/Aerospace, Energy Harvesting, Acoustics & Optics, Volume 9: Proceedings of the 34th IMAC, A Conference and Exposition on Structural Dynamics 2016*. Ed. by A. Brandt and R. Singhal. Cham: Springer International Publishing, 2016, pp. 167–178. ISBN: 978-3-319-30087-0. DOI: 10.1007/978-3-319-30087-0_15.

[15] M. Breitfuss et al. "DEIM for the Efficient Computation of Contact Interface Stresses." In: *Dynamics of Coupled Structures, Volume 1: Proceedings of the 32nd IMAC, A Conference and Exposition on Structural Dynamics, 2014*. Ed. by M. Allen, R. Mayes, and D. Rixen. Cham: Springer International Publishing, 2014, pp. 435–445. ISBN: 978-3-319-04501-6. DOI: 10.1007/978-3-319-04501-6_41.

[16] C. Canudas De Wit et al. "A new model for control of systems with friction." In: *Automatic Control, IEEE Transactions on* 40.3 (1995), pp. 419–425. ISSN: 0018-9286. DOI: 10.1109/9.376053.

[17] A. Chatterjee. "An Introduction to the Proper Orthogonal Decomposition." In: *Current Science* 78.7 (2000), pp. 808–817.

[18] S. Chaturantabut and D. C. Sorensen. "Nonlinear Model Reduction via Discrete Empirical Interpolation." In: *SIAM Journal on Scientific Computing* 32.5 (2010), pp. 2737–2764. DOI: 10.1137/090766498.

[19] T. B. Co. *Methods of Applied Mathematics for Engineers and Scientists*. Cambridge: Cambridge University Press, 2012. ISBN: 9781139021821. DOI: 10.1017/CBO9781139021821.

[20] R. R. Craig. "A Review of Time-Domain and Frequency-Domain Component Mode Synthesis Method." In: *Combined experimental/analytical modeling of dynamic structural systems; Proceedings of the Joint Mechanics Conference*. 1985, pp. 1–30.

[21] R. R. Craig. "Coupling of substructures for dynamic analyses: An overview." In: *41st Structures, Structural Dynamics, and Materials Conference and Exhibit*. Structures, Structural Dynamics, and Materials and Co-located Conferences. American Institute of Aeronautics and Astronautics, 2000, pp. 1–12. DOI: 10.2514/6.2000-1573.

[22] R. R. Craig and M. C. C. Bampton. "Coupling of substructures for dynamic analysis." In: *AIAA Journal* 6.7 (1968), pp. 1313–1319. ISSN: 0001-1452. DOI: 10.2514/3.4741.

[23] R. R. Craig and A. J. Kurdila. *Fundamentals of Structural Dynamics*. 2nd ed. Hoboken, New Jersey: John Wiley & Sons, Inc., 2006. ISBN: 978-0-471-43044-5.

[24] P. R. Dahl. "A Solid Friction Model." In: *Aerospace Corporation, El Segundo, CA, Tech. Rep. TOR-0158(3107-18)-1* (1968).

[25] P. R. Dahl. "Solid Friction Damping of Mechanical Vibrations." In: *AIAA Journal* 14.12 (1976), pp. 1675–1682. ISSN: 0001-1452. DOI: 10.2514/3.61511.

[26] Dassault Systemes. *Abaqus 6.12-3*.

[27] Dassault Systemes. *Abaqus Theory Manual 6.12*. 2012.

[28] E. Eich-Soellner and C. Führer. *Numerical Methods in Multibody Dynamics*. Vieweg+Teubner Verlag, 1998. DOI: 10.1007/978-3-663-09828-7.

[29] Engineering center steyr. *MAMBA*.

[30] J. Escalona et al. "Reference motion in deformable bodies under rigid body motion and vibration. Part I: theory." In: *Journal of Sound and Vibration* 264.5 (2003), pp. 1045–1056. ISSN: 0022-460X. DOI: 10.1016/S0022-460X(02)01187-2.

[31] C. Farhat, T. Chapman, and P. Avery. "Structure-preserving, stability, and accuracy properties of the energy-conserving sampling and weighting method for the hyper reduction of nonlinear finite element dynamic models." In: *International Journal for Numerical Methods in Engineering* 102.5 (2015), pp. 1077–1110. DOI: 10.1002/nme.4820.

[32] C. Farhat and M. Geradin. "A hybrid formulation of a component mode synthesis method." In: *33rd Structural Dynamics and Materials Conference*. Vol. AIAA-92-2383-CP, pp. 1783–1796. DOI: 10.2514/6.1992-2383.

[33] C. Farhat et al. "Dimensional reduction of nonlinear finite element dynamic models with finite rotations and energy-based mesh sampling and weighting for computational efficiency." In: *International Journal for Numerical Methods in Engineering* 98.9 (2014), pp. 625–662. DOI: 10.1002/nme.4668.

[34] B. F. Feeny and R. Kappagantu. "On the physical interpretation of proper orthogonal modes in vibrations." In: *Journal of Sound and Vibration* 211.4 (1998), pp. 607–616. ISSN: 0022-460X. DOI: 10.1006/jsvi.1997.1386.

[35] R. H. B. Fey, D. H. van Campen, and A. de Kraker. "Long Term Structural Dynamics of Mechanical Systems With Local Nonlinearities." In: *Journal of Vibration and Acoustics* 118.2 (1996), pp. 147–153. ISSN: 0739-3717. DOI: 10.1115/1.2889642.

[36] P. Fischer and M. Engelbrechtsmüller. "Local Damping Effects in Acoustic Analysis of Large FE Engine Structures." In: *Proceedings of ISMA 25th*. 2000, pp. 1293–1299.

[37] O. Friberg and V. Karhu. "Use of mode orthogonalization and modal damping in flexible multibody dynamics." In: *Finite Elements in Analysis and Design* 7.1 (1990), pp. 51–59. ISSN: 0168-874X. DOI: 10.1016/0168-874X(90)90014-6.

[38] M. Friswell, J. Penny, and S. Garvey. "Using linear model reduction to investigate the dynamics of structures with local non-linearities." In: *Mechanical Systems and Signal Processing* 9.3 (1995), pp. 317–328. ISSN: 0888-3270. DOI: 10.1006/mssp.1995.0026.

[39] C. G. Garino and J.-P. Ponthot. "A quasi-coulomb model for frictional contact interfaces: Application to metal forming simulations." In: *Latin American Applied Research* 38.2 (2008), pp. 95–104.

[40] L. Gaul and R. Nitsche. "The Role of Friction in Mechanical Joints." In: *Applied Mechanics Reviews* 54.2 (2001), pp. 93–106. ISSN: 0003-6900. DOI: 10.1115/1.3097294.

[41] L. Gaul and J. Becker. "Damping Prediction of Structures with Bolted Joints." In: *Shock and Vibration* 17.4-5 (2010), pp. 359–371. DOI: 10.3233/SAV-2010-0532.

[42] L. Gaul and J. Lenz. "Nonlinear dynamics of structures assembled by bolted joints." In: *Acta Mechanica* 125.1-4 (1997), pp. 169–181. ISSN: 0001-5970. DOI: 10.1007/BF01177306.

[43] L. Gaul and M. Mayer. "Modeling of Contact Interfaces in Built-up Structures by Zero-thickness Elements." In: *Proceedings of the IMAC XXVI*. 2008.

[44] M. Geradin and D. J. Rixen. *Mechanical Vibrations - Theory and Application to Structural Dynamics*. 3. Aufl. New York: John Wiley & Sons, 2015. ISBN: 978-1-118-90020-8.

[45] M. Géradin and D. J. Rixen. "A 'nodeless' dual superelement formulation for structural and multibody dynamics application to reduction of contact problems." In: *International Journal for Numerical Methods in Engineering* 106.10 (2016), pp. 773–798. DOI: 10.1002/nme.5136.

[46] J. Gerstmayr et al. "The Absolute Nodal Coordinate Formulation." In: *Structure-preserving Integrators in Nonlinear Structural Dynamics and Flexible Multibody Dynamics*. Ed. by P. Betsch. Cham: Springer International Publishing, 2016, pp. 159–200. ISBN: 978-3-319-31879-0. DOI: 10.1007/978-3-319-31879-0_4.

[47] J. H. Gordis and J. Radwick. "Efficient Transient Analysis for Large Locally Nonlinear Structures." In: *Shock and Vibration* 6.1 (1999). DOI: 10.1155/1999/269370.

[48] J. A. Greenwood and J. B. P. Williamson. "Contact of nominally flat surfaces." In: *Proceedings of the Royal Society* vol. 295 no. 1442 (1966), pp. 300–319. DOI: 10.1098/rspa.1966.0242.

[49] R. J. Guyan. "Reduction of stiffness and mass matrices." In: *AIAA Journal* 3.2 (1965), p. 380. ISSN: 0001-1452. DOI: 10.2514/3.2874.

[50] P. Hagedorn and W. Schramm. "On the Dynamics of Large Systems With Localized Nonlinearities." In: *Journal of Applied Mechanics* 55.4 (1988), pp. 946–951. ISSN: 0021-8936. DOI: 10.1115/1.3173746.

[51] S. Han and B. Feeny. "APPLICATION OF PROPER ORTHOGONAL DECOMPOSITION TO STRUCTURAL VIBRATION ANALYSIS." In: *Mechanical Systems and Signal Processing* 17.5 (2003), pp. 989–1001. ISSN: 0888-3270. DOI: 10.1006/mssp.2002.1570.

[52] H. M. Hilber, T. J. R. Hughes, and R. L. Taylor. "Improved numerical dissipation for time integration algorithms in structural dynamics." In: *Earthquake Engineering & Structural Dynamics* 5.3 (1977), pp. 283–292. ISSN: 1096-9845. DOI: 10.1002/eqe.4290050306.

[53] T. J. R. Hughes. *The Finite Element Method: Linear Static and Dynamic Finite Element Analysis*. Englewood Cliffs, New Jersey: Prentice Hall, 1987. ISBN: 013317025X.

[54] W. C. Hurty. "Dynamic analysis of structural systems using component modes." In: *AIAA Journal* 3.4 (1965), pp. 678–685. ISSN: 0001-1452. DOI: 10.2514/3.2947.

[55] S. R. Idelsohn and A. Cardona. "A load-dependent basis for reduced nonlinear structural dynamics." In: *Computers & Structures* 20.1-3 (1985), pp. 203–210. ISSN: 0045-7949. DOI: 10.1016/0045-7949(85)90069-0.

[56] S. R. Idelsohn and A. Cardona. "A reduction method for nonlinear structural dynamic analysis." In: *Computer Methods in Applied Mechanics and Engineering* 49.3 (1985), pp. 253–279. ISSN: 0045-7825. DOI: 10.1016/0045-7825(85)90125-2.

[57] S. Jain et al. "A quadratic manifold for model order reduction of nonlinear structural dynamics." In: *Computers & Structures* 188 (2017), pp. 80–94. ISSN: 0045-7949. DOI: 10.1016/j.compstruc.2017.04.005.

[58] G. Kerschen et al. "The Method of Proper Orthogonal Decomposition for Dynamical Characterization and Order Reduction of Mechanical Systems: An Overview." In: *Nonlinear Dynamics* 41.1 (2005), pp. 147–169. ISSN: 0924-090X. DOI: 10.1007/s11071-005-2803-2.

[59] P. Koutsovasilis and M. Beitelschmidt. "Comparison of model reduction techniques for large mechanical systems." In: *Multibody System Dynamics* 20.2 (2008), pp. 111–128. ISSN: 1573-272X. DOI: 10.1007/s11044-008-9116-4.

[60] T. A. Laursen. *Computational Contact and Impact Mechanics: Fundamentals of Modeling Interfacial Phenomena in Nonlinear Finite Element Analysis*. Springer-Verlag Berlin Heidelberg, 2002. ISBN: 978-3-540-42906-7. DOI: 10.1007/978-3-662-04864-1.

[61] J. Lenz. "Strukturdynamik unter dem Einfluß von Mikro- und Makroschlupf in Fügestellen." PhD thesis. Universität der Bundeswehr Hamburg, 1997.

[62] J. Lenz and L. Gaul. "The Influence of Microslip on the Dynamic Behavior of Bolted Joints." In: *Proceedings of the IMAC XIII*. Society of experimental mechanics, 1995, pp. 248–254.

[63] C. Lerch and C. H. Meyer. "Modellordnungsreduktion für parametrische nichtlineare mechanische Systeme mittels erweiterter simulationsfreier Basen und Hyperreduktion." In: *Methoden und Anwendungen der Regelungstechnik*. Ed. by B. Lohmann and G. Roppenecker. Shaker Verlag, 2017, pp. 67–86.

[64] Y. C. Liang et al. "Proper Orthogonal Decomposition and its Applications - Part I: Theory." In: *Journal of Sound and Vibration* 252.3 (2002), pp. 527–544. ISSN: 0022-460X. DOI: 10.1006/jsvi.2001.4041.

[65] Y. C. Liang et al. "Proper orthogonal decomposition and its applications – part II: model reduction for MEMS dynamical analysis." In: *Journal of Sound and Vibration* 256.3 (2002), pp. 515–532. ISSN: 0022-460X. DOI: 10.1006/jsvi.2002.5007.

[66] P. W. Likins. "Modal method for analysis of free rotations of spacecraft." In: *AIAA Journal* 5.7 (1967), pp. 1304–1308. ISSN: 0001-1452. DOI: 10.2514/3.4188.

[67] R. H. MacNeal. "A hybrid method of component mode synthesis." In: *Special Issue on Structural Dynamics* 1.4 (1971), pp. 581–601. ISSN: 0045-7949. DOI: 10.1016/0045-7949(71)90031-9.

[68] F. Marques, P. Flores, and H. M. Lankarani. "On the Frictional Contacts in Multibody System Dynamics." In: *Multibody Dynamics: Computational Methods and Applications*. Ed. by M. J. Font-Llagunes. Cham: Springer International Publishing, 2016, pp. 67–91. ISBN: 978-3-319-30614-8. DOI: 10.1007/978-3-319-30614-8_4.

[69] M. Mayer and L. Gaul. "Modeling of Contact Interfaces using Segment-to-Segment-Elements for FE Vibration Analysis." In: *Proceedings of the IMAC XXIII*. 2005, pp. 1–12.

[70] L. Meirovitch. *Computational Methods in Structural Dynamics*. Mechanics: Dynamical Systems. Springer, 1980. ISBN: 978-90-286-0580-0.

[71] M. P. Mignolet et al. "A review of indirect/non-intrusive reduced order modeling of nonlinear geometric structures." In: *Journal of Sound and Vibration* 332.10 (2013), pp. 2437–2460. ISSN: 0022-460X. DOI: 10.1016/j.jsv.2012.10.017.

[72] B. Miled, D. Ryckelynck, and S. Cantournet. "A priori hyper-reduction method for coupled viscoelastic–viscoplastic composites." In: *Computers & Structures* 119 (2013), pp. 95–103. ISSN: 0045-7949. DOI: 10.1016/j.compstruc.2012.11.017.

[73] MSC Software Corporation. *MSC.ADAMS V2012*.

[74] MSC Software Corporation. *MSC.NASTRAN V2013.1.1*.

[75] D. Negrut et al. "On an Implementation of the Hilber-Hughes-Taylor Method in the Context of Index 3 Differential-Algebraic Equations of Multibody Dynamics (DETC2005-85096)." In: *Journal of Computational and Nonlinear Dynamics* 2.1 (2006), pp. 73–85. ISSN: 1555-1415. DOI: 10.1115/1.2389231.

[76] D. Negrut et al. "On the Use of the HHT Method in the Context of Index 3 Differential Algebraic Equations of Multibody Dynamics." In: *ASME 2005 International Design Engineering Technical Conferences and Computers and Information in Engineering Conference*. Vol. 6: 5th International Conference on Multibody Systems, Nonlinear Dynamics, and Control, Parts A, B, and C. 2005, pp. 1–12.

[77] R. B. Nelson. "Simplified calculation of eigenvector derivatives." In: *AIAA Journal* 14.9 (1976), pp. 1201–1205. ISSN: 0001-1452. DOI: 10.2514/3.7211.

[78] N. M. Newmark. "A Method of Computation for Structural Dynamics." In: *Journal of the Engineering Mechanics Division* Vol. 85, Issue 3 (1959), pp. 67–94.

[79] H. Olsson. "Control Systems with Friction." PhD thesis. Lund Institute of Technology - Department of Automatic Control, 1996.

[80] H. Olsson et al. "Friction Models and Friction Compensation." In: *European Journal of Control* 4.3 (1998), pp. 176–195. ISSN: 0947-3580. DOI: 10.1016/S0947-3580(98)70113-X.

[81] A. Padthe et al. "Duhem modeling of friction-induced hysteresis." In: *Control Systems, IEEE* 28.5 (2008), pp. 90–107. ISSN: 1066-033X. DOI: 10.1109/MCS.2008.927331.

[82] H. Parkus. *Mechanik der festen Körper*. 2., neubearb. u. um 123 Aufgaben erw. Aufl., 6. unveränd. Nachdr. Wien [u.a.]: Springer, 2005. ISBN: 3-211-80777-2.

[83] E. Pennestrì, P. P. Valentini, and L. Vita. "Multibody dynamics simulation of planar linkages with Dahl friction." In: *Multibody System Dynamics* 17.4 (2007), pp. 321–347. ISSN: 1573-272X. DOI: 10.1007/s11044-007-9047-5.

[84] E. Pennestrì et al. "Review and comparison of dry friction force models." In: *Nonlinear Dynamics* 83.4 (2016), pp. 1785–1801. ISSN: 0924-090X. DOI: 10.1007/s11071-015-2485-3.

[85] F. Pfeiffer. *Einführung in die Dynamik*. 3. Aufl. 2014. Berlin, Heidelberg: Springer Berlin Heidelberg, 2014. ISBN: 978-3-642-41046-8.

[86] F. Pfeiffer. *Mechanical system dynamics*. corr. 2. print. Vol. 40. Lecture notes in applied and computational mechanics. Berlin [u.a.]: Springer, 2008. ISBN: 3-540-79435-2.

[87] F. Pichler. "Effizientes Verfahren zur Berechnung mehrfach geschichteter Blechstrukturen auf Basis modaler Ableitungen." Master thesis. University of Applied Sciences Upper Austria - Campus Wels, 2013.

[88] F. Pichler and W. Witteveen. "Efficient Reduction Method based on Trial Vector Derivatives for Nonlinear Transient Analysis of Multilayer Sheet Structures." In: *PAMM* 14.1 (2014), pp. 37–38. ISSN: 1617-7061. DOI: 10.1002/pamm.201410011.

[89] F. Pichler, W. Witteveen, and P. Fischer. "A complete strategy for efficient and accurate multibody dynamics of flexible structures with large lap joints considering contact and friction." In: *Multibody System Dynamics* 40.4 (2017), pp. 407–436. ISSN: 1573-272X. DOI: 10.1007/s11044-016-9555-2.

[90] F. Pichler, W. Witteveen, and P. Fischer. "Efficient and Accurate Consideration of Nonlinear Joint Contact Within Multibody Simulation." In: *Nonlinear Dynamics, Volume 1*. Ed. by G. Kerschen. Conference Proceedings of the Society for Experimental Mechanics Series. Springer International Publishing, 2016, pp. 441–448. ISBN: 978-3-319-15220-2. DOI: 10.1007/978-3-319-15221-9_38.

[91] F. Pichler, W. Witteveen, and P. Fischer. "Reduced-order modeling of preloaded bolted structures in multibody systems by the use of trial vector derivatives." In: *Journal of Computational and Nonlinear Dynamics* 12.5 (2017), pp. 051032-051032-12. ISSN: 1555-1415. DOI: 10.1115/1.4036989.

[92] G. Prechtl. "Efficient consideration of non-linear friction in the joints of modal reduced structures." Master thesis. University of Applied Sciences Upper Austria - Campus Wels, 2011.

[93] Z.-Q. Qu. *Model Order Reduction Techniques with Applications in Finite Element Analysis*. Springer-London, 2004. ISBN: 978-1-4471-3827-3. DOI: 10.1007/978-1-4471-3827-3.

[94] Z.-Q. Qu. "Model Reduction for Dynamical Systems with Local Nonlinearities." In: *AIAA Journal* 40.2 (2002), pp. 327–333. ISSN: 0001-1452. DOI: 10.2514/2.1649.

[95] G. Rill and T. Schaeffer. *Grundlagen und Methodik der Mehrkörpersimulation*. Springer Nature, 2017. ISBN: 978-3-658-16008-1. DOI: 10.1007/978-3-658-16009-8.

[96] D. J. Rixen. "A dual Craig–Bampton method for dynamic substructuring." In: *Journal of Computational and Applied Mathematics* 168.1–2 (2004), pp. 383–391. ISSN: 0377-0427. DOI: 10.1016/j.cam.2003.12.014.

[97] D. J. Rixen and J. Rutzmoser. *Model reduction of non-linear structural dynamics models: A path in the jungle*. Zürich, 13.09.2016.

[98] T. Royston and R. Singh. "Periodic response of mechanical systems with local nonlinearities using an enhanced Galerkin technique." In: *Journal of Sound and Vibration* 194.2 (1996), pp. 243–263. ISSN: 0022-460X. DOI: 10.1006/jsvi.1996.0355.

[99] S. Rubin. "Improved Component-Mode Representation for Structural Dynamic Analysis." In: *AIAA Journal* 13.8 (1975), pp. 995–1006. ISSN: 0001-1452. DOI: 10.2514/3.60497.

[100] J. B. Rutzmoser et al. "Generalization of Quadratic Manifolds for Reduced Order Modeling of Nonlinear Structural Dynamics." In: ().

[101] D. Ryckelynck. "A priori hypereduction method: An adaptive approach." In: *Journal of Computational Physics* 202.1 (2005), pp. 346–366.

[102] D. Ryckelynck. "Hyper-reduction of mechanical models involving internal variables." In: *International Journal for Numerical Methods in Engineering* 77.1 (2009), pp. 75–89. DOI: 10.1002/nme.2406.

[103] D. Ryckelynck and D. M. Benziane. "Multi-level A Priori Hyper-Reduction of mechanical models involving internal variables." In: *Computer Methods in Applied Mechanics and Engineering* 199.17–20 (2010), pp. 1134–1142. ISSN: 0045-7825. DOI: 10.1016/j.cma.2009.12.003.

[104] W. Schiehlen. "Multibody System Dynamics: Roots and Perspectives." In: *Multibody System Dynamics* 1.2 (1997), pp. 149–188. ISSN: 1573-272X. DOI: 10.1023/A:1009745432698.

[105] A. Schmidt and L. Gaul. "Finite Element Formulation of Viscoelastic Constitutive Equations Using Fractional Time Derivatives." In: *Nonlinear Dynamics* 29.1-4 (2002), pp. 37–55. ISSN: 0924-090X. DOI: 10.1023/A:1016552503411.

[106] A. Schmidt and L. Gaul. "On the numerical evaluation of fractional derivatives in multi-degree-of-freedom systems." In: *Signal Processing* 86.10 (2006), pp. 2592–2601. ISSN: 0165-1684. DOI: 10.1016/j.sigpro.2006.02.006.

[107] W. Schroeder, K. Martin, and B. Lorensen. *The Visualization Toolkit: An Object-Oriented Approach to 3D Graphics*. 4th ed. Kitware, 2006. ISBN: 1-930934-19-X.

[108] R. V. Schwerin. *Multibody System Simulation: Numerical Methods, Algorithms, and Software*. Secaucus, NJ, USA: Springer-Verlag New York, Inc, 2000. ISBN: 3540656626.

[109] R. Schwertassek, S. V. Dombrowski, and O. Wallrapp. "Modal Representation of Stress in Flexible Multibody Simulation." In: *Nonlinear Dynamics* 20.4 (1999), pp. 381–399. ISSN: 0924-090X. DOI: 10.1023/A:1008322210909.

[110] Scilab. *Version 5.5.0, http://www.scilab.org*.

[111] D. J. Segalman. "Model Reduction of Systems With Localized Nonlinearities." In: *Journal of Computational and Nonlinear Dynamics* 2.3 (2007), pp. 249–266. ISSN: 1555-1415. DOI: 10.1115/1.2727495.

[112] P. Seshu. "Substructuring and Component Mode Synthesis." In: *Shock and Vibration* 4.3 (1997), pp. 199–210. DOI: 10.3233/SAV-1997-4306.

[113] A. A. Shabana. "Definition of the Slopes and the Finite Element Absolute Nodal Coordinate Formulation." In: *Multibody System Dynamics* 1.3 (1997), pp. 339–348. ISSN: 1573-272X. DOI: 10.1023/A:1009740800463.

[114] A. A. Shabana. *Dynamics of Multibody Systems*. Cambridge, UK: Cambridge University Press, 2005. ISBN: 9780511610523. DOI: 10.1017/CBO9780511610523.

[115] A. A. Shabana. "Flexible Multibody Dynamics: Review of Past and Recent Developments." In: *Multibody System Dynamics* 1.2 (1997), pp. 189–222. ISSN: 1573-272X. DOI: 10.1023/A:1009773505418.

[116] K. Sherif. "Novel computationally efficient formulations for the equations of motion of a modally reduced flexible member undergoing large rigid body motion." Dissertation. Linz: Johannes Kepler Universität Linz, 2013.

[117] K. Sherif, H. Irschik, and W. Witteveen. "Transformation of Arbitrary Elastic Mode Shapes Into Pseudo-Free-Surface and Rigid Body Modes for Multibody Dynamic Systems." In: *Journal of Computational and Nonlinear Dynamics* 7.2 (2012), p. 021008. ISSN: 1555-1415. DOI: 10.1115/1.4005237.

[118] K. Sherif and K. Nachbagauer. "A Detailed Derivation of the Velocity-Dependent Inertia Forces in the Floating Frame of Reference Formulation." In: *Journal of Computational and Nonlinear Dynamics* 9.4 (2014), p. 044501. ISSN: 1555-1415. DOI: 10.1115/1.4026083.

[119] K. Sherif, W. Witteveen, and K. Mayrhofer. "Quasi-static consideration of high-frequency modes for more efficient flexible multibody simulations." In: *Acta Mechanica* 223.6 (2012), pp. 1285–1305. ISSN: 0001-5970. DOI: 10.1007/s00707-012-0624-1.

[120] V. Siddhi. "A generalized approach for calculation of the eigenvector sensitivity for various eigenvector normalizations." PhD thesis. University of Missouri – Columbia, 2005.

[121] P. Slaats, J. de Jongh, and A. Sauren. "Model reduction tools for nonlinear structural dynamics." In: *Computers & Structures* 54.6 (1995), pp. 1155–1171. ISSN: 0045-7949. DOI: 10.1016/0045-7949(94)00389-K.

[122] M. J. Smith and S. G. Hutton. "A Comparison of Fixed-interface and Free-interface Component Mode Synthesis Methods for Finite Element Models." In: *Proceedings of the IMAC XXII*. 1994, pp. 390–396.

[123] C. Sombroek et al. "Bridging the Gap Between Nonlinear Normal Modes and Modal Derivatives." In: *Nonlinear Dynamics, Volume 1: Proceedings of the 33rd IMAC, A Conference and Exposition on Structural Dynamics, 2015*. Ed. by G. Kerschen. Cham: Springer International Publishing, 2016, pp. 349–361. ISBN: 978-3-319-15221-9. DOI: 10.1007/978-3-319-15221-9_32.

[124] D. Stadlmayr, W. Witteveen, and W. Steiner. "Reduction of Physical and Constraint Degrees-of-Freedom of Redundant Formulated Multibody Systems." In: *Journal of Computational and Nonlinear Dynamics* 11.3 (2015), p. 031010. ISSN: 1555-1415. DOI: 10.1115/1.4031553.

[125] A. Steindl and H. Troger. "Methods for dimension reduction and their application in nonlinear dynamics." In: *International Journal of Solids and Structures* 38.10–13 (2001), pp. 2131–2147. ISSN: 0020-7683. DOI: 10.1016/S0020-7683(00)00157-8.

[126] W. Steiner. "Multibody Dynamics." Lecture notes. Wels: University of Applied Sciences Upper Austria - Campus Wels, 2012.

[127] E. Süli and D. F. Mayers. *An Introduction to Numerical Analysis*. Cambridge University Press, 2003. ISBN: 0521007941.

[128] P. Tiso. "Optimal second order reduction basis selection for nonlinear transient analysis." In: *Modal Analysis Topics, Volume 3: Proceedings of the 29th IMAC, A Conference on Structural Dynamics, 2011*. Ed. by T. Proulx. New York, NY: Springer New York, 2011, pp. 27–39. ISBN: 978-1-4419-9299-4. DOI: 10.1007/978-1-4419-9299-4_3.

[129] P. Tiso, E. Jansen, and M. Abdalla. "Reduction Method for Finite Element Nonlinear Dynamic Analysis of Shells." In: *AIAA Journal* 49.10 (2011), pp. 2295–2304. ISSN: 0001-1452. DOI: 10.2514/1.J051003.

[130] P. Tiso and D. J. Rixen. "Discrete Empirical Interpolation Method for Finite Element Structural Dynamics." In: *Topics in Nonlinear Dynamics, Volume 1: Proceedings of the 31st IMAC, A Conference on Structural Dynamics, 2013*. Ed. by G. Kerschen, D. Adams, and A. Carrella. New York, NY: Springer New York, 2013, pp. 203–212. ISBN: 978-1-4614-6570-6. DOI: 10.1007/978-1-4614-6570-6_18.

[131] D.-M. Tran. "Component mode synthesis methods using interface modes. Application to structures with cyclic symmetry." In: *Computers & Structures* 79.2 (2001), pp. 209–222. ISSN: 0045-7949. DOI: 10.1016/S0045-7949(00)00121-8.

[132] University of Applied Sciences Upper Austria – Campus Wels. *FreeDyn: a free multibody dynamics simulation software*. 2016.

[133] S. Volkwein. *Model Reduction using Proper Orthogonal Decomposition*. December 7, 2011.

[134] T. M. Wasfy and A. K. Noor. "Computational strategies for flexible multibody systems." In: *Applied Mechanics Reviews* 56.6 (2003), pp. 553–613. ISSN: 0003-6900. DOI: 10.1115/1.1590354.

[135] O. Weeger, U. Wever, and B. Simeon. "On the use of modal derivatives for nonlinear model order reduction." In: *International Journal for Numerical Methods in Engineering* 108.13 (2016), pp. 1579–1602. ISSN: 1097-0207. DOI: 10.1002/nme.5267.

[136] K. Willner. "Ein statistisches Modell für den Kontakt metallischer Körper." PhD thesis. Universität der Bundeswehr Hamburg, 1995.

[137] K. Willner and L. Gaul. "A penalty approach for contact description by FEM based on interface physics." In: *Proceedings of Contact Mechanics II*. Ed. by M. H. Aliabadi and C. Allesandri. Vol. 7. Computational Mechanics Publications, 1995, pp. 257–264.

[138] W. Witteveen. "Modal based computation of jointed structures." Dissertation. Linz: Johannes Kepler Universität Linz, 2007.

[139] W. Witteveen and H. Irschik. "Efficient Computation of Joint Interface Modes." In: *Proceedings of the IMAC XXVII 2009*. Orlando, Florida USA, 2009, pp. 1–8.

[140] W. Witteveen and H. Irschik. "Efficient Mode-Based Computational Approach for Jointed Structures: Joint Interface Modes." In: *AIAA Journal* 47.1 (2009), pp. 252–263. ISSN: 0001-1452. DOI: 10.2514/1.38436.

[141] W. Witteveen and F. Pichler. "Efficient Model Order Reduction for the Dynamics of Nonlinear Multilayer Sheet Structures with Trial Vector Derivatives." In: *Shock and Vibration* 2014 (2014), 16 pages. DOI: 10.1155/2014/913136.

[142] W. Witteveen and F. Pichler. "Efficient Model Order Reduction for the Nonlinear Dynamics of Jointed Structures by the Use of Trial Vector Derivatives." In: *Dynamics of Coupled Structures, Volume 1*. Conference Proceedings of the Society for Experimental Mechanics Series. Cham: Springer International Publishing, 2014, pp. 147–155. ISBN: 978-3-319-04500-9. DOI: 10.1007/978-3-319-04501-6_13.

[143] W. Witteveen and F. Pichler. "Effiziente und genaue Berücksichtigung gefügter Flächen in der elastischen Mehrkörpersimulation auf Basis modaler Ableitungen." In: *Tagungsband NAFEMS DACH Regionalkonferenz*. Bamberg, 2016, pp. 226–229.

[144] W. Witteveen and K. Sherif. "POD based computation of Joint Interface Modes." In: *Linking Models and Experiments, Volume 2: Proceedings of the 29th IMAC, A Conference on Structural Dynamics, 2011*. Ed. by T. Proulx. New York: Springer, 2011, pp. 19–28. ISBN: 978-1-4419-9305-2. DOI: 10.1007/978-1-4419-9305-2_2.

[145] P. Wriggers, T. Vu Van, and E. Stein. "Finite element formulation of large deformation impact-contact problems with friction." In: *Computers & Structures* 37.3 (1990), pp. 319–331. ISSN: 0045-7949. DOI: 10.1016/0045-7949(90)90324-U.

[146] P. Wriggers. *Computational Contact Mechanics*. 2nd. Springer-Verlag Berlin Heidelberg, 2006. ISBN: 3-540-32608-1.

[147] L. Wu and P. Tiso. "Nonlinear model order reduction for flexible multibody dynamics: a modal derivatives approach." In: *Multibody System Dynamics* 36.4 (2016), pp. 405–425. ISSN: 1573-272X. DOI: 10.1007/s11044-015-9476-5.

[148] F. Ziegler. *Technische Mechanik der festen und flüssigen Körper*. Wien [u.a.]: Springer, 1985. ISBN: 3-211-81791-3.

[149] O. C. Zienkiewicz and R. L. Taylor. *The Finite Element Method for Solid and Structural Mechanics*. 6th ed. Elsevier Butterworth-Heinemann, 2005. ISBN: 0-7506-6321-9.

Appendix

Appendix A

Mathematical basics

This appendix outlines some mathematical basics used in the dissertation. The mathematical descriptions are mainly taken from the textbook of Co [19].

A.1 Eigenvalues and Eigenvectors

For a quadratic matrix $\mathbf{A}$ of size $(n \times n)$ a scalar λ_i is called eigenvalue of $\mathbf{A}$, if a vector $\mathbf{v}_i \neq \mathbf{0}$ of size $(n \times 1)$ can be found which fulfills the condition

$$\begin{aligned} \mathbf{A}\mathbf{v}_i &= \lambda_i \mathbf{v}_i \\ (\mathbf{A} - \lambda_i \mathbf{I})\, \mathbf{v}_i &= \mathbf{0}. \end{aligned} \tag{A.1}$$

Such vectors $\mathbf{v}_i$ are called eigenvectors of $\mathbf{A}$ and have the distinct property that the only effect $\mathbf{A}$ has on them is a scaling operation. Also $\mathbf{v}_i = \mathbf{0}$ is always a solution of eq. (A.1) and is known as the trivial solution (trivial vector).

To evaluate the eigenvectors of $\mathbf{A}$, $(\mathbf{A} - \lambda_i \mathbf{I})$ needs to be singular, that means,

$$\det(\mathbf{A} - \lambda_i \mathbf{I}) = 0. \tag{A.2}$$

The latter equation is called the characteristics equation of $\mathbf{A}$ and can be expanded into the characteristic polynomial. This characteristic polynomial leads to n roots for either real or complex eigenvalues λ_i. Based on the computed eigenvalues the corresponding eigenvector can be obtained by substituting each eigenvalue one at a time into eq. (A.1). The computed eigenvectors are often normalized to $\|\mathbf{v}_i\|_2 = 1$ to get an unique solution.

If the eigenvectors $\mathbf{v}_1, \ldots, \mathbf{v}_n$ are linear independent a nonsingular $(n \times n)$ matrix $\mathbf{T} = [\mathbf{v}_1, \ldots, \mathbf{v}_n]$ can be formed which fulfills

$$\mathbf{T}^{-1}\mathbf{A}\mathbf{T} = \begin{bmatrix} \lambda_1 & & 0 \\ & \ddots & \\ 0 & & \lambda_n \end{bmatrix} = \mathbf{\Lambda}. \tag{A.3}$$

If such a matrix $\mathbf{T}$ can be found, matrix $\mathbf{A}$ is called diagonalizable. Furthermore, if $\mathbf{A}$ is a symmetric matrix the eigenvectors are orthonormal and $\mathbf{A}$ is diagonalizable by

$$\mathbf{T}^\mathsf{T}\mathbf{A}\mathbf{T} = \mathbf{\Lambda}. \tag{A.4}$$

A generalized eigenvalue problem can be defined by finding a vector $\mathbf{v}_i$ that fulfills

$$\mathbf{A}\mathbf{v}_i = \lambda_i \mathbf{B}\mathbf{v}_i. \tag{A.5}$$

For symmetric and positive definite matrices $\mathbf{A}, \mathbf{B}$ real and positive eigenvalues λ_i are obtained. With suitable normalization of the eigenvectors it can be obtained that

$$\begin{aligned} \mathbf{T}^\mathsf{T}\mathbf{A}\mathbf{T} &= \mathbf{\Lambda} \\ \mathbf{T}^\mathsf{T}\mathbf{B}\mathbf{T} &= \mathbf{I}. \end{aligned} \tag{A.6}$$

A.2 Singular Value Decomposition (SVD)

One method for analyzing not square matrices, like $\mathbf{A}$ of size $(n \times m)$ is the so called singular value decomposition (SVD). For the matrix $\mathbf{A}$, a square and positive semidefinite and Hermitian matrix can be computed by $\mathbf{A}^\mathsf{T}\mathbf{A}$.

For any matrix, there exists a decomposition of the form

$$\mathbf{A} = \mathbf{U}\mathbf{S}\mathbf{V}^\mathsf{T}, \tag{A.7}$$

which is called SVD. The matrices $\mathbf{U}$ of size $(n \times n)$ and $\mathbf{V}$ of size $(m \times m)$ are both unitary. The $(n \times m)$ matrix $\mathbf{S}$ is a diagonal matrix of the form

$$\mathbf{S} = \left[\begin{array}{ccc|c} \sigma_1 & & 0 & \\ & \ddots & & \mathbf{0}_{[r \times m-r]} \\ 0 & & \sigma_r & \\ \hline & \mathbf{0}_{[n-r \times r]} & & \mathbf{0}_{[n-r \times m-r]} \end{array}\right], \tag{A.8}$$

which contains the r nonzero singular values $\sigma_1 \geq \sigma_2 \geq \sigma_r$ of $\mathbf{A}$, whereby r is the rank of $\mathbf{A}$. Furthermore, the singular values of $\mathbf{A}$ are given by

$$\sigma_i = \sqrt{\lambda_i}, \tag{A.9}$$

with λ_i being one eigenvalue of the matrix $\mathbf{A}^\mathsf{T}\mathbf{A}$.

Appendix B

Useful identities in the context of MBS

B.1 Rotation matrix and their time derivative

The (3×3) rotation matrix of a body $\mathbf{B}^i$ transforms a quantity described in an body coordinate system into the inertial coordinate system. The columns of the rotation matrix are the orthogonal unity-vectors $\vec{e}^{\,i}_1$, $\vec{e}^{\,i}_2$, $\vec{e}^{\,i}_3$. Due to the orthonormal conditions of these vectors

$$\vec{e}^{\,i}_k{}^{\mathsf{T}} \vec{e}^{\,i}_l = \begin{cases} 1 & \text{if } k = l \\ 0 & \text{if } k \neq l \end{cases} \tag{B.1}$$

the number of independent components of the rotation matrix reduces from nine to three. Hence, the rotation matrix can be parametrized with three degrees of freedom. The relations described by eq. (B.1) can be written as

$$\mathbf{B}^{i\mathsf{T}} \mathbf{B}^i = \mathbf{I} \tag{B.2}$$

or

$$\mathbf{B}^{i\mathsf{T}} = \mathbf{B}^{i-1} \tag{B.3}$$

which means, that the rotation matrix is a orthogonal matrix, and hence has only eigenvalues equal to 1 (if a right-hand coordinate system is formed).

Finding a proper parameterization of the rotation matrix is a main issue in rigid body kinematics. In literature [114, 126] different parameterizations like *Euler angles, Rodriguez parameters* or *Euler parameters* can be found. Irrespective of the used parameterization the rotation matrix is a function of the rotational coordinates $\mathbf{B}^i = \mathbf{B}^i(\boldsymbol{\theta}^i)$. The time derivative of the rotation matrix can therefore be written as

$$\dot{\mathbf{B}}^i = \sum_{k=1}^{n_r} \frac{\partial \mathbf{B}^i}{\partial \theta^i_k} \dot{\theta}^i_k, \tag{B.4}$$

where n_r is the number of rotational degrees of freedom in $\boldsymbol{\theta}^i$.

Differentiating the orthogonality property of the rotation matrix (eq. (B.2)) with respect to time leads to

$$\frac{d}{dt}\left(\mathbf{B}^{i\mathsf{T}} \mathbf{B}^i\right) = \mathbf{B}^{i\mathsf{T}} \dot{\mathbf{B}}^i + \dot{\mathbf{B}}^{i\mathsf{T}} \mathbf{B}^i = \mathbf{B}^{i\mathsf{T}} \dot{\mathbf{B}}^i + \left(\mathbf{B}^{i\mathsf{T}} \dot{\mathbf{B}}^i\right)^{\mathsf{T}} = \mathbf{0}. \tag{B.5}$$

This equation implies, that the term ${\mathbf{B}^i}^\mathsf{T}\dot{\mathbf{B}}^i$ is negative to its transpose, and hence must be a skew-symmetric matrix. This skew-symmetric matrix is defined as

$$\tilde{\boldsymbol{\omega}}^i = {\mathbf{B}^i}^\mathsf{T}\dot{\mathbf{B}}^i = \begin{bmatrix} 0 & -\omega_z & \omega_y \\ \omega_z & 0 & -\omega_x \\ -\omega_y & \omega_x & 0 \end{bmatrix} \tag{B.6}$$

with the three parameters $\omega_x, \omega_y, \omega_z$, which can be associated to the angular velocity vector $\vec{\boldsymbol{\omega}}^i = \begin{bmatrix}\omega_x & \omega_y & \omega_z\end{bmatrix}^\mathsf{T}$. With the skew-symmetric matrix $\tilde{\boldsymbol{\omega}}^i$ the time derivative of the rotation matrix can be expressed as

$$\dot{\mathbf{B}}^i = \mathbf{B}^i\tilde{\boldsymbol{\omega}}^i. \tag{B.7}$$

Inserting eq. (B.4) into eq. (B.6) leads to

$$\tilde{\boldsymbol{\omega}}^i = {\mathbf{B}^i}^\mathsf{T}\dot{\mathbf{B}}^i = \sum_{k=1}^{n_r} {\mathbf{B}^i}^\mathsf{T}\frac{\partial \mathbf{B}^i}{\partial \theta_k^i}\dot{\theta}_k^i = \sum_{k=1}^{n_r} \mathbf{G}_k^i\dot{\theta}_k^i \tag{B.8}$$

with

$$\mathbf{G}_k^i = {\mathbf{B}^i}^\mathsf{T}\frac{\partial \mathbf{B}^i}{\partial \theta_k^i}. \tag{B.9}$$

Since $\tilde{\boldsymbol{\omega}}^i$ is a skew-symmetric matrix only the three components $\mathbf{G}_k^i(2,3), \mathbf{G}_k^i(1,3), \mathbf{G}_k^i(2,1)$ must be considered. Introducing the vector $\vec{G}_k^i$ with this three components, eq. (B.8) can be rewritten as

$$\vec{\boldsymbol{\omega}}^i = \sum_{k=1}^{n_r} \vec{G}_k^i\dot{\theta}_k^i = \mathbf{G}\dot{\boldsymbol{\theta}}^i, \tag{B.10}$$

where the $(3 \times n_r)$ matrix $\mathbf{G}$ maps the rotational velocities $\dot{\boldsymbol{\theta}}^i$ to the angular velocity vector. The matrix $\mathbf{G}$ is thereby depending on the rotational coordinates $\mathbf{G} = \mathbf{G}(\boldsymbol{\theta}^i)$.

B.2 Virtual work of joint forces in the context of the FEM

From the theory of finite elements, the virtual work of joint forces is given by (see [60, 146])

$$\delta W_{nl} = \int_{\Gamma_c^S} \left[p_N\delta g_N + \tau_{F,1}\delta s_1 + \tau_{F,2}\delta s_2\right]\, d\Gamma_c, \tag{B.11}$$

where p_N denotes the contact pressure, δg_N denotes the variation of the normal gap, $\tau_{F,1}, \tau_{F,2}$ are the magnitudes of the frictional stresses in the two principal directions, and $\delta s_1, \delta s_2$ are the variations of the tangential displacements in these directions. Since the elastic deformations are defined with respect to the reference frame, the normal gap and the tangential displacements of the contacting master-slave particles P^M, P^S can be expressed

as a function of the deformation vectors $\vec{u}_f^M, \vec{u}_f^S$. In terms of generalized coordinates the deformations $\vec{u}_f^M, \vec{u}_f^S$ can be written as

$$\vec{u}_f^M = \mathbf{S}^M \boldsymbol{\zeta} \tag{B.12a}$$

$$\vec{u}_f^S = \mathbf{S}^S \boldsymbol{\zeta}. \tag{B.12b}$$

Hence, the variations $\delta g_N, \delta s_1, \delta s_2$ in eq. (B.11) are only depending on $\boldsymbol{\zeta}$, and the virtual work of joint forces can be written as

$$\delta W_{nl} = \mathbf{Q}_{nl}^{\mathsf{T}} \delta \mathbf{q} = \begin{bmatrix} (\mathbf{Q}_{nl})_R^{\mathsf{T}} & (\mathbf{Q}_{nl})_\theta^{\mathsf{T}} & (\mathbf{Q}_{nl})_f^{\mathsf{T}} \end{bmatrix} \begin{bmatrix} \delta \mathbf{R} \\ \delta \boldsymbol{\theta} \\ \delta \boldsymbol{\zeta} \end{bmatrix}, \tag{B.13}$$

were the vector generalized nonlinear joint forces $\mathbf{Q}_{nl}$ is defined as

$$\mathbf{Q}_{nl} = \begin{bmatrix} (\mathbf{Q}_{nl})_R \\ (\mathbf{Q}_{nl})_\theta \\ (\mathbf{Q}_{nl})_f \end{bmatrix} = \begin{bmatrix} \mathbf{0}_R \\ \mathbf{0}_\theta \\ (\mathbf{Q}_{nl})_f \end{bmatrix}. \tag{B.14}$$

Appendix C

Additional information on joint modes

C.1 Selection criteria for TVDs

Different selection criteria for direct use of TVDs in the reduction basis are reviewed in the following sections. These strategies are mentioned for the sake of completeness, but they have not considered in the investigations of this thesis.

C.1.1 Consideration of self derivatives $\frac{\partial \boldsymbol{\phi}_i}{\partial \zeta_i}$ only

One possible selection criterion is to consider only the TVD of a mode shape due to its own variation. This means that only $\frac{\partial \boldsymbol{\phi}_i}{\partial \zeta_i}$ TVDs are considered. Such an approach is used in some computations of [129]. This strategy completely neglects the dependency on other mode shapes, which might lead to poor results if modal interaction introduced through nonlinearities occurs.

C.1.2 Maximum Modal Interaction

Reference [57, 128] suggested a selection criterion for TVDs which are expected to be important. The selection strategy is based on *maximum modal interaction*, which uses the modal interaction factor

$$W_{i,j} = \int_0^T |\zeta_i(t)\zeta_j(t)| \, \mathrm{d}t \tag{C.1}$$

of the modal coordinates obtained from a linear simulation run over the time period $[0, T]$. It is assumed that if the modal interaction factor of the linear simulation is high for the modal coordinates $\zeta_i(t), \zeta_j(t)$, the corresponding TVDs might be important. Since the modal coordinates are obtained from a linear simulation, the modal interaction factor is cheap to compute. Nevertheless, this strategy does not consider the interaction of modes and neither if a certain mode shape becomes important due to the imposed nonlinearity.

C.1.3 Modal Virtual Work

In [57] a strategy based on the virtual work done by nonlinear forces from mode $\boldsymbol{\phi}_i$ upon another mode $\boldsymbol{\phi}_j$ is presented. For calculating the internal forces $\mathbf{f}(\mathbf{x})$ the maximum modal coordinates of a linear simulation are multiplied with the corresponding mode. Hence, a weighting factor $W_{i,j}$ along

$$\begin{aligned} t_{max} &= \arg\max|\zeta_i(t)| \qquad t \in T, \\ W_{i,j} &= |\boldsymbol{\phi}_j{}^{\mathsf{T}} \mathbf{f}(\zeta_i(t_{max})\,\boldsymbol{\phi}_i)|, \end{aligned} \tag{C.2}$$

can be defined. This weighting factor $W_{i,j}$ is used to capture the interaction of the modes $\boldsymbol{\phi}_j, \boldsymbol{\phi}_i$ and thereby estimating the importance of the associated TVD. Similar to the strategy mentioned in appendix C.1.2, the modal coordinates are obtained from a linear analysis, and consequently the weights cannot be used as reliable quantity for a nonlinear simulation.

Appendix D

Additional information on the implementation

D.1 Preprocessing

Computation of a local coordinate system In general a normal vector $\vec{n}$ with length $\|\vec{n}\|_2 = 1$ from an arbitrary point $\vec{X}$ on a finite element can be computed along

$$\vec{n} = \frac{\vec{X}_{,\xi} \times \vec{X}_{,\eta}}{\|\vec{X}_{,\xi} \times \vec{X}_{,\eta}\|_2}, \tag{D.1}$$

where $() \times ()$ denotes the cross product of two vectors, and $\vec{X}_{,\xi} = \frac{\partial \vec{X}}{\partial \xi}, \vec{X}_{,\eta} = \frac{\partial \vec{X}}{\partial \eta}$ are the partial derivatives of the point with respect to the isoparametric coordinates ξ, η of the finite element.

For an isoparametric element the position vector of an arbitrary point $\vec{X}$ is approximated by

$$\begin{aligned}
\vec{X} &= \sum_{i=1}^{n_{\mathrm{FE}}^e} N_i^e(\xi,\eta)\, \vec{X}_i \\
&= \left[\begin{array}{ccc|ccc|c|ccc} N_1^e & 0 & 0 & N_2^e & 0 & 0 & \cdots & N_{n_{\mathrm{FE}}^e}^e & 0 & 0 \\ 0 & N_1^e & 0 & 0 & N_2^e & 0 & & 0 & N_{n_{\mathrm{FE}}^e}^e & 0 \\ 0 & 0 & N_1^e & 0 & 0 & N_2^e & & 0 & 0 & N_{n_{\mathrm{FE}}^e}^e \end{array}\right] \left[\begin{array}{c} \vec{X}_1 \\ \vec{X}_2 \\ \vdots \\ \vec{X}_{n_{\mathrm{FE}}^e} \end{array}\right] \\
&= \mathbf{N}^e(\xi,\eta)\mathbf{X}^e
\end{aligned} \tag{D.2}$$

where n_{FE}^e denotes the number of FE nodes of the element, $\mathbf{N}^e(\xi,\eta)$ is the $(3 \times 3n_{\mathrm{FE}}^e)$ matrix containing the element shape functions, and the $(3n_{\mathrm{FE}}^e \times 1)$ vector $\mathbf{X}^e$ contains the coordinates of the element nodes. The FE shape functions N_i^e are thereby defined as a function of the isoparametric coordinates $N_i = N_i(\xi,\eta)$ for each element type.

Based on eq. (D.2) the required derivatives $\vec{X}_{,\xi}, \vec{X}_{,\eta}$ for the computation of the normal vector can be written as

$$\vec{X}_{,\xi} = \mathbf{N}_{,\xi}^e \mathbf{X}^e \tag{D.3a}$$

$$\vec{X}_{,\eta} = \mathbf{N}_{,\eta}^e \mathbf{X}^e \tag{D.3b}$$

with the $(3 \times 3n_{\mathrm{FE}}^e)$ matrices $\mathbf{N}_{,\xi}^e = \frac{\partial \mathbf{N}^e}{\partial \xi}, \mathbf{N}_{,\eta}^e = \frac{\partial \mathbf{N}^e}{\partial \eta}$. These matrices can be evaluated in general for each element type based on the isoparametric shape functions.

For the local coordinate system, the tangential vectors $\vec{t}^1$, $\vec{t}^2$ have to form a plane which is orthogonal to the normal vector $\vec{n}$. The first tangential vector can be chosen in an arbitrary direction normal to $\vec{n}$. It has to be mentioned that for numerical reasons the tangential vectors of neighboring contact pairs should have similar or equal orientation. One possibility is, to choose the first tangential vector $\vec{t}^1$ in the direction of the isoparametric coordinate ξ at the point $\vec{X}$. Hence, the tangential vector $\vec{t}^1$ is given by

$$\vec{t}^1 = \frac{\vec{X}_{,\xi}}{\|\vec{X}_{,\xi}\|_2}. \tag{D.4}$$

The second tangential vector for the local coordinate system is computed with the cross product of $\vec{n}$ and $\vec{t}^1$ yielding

$$\vec{t}^2 = \frac{\vec{n} \times \vec{t}^1}{\|\vec{n} \times \vec{t}^1\|_2}. \tag{D.5}$$

Detection of intersections point Mathematically the detection of an intersection point $\vec{\overline{X}}^M(\overline{\xi}, \overline{\eta})$ on the master surface can be formulated as

$$\left[\vec{X}^S - \vec{\overline{X}}^M(\overline{\xi}, \overline{\eta})\right] = \lambda \vec{n}^M(\overline{\xi}, \overline{\eta}), \tag{D.6}$$

where λ denotes the distance between $\vec{X}^S$ and $\vec{\overline{X}}^M(\overline{\xi}, \overline{\eta})$.

This condition can be formulated in an alternative way since there has to be a right angle between the vector $\left[\vec{X}^S - \vec{\overline{X}}^M(\overline{\xi}, \overline{\eta})\right]$ and the tangential vectors $\vec{\overline{X}}_{,\xi}, \vec{\overline{X}}_{,\eta}$. Mathematically this condition is expressed with the dot product $() \cdot ()$ and leads to two equations

$$\left[\vec{X}^S - \vec{\overline{X}}^M(\overline{\xi}, \overline{\eta})\right] \cdot \vec{\overline{X}}_{,\xi} = 0, \tag{D.7a}$$

$$\left[\vec{X}^S - \vec{\overline{X}}^M(\overline{\xi}, \overline{\eta})\right] \cdot \vec{\overline{X}}_{,\eta} = 0, \tag{D.7b}$$

for the unknowns $\overline{\xi}, \overline{\eta}$. In general eq. (D.7) cannot be solved explicitly for all element types. Hence, the computation of the intersection point $\vec{\overline{X}}^M(\overline{\xi}, \overline{\eta})$ has to be performed iteratively.

D.2 MBS including contact and friction forces

The equations in section 3.3.2 have been described for one contact pair. In this section these equations are extended to all n_{CP} contact pairs.

Coordinate transformation for all contact pairs For all n_{CP} contact pairs the transformation between the local coordinate system of the contact pairs and the body coordinate system can be written as

$$ {}^{B}\mathbf{x} = \mathbf{Q}\,{}^{C}\mathbf{x} = \begin{bmatrix} \mathbf{Q}_1 & \mathbf{0} & \cdots & \mathbf{0} \\ \mathbf{0} & \mathbf{Q}_2 & \cdots & \mathbf{0} \\ \vdots & \vdots & \ddots & \vdots \\ \mathbf{0} & \mathbf{0} & \cdots & \mathbf{Q}_{n_{\mathrm{CP}}} \end{bmatrix} \begin{bmatrix} {}^{C_1}\vec{x}_1 \\ {}^{C_2}\vec{x}_2 \\ \vdots \\ {}^{C_{n_{\mathrm{CP}}}}\vec{x}_{n_{\mathrm{CP}}} \end{bmatrix} \tag{D.8} $$

with the block diagonal $(3n_{\mathrm{CP}} \times 3n_{\mathrm{CP}})$ matrix $\mathbf{Q}$ and the $(3n_{\mathrm{CP}} \times 1)$ vectors ${}^{B}\mathbf{x}$ and ${}^{C}\mathbf{x}$. The inverse transformation from the body reference frame into the local coordinate systems can be written as

$$ {}^{C}\mathbf{x} = \mathbf{Q}^{\mathsf{T}}\,{}^{B}\mathbf{x}. \tag{D.9} $$

Displacements of all slave nodes For all n_{CP} slave nodes the displacements in the local coordinate systems can be collected in the $(3n_{\mathrm{CP}} \times 1)$ vector ${}^{C}\mathbf{x}^{S}$ defined as

$$ {}^{C}\mathbf{x}^{S} = \begin{bmatrix} {}^{C_1}\vec{x}_1^{S\mathsf{T}} & \dots & {}^{C_i}\vec{x}_i^{S\mathsf{T}} & \dots & {}^{C_{n_{\mathrm{CP}}}}\vec{x}_{n_{\mathrm{CP}}}^{S\mathsf{T}} \end{bmatrix}^{\mathsf{T}}. \tag{D.10} $$

Applying the definition of ${}^{C_i}\vec{x}_i^{S}$ given by eq. (3.75), the vector of all slave displacements can be written as

$$ {}^{C}\mathbf{x}^{S} = \mathbf{Q}^{\mathsf{T}}\mathbf{P}_1\boldsymbol{\Phi}\boldsymbol{\zeta}, \tag{D.11} $$

where $\mathbf{P}_1$ denotes a $(3n_{\mathrm{CP}} \times n_{\mathrm{FE}})$ assignment matrix that extracts the trial vectors associated to the slave nodes out of all trial vectors given by the $(n_{\mathrm{FE}} \times r)$ matrix $\boldsymbol{\Phi}$.

Displacements of all intersection points For all n_{CP} intersection points the displacements in the local coordinate systems can be combined in the $(3n_{\mathrm{CP}} \times 1)$ vector ${}^{C}\mathbf{x}^{M}$ which can be written as

$$ {}^{C}\mathbf{x}^{M} = \begin{bmatrix} {}^{C_1}\vec{x}_1^{M\mathsf{T}} & \dots & {}^{C_i}\vec{x}_i^{M\mathsf{T}} & \dots & {}^{C_{n_{\mathrm{CP}}}}\vec{x}_{n_{\mathrm{CP}}}^{M\mathsf{T}} \end{bmatrix}^{\mathsf{T}}. \tag{D.12} $$

Applying the definition of ${}^{C_i}\vec{x}_i^{M}$ given by eq. (3.78) to the previous equation the vector ${}^{C}\mathbf{x}^{M}$ can be written as

$$ {}^{C}\mathbf{x}^{M} = \mathbf{Q}^{\mathsf{T}}\overline{\mathbf{N}}\mathbf{P}_0\boldsymbol{\Phi}\boldsymbol{\zeta}, \tag{D.13} $$

with the $(3n_{\mathrm{CP}} \times 3n_{\mathrm{CP}}n_{\mathrm{FE}}^{e})$ matrix

$$ \overline{\mathbf{N}} = \begin{bmatrix} \overline{\mathbf{N}}_1^{e} & \mathbf{0} & \cdots & \mathbf{0} \\ \mathbf{0} & \overline{\mathbf{N}}_2^{e} & \cdots & \mathbf{0} \\ \vdots & \vdots & \ddots & \vdots \\ \mathbf{0} & \mathbf{0} & \cdots & \overline{\mathbf{N}}_{n_{\mathrm{CP}}}^{e} \end{bmatrix}, \tag{D.14} $$

the $(3n_{\mathrm{CP}}n_{\mathrm{FE}}^{e} \times n_{\mathrm{FE}})$ assignment matrix $\mathbf{P}_0$, and the $(n_{\mathrm{FE}} \times r)$ matrix $\boldsymbol{\Phi}$ containing the trial vectors for all FE nodes. The assignment matrix $\mathbf{P}_0$ extracts the trial vectors of the FE nodes included in the master surface out of all FE trail vectors.

Relative displacements for all contact pairs For all n_{CP} contact pairs the relative displacements are collected in the $(3n_{\mathrm{CP}} \times 1)$ vector ${}^{C}\mathbf{y}^{MS}$. This vector can be computed along

$$ {}^{C}\mathbf{y}^{MS} = {}^{C}\mathbf{x}^{M} - {}^{C}\mathbf{x}^{S} = {}^{C}\mathbf{\Phi}^{MS}\,\boldsymbol{\zeta} \tag{D.15} $$

with the $(3n_{\mathrm{CP}} \times r)$ matrix

$$ {}^{C}\mathbf{\Phi}^{MS} = \mathbf{Q}^{\mathsf{T}}\left[\overline{\mathbf{N}}\mathbf{P}_0 - \mathbf{P}_1\right]\mathbf{\Phi}, \tag{D.16} $$

whereby the matrices defined in the previous paragraphs are used.

For the consideration of the initial gaps and the tangential displacements before contact closure, the tangential and normal components are separated. For the entire system of all n_{CP} contact pairs the normal gaps are collected in the $(n_{\mathrm{CP}} \times 1)$ vector

$$ {}^{C}\mathbf{g}_N = \begin{bmatrix} {}^{C_1}g_{N,1,0} \\ \vdots \\ {}^{C_i}g_{N,i,0} \\ \vdots \\ {}^{C_{n_{\mathrm{CP}}}}g_{N,n_{\mathrm{CP}},0} \end{bmatrix} + \begin{bmatrix} {}^{C_1}\mathbf{\Phi}^{MS}_{1,n} \\ \vdots \\ {}^{C_i}\mathbf{\Phi}^{MS}_{i,n} \\ \vdots \\ {}^{C_{n_{\mathrm{CP}}}}\mathbf{\Phi}^{MS}_{n_{\mathrm{CP}},n} \end{bmatrix}^{\mathsf{T}} \boldsymbol{\zeta} = {}^{C}\mathbf{g}_{N,0} + {}^{C}\mathbf{\Phi}^{MS}_{n}\,\boldsymbol{\zeta} \tag{D.17} $$

and the tangential displacements in the $(2n_{\mathrm{CP}} \times 1)$ vector

$$ {}^{C}\mathbf{s} = -\begin{bmatrix} {}^{C_1}s_{1,1,t^*} \\ {}^{C_1}s_{2,1,t^*} \\ \vdots \\ {}^{C_i}s_{1,i,t^*} \\ {}^{C_i}s_{2,i,t^*} \\ \vdots \\ {}^{C_{n_{\mathrm{CP}}}}s_{1,n_{\mathrm{CP}},t^*} \\ {}^{C_{n_{\mathrm{CP}}}}s_{2,n_{\mathrm{CP}},t^*} \end{bmatrix} + \begin{bmatrix} {}^{C_1}\mathbf{\Phi}^{MS}_{1,t1} \\ {}^{C_1}\mathbf{\Phi}^{MS}_{1,t2} \\ \vdots \\ {}^{C_i}\mathbf{\Phi}^{MS}_{i,t1} \\ {}^{C_i}\mathbf{\Phi}^{MS}_{i,t2} \\ \vdots \\ {}^{C_{n_{\mathrm{CP}}}}\mathbf{\Phi}^{MS}_{n_{\mathrm{CP}},t1} \\ {}^{C_{n_{\mathrm{CP}}}}\mathbf{\Phi}^{MS}_{n_{\mathrm{CP}},t2} \end{bmatrix} \boldsymbol{\zeta} = {}^{C}\mathbf{s}_{t^*} + {}^{C}\mathbf{\Phi}^{MS}_{t}\,\boldsymbol{\zeta} \tag{D.18} $$

Nonlinear forces on slave surface Applying the definition of the vector ${}^{C_i}\vec{\nu}_i$ given by eq. (3.81) to all contact pairs yields the $(3n_{\mathrm{CP}} \times 1)$ vector

$$ {}^{C}\boldsymbol{\nu}^{S} = \begin{bmatrix} {}^{C_1}\vec{\nu}_1^{\,\mathsf{T}} & \dots & {}^{C_i}\vec{\nu}_i^{\,\mathsf{T}} & \dots & {}^{C_{n_{\mathrm{CP}}}}\vec{\nu}_{n_{\mathrm{CP}}}^{\mathsf{T}} \end{bmatrix}^{\mathsf{T}}. \tag{D.19} $$

The vector ${}^{C}\boldsymbol{\nu}^{S}$ can be transformed in the body reference frame with the matrix $\mathbf{Q}$ defined by eq. (D.8), yielding

$$ {}^{B}\boldsymbol{\nu}^{S} = \mathbf{Q}\,{}^{C}\boldsymbol{\nu}^{S}. \tag{D.20} $$

The nodal forces for all contact pairs on the slave surface can be written according to eq. (3.82) in a $(3n_{\mathrm{CP}} \times 1)$ vector

$$ {}^{B}\mathbf{f}^{S} = \mathbf{A}\,{}^{B}\boldsymbol{\nu}^{S} = \mathbf{A}\mathbf{Q}\,{}^{C}\boldsymbol{\nu}^{S}, \tag{D.21} $$

where the $(3n_{\mathrm{CP}} \times 3n_{\mathrm{CP}})$ matrix $\mathbf{A}$ holds an assembly of the surface integrals of the finite elements involved on the slave surface.

Modal force on slave surface Applying the computation of the modal forces for the slave surface as defined by eq. (3.83) yields the $(r \times 1)$ vector

$$\mathbf{f}^{m,S} = \mathbf{\Phi}^{S^{\mathsf{T}}}\, {}^{B}\mathbf{f}^{S} = \mathbf{\Phi}^{S^{\mathsf{T}}}\, \mathbf{A}\mathbf{Q}\, {}^{C}\boldsymbol{\nu}^{S}, \tag{D.22}$$

where the $(3n_{\mathrm{CP}} \times r)$ matrix $\mathbf{\Phi}^{S}$ is defined by $\mathbf{\Phi}^{S} = \mathbf{P}_1\mathbf{\Phi}$.

This equation can be written in a more compact form along

$$\mathbf{f}^{m,S} = \mathbf{\Theta}^{S}\, {}^{C}\boldsymbol{\nu}^{S} \tag{D.23}$$

with the $(r \times 3n_{\mathrm{CP}})$ matrix $\mathbf{\Theta}^{S} = \mathbf{\Phi}^{S^{\mathsf{T}}}\, \mathbf{A}\mathbf{Q}$.

Nonlinear forces on master surface To get the nodal forces for the entire master surface, the forces of all finite elements on the master surface need to systematically assembled. For this purpose the $(3n_{\mathrm{CP}}n^{e}_{\mathrm{FE}} \times 1)$ vector ${}^{B}\mathbf{f}^{D}$

$${}^{B}\mathbf{f}^{D} = \left[{}^{B}\mathbf{f}^{e}_{1}{}^{\mathsf{T}} \quad \dots \quad {}^{B}\mathbf{f}^{e}_{i}{}^{\mathsf{T}} \quad \dots \quad {}^{B}\mathbf{f}^{e}_{n_{\mathrm{CP}}}{}^{\mathsf{T}} \right]^{\mathsf{T}} \tag{D.24}$$

is defined. If one element on the master surface has more than one intersection point with slave points this finite element appears several times in the vector ${}^{B}\mathbf{f}^{D}$. By using the definition of eq. (3.85) for all elements on the master surface the vector defined in eq. (D.24) can be written as

$${}^{B}\mathbf{f}^{D} = \widetilde{\mathbf{N}}\, {}^{B}\mathbf{f}^{S} \tag{D.25}$$

with the $(3n_{\mathrm{CP}}n^{e}_{\mathrm{FE}} \times 3n_{\mathrm{CP}})$ sparse block matrix

$$\widetilde{\mathbf{N}} = \begin{bmatrix} \widetilde{\mathbf{N}}^{e}_{1} & \mathbf{0} & \cdots & \mathbf{0} \\ \mathbf{0} & \widetilde{\mathbf{N}}^{e}_{2} & \cdots & \mathbf{0} \\ \vdots & \vdots & \ddots & \vdots \\ \mathbf{0} & \mathbf{0} & \cdots & \widetilde{\mathbf{N}}^{e}_{n_{\mathrm{CP}}} \end{bmatrix}, \tag{D.26}$$

with the $(3n^{e}_{\mathrm{FE}} \times 3)$ submatrices $\widetilde{\mathbf{N}}^{e}_{i} = -\left[\mathbf{N}^{e}\left(\overline{\xi}_i, \overline{\eta}_i\right)\right]^{\mathsf{T}}$ and ${}^{B}\mathbf{f}^{S}$ being defined by eq. (D.21).

As already mentioned in the vector ${}^{B}\mathbf{f}^{D}$ one FE node can appear several times. Hence, a mapping of the vector ${}^{B}\mathbf{f}^{D}$ on the $(3n_{\mathrm{Ma}} \times 1)$ vector ${}^{B}\mathbf{f}^{M}$ is required. Whereby n_{Ma} denotes the number of FE nodes on the master surface. The mentioned task is achieved by a matrix multiplication in the form

$${}^{B}\mathbf{f}^{M} = \mathbf{P}_4\, {}^{B}\mathbf{f}^{D} \tag{D.27}$$

with the $(n_{\mathrm{Ma}} \times 3n_{\mathrm{CP}}n^{e}_{\mathrm{FE}})$ sparse block matrix

$$\mathbf{P}_4 = \begin{bmatrix} \ddots & & \\ & \mathbf{P}_{4,ij} & \\ & & \ddots \end{bmatrix}, \tag{D.28}$$

where the (3×3) submatrix $\mathbf{P}_{4,ij}$ is a identity matrix if the node i of the vector ${}^{B}\mathbf{f}^{M}$ is identical with the node j of the vector ${}^{B}\mathbf{f}^{D}$. Otherwise $\mathbf{P}_{4,ij}$ is a zero matrix.

Combining the previous introduced formulas the vector ${}^{B}\mathbf{f}^{M}$ can be computed along

$$ {}^{B}\mathbf{f}^{M} = \mathbf{P}_4 \widetilde{\mathbf{N}} \, {}^{B}\mathbf{f}^{S} = \mathbf{P}_4 \widetilde{\mathbf{N}} \mathbf{A} \mathbf{Q} \, {}^{C}\boldsymbol{\nu}^{S}. \tag{D.29} $$

Modal force on master surface For the inclusion of the nodal forces in the context of MBS the vector eq. (D.29) is pre-multiplied with the transposed $(3n_{\mathrm{Ma}} \times r)$ matrix of trial vectors $\boldsymbol{\Phi}^{Ma}$ corresponding to the FE nodes in the vector ${}^{B}\mathbf{f}^{M}$. This yields the $(r \times 1)$ vector

$$ \mathbf{f}^{m,M} = \left[\boldsymbol{\Phi}^{Ma}\right]^{\mathsf{T}} \, {}^{B}\mathbf{f}^{M} = \left[\boldsymbol{\Phi}^{Ma}\right]^{\mathsf{T}} \mathbf{P}_4 \widetilde{\mathbf{N}} \mathbf{A} \mathbf{Q} {}^{C}\boldsymbol{\nu}^{S} = \boldsymbol{\Theta}^{M} \, {}^{C}\boldsymbol{\nu}^{S}, \tag{D.30} $$

with the $(r \times 3n_{\mathrm{CP}})$ matrix $\boldsymbol{\Theta}^{M} = \left[\boldsymbol{\Phi}^{Ma}\right]^{\mathsf{T}} \mathbf{P}_4 \widetilde{\mathbf{N}} \mathbf{A} \mathbf{Q}$.

Computation of overall modal force The overall modal forces due to the slave nodes (see eq. (D.23)) and due to the master surface (see eq. (D.30)) can be combined in the $(r \times 1)$ vector

$$ \mathbf{f}^{m} = \mathbf{f}^{m,S} + \mathbf{f}^{m,M} = \boldsymbol{\Theta}^{S} \, {}^{C}\boldsymbol{\nu}^{S} + \boldsymbol{\Theta}^{M} \, {}^{C}\boldsymbol{\nu}^{S} = \boldsymbol{\Theta} \, {}^{C}\boldsymbol{\nu}^{S}, \tag{D.31} $$

with the $(r \times 3n_{\mathrm{CP}})$ matrix $\boldsymbol{\Theta} = \boldsymbol{\Theta}^{S} + \boldsymbol{\Theta}^{M}$.

Appendix E

Additional information on contact and friction models

E.1 Additional friction models

In the literature several friction models can be found which do not fulfill the defined criteria mentioned in sec. 2.4.1 or have some critical disadvantages. Some of these models are shortly reviewed and discussed in this section.

LuGre friction model The LuGre friction model introduced in [16] is an extension of the Dahl friction model. In [79] a detailed investigation of the model and its applications can be found. Additionally to the Dahl friction model the Striebeck effect can be captured with the LuGre model. For the computation of friction inside joints the Striebeck effect is not relevant, and hence the LuGre friction was not investigated in detail.

Models with fractional derivatives A generalization of viscous damping is the use of fractional derivatives, see [105, 106] and the literature cited there. This element can be used to replace the damping elements in the viscous damping models of fig. 2.12. The use of such fractional elements allows to influence the frequency dependency of the friction model, but frequency independence cannot be achieved. With respect to the criteria mentioned in sec. 2.4.1 the conclusions are very similar to the ones for viscous damping:

- There is always a frequency dependency, even if it can be influenced.
- It is not possible in a straight forward matter to model two separated stiffness regimes for sticking and slipping.
- Consequently, there is always energy dissipation. It is not possible to restrict the energy dissipation to the slipping regime.

Due to the latter mentioned significant shortcomings in terms of the required joint model characteristics no detailed investigations of the numerical characteristics were performed.

Masing approximation The series connection of a spring with stiffness c_1 and a Coulomb element with the sticking stress limit R_G as used in the reference model (see fig. 2.4) can be described with the differential equation (see [61])

$$\dot{\tau}_M = \frac{1}{2} c_1 \dot{s} \left(1 - \operatorname{sgn}\left(\tau_M^2 - R_G^2\right) - \operatorname{sgn}\left(\dot{s}\tau_M\right)\left(1 + \operatorname{sgn}\left(\tau_M^2 - R_G^2\right)\right)\right). \tag{E.1}$$

In order to overcome the numerical stability problems caused by eq. (E.1) a regularized approximation of the signum function in the form of

$$\operatorname{sgn}\left(\tau_M^2 - R_G^2\right) \approx \left|\frac{\tau_M}{R_G}\right|^n - 1, \tag{E.2}$$

can be used. Inserting this approximation into eq. E.1 leads to the Masing approximation for the friction stress

$$\dot{\tau}_M = c_1 \dot{s} \left(1 - \frac{1}{2}\left|\frac{\tau_M}{R_G}\right|^n \left(1 + \operatorname{sgn}\left(\dot{s}\tau_M\right)\right)\right), \tag{E.3}$$

which produces a good representation of the series spring - Coulomb element connection for increasing exponents $n > 0$ in the value domain of $-R_G \leq \tau_M \leq R_G$. In [61] it is mentioned that the differential equations for the Masing approximation and the Bouc–Wen model eq. (2.122) have the same structure, and hence the Masing approximation was not considered in the detailed investigation.

E.2 Derivative $\frac{\partial p_{N,i}}{\partial g_{N,i}}$ for selected penalty models

Linear penalty model

$$\frac{\partial p_N}{\partial g_N} = \begin{cases} 0 & \text{if } g_N \geq 0, \\ -\varepsilon_N & \text{if } g_N < 0. \end{cases} \tag{E.4}$$

Multi-stage linear penalty model

$$\frac{\partial p_N}{\partial g_N} = \begin{cases} 0 & \text{if } g_N \geq 0, \\ -\varepsilon_{N0} & \text{if } g_{N0} > g_N > g_{N1}, \\ -\varepsilon_{N1} & \text{if } g_N \leq g_{N1}. \end{cases} \tag{E.5}$$

Power-function-based nonlinear penalty model

$$\frac{\partial p_N}{\partial g_N} = \begin{cases} 0 & \text{if } g_N \geq 0, \\ -m\varepsilon_N |\ g_{N,i}\ |^{m-1} & \text{if } g_N < 0. \end{cases} \tag{E.6}$$

Combined quadratic-linear penalty model

$$\frac{\partial p_N}{\partial g_N} = \begin{cases} 0 & \text{if } g_N \geq g_{N0}, \\ -\frac{1}{g_{N1}-g_{N0}} \varepsilon_N \left(g_N - g_{N0}\right) & \text{if } g_{N0} > g_N > g_{N1}, \\ -\varepsilon_N & \text{if } g_N \leq g_{N1}. \end{cases} \tag{E.7}$$

Exponential penalty model

$$\frac{\partial p_N}{\partial g_N} = \begin{cases} 0 & \text{if } g_N \geq g_{N0}, \\ \frac{p_{N0}}{\exp(1)-1} \left[\frac{1}{g_{N0}} \left(\frac{-g_{N,i}}{g_{N0}} + 2 \right) \exp\left(\frac{-g_N}{g_{N0}} + 1 \right) - \frac{1}{g_{N0}} \right] & \text{if } g_N < g_{N0}. \end{cases} \tag{E.8}$$

Joint-adapted exponential penalty model

$$\frac{\partial p_N}{\partial g_N} = \begin{cases} 0 & \text{if } g_N \geq g_0, \\ -\varepsilon_N \left(\exp\left(\lambda_N \left(-g_N + g_{N0}\right)\right) - 1\right) & \\ \quad - \lambda_N \varepsilon_N \left(-g_N + g_{N0}\right) \exp\left(\lambda_N \left(-g_N + g_{N0}\right)\right) & \text{if } g_N < g_{N0}. \end{cases} \tag{E.9}$$

Appendix F

Additional information on the examples

F.1 Additional results for the bolted bearing cap

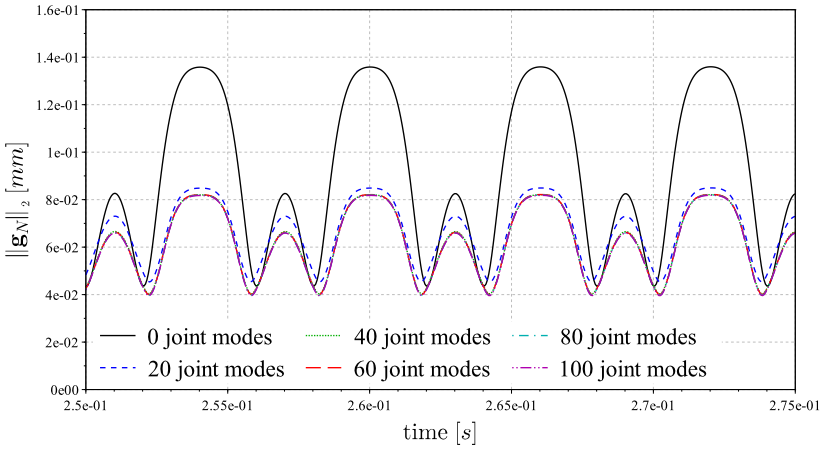

Figure F.1: Dynamic convergence of $\|\mathbf{g}_N\|_2$: joint modes based on wPOD of TVDs

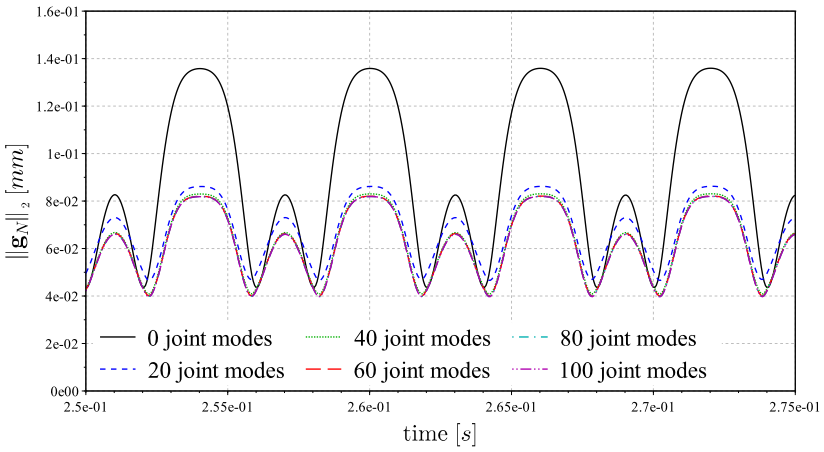

Figure F.2: Dynamic convergence of $\|\mathbf{g}_N\|_2$: joint modes based on POD of TVDs

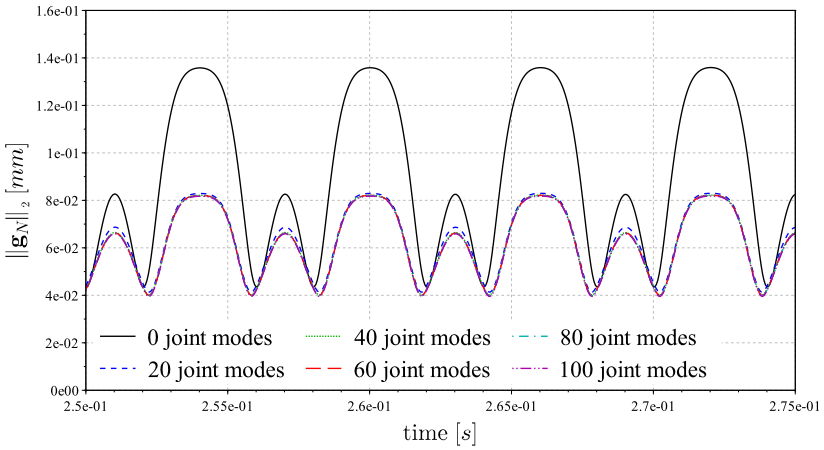

Figure F.3: Dynamic convergence of $\|\mathbf{g}_N\|_2$: joint modes based on POD of forces

Results of dynamic convergence study of section 4.2.1

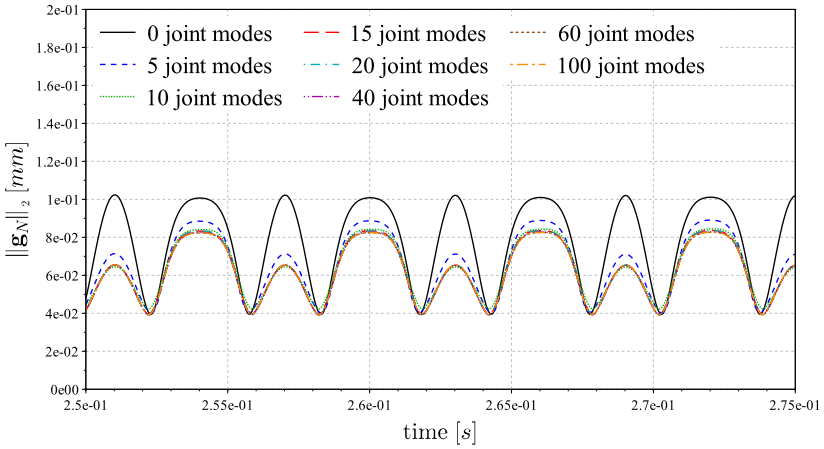

Figure F.4: Dynamic convergence of $\|\mathbf{g}_N\|_2$: 1 PLM – wPOD only PLM TVDs

Results of dynamic convergence study of section 4.2.2

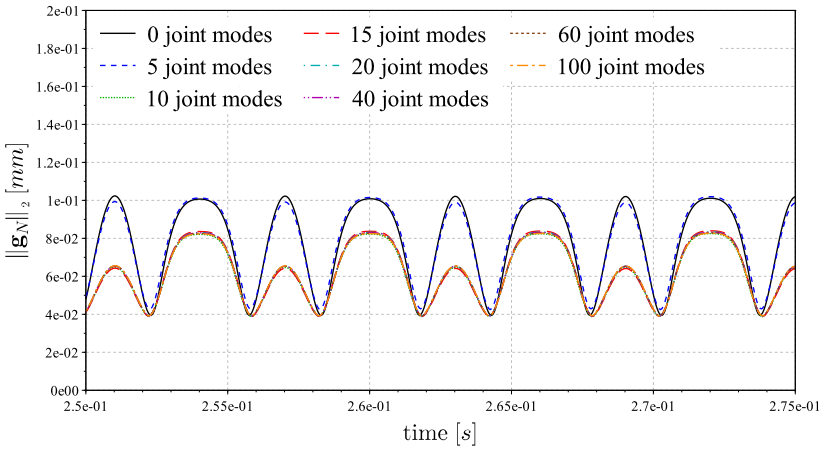

Figure F.5: Dynamic convergence of $\|\mathbf{g}_N\|_2$: 1 PLM – wPOD all TVDs

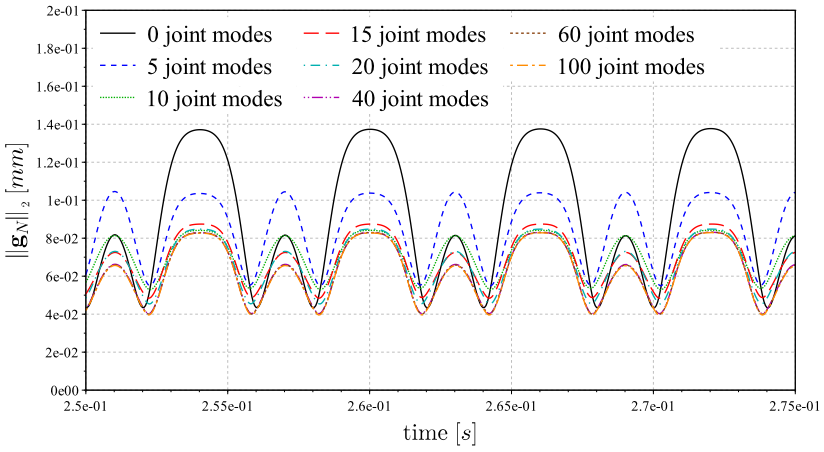

Figure F.6: Dynamic convergence of $\|\mathbf{g}_N\|_2$: 0 PLM – wPOD all TVDs

F.2 Evaluation of the reduction basis for the 2D car pendulum

In this section the convergence study for the 2D car pendulum used for the evaluation of contact models is complemented. These results can also be found in the already published work [89].

In fig. F.7 the first 18 free-free modes of the reduction basis, computed with mode shape orthogonalization out of $v = 5$ bending vibration modes, $s = 6$ static deformation modes and $g = 20$ joint modes based on wPOD of TVDs are shown. The first five trial vectors in this figure correspond to the vibration modes, whereas the other trial vectors are joint modes. The eigenfrequencies of the five vibration modes is in the range of 30 Hz and 510 Hz The figure shows the increased flexibility of joint modes between the metal sheets in the joint area. The external force f_{ext} was applied for this convergence study as a smoothed step function (force0) using a half-wave cosine with a short period of $T = 0.05$ s as shown in

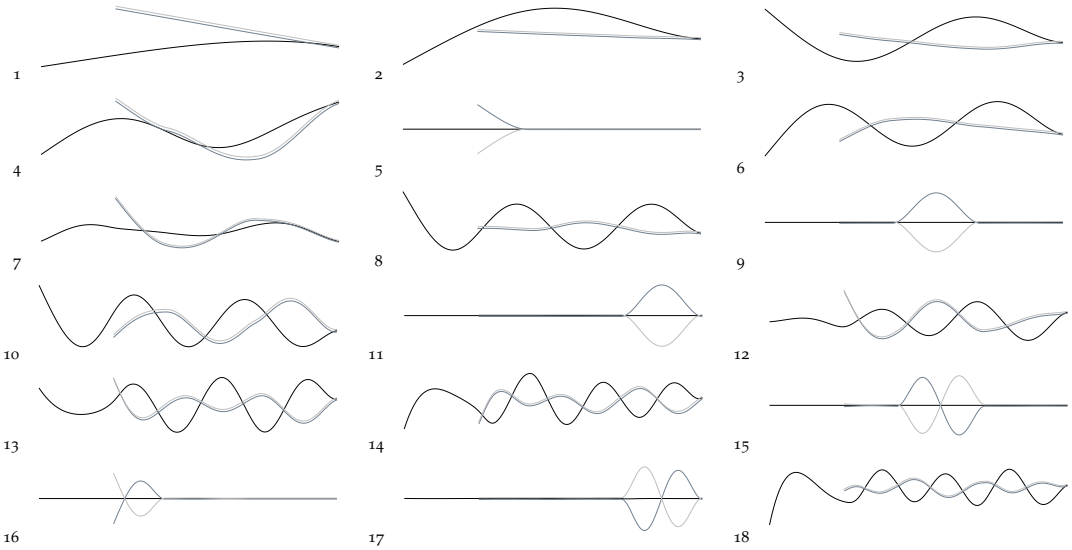

Figure F.7: Used trial vectors $\mathbf{\Phi}_{free}$

fig. 4.33. As a convergence criterion the Euclidean norm of the contact force vector $\mathbf{f}_c$ was used and plotted for different number of joint modes in fig. F.8. For this convergence study the linear penalty model was used, but it was observed that the use of other contact models does not influence the convergence in terms of joint modes.

Without the use of additional joint modes the contact forces are distinctly overestimated. The contact forces computed with $g = 60$ joint modes are very close to the converged solution and, therefore all further computations are executed with $g = 60$ joint modes.

In terms of computational time it can be reported, that the simulation with $g = 60$ joint modes needs only 0.2 % of the CPU time required for a simulation where all 903 contact pairs are considered separately.

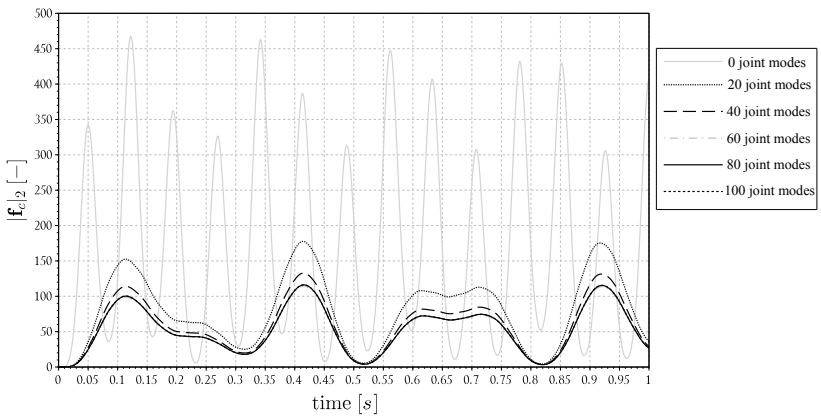

Figure F.8: Convergence study for number of joint modes